DEFORMATION MECHANISMS IN SINGLE CRYSTALLINE AND ULTRAFINE POLYCRYSTALLINE MEDIUM AND HIGH ENTROPY ALLOYS

A Dissertation

by

SEZER PICAK

Submitted to the Graduate and Professional School of
Texas A&M University
in partial fulfillment of the requirements for the degree of

DOCTOR OF PHILOSOPHY

Chair of Committee,	Ibrahim Karaman
Committee Members,	Bruce Tai
	Justin Wilkerson
	Yu Xie
Head of Department,	Andreas A. Polycarpou

August 2021

Major Subject: Mechanical Engineering

ABSTRACT

Medium- and high-entropy alloys (M/HEAs) offer a much larger and richer design space than conventional alloys, providing new opportunities for discovering unexplored physics and functionalism. Some of these alloys exhibit an outstanding combination of high strength and ductility, which has been linked to the activation of various deformation modes triggered by low and medium-energy stacking faults. Although there are many recent works uncovering the microscopic and macroscopic features of these materials, there is a striking paucity on the investigation of single crystalline M/HEAs that would allow for a superior understanding of the fundamental deformation mechanisms. Therefore, exact atomistic and microstructural reasons for the exceptional mechanical response of these alloys are not fully understood. With this need, the present study is focused on the fabrication and characterization of M/HEA single and polycrystals to explore the underlying deformation mechanisms providing outstanding mechanical properties.

In the present work, NiCoCr, $Fe_{40}Mn_{40}Co_{10}Cr_{10}$, CoCrFeMnNi and $Fe_{50}Mn_{30}Co_9Cr_9$ + 2C at.% M/HEAs have been studied for a multitude of reasons. The orientation dependence of tensile deformation in NiCoCr MEA and $Fe_{40}Mn_{40}Co_{10}Cr_{10}$ HEA was investigated in [001], [011], [111] and [123] oriented single crystals. Several microstructural investigations were performed to reveal the major mechanisms controlling the deformation stages. Later, using extensive microstructural characterization of bulk single crystal experiments, it was discovered that the extraordinary mechanical properties of NiCoCr arise from the existence of short range atomic order (SRO), which triggers the simultaneous activation of deformation twinning-induced plasticity and martensitic transformation-induced plasticity (TWIP and TRIP), and leads to dynamic hardening against dislocation motion due to continuously refining length scales as a result of the nano twin and nano-martensite boundaries. By controlling the degree of SRO through aging at high

temperatures, the level of twinning and strain-induced phase transformation was increased, further enhancing the ductility levels in NiCoCr. These results indicate that the interplay of SRO and plasticity could be exploited to trigger various deformation modes to discover new M/HEAs with unprecedented mechanical properties.

However, the yield strength levels of some of the M/HEAs are still low as compared to other high strength materials. Therefore, the present work also aims to reveal the effect of interstitial solid solution hardening, grain refinement on the post processing mechanical properties using the equal channel angular pressing (ECAP), and precipitation hardening. An experimental study was performed on the CoCrFeMnNi HEA single crystals with and without carbon addition. Carbon addition shows a simultaneous improvement in strength and ductility. In the carbon doped single crystals, more twining density suppressed the neck instability and significantly enhanced the ductility. ECAP was employed to improve the mechanical behavior of the most well-known HEA, CoCrFeMnNi, through microstructural refinement. Very high yield strength levels around 1 GPa were obtained after ECAP via grain refinement, high dislocation density, and the activation of TWIP/TRIP that are anomalous at high temperatures. Finally, the superior mechanical behavior of medium entropy Fe-30Mn-8.5Al-0.9Si-0.9C-0.5Mo (wt.%) lightweight steel was reported owing to nanoscale ordered κ-carbide precipitates. However, the precipitate distribution in the microstructure was not always homogeneous, which caused an anisotropic mechanical behavior. In this study, reasons for the anisotropic mechanical properties were attributed to the chemical segregation bands.

Finally, data reporting on the fatigue properties of M/HEAs is only available scarcely in polycrystalline materials and there is no single crystalline study exploring orientation dependence of cyclic loading of HEAs so far. In this study, the cyclic response of single crystalline $Fe_{50}Mn_{30}Co_9Cr_9$ + 2C at.% and polycrystalline CoCrFeMnNi HEAs was also investigated during

strain-controlled low cycle fatigue tests under fully reversed push-pull loading at room temperature. The microstructural evolution during cyclic loading was compared to the microstructure under quasi-static monotonic loading. The orientation dependence of the fatigue life and cyclic hardening was presented. The fatigue life and cyclic hardening behavior were governed by the refined grain size, high density dislocation walls, and the annihilation of existing dislocations resulting in the formation of cell structures in the polycrystalline specimens.

DEDICATION

To my family

and

To Mustafa Kemal Ataturk, the founder of the modern Turkish Republic.

ACKNOWLEDGEMENTS

I would like to express my respect and gratitude to my graduate advisor, Dr. Ibrahim Karaman, for always supporting me and giving me the chance to pursue a doctoral degree. During my PhD education, he has been a role model for me with his unparalleled discipline, perseverance, and hard work in every aspect of life and his great enthusiasm for research.

I would like to thank my committee members, Dr. Justin Wilkerson, Dr. Bruce Tai, and Dr. Yu Xie, for their guidance and support throughout the course of this research.

I would like to thank Professor Yuriy I. Chumlyakov and Professor Thomas Niendorf. Professor Chumlyakov provided the single crystals utilized in this study. The excitement of Prof. Chumlyakov for the research findings, his vision on many scientific issues, and long fruitful discussions piqued the author`s attention to question the details of the problems. The author would also like to thank Prof. Niendorf to give an opportunity to performed low-cycle fatigue experiments during my visit at University of Kassel. Working with Prof. Niendorf in a daily basis during the author visit at University of Kassel helped me to understand the microstructural evaluation of HEAs under cyclic loading. While working with Dr. Xie, his patience for answering the author`s questions helped me to properly link the mechanical properties to the microstructure using transmission electron microscopy results.

I would like to acknowledge Dr. Prashant Singh, Dr. Ceylan Hayrettin, Dr. Tejas Umale, Dr. Abhinav Srivastava, Dr. Daniel Salas, Dr. Peyman Samimi, Dr. Thomas

Wegener, Dr. Sayedvahid Sajjadifar, Dr. Cesar Sabero, Dexin Zhao, Dr. Omer Karakoc, Dr. Wahaz Nasim, Cansu Havva Yilmaz and Mustafa Cilkiz. Special thanks to Dr. Okan Demir and Dr. Haluk Burak Kaybal for their precious support for my PhD education. I am grateful to Prashant for his assistance in density factional theory calculations, in-depth discussion, and sharing his results. Ceylan, Tejas, Abhinav, and Wahaz helped with the experiments early on in my research. Thomas, Sayedvahid, and Cesar helped with low-cycle fatigue tests at The University of Kassel. Thanks also go to my friends, colleagues, and department faculty and staff for making my time at Texas A&M University a great experience.

I would like to dedicate this dissertation to my family, Nafiye and Yusuf and Rabia Picak, who never stop supporting me and giving their endless love to me. Thank you forever. Additionally, this dissertation is dedicated to Mustafa Kemal Ataturk who is the source of my endless motivation. If nothing works, the author always follows Ataturk`s suggestions. As Ataturk said “science is the most reliable guide for civilization, for life, for success in the world”. He also said “if one day any words are against science, choose science.” Keeping his valuable advises in mind, I always believe in science and myself, listen to others, speak out, and never give up.

CONTRIBUTORS AND FUNDING SOURCES

Contributors

This work was supervised by a thesis committee consisting of Professor Ibrahim Karaman of the Department of Material Science and Engineering (advisor), Dr. Yu Xie of the Department of Material Science and Engineering and Dr. Justin Wilkerson of the Department of Mechanical Engineering and Dr. Brice Tai of the Department of Mechanical Engineering.

All density functional theory calculations and molecular dynamic calculations were provided by Prashant Singh. Dr. Jun Liu helped for the TEM works in Chapter 3 and Chapter 4, but all TEM results were analyzed and interrupted by the student.

All other work conducted for the thesis was completed by the student independently.

Funding Sources

The present research was supported by the Chevron Professorship I at Texas A&M University. The research of FeMnAl is sponsored by the DLA-Troop Support, Philadelphia, PA and the Defense Logistics Agency Information Operations, J68, Research & Development, Ft. Belvoir, VA. Sezer Picak acknowledges a graduate scholarship from the Ministry of National Education of Turkey.

NOMENCLATURE

ASTM	American Society for Testing and Materials
BSE	Backscattered electron
CDR	Cyclic Deformation Response
CG	Coarse Grained
CRSS	Critical Resolved Shear Stress
DSA	Dynamic Strain Aging
EBSD	Electron Backscatter Diffraction
ECAP	Equal Channel Angular Pressing
EDM	Electrical Discharge Machining
HEA	High Entropy Alloy
HCF	High-Cycle Fatigue
HDDW	High Density Dislocation Wall
HPT	High Pressure Torsion
HRTEM	High Resolution Transmission Electron Microscopy
LCF	Low Cycle Fatigue
MEA	Medium Entropy Alloy
MPEA	Multi-Principal Element Alloy
SEM	Scanning Electron Microscopy
SFE	Stacking Fault Energy
SPD	Severe plastic deformation

T	Temperature
TEM	Transmission Electron Microscopy
UFG	Ultra-Fine Grained
WDS	Wavelength Dispersive Spectroscopy
XRD	Stacking Fault Energy
ΔG_{mix}	Gibbs free energy of mixing
ΔH_{mix}	Mixing Enthalpy
ΔS_{mix}	Mixing Entropy
ΔS_{conf}	The difference in configurational entropy per mole of a system
fcc	Face Centered Cubic
A_0	Initial area
A_f	Final area
ψ	The die corner angel
ϕ	The channel angel
τ_{cr}^{sl}	Critical shear stress for slip
τ_{cr}^{tw}	Critical shear stress for twinning
m_{slip}	Schmid factor for slip
$m_{twinning}$	Schmid factor for twinning

TABLE OF CONTENTS

Page

LIST OF FIGURES

Page

LIST OF TABLES

Page

1. INTRODUCTION [1234]

1.1. Background and Motivation

For Ages, humans have been endeavoring to alter properties of materials via alloying in metallic systems. Typically, a primary element includes a percent of secondary element since the Bronze Age. For example, conventional steels are composed primarily of iron with relatively small amounts of carbon and chromium for strength and corrosion resistance, respectively. However, the basic alloying strategy restricts the compositional space for the alloying. Therefore, a new alloying strategy has been needed to extend the compositional space for alloy design. Recently, Medium-entropy alloys and high-entropy alloys (MEAs/HEAs) represent a new path for future alloy design strategies, and are a

---

[1] Reprinted with permission from "On the Mechanical Response and Microstructure Evolution of NiCoCr Single Crystalline Medium Entropy Alloys" by Uzer B, Picak S, Lui J, Jozaghi T, Canadinc D, Karaman I, Chumlyakov Y, Kireeva I, 2018. Materials Research Letters, 6, pp. 442-449, Copyright 2010 by Taylor & Francis Online.

[2] Reprinted with permission from "Anomalous Work Hardening Behavior of $Fe_{40}Mn_{40}Cr_{10}Co_{10}$ High Entropy Alloy Single Crystals Deformed by Twinning and Slip" PICAK S, Liu J, Hayrettin C, Nasim W, Canadinc D, Xie K, Chumlyakov Y, Kireeva, Karaman I, 2019. Acta Materialia, 181, pp. 555-569, Copyright 2019 by Acta Materialia Inc. published by Elsevier Ltd.

[3] Reprinted with permission from "Simultaneous deformation twinning and martensitic transformation in CoCrFeMnNi high entropy alloy at high temperatures" PICAK S, Yilmaz H, Karaman I, 2021, Scripta Materialia, 202, pp. 113995, Copyright 2019 by Scripta Materialia Inc. published by Elsevier Ltd.

[4] Reprinted with permission from "On the low-cycle fatigue response of CoCrNiFeMn high entropy alloy with ultra-fine grain structure" PICAK S, Wegener T, Sajadifar SV, Sabero C, Ritcher J, Kim H, Niendorf T, Karaman I, 2021. Acta Materialia, 205, pp. 116540, Copyright 2021 by Acta Materialia Inc. published by Elsevier Ltd.

subgroup of multi-principal element alloys (MPEAs) with N≥ 3 (N: number of elements). Unlike conventional alloys, MPEAs offer a much larger and richer materials design space, which has motivated a large number of systematic and extensive design studies due to the tremendous opportunities for discovering new physics and functionalities [1,2]. Some of the recently discovered MPEAs have been reported to exhibit considerably better specific strengths [3], higher fracture resistance [4], better magnetic properties [5] as well as corrosion and oxidation resistance [6,7] than conventional alloys. The mechanical properties in MPEAs are of special interest as the scientific community seeks to achieve high strength and high fracture resistance that are beyond conventional alloys.

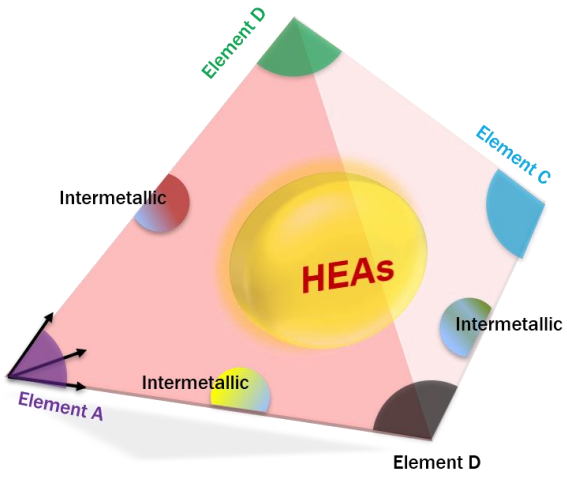

Figure 1.1 Schematic illustration of the compositional space for alloy design.

1.2. Atomistic structure and thermodynamics

Following the history of HEAs, the idea of MPEAs in high concentrations were introduced by Cantor et al. [2] and Yeh et al. [1]. Cantor et al. worked on the many equiatomic alloy systems and explored the single phase face centered cubic (fcc)

CoCrFeMnNi HEA (called as the Cantor Alloy) [2]. On the other hand, Yeh et al. introduced a HEA system with five principal elements or more. The atomic percentage of each component can range between 5% and 35%, which produced high mixing entropy tending to form a massive solid solution phase. From thermodynamics, if Gibbs free energy of mixing is less negative than intermetallic Gibbs free energy, alloys system achieves an equilibrium state to produce solid solution phase. Gibbs free energy of mixing has less negative value as mixing entropy increases according to Equation 1.1,

$$\Delta G_{mix} = \Delta H_{mix} - T\Delta S_{mix} \quad (1.1)$$

where ΔG_{mix} is Gibbs free energy of mixing and $\Delta H_{mix,}$ T, ΔS_{mix} are mixing enthalpy, temperature and mixing entropy, respectively. According to statistical thermodynamics, ΔS_{conf} identifies the portion of a system`s entropy as a measure of the disorder of thermodynamic system, which can be calculated using Boltzmann`s equation,

$$\Delta S_{conf} = k_b ln w \ (1.2) \quad (1.2)$$

where ΔS_{conf} is the difference in configurational entropy per mole of a system, where the atomic percentage of each element ranges between 5% and 35 %. Boltzmann`s constant is k_b and w represents the number of microstates [8]. ΔS_{mix} can be replaced by configurational entropy since ΔS_{conf} dominates the three contributors of ΔS_{mix} that has four contributors; configurational vibrational, magnetic dipole and electronic randomness and configurational entropy. Finally, ΔS_{conf} can be written as Equation 1.3 [9].

$$\Delta S_{conf} = -R \sum_{i=1}^{n} \frac{1}{n} ln X_i \quad (1.3)$$

where n is the number of elements, X_i is mole fractions of i-th element and R is the gas constant (8.31 Joule/Mol.K).

MPEAs can be defined as HEAs if the configurational entropy is equal or greater than 1.5R at a random solution state according to Equation 1.3 [2]. Conventional alloys consisting of one to two elements are called as low entropy alloys, while three component alloy systems are recognized as medium entropy alloy as shown in **Fig. 1.2** and **Table. 1.2**.

The phase stability of these alloys, which is what makes them practically appealing, is enhanced by high mixing entropies of the single phase solid solution in proportion to individual metallic constituents [10]. HEAs share four major characteristics: high entropy levels, sluggish diffusion, relatively large lattice distortion, and so-called cocktail effect [11], which distinguish them from conventional alloys [12]. HEA lattices are highly distorted since all solid atoms have different atomic sizes [13]. High lattice distortion contributes to their relatively high strength [13], and hinders atomic movement, which restricts the diffusion rate (sluggish diffusion) [1]. Moreover, HEAs have been considered as a composite material at atomic scale because of the incorporation of multi-principle elements (cocktail effect) [14]. The alloy properties can be modified through adjusting multi-component element types by using lighter elements (for low density) [15], passive oxide scale forming elements (for higher corrosion resistance) [16], or similar [11]. In addition, classical metallurgical strengthening and toughening mechanisms can be employed through precipitation hardening [17], deformation twinning [18,19], and martensitic transformation [20].

Table 1.1 ΔS_{conf} of equimolar alloys with up to 8 elements								
n	1	2	3	4	5	6	7	8
ΔS_{conf}	0	0.69	1.1R	1.39R	1.61R	1.79R	1.95R	2.08R
Alloys	Low Entropy $\Delta S_{conf} \leq R$		Medium Entropy ($R \leq \Delta S_{conf} \leq 1.5R$)			High Entropy ($\Delta S_{conf} \geq 1.5R$)		

Some of the recently discovered M/HEAs have been reported to exhibit considerably better specific strengths [3], higher fracture resistance [4], better magnetic properties [5] as well as corrosion and oxidation resistance [6,7] than conventional alloys. The mechanical properties in M/HEAs are of special interest as the scientific community seeks to achieve high strength and high fracture resistance that are beyond conventional alloys. These outstanding mechanical behaviors in M/HEAs demands a fundamental experimental investigation to answer the following question: What atomistic mechanisms are promoting different deformation modes simultaneously, which are not common in other fcc alloys, and how does the microstructure (e.g., crystallographic orientation) influences activity of the deformation modes?

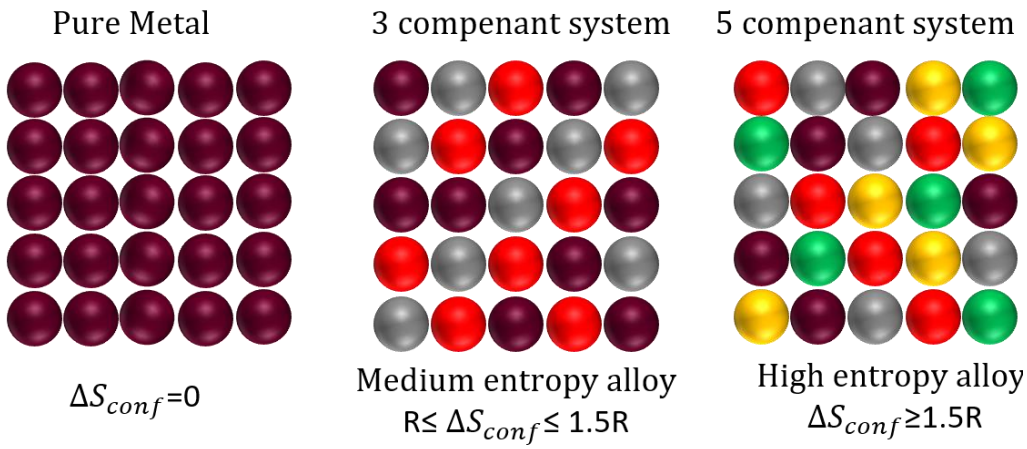

Figure 1.2 Configurational entropy chance in metallic systems by increasing the number of elements.

1.3. Plastic Deformation Mechanisms

One of the most promising HEAs, and the first discovered one, is the equiatomic CoCrFeMnNi, mainly owing to its stable single phase with a fcc crystal structure. Efforts have been devoted to study the deformation mechanisms and texture evolution in polycrystalline CoCrFeMnNi HEA as a function of heat treatment and temperature [21,22]. In addition, single crystals (SCs) of CoCrFeMnNi have also been the subject of several studies [4,21,23–26] that aimed at establishing a better understanding of the complex mechanisms governing the deformation response of this HEA. These investigations have shown that the CoCrFeMnNi HEA possesses a low stacking fault energy (SFE) between 0.018 and 0.027 J/m2 [24,27] and exhibits similar mechanical properties and microstructure evolution to those of low SFE fcc single crystals of conventional Fe-Mn alloys, also known as Twinning-Induced Plasticity (TWIP) steels [28–30], especially at low temperatures. Previous studies on single crystalline austenitic stainless steels (SS316, SS316L) [31] and Hadfield steel (Fe-12Mn-1C) [28,32] demonstrated that deformation twining is almost always active at the onset of plastic deformation in the [111]-oriented crystals under tension at room temperature, and at the later stages of deformation along other orientations. However, deformation twins do not prevail in CoCrFeMnNi HEA at room temperature under tension [21,23], although TWIP effect was observed to contribute significantly to the excellent mechanical response at cryogenic conditions [4,21].

Deformation twinning is, therefore, a key ingredient that drew recent attention to fcc HEAs due to this TWIP effect. HEAs which would deform by twinning is expected to

be akin to TWIP steels, in which both twin/twin and twin/slip interactions lead to very high strain hardening levels, and consequently enhance ductility by postponing necking instability [28,29,33]. Therefore, there has been emerging interest in developing new MPEAs with low SFE that would experience deformation twinning, and/or martensitic transformation and thus, exhibit ultrahigh tensile ductility, at room and higher temperatures [21].

Moreover, it has recently been shown that maximizing configurational entropy is not a strict criterion for detecting massive solid solution formation [34,35], opening a venue for producing non-equiatomic HEAs with a wide range of compositions, especially for HEAs with low SFE. Lowering SFE in HEA can be achieved by adding more elements such as Mn, or removing part or all of some elements, such as Ni, from equiatomic composition [35]. Removing Ni completely and maintaining the equiatomic composition in the CoCrFeMnNi HEA system leads to the multi-phase microstructure [36]. Therefore, Deng et al. [35] reduced the Cr and Co content to avoid the σ phase in CoCrFeMnNi system and attain single fcc phase. Increase in Mn content, in return, lowers SFE and promotes extensive twinning activity at both cryogenic and ambient temperatures, especially in polycrystalline $Fe_{40}Mn_{40}Cr_{10}Co_{10}$ off-stoichiometric HEA.

Similar to HEAs, NiCoCr and VCoNi MEAs are such MPEA with fcc crystal structure that exhibits one of the best strength-ductility combinations among all fcc MPEAs reported to date [37–39]. In addition, NiCoCr possesses the best strength-ductility combination in a very wide temperature range [3–5]. However, the exact atomistic and microstructural reasons for this exceptional mechanical response is unclear. Twinning and

transformation-induced plasticity (TWIP/TRIP) from fcc to hexagonal-closed-packed (hcp) structure have been reported as the reason for the outstanding mechanical behavior in NiCoCr [40,41], yet, the ultra-high yield strength in VCoNi is correlated with lattice distortion. Therefore, whether these mechanisms are the main reasons for unprecedented mechanical behavior is not clear due to date.

Besides formation energies (relative stability) and planar-defect energies (e.g., SFEs), SRO, i.e., the pairwise correlated occupation of local lattice sites, is another key factor that influence dislocation plasticity in complex solid-solution alloys [42–45]. Order and disorder designate the presence or absence of some symmetry or correlation in a many-particle system. The state of the random solute solution is achieved at high temperatures and is preserved with fast cooling rate, if a disorder stare is not a in thermodynamic equilibrium [46]. On the other hand, Long-range order is the differentiation of probabilities of particular sublattice sites being occupied by particular atoms (see **Fig. 1.3**).

SRO inhibits cross-slip in fcc solid solutions and can trigger dislocation pile ups [42–45]. The existence of SRO and its effects on dislocation plasticity has been reported recently in M/HEAs [47–50]. However, there are currently disagreements among existing theories and experiments describing how SRO affects the deformation behavior of NiCoCr. Zhang et al. have recently claimed that as-quenched polycrystalline NiCoCr does not exhibit planar dislocations due to a lack of SRO even though it has a very low stacking-fault energy (8.18 ± 1.43 mJ/m^2), while the aged samples (with a higher degree of SRO and no second phase precipitates) experience pronounced planar slip even though aged

samples have a three times higher SFE (23.33 ± 4.31 mJ/m^2) than the as-quenched sample [50]. However, these findings contradict previous experiments on the as-quenched NiCoCr that show pronounced planar slip with a medium SFE (22 ± 5 mJ/m^2) [3,51,52]. Furthermore, the claim that the aged-NiCoCr with high degree of SRO but without precipitates has higher yield strength and hardness [50] than as-quenched case is also contrary to the results of Yin et al. who found no measurable effects of SRO on the yield strength and hardness in NiCoCr [53]. It is well-known that the type of dislocation structure observed in fcc materials upon deformation depends on the grain orientation with respect to deformation direction, SRO, stacking faulty energy, as well as the presence of precipitates [42,54]. Thus, the disagreements might originate from either different crystal orientation or the formation of precipitates, leading to higher yield strength and hardness, instead of SRO. Clearly, a more controlled investigation of the effect of SRO on the deformation behavior of M/HEAs is needed to address this contradiction and reveal fundamental mechanisms responsible for high strength-ductility combination in NiCoCr such that better MPEAs can be designed. Finally, the question remains: is the plasticity of these M/HEAs governed only by SFE, or does atomic SRO play a role?

To the author's best knowledge, a systematic investigation on the effect of SRO, degree of SRO, and crystal orientation on the plastic deformation mechanisms, and strength and ductility levels in NiCoCr has not yet been studied. Moreover, it is still not known whether SRO has an effect on TWIP and TRIP in MPEAs. Clear understanding of the mechanisms responsible for unprecedented mechanical behavior of recently discovered MPEAs offer strategies to discover new classes of structural alloys with

applications in a wide range of critical technologies. Indeed, understanding and control of SRO in MPEAs is likely to emerge as the dominant design paradigm for this type of materials in the following years. Moreover, the impact of the findings in the present work will go beyond structural properties because the main mechanism responsible for high strength, ductility, and toughness combinations, i.e., SRO discovered in this study, is also known to affect magnetic, thermal and electronic properties in conventional materials. In summary, this knowledge is expected to open completely new areas of research in functional alloys.

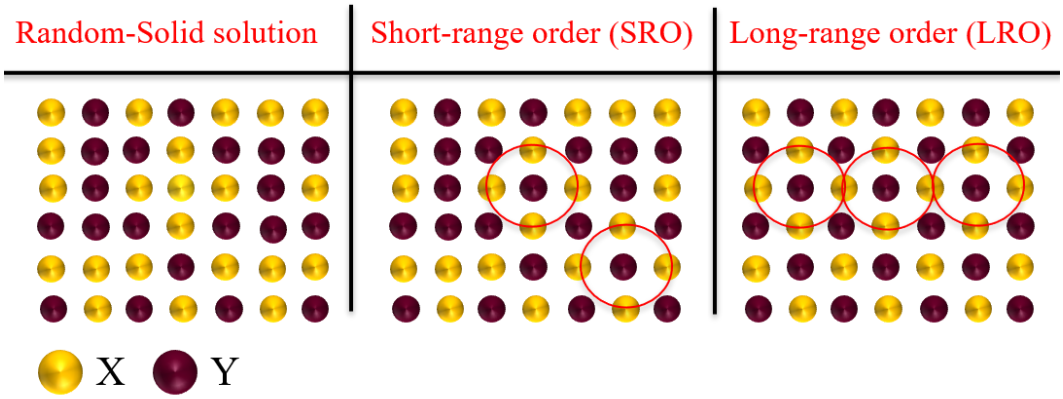

Figure 1.3 Schematic illustration of random solid solution, short-order and long-range order in a binary system.

1.4. Mechanical Properties

The inherently low yield strength of M/HEAs is a major roadblock towards application [55]. Recently, traditional strengthening mechanisms, such as dislocation strengthening, precipitation and grain boundary strengthening have been applied to improve the yield strength of the fcc structures [56–58]. Results obtained in these studies revealed that various strengthening mechanisms can generally lead to the enhancement in the strength

of HEAs and eventually improve the mechanical properties of these alloys under monotonic and non-monotonic loading.

Interstitial addition in fcc alloys offers improvement in mechanical properties. In some cases, the interstitial doped alloys show not only higher strength but also higher plastic deformation ability [52,59–61]. For example, 1.1 at.% carbon added to $Fe_{40.4}Ni_{11.3}Mn_{34.8}Al_{7.5}Cr_6$ exhibits simultaneous improvement of strength and ductility with the higher hardening rate [60]. The simultaneous improvement has been correlated to the suppression of cell structure formation, causing the localization via higher lattice resistance and lower SFE in carbon doped alloy. However, the addition of the carbon (0-0.75 at.%) in the equiatomic NiCoCr medium entropy alloy improves the strength without at the expense of ductility by increasing SFE, delaying the twinning formation with the thinner structure and decreasing the localization rate [52]. Moreover, the addition of carbon (0.5 at.%) increases the strength in CoCrFeMnNi by promoting twinning activity at the expense of ductility. In this study, the twinning ability has been detected in the [111] oriented grains but not in the [001] oriented grains [59].

For engineering applications, severe plastic deformation (SPD) methods can be used in an effort to enhance the yield strength by decreasing grain size and increasing dislocation density [62–68]. Most common SPD methods for attaining ultra-fine grained (UFG) materials are high pressure torsion, accumulative roll bonding and equal channel angular pressing (ECAP) [69–73]. Among these SPD methods, ECAP is more advantageous for processing bulk samples with all dimensions larger than a centimeter and it offers more uniform microstructures as compared to the other techniques [71]. In

addition, ECAP process can be repeated multiple times, if the material allows doing so without failure, since the cross section of the sample does not change during the process, theoretically allowing ultra-high deformation levels.

The effects of grain refinement via different thermomechanical processing routes on the mechanical behavior of HEAs have been recently investigated under uniaxial loading [74–81]. High pressure torsion (HPT, an SPD technique) has been used to improve the strength level and hardening of CoCrFeMnNi HEA [76–81]. Although HPT results in a high strength level, the low ductility level is the major drawback of HPT samples [80,81]. To overcome this, annealing is usually used as an additional processing step [80,81]. Annealing leads to grain growth, reducing the strength level, and phase decomposition, making the microstructure more complicated [80,81]. HPT has also been performed on other HEAs to improve strength at the expense of favorable strength-ductility combination [82,83]. Shahmir et al. recently demonstrated a good strength and ductility combinations in CoCrFeMnNi via ECAP [75].

On the other hand, lightweight metals are in high demand for maneuverability, energy conservation and thus further operation ranges, and increased payload capability for defense transportation systems and armored vehicles. Recently , Fe-Mn-Al-C steels have been developed as lightweight alternatives to traditional steels with high specific strength and stiffness [84,85]. The addition of Al lowers steel's density by 1.3% for every 1 wt.% Al added, which is a consequence of Al's low atomic mass and its effect on the lattice parameters [29]. As a result, Al additions allow for significant reductions in density as compared to conventional steel alloys. The effect of Al content on density is that an

alloying addition of 9 wt.% Al can reduce density from roughly 8 g/cm^3 to 7 g/cm^3 (~12% reduction) [86]. Moreover, Al and C activate the formation of κ-carbide precipitates. An interstitial element, C, in a Fe-Mn-Al-C light weight alloy system provides a high level of solid solution hardening [87] and stabilizes the austenite phase similar to Mn [88].

Al also has the effect of stabilizing the fcc phase in steels by increasing the stacking fault energy (SFE). A low SFE leads to TWIP/TRIP to occur which results in high strain hardening rates [89]. However, increasing Al content increases SFE around 80 mJ/m^2-100 mJ/m^2 and mostly suppresses TWIP and TRIP effects [90,91]. Therefore, the deformation of high Al content steels is controlled by dislocation glide rather than TWIP/TRIP effects. Therefore, current literature on strengthening Fe-Mn-Al-C steels has focused on precipitation hardening instead of TWIP/TRIP. This is typically achieved via solution heat treatment (SHT) at high temperatures (1100-1250°C) followed by aging at low temperatures (500°C-900°C) to produce κ-carbides [85]. Choi et al. [85] studied the effects of different types of κ-carbide precipitates on mechanical properties in Fe-28Mn-9Al-0.8C and showed that nanosized precipitates lead to planar slip in this steel. Although planar slip is generally correlated with low SFE in the literature, it has been claimed that short range ordering (SRO) and interstitials promote planar slip [42]. In addition to precipitation, the formation of micro shear bands can improve hardening behavior in Fe-Mn-Al-C steels [92]. Typical fundamental strengthening mechanisms in FCC light weight steels have been thoroughly studied in existing literature. However, the chemical content distribution in Fe-Mn-Al-C steels and whether or not the mechanical response of lightweight steels is isotropic has not yet been studied.

Engineering alloys are usually exposed to non-monotonic loading in applications. Moreover, microstructural evolution in conventional alloys can vary considerably under different loading conditions, especially under cyclic loading [93,94]. Therefore, investigations focusing on the non-monotonic response of M/HEAs are crucially needed to reveal their cyclic deformation behavior, determine their fatigue lives, and eventually design fatigue resistance HEAs. Fatigue failures already can occur in structures that are exposed to relatively low stresses, especially when the number of cycles is high. Furthermore, many applications are characterized by relatively high loads and, thus, components are subjected to at least minor yielding in each single cycle, eventually resulting in failure at a relatively small number of fatigue cycles [95]. The low-cycle fatigue (LCF) behavior of conventionally processed engineering alloys has been well-established [93–99]. However, data reporting on the fatigue behavior of HEAs are only available scarcely [100–105] and mostly focuses on the high-cycle fatigue (HCF) regime. All of these few recent studies were conducted on completely different HEAs.

Moreover, the grain orientation is a key ingredient governing the deformation modes and hardening behavior of HEAs under monotonic loadings [3,89], similar to conventional alloys both under monotonic [28] and cyclic loading conditions [106]. For example, the tensile deformation along the [123] orientation is dominated by single slip resulting in easy glide in the low SFE Hadfield steel single crystals at early stages of deformation leading to hardening rates significantly lower than the [111] orientation deformed via twinning [28]. Similarly, the grain orientation is one of the most important parameters on the cyclic dislocation structure in fcc materials [106]. Depending on the

different regions of the stereographic triangle, the dislocation structure can be observed as vein, labyrinth, walls or cell structure as cyclic deformation modes [107–109]. However, there is still no data reporting on the fatigue behavior of single crystalline HEAs so far. It is also well-known that fatigue life is orientation dependent and it is vital in modern engines for turbine blades [110,111]. Moreover, trustworthy process-microstructure-property relationships for various cyclic loading regimes of single crystalline HEAs have not been deep-rooted yet. Therefore, the understanding of the orientation dependence of cyclic deformation in single phase HEAs can be pioneer studies for future high-temperature HEA applications.

Superior fatigue properties have been reported in an UFG Al0.3CoCrFeNi HEA due to the nucleation of deformation induced nano-twins [100]. The effect of grain size on the cyclic deformation response (CDR) of the CoCrFeMnNi HEA has already been investigated, revealing a higher fatigue strength and stability in UFG material as compared to that of the coarse grained (CG) counterpart [101]. However, in that study only the HCF regime was studied. Focusing on the LCF behavior, some of the current authors have shown a considerably different hardening behavior than normally found under monotonic loading for a $Fe_{50}Mn_{30}Co_{10}Cr_{10}$ alloy [105]. In this metastable HEA, microstructure evolution was governed by martensitic phase transformation both under monotonic and cyclic loading conditions [20,105]. However, under cyclic loading martensitic transformation did not lead to significant hardening. Moreover, the CDR under push-pull loading was characterized by a saturation state of the stress amplitude in the CDR after initial transient behavior without any hardening [105], despite the fact that pronounced

work hardening was observed in this metastable HEA in tensile tests [20]. The lack of hardening under cyclic loading was also reported for a coarse grained CoCuFeMnNi. However, in case of this HEA, the microstructure evolution was only governed by dislocation activity [104].

In summary, the lack of consistent studies reporting on the CDR of HEAs can be considered a major roadblock towards the practical applications of these new class of materials. Reliable process-microstructure-property relationships for different fatigue regimes of one common HEA have not been established yet. Moreover, a fundamental understanding of the LCF response of the single-phase HEAs as a function of different microstructural conditions is missing in the literature.

In the last two decades, the fatigue behavior of UFG materials has been studied in depth. In numerous studies it was shown that the fatigue strength of the UFG alloys in the high-cycle fatigue (HCF) regime is superior to their coarse-grained counterparts due to their significantly increased monotonic strength [112–114]. However, fatigue lives in the LCF regime were shown to be inferior in many studies [115–120]. This was attributed to several potential mechanisms. A deteriorated LCF response could be related to localized initiation of damage due to inhomogeneities stemming from imperfect material flow during SPD [121,122]. Furthermore, it has to be considered that total fatigue life includes both crack initiation and crack propagation lives. In this regard, it was found by numerous researchers that severely deformed materials exhibit good resistance to the crack initiation, however, suffer rapid crack propagation [123,124]. Most importantly, during the LCF experiments in numerous SPD processed alloys microstructural instability was reported.

It was shown for UFG Cu [116,125], UFG Al-alloys [126–128], UFG bcc steels and Nb-Zr alloy [115,121] as well as UFG Ti-alloys [129] that dynamic recrystallization, re-arrangement of dislocations and concomitant damage localization lead to inferior fatigue properties at relatively low homologous temperatures and small numbers of cycles. One key for stabilization of the UFG microstructure and CDR was found to be the use of minor amounts of interstitials and introduction of precipitates [127,128].

To date, there has not been a systematic study on the monotonic and cyclic response characterization of single crystalline M/HEAs. There is an urgent need to reveal the orientation dependence of deformation modes in M/HEAs. Moreover, it is important to study the LCF behavior of UFG HEAs processed by ECAP in order to assess their structural integrity. Studies have to focus on the CDR, microstructural stability and fatigue lives in these alloys. In this regard the transient behavior, i.e., softening or hardening, of HEAs under cyclic loading needs to be studied in the LCF regime to shed light on the nature of the most detrimental mechanisms leading to cyclic degradation. Therefore, the present study focuses on the LCF experiments conducted at room temperature for single crystalline and polycrystalline M/HEAs.

1.5. Significance of Work

With this short background, the purpose of the present research is to establish a better understanding of the atomic (short range ordering) and microscopic aspects of deformation (orientation, stacking fault energy and solute solution content dependence) governing the hardening response of M/HEAs under monotonic and cyclic loading.

This research study will be helpful for a fundamental understanding of mechanical behavior of low to medium SFE single crystals M/HEAs on crystal orientation, critical resolved shear stress (CRSS) for twinning /slip and chemical content. Undoubtedly, the single crystals allow for a superior understanding of the fundamental deformation mechanisms by circumventing the complications associated with grain boundaries and texture effects in polycrystalline materials. Clear understanding of the mechanisms responsible for unprecedented mechanical behavior of recently discovered MPEAs offer strategies to discover new classes of structural alloys with applications in a wide range of critical technologies. Indeed, understanding and control of SRO in MPEAs is likely to emerge as the dominant design paradigm for this type of materials in the following years. Moreover, the impact of the findings in the present work will go beyond structural properties because the main mechanism responsible for high strength, ductility, and toughness combinations, i.e., SRO discovered here, is also known to affect magnetic, thermal and electronic properties in conventional materials. In summary, this knowledge is expected to open completely new areas of research in functional alloys.

An alternative alloying with carbon for M/HEAs used in this research as model materials will be suggested and mechanical properties of carbon alloyed M/HEAs will be compared with carbon free materials. Consequently, the fundamental knowledge obtained via this single crystalline study will be helpful to apprehend polycrystalline behavior and to develop stronger new M/HEAs. Finally, the fundamental understanding obtained via single crystalline studies will be applied to polycrystalline systems exposed to grain refinement and thermomechanical processing.

1.6. Objectives and Outline

The overall objectives of the current study are explicitly stated below:

1) The deformation response of different single crystal orientations ([001], [110], [111] and [123]) strained to different deformation levels from the onset of plastic deformation to the failure in NiCoCr MEA, CoCrFeMnNi HEA, $(CoCrFeMnNi)_{99.25} + C_2$ at.% HEA $Fe_{40}Mn_{40}Cr_{10}Co_{10}$ HEA and $Fe_{50}Mn_{30}Co_9Cr_9 + C_2$ at.% at room temperature. Detailed transmission electron microscopy (TEM) observations, electron back scatter diffraction (EBSD) and digital image correlation (DIC) were used for the microstructural investigations. The rational for choosing these crystallographic orientations is to exemplify different regions of the stereographic triangle and thereby to form different number of slip and twinning systems at various stages of deformation, as well as monitoring the orientation dependence of the strain level at which twinning initiates, and how twinning evolves. Analysis of differently oriented samples can elucidate the effective mechanisms and their interactions governing the deformation response.
2) The atomistic factors and microstructural mechanisms responsible for the extraordinary mechanical behavior in these kinds of MPEAs in order to discover the underlying mechanisms and eventually design better MPEAs. Therefore, here we aim to theoretically and experimentally explore the existence of SRO and investigate the interplay of TWIP/TRIP and SRO on the exceptional mechanical properties.

3) The microstructural evolution of equiatomic CoCrFeMnNi HEA via ECAP at homologous temperatures. It has been aimed at improving our understanding on these three points, namely: (i) microstructural evolution of the M/HEAs after ECAP, (ii) the effect of the deformation induced twinning or ε-martensitic transformation on the mechanical properties, and (iii) the reasons for the deformation induced twinning and ε-martensitic transformation at high temperature.
4) Understanding of microstructural evolution of high strength lightweight medium entropy Fe-Mn-Al-C MEA through extensive experimentation and structural characterization to reveal correlations with the effect of precipitation distribution and to eventually design a better manufacturing method for better mechanical properties.
5) The fatigue performance of single crystalline, CG HEAs and UFG HEAs in differing fatigue regimes in order to assess their structural integrity. Studies have to focus on the CDR, microstructural stability and fatigue lives in these alloys. In this regard the transient behavior, i.e., softening or hardening, of HEAs under cyclic loading needs to be studied in the LCF regime to shed light on the nature of the most detrimental mechanisms leading to cyclic degradation. Three different strain amplitudes will be considered to investigate the microstructural evolution under high-load cycling in single crystalline and polycrystalline M/HEAs.

With these objectives, the outline of the dissertation is structured as follows. Chapter 2 will focus on the experimental methods and materials used in this study. Chapter 3

investigates the room temperature stress-strain behavior of NiCoCr MEA together with a meticulous investigation of the hardening stages to reveal the dislocation structure, twin-slip and twin-twin interactions. In Chapter 4, room temperature stress-strain behavior of HEAs together with a meticulous investigation of the hardening stages to reveal the dislocation structure, twin-slip and twin-twin interactions. In Chapter 5, the effect of short-range ordering on the plastic deformation of NiCoCr is presented. In Chapter 6, the orientation and carbon dependence of twinning in single crystalline the most well-known HEA, CoCrFeMnNi, was studied. Later, ECAP was employed to improve the mechanical behavior of the CoCrFeMnNi HEA through microstructural refinement. Finally, the precipitation hardening is investigated in medium entropy FeMnAl-C lightweight steel. In Chapter 7 focused on the fatigue performance of single crystalline $Fe_{50}Mn_{30}Co_9Cr_9 + C_2$ at.% HEA in differing fatigue regimes in order to assess the effect of twinning on the LCF regime. Chapter 8 explore the fatigue performance of CG CoCrFeMnNi HEA and UFG CoCrFeMnNi HEA in differing fatigue regimes in order to assess their structural integrity. In Chapter 9, main conclusions are summarized.

2. EXPERIMENTAL METHODS [1][2][3][4]

Metallurgy of specimens such as single crystal growth, heat treatment and test specimens shape and their characterization methods before and after testing are discussed in this chapter.

2.1. Materials

Single crystals of M/HEA were artificially grown using the Bridgman technique in an inert helium atmosphere at Tomsk State University in Russia. To be able to compare the tensile response of these new class of M/HEAs with more conventional, low stacking fault energy austenitic steels, 316 stainless steel (SS316) and Hadfield steel (Fe-12Mn-

[1] Reprinted with permission from "On the Mechanical Response and Microstructure Evolution of NiCoCr Single Crystalline Medium Entropy Alloys" by Uzer B, Picak S, Lui J, Jozaghi T, Canadinc D, Karaman I, Chumlyakov Y, Kireeva I, 2018. Materials Research Letters, 6, pp. 442-449, Copyright 2010 by Taylor & Francis Online.

[2] Reprinted with permission from "Anomalous Work Hardening Behavior of $Fe_{40}Mn_{40}Cr_{10}Co_{10}$ High Entropy Alloy Single Crystals Deformed by Twinning and Slip" PICAK S, Liu J, Hayrettin C, Nasim W, Canadinc D, Xie K, Chumlyakov Y, Kireeva, Karaman I, 2019. Acta Materialia, 181, pp. 555-569, Copyright 2019 by Acta Materialia Inc. published by Elsevier Ltd.

[3] Reprinted with permission from "Simultaneous deformation twinning and martensitic transformation in CoCrFeMnNi high entropy alloy at high temperatures" PICAK S, Yilmaz H, Karaman I, 2021, Scripta Materialia, 202, pp. 113995, Copyright 2019 by Scripta Materialia Inc. published by Elsevier Ltd.

[4] Reprinted with permission from "On the low-cycle fatigue response of CoCrNiFeMn high entropy alloy with ultra-fine grain structure" PICAK S, Wegener T, Sajadifar SV, Sabero C, Ritcher J, Kim H, Niendorf T, Karaman I, 2021. Acta Materialia, 205, pp. 116540, Copyright 2021 by Acta Materialia Inc. published by Elsevier Ltd.

1C, in weight) were also grown using the same technique. Following the growth, the crystals were homogenized in an inert gas at 1473 K for 24 h, and quenched in ambient temperature water. Fe-Mn-Al-C polycrystalline materials are kindly supplied by Army Research Lab. The compositions of the materials are determined by IMR Test Labs, Lansing, NY. Carbon concentrations in the specimens are determined by inert gas fusion-thermal conductivity according to ASTM E 1019-18. The orientation of the bulk crystal was determined from Laue back-reflection images. Dog bone shaped tension specimens were extracted from the single crystals using wire electrical discharge machining (EDM) such that their tensile axes were along the [111], [123] and [001] crystallographic orientations. These orientations were selected to activate deformation mechanisms biased towards predominantly slip or twinning and maximize the Schmid factors for slip and twining. The Schmid factors for slip and twinning are presented in Table 4.1 and Table 5.2 for the used orientations. In addition, we list the number of most favorable slip or twin systems with equivalent Schmid factors. As expected, this number ranges from 1 to 8. Based on the Schmid factor evaluations, Tables suggests that the favored deformation mechanism depends upon the crystallographic orientation. The Schmid factors for the leading and trailing Shockley partials are also tabulated in Table 4.1 and Table 5.2. These values are pertinent because partial components of an intrinsic stacking fault (SF) play a role in twinning, as it will be discussed throughout the thesis.

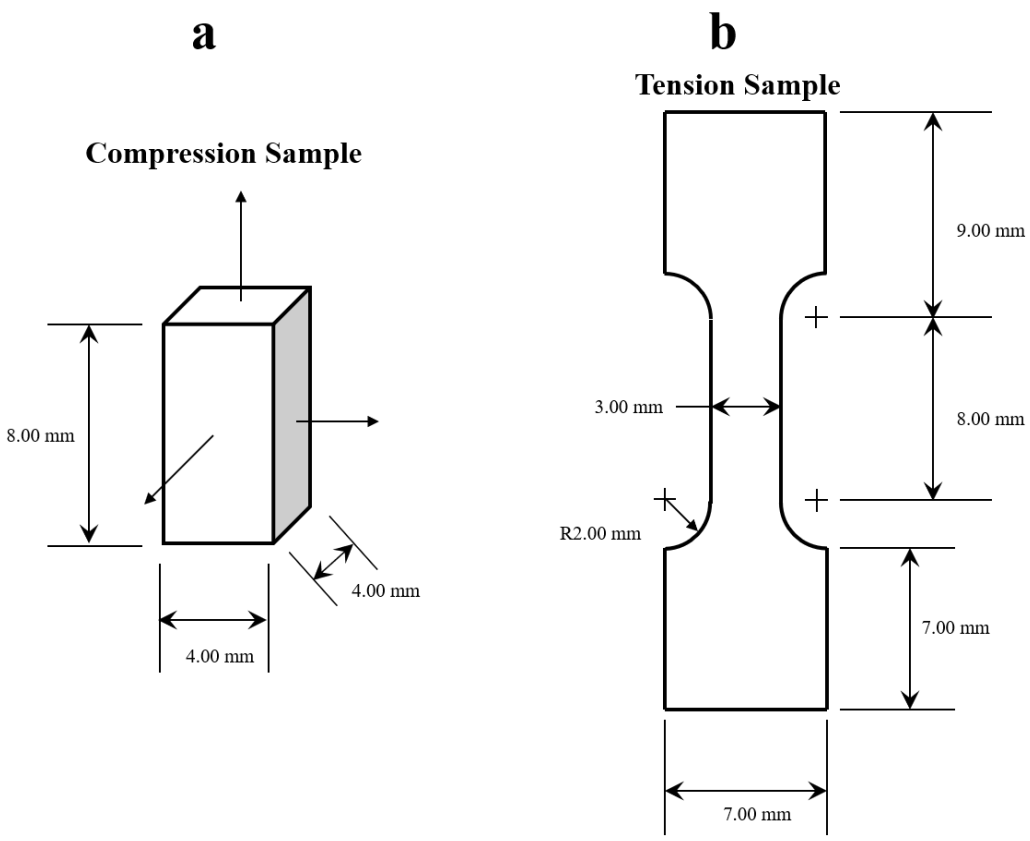

Figure 2.1 Small scale specimens designed for tensile and compression tests at room temperature.

2.2. Equal Channel Angular Pressing Processing

ECAP is an SPD process where the sample is pressed through a die (**Fig. 2.1**). The CoCrFeMnNi equiatomic HEA studied in the present work was fabricated using vacuum induction melting of high purity constituents in the form of a cylindrical rod with 7.62 cm diameter and 50.8 cm length. The as-cast billet, encapsulated in a mild-steel can, was first subjected to hot extrusion at 900^{o}C to remove impurities and voids caused by casting. The diameter of the billet was reduced from 7.62 cm to 3.175 cm during hot extrusion. Part of

the hot-extruded (HE) billet was then exposed to ECAP following route 2C at 300^{o}C in order to increase the density of stored dislocations, and as a result, achieve significant grain refinement. The HE billet was machined down to a 25 × 25 mm^2 cross-section and cut into 17.78 cm length samples before ECAP. After each ECAP pass, the billet was water quenched at room temperature to maintain the microstructure induced by ECAE. The extrusion rate was 7.62 mm / min. The die temperature kept at 300°C ± 10°C throughout the process. Route C, used in this study for ECAP, involves +180° rotation between each pass.

The total strain can be calculated with following equations:

$$\text{Reduction Ratio: } \frac{A_0}{A_f} \tag{2.1}$$

where A_0 is initial area, and A_f is final area. The total strain due to extrusion is calculated ε ≈1.1, since reduction ratio=exp (ε) [69]. The equivalent strain (ε) generated during one pass ECAP can be calculated by the fallowing equation [130]:

$$\varepsilon=\frac{1}{\sqrt{3}}\left[2cot\left(\frac{\psi}{2}+\frac{\phi}{2}\right)+\psi cosec\left(\frac{\psi}{2}+\frac{\phi}{2}\right)\right] \tag{2.2}$$

where ψ is the die corner angel (0^{o}), and ϕ (90^{o}) is the channel angel. According to Equation (1), the effective strain is 1.15, which is the highest strain level that can be achieved. Therefore, the cumulative strain due to hot-extrusion and ECAP is 1.15*2 (2 pass) +(1.1) =3.4 Therefore, the total strain as a result of ECAP after 2 passes is 1.15*2=2.3, and the cumulative strain due to ECAP and hot-extrusion is 2.3+1.1=3.4.

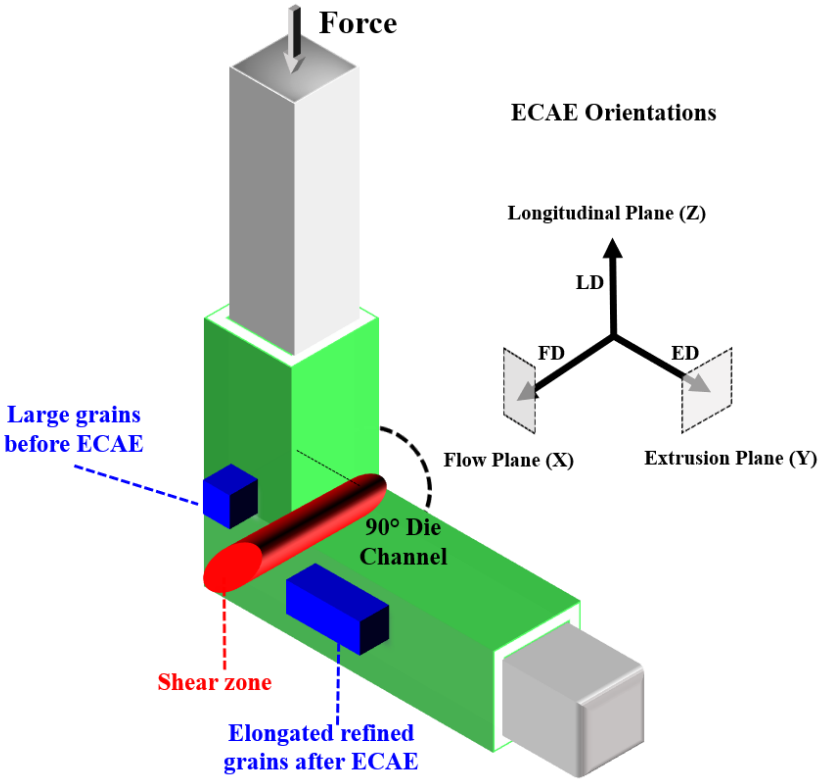

Figure 2.2 A schematic of the ECAP process showing different planes on the extruded billet.

2.3. Uniaxial Tensile Test Results at Room Temperature

The samples were mechanically polished utilizing a series of metallographic grinding papers with the coarsest being 800 grit, before finally utilizing a 0.1 µm diamond solution in order to get a final surface finish prior to tensile tests. Room temperature uniaxial tension experiments were performed on a servohydraulic MTS machine equipped with a specially designed gripping system [131], employing an effective strain rate of $5x10^{-4}$ s^{-1}. Tension specimens had a gage section with dimensions of 8 mm x 3 mm x 1.0 to 1.2 mm thickness (**Fig. 2.1**). This slow strain rate was chosen in order to avoid possible

rate effects. The compression samples were cut into rectangular prisms of 4 mm x 4 mm x 8 mm (**Fig. 2.1**). Tungsten carbide platens are used during the compression tests. To minimize the frictions reduction, thick teflon tapes were used between the sample and platens during compression tests. Strains were measured using an MTS extensometer directly attached to the gage section of the specimens and loads were measured with a load cell. All experiments were repeated at least 4 times. The CRSS levels for slip and twinning were calculated using the expression $\tau_{cr}^{sl} = \sigma_{\varepsilon}^{sl} m_{slip}$ or $\tau_{cr}^{tw} = \sigma_{\varepsilon}^{tw} m_{twinning}$, where $\sigma_{\varepsilon}^{sl}$ or $\sigma_{\varepsilon}^{tw}$ is the uniaxial stress at the minimum strain level that slip or twinning deformation is activated at, respectively, based on the digital image correlation (DIC) and electron backscatter diffraction (EBSD) analyses. Some experiments were interrupted at different strain levels before failure in order to explore the microstructural evolution of the single crystals.

Nanoindentation tests were performed on the Hysitron TI 950 Triboindenter. The peak load was 10000 μN. Nanoindentation hardness values were averaged from the 150 indentations with corresponding ±standard deviations.

2.4. Digital Image Correlation Experiments

In situ 2-D DIC was utilized to track local strain evolution and identify the strain localization at various levels of macro-scale deformation. An adherent layer of black paint was airbrushed onto the polished surfaces as the background layer and then a fine speckle pattern was obtained by airbrushing white paint on top. An optical Keyence VHX-600 microscope (4800 x 3600 pixels) was used to capture high-resolution images of the reference and deformed states of the surfaces. Images were captured every 5 seconds. In

addition, higher resolution *ex situ* DIC was utilized to identify the number of active deformation systems and to distinguish strain localization at various stages of deformation. The acquired DIC images were processed using Ncorr software that is an open source 2D Matlab program.

2.5. Microstructural Characterization

X-ray diffraction (XRD) measurements were conducted for phase and texture analysis. XRD pole figures and diffractograms were determined using a Seifert Analytical X-Ray diffractometer operated at 35 kV and 30 mA and equipped with a Mn tube (Kα1/Kα2 lines) and a monochromator. Microstructures were observed using an optical microscope (Keyence VHX-600 microscope), a scanning electron microscope (FERA-FIB SEM with EBSD) and transmission electron microscopy (an FEI Tecnai G2 F20 FE-TEM operated at 200 kV). The accelerating voltage, probe current and walking distance of EBSD were 20kV, 12nA and 9mm, respectively. The chemical distributions of specimens were observed using wave-dispersive X-ray spectroscopy (WDS) in the Cameca SXFive electron microprobe. The SEM and EBSD samples were mechanically polished utilizing a series of metallographic grinding papers, and using a suspension including a 0.04 μm colloidal silica particles. The EBSD KAM analysis was performed using an average misorientation angle around a measurement point regarding third nearest neighbor points.

2.6. High-Energy Synchrotron Transmission XRD Experiments

Experiments were carried out at the 11-ID-C beamline at Advance Photon Source in Argonne National Laboratory. Two NiCoCr tensile samples were prepared; the first

was undeformed with only the homogenization heat treatment (as quenched) and the second was, in addition, deformed to failure along the [110] crystallographic direction during uniaxial tension tests. The samples were irradiated at room temperature with monochromatic synchrotron radiation with a wavelength of 0.1173 Å and their polar diffraction spectra were collected using a 2D Perkin Elmer XRD1621 amorphous silicon detector. During the experiments, the samples were rotated 30 degree in [110] axis in an attempt to capture a higher number of characteristic peaks of possible phases. In this configuration, the $[011]_{fcc}$ crystallographic direction of the samples (before deformation) was parallel to the incident beam at the middle point of the rotation arc. Following, the acquired polar diffraction data was integrated along the azimuthal angle for obtaining the typical diffraction spectrum as a function of Bragg angle.

2.7. Transmission Electron Microscopy Investigations

Microstructural features were investigated using FEI Tecnai 20ST transmission electron microscope (TEM) operating at 200kV. Energy-filtered TEM investigations to minimize the signal-to-noise ration of the diffraction contrast from the existing SRO [50,132] and HRTEM observations were conducted on the Titan Themis 300 S/TEM (operating at 300kV). TEM foils were prepared by grinding the samples down to 50 to 70 µm thickness, which were twin-jet electropolished at -20°C with an electrolyte consisting of 80% of methanol and 20% of nitric acid at 10 V. Dislocation analysis were performed using Titan Themis 300 S/TEM in water-quenched NiCoCr MPEA. Weak-Beam bright-filed images for the '**g.b**' analysis of the partial dislocations was used to calculate SFE of NiCoCr MPEA. Burgers vectors of the partial dislocations were detected using a

diffraction condition normal to the Burgers vector to obtain **g.b**=0. The partial dislocation separation distances were measured using an open-source software Image J.. SFE was calculated using Eq. 2.3.

$$SFE=\frac{Gb_p^2}{8\pi d}\left(\frac{2-v}{1-v}\right)\left(1-\frac{2v-\cos(2\beta)}{2-v}\right) \quad (2.3)$$

where G is the shear modulus, b_p is the magnitude of the Shockley partial dislocation, d is the distance between Shockley partial pairs, and v is the Poisson`s ratio of NiCoCr MPEA. Total 300 individual measurements were obtained on 3 different regions far away from the thin foil hole to minimize the surface effects. Calculated standard deviations were in agreement with in each other.

3. MECHANICAL RESPONSE AND MICROSTRUCTURE EVOLUTION OF NiCoCr SINGLE CRYSTALLINE MEDIUM ENTROPY ALLOY [*]

This chapter investigates the room temperature stress-strain behavior of NiCoCr (33%Ni, 33% Co, 33% Cr, in at%) single crystals MEAs is presented for selected crystallographic orientations ([110], [111] and [123]) under tension loading. The overall stress-strain response is strongly orientation dependent, which shows unusual strain hardening response and ductility in NiCoCr equiatomic alloy. Nano-twinning prevailed at, as early as, 4% strain along the [110] orientation, providing a steady work hardening, and thereby a significant ductility. While single slip dominated in the [123] orientation at the early stages of deformation, multiple slip and nanotwinning were prominent in the [111] orientation. Significant dislocation storage capability and resistance to necking due to nanotwinning provided unprecedented ductility to NiCoCr medium entropy alloys, making it superior than quinary variants, and conventional low and medium stacking fault energy steels.

---

[*] Reprinted with permission from "On the Mechanical Response and Microstructure Evolution of NiCoCr Single Crystalline Medium Entropy Alloys" by Uzer B, Picak S, Lui J, Jozaghi T, Canadinc D, Karaman I, Chumlyakov Y, Kireeva I, 2018. Materials Research Letters, 6, pp. 442-449, Copyright 2010 by Taylor & Francis Online.

3.1. Stress-Strain Response

The stress-strain response of the samples deformed up to failure is presented in **Fig. 3.1a**. From these experiments and the results on the several companion samples for each orientation, the Young's modulus of each orientation is determined as: $E_{[111]}$ = 375±32 GPa, $E_{[110]}$ = 300±28 GPa, and $E_{[123]}$ = 280±35 GPa. While the [110] and [123] orientations exhibit upper and lower yield strengths, and Lüder's type propagation of localized deformation, the [111] orientation demonstrates a linear hardening from the beginning of the deformation. This is associated with the different types and number of active deformation systems: single deformation system prevails early in the [123] orientation, while multiple deformation systems are promoted in the [111] samples [28]. Therefore, the [111] crystals do not exhibit extended stage I hardening region. [123] samples lead to a low work hardening rate in Stage I. In the [111] orientation, two or more active deformation systems interact with each other, leading to the start of Stage II deformation almost at the onset of plastic deformation. In the [110] direction, twinning nucleation causes Lüder's type propagation of deformation in Stage I.

3.2. Microstructural Investigations

The TEM images of the [110] sample deformed to 4% strain show planar dislocations on a single slip system (**Fig. 3.2a**) and the formation of two twin systems with a twin thickness of 1-2 nm (**Fig. 3.2b**) on the {111} planes. Planar dislocation motion in this orientation is associated with the difficulty of cross slip due to low SFE and high resistance to cross slip imposed by the substitutional atoms [133]. At the early stages, plasticity takes place by the splitting of the 1/2<110> type perfect dislocations into

1/6<112> type Shockley partials. As a result of the coordinated glide of these partial dislocations on consecutive {111}-type planes, stacking faults are formed, which interact with the dislocations [134]. It should be noted that the formation of stacking faults in the early stages of plasticity of low SFE alloys contribute to the nucleation of twins by serving as precursors [135].

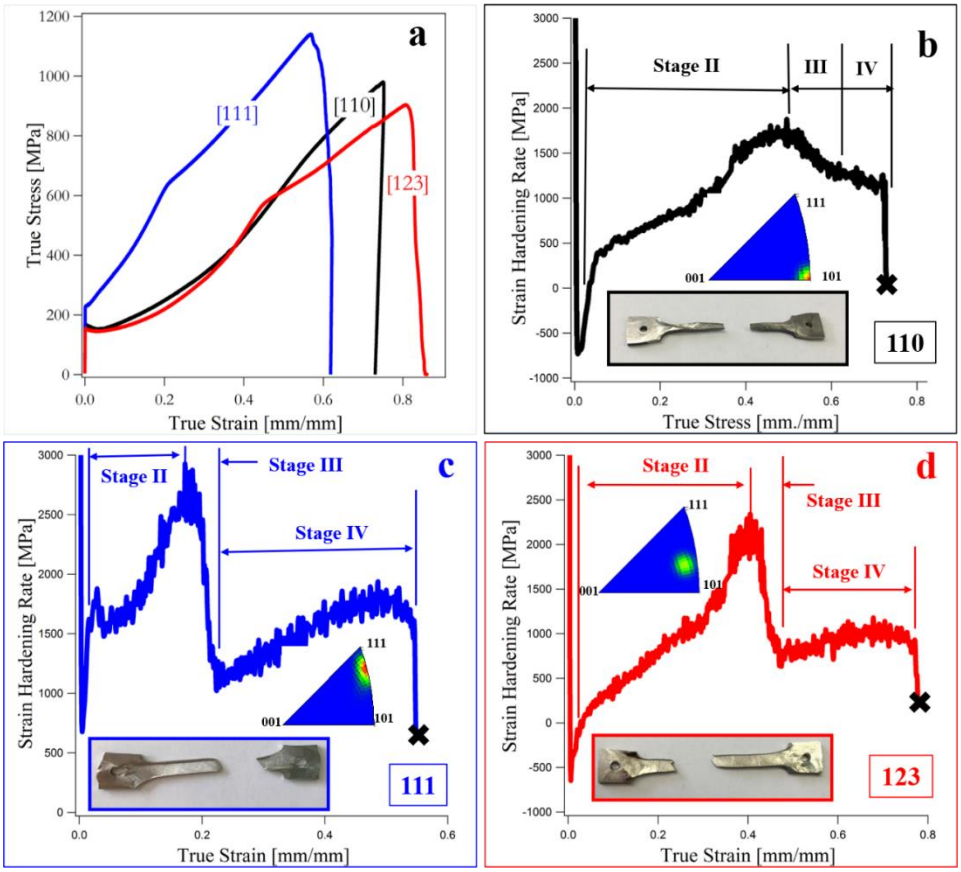

Figure 3.1 (a) True stress - true strain response of the NiCoCr medium entropy alloy single crystal samples oriented along the [110], [111] and [123] orientations deformed to failure under uniaxial tensile loading. Evolution of strain hardening rate as a function of true strain in the (b) [110], (c) [111] and (d) [123] orientations.

Activation of two different nanotwin systems, and their interactions with dislocations and stacking faults promote an increased work hardening rate (WHR) in this sample following Stage I. Recently, nanotwin formation was reported to take place between 4.0-6.7% true strain in polycrystalline NiCoCr MEA subjected to tensile loading at 77K [51]; however, to the best of the authors' knowledge, the present work is the first reporting the evidence of nanotwin formation at such small strains at room temperature in this material.

The strain hardening response of the [110] orientation in Stage II (**Fig. 3.1b**) is primarily governed by multi-twin systems shown in **Fig. 3.2b and 3.2d**. The sharp increase in strain hardening curve in Stage II in **Fig. 3.1b** is associated with twin boundaries where they act as barriers to dislocation motion [28]. Moreover, TEM image of the [110] sample deformed to 18% revealed a second slip system interacting with the primary one (**Fig. 3.2c**). The interaction of the slip systems forms the carpet structure (**Fig. 3.2c**), which is commonly observed in low SFE materials [136], such as 316L stainless steel [31]. Increase of dislocation density concomitant with plastic deformation gives rise to the rows of positive and negative edge dislocations, increasing the stress [136]. Once a critical stress value is achieved, these dislocation multipoles, which block the initial slip plane, promote dislocation activity on fresh slip planes in order to accommodate the imposed strain. The initiation of dislocation glide on interacting systems creates these carpet structures [136], eventually leading to high density dislocation walls (HDDWs) [137]. The twin density also increases in Stage II (**Fig. 3.2d**), ultimately decreasing the mean free path of the dislocations and enhancing dislocation storage [135]. Twin

boundaries impede dislocation glide, a phenomenon known as dynamic Hall-Petch effect, which increases the WHR. Overall, the strain hardening in Stage II in the [011] orientation is strongly influenced by deformation twinning and HDDWs since they act as a strong obstacle to dislocation motion by reducing dislocation mean free path (MFP).

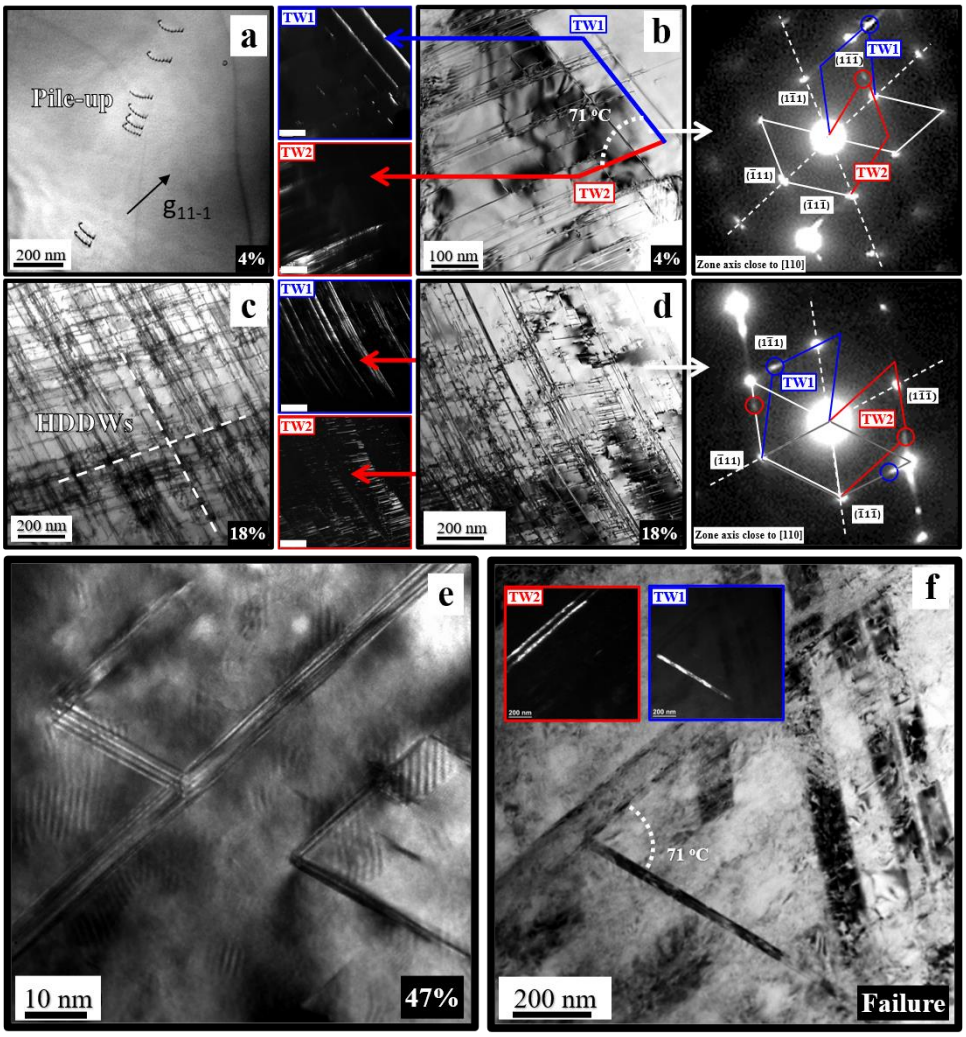

Figure 3.2 Bright field TEM images and corresponding diffraction patterns of the [110] oriented samples deformed up to ((a) and (b)) 4%, ((c) and (d)) 18%, (e) 47% and (f) failure.

An additional increase in Stage II hardening (max WHR=G/45, where G is the shear modulus) is clear at the later stage of the deformation in **Fig. 3.2b**, the reason of which was investigated using TEM in the [110] sample deformed to 47% of strain, As shown in **Fig. 3.2e**, notable amount of stacking faults were observed on multiple {111} planes, forming so-called "parallelepipeds" [89]. The interaction of stacking faults gives rise to the formation of these parallelepipeds, which act as additional barriers to dislocation motion, and further increase the strain hardening rate. Stage II hardening is followed by Stage III where dislocation recovery takes place leading to reduction in strain hardening coefficient. Stage III is then interrupted by Stage IV hardening where more twinning activity takes place. At Stage IV, the thicknesses of the pre-existing and the newly formed twins increase, facilitating interactions with each other and existing dislocation substructure (**Fig. 3.2f**). These changes in the twin activity result in further increase in ductility, since they supress deformation localization and necking.

Similar to the [110] samples, stress-strain response of [111] samples can be divided into clearly distinguishable four stages (**Fig. 3.1c**). In order to understand the governing mechanisms in the early stages of plastic deformation, the sample was deformed to 10% strain. The TEM image in **Fig. 3.3a** shows the activation of twinning and twin/slip interaction, which provides a high WHR throughout Stage II (with a maximum of G/30). Through the activation of multi-slip systems, dislocation tangles and multipoles (**Fig. 3.3b**) is formed in the early stages of deformation. The dislocations on primary and conjugate slip systems form the Lomer-Cottrell locks, which involves the sessile

dislocation configuration blocking slip . Specifically, the interaction of partial dislocations with the Lomer-Cottrell locks increases local stress concentration, facilitating the formation of additional deformation twins at the later stages of deformation. The mutual interaction of these mechanisms promotes the strengthening of the material and provide the high WHR in the deformation stage II.

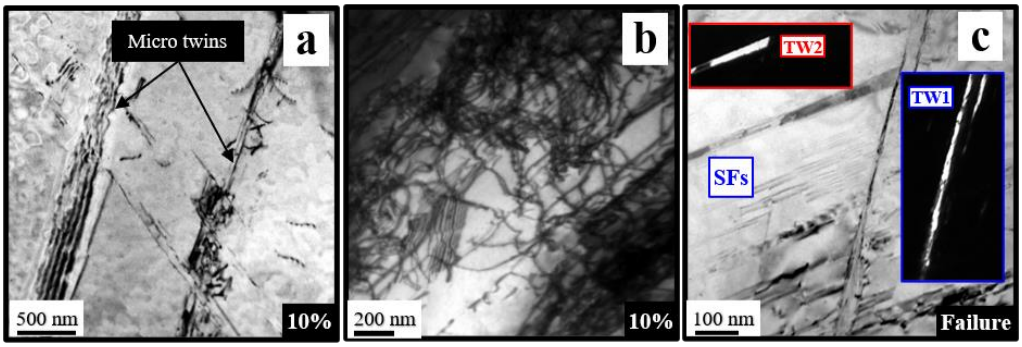

Figure 3.3 TEM images and diffraction patterns of the [111] oriented samples deformed up to (a)-(b) 10% and (c) failure.

In the [111] orientation, following Stage II, Stage III deformation takes place where dislocation recovery occurs causing a decrease in strain hardening rate from G/30 to G/65. However, the decrease in WHR in Stage III is terminated with the start of Stage IV due to the well-known TWIP effect [137]. In order to elucidate the dominant deformation mechanisms at later deformation stages, the [111] orientation was deformed up to failure: two active twin systems with the average thicknesses of 20 and 30 nm were observed and the thicker twins block the propagation of the thinner ones (**Fig. 3.3c**). These nanotwins also interact with the stacking faults and dislocations, delaying the onset of necking and thereby increasing the ductility [138]. The above observations about the propensity of

twins in this alloy are also supported by a recent study, where the twinnability of this alloy was reported to be higher than all pure FCC metals and comparable to that of the Fe-Cr-Ni TWIP steels [139].

Stage I deformation in the [123] orientation is governed by single planar slip system which leads to low hardening. However, the nano-twins observed in the [123] samples deformed to 10% (**see Fig. 3.4a to 3.4c**) bring about a sharp increase in WHR, similar to the [111] and the [110] oriented samples. In addition, twin-slip interaction causes an increase in strain hardening rate through Stage II. The transition from Stage II to Stage III (max WHR=G/40) represents dislocation recovery stage similar to the behaviour in the [110] and [111] orientations. This stage ended at WHR=G/80 due to the formation of new twin systems, similar to those observed in TWIP steels [140], representing the onset of Stage IV (Figure 1(d)). The activation of multiple twin systems in the Stage IV deformation of the [123] orientation creates a 3D twin network (Figure 4(e)), which offers multiple pathways for the dislocation motion [139] and more boundaries for dislocation storage, enhancing the ductility of the material and delaying the onset of necking. Furthermore, formation of dislocation cells between the twin lamellae (Figure 4(d)) in the [123] orientation creates dislocation-free regions, promoting easy glide, similar to what was observed in 316L stainless steel single crystals [135].

Based on the above observations, we attempted to calculate the CRSS for slip and twinning in the NiCoCr MEA by assuming that in all three orientations the onset of plastic deformation (i.e. yield strength) occurred due to dislocation slip, and twinning has started in [111] and [110] orientations at a strain level around 4-5% strain and in the [123]

orientation at around 10%. Based on these assumptions, the CRSS for slip was found to be 69 ± 3 MPa and the CRSS for twinning was determined to be 78 ± 5 MPa.

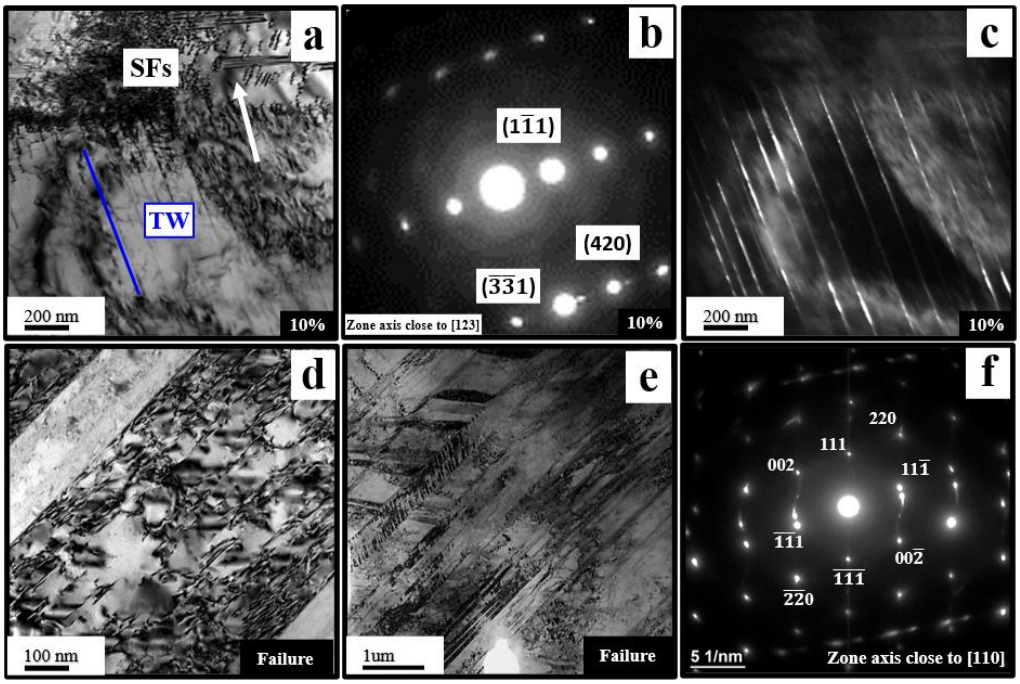

Figure 3.4 TEM images and diffraction patterns of the [123] oriented samples deformed up to (a)-(c) 10% and (d)-(f) failure.

It should be noted that the uniaxial tensile responses of three orientations of equiatomic NiCoCr MEA single crystals investigated here is quite similar to those observed in 316L stainless steel [135] and Fe-12%Mn-1%C Hadfield steel [28] single crystals, in terms of the hardening response, stages of the deformation, and relative hardening rates. The main differences between this MEA and the latter steels are that the steels exhibit higher yield strengths (i.e. their critical resolved shear stresses are higher than that of the NiCoCr MEA), however, the NiCoCr MEA crystals demonstrate much higher ductility, i.e. more

than 50% higher. The main difference between NiCoCr MEA and 316 stainless steel / Hadfield steel single crystals is the extent of Stage IV hardening in the orientations studied (i.e. [111], [123], and [110]). In NiCoCr single crystals the total strain levels for combined stage III and stage IV are significantly more than those in both 316 stainless steel and Hadfield steel. This indicates that the secondary twinning and/or twin networks are quite effective in Stage IV deformation of NiCoCr crystals in suppressing necking and increasing the ductility. One potential reason is that the twins in NiCoCr seem to be thinner than 316 stainless steel and Hadfield steel in Stage IV, probably providing more boundaries for slip to interact. This indicates that dislocation storage capability and resistance to necking instability of NiCoCr should be better than these conventional low and medium SFE steels.

3.3. Summary and Conclusions

The findings presented in this chapter demonstrate that the superior mechanical properties of NiCoCr MEA are strongly orientation dependent. More importantly, nanotwin formation was shown to start as early as 4% strain, contributing to the significant ductility by promoting a steady work hardening response and postponing necking. Multi twin systems were observed in all three orientations studied here at different strain levels. Furthermore, the current results also imply that a higher configurational entropy does not necessarily warrant improved mechanical properties, as in the case of the NiCoCr MEA as compared to its HEA counterparts. Overall, the current findings shed light on the complicated microstructural evolution and strain hardening response of NiCoCr MEAs.

4. MECHANICAL RESPONSE AND MICROSTRUCTUR EVOLUTION OF $Fe_{40}Mn_{40}Co_{10}Cr_{10}$ SINGLE CRYSTALLINE HIGH ENTROPY ALLOY[*]

In this chapter, the orientation dependence of tensile deformation in $Fe_{40}Mn_{40}Co_{10}Cr_{10}$ high entropy alloy (HEA) was investigated in [111], [001] and [123] oriented single crystals. Transmission electron microscopy investigations revealed three major mechanisms controlling the deformation stages, depending on the orientation: (i) deformation twinning, (ii) planar slip and (iii) dislocation wall/network formation. While twinning and planar slip were strongly orientation dependent, dislocation walls were observed in all orientations. Twinning was the dominant deformation mode in [111] crystals, while only multi-slip was observed in [001]. Both twins and planar slip were activated in [123] crystals. [111] crystals exhibited the highest strain hardening coefficients and ultimate tensile strength due to the strong twin-twin and twin-slip interactions where twin boundaries reduce the mean free path of dislocations, leading to dynamic Hall-Petch hardening. The decent ductility levels (~45%) were attained in [111] due to nanoscale internal twins and tertiary twin system forming at the later stages of deformation and suppressing necking. In contrast, no twins or stacking faults were observed in [001] crystals, which is consistent with the Copley-Kear effect. [123] crystals had outstanding tensile ductility (~65%), due to the activation of planar slip and twinning.

---

[*] Reprinted with permission from "Anomalous Work Hardening Behavior of $Fe_{40}Mn_{40}Cr_{10}Co_{10}$ High Entropy Alloy Single Crystals Deformed by Twinning and Slip**"** PICAK S, Liu J, Hayrettin C, Nasim W, Canadinc D, Xie K, Chumlyakov Y, Kireeva, Karaman I, 2019. Acta Materialia, 181, pp. 555-569, Copyright 2019 by Acta Materialia Inc. published by Elsevier Ltd.

Overall, in this off-stoichiometric HEA, we have determined the stacking faculty energy and critical resolved shear stresses for both twinning and slip, and demonstrated the formation of high dislocation density walls and wavy slip in [001], while the hardening stages of [123] and [111] are primarily governed by planar slip and twinning, which can be rationalized by the Copley-Kear effect.

4.1. Uniaxial Tensile Deformation Response and Digital Image Correlation Analysis

The true stress - strain responses and strain hardening coefficient (θ) - true strain curves obtained from the room temperature uniaxial tension experiments are shown in **Fig. 4.1.** The [111]-oriented samples had the highest ultimate tensile strength (UTS) of 860±5 MPa, whereas the [123]-oriented crystals exhibited an UTS of 580±5 MPa and the [001]-oriented crystals reached a UTS of 475±5 MPa. The [111]-oriented samples displayed a good combination of strength and ductility, both being significantly better than the [001] oriented single crystals. However, the [123] orientation exhibited a significantly superior ductility of about 65% as compared to the other two orientations. We also noted that the [123] orientation displays Luder`s type propagation of localized deformation with mostly single slip trace, whilst the [111] and [001] orientations demonstrate an increasing hardening rate at the beginning of the deformation with multi-deformation mechanisms activated (see optical image insets in **Fig. 4.1**). The variations in hardening response are governed by different types and numbers of active deformation mechanisms, as described below. Clearly, the plastic flow behavior in these HEA single crystals are highly dependent on the crystallographic orientation, similar to single crystals of medium entropy alloys [3], low SFE stainless steels [31] and Hadfield steels [24,28,32,137,141–144].

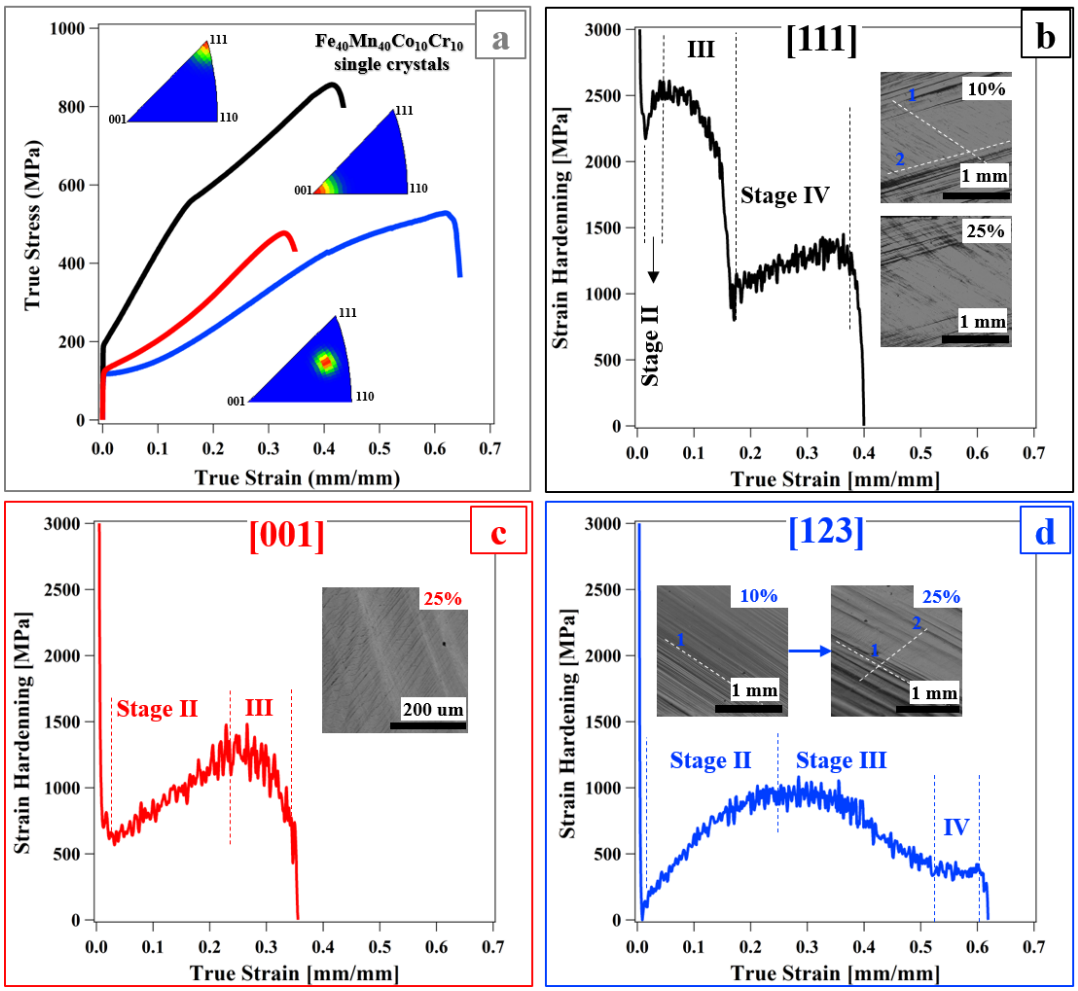

Figure 4.1 (a) The room temperature true stress - true strain tension responses of the [111], [001]- and [123]-oriented single crystals of the $Fe_{40}Mn_{40}Co_{10}Cr_{10}$ HEA. Inverse pole figures show the initial loading directions for three orientations, measured using EBSD. The evolution of θ ($\mathbf{d\sigma/d\varepsilon}$), with true strain for the (b) [111], (c) [001] and (d) [123]-oriented crystals. Optical microscopy insets provide the surface relieves at different strain levels indicated. The stages of deformation were also marked for each orientation.

Fig. 4.1 also displays the evolution of strain hardening coefficients along the three orientations as a function of the applied strain level. Strain hardening responses of the [111]- and [123]-oriented samples can be divided into five distinct stages (**Figs. 4.1b** and **4.1d**). Dislocation glide, twinning, and their interplay contribute to the overall hardening

behavior at various stages in these two orientations. In contrast, the [001] orientation exhibits 3 stages (**Fig. 5.1c**), where only dislocation glide prevailed (as shown by the TEM investigations presented below). Particularly, at the early stages of deformation, the [111] oriented crystals exhibited a much higher θ than the others, leading to the highest UTS. The observed high hardening coefficient is associated with the coexistence of twin-twin and twin-slip interactions in this orientation [137,145,146], as supported by the TEM investigations shown below. The lowest θ was observed along the [123] orientation, but it was comparable to that of the [001] orientation. Generally, the [001] orientation is expected to exhibit a significantly higher strain hardening rate than that of the [123] orientation, mainly owing to the expected simultaneous multiple slip activities and the corresponding slip-slip interactions in stage 2. For example, the tensile deformation along the [123] orientation is dominated by single slip resulting in easy glide in the low SFE Hadfield steel single crystals at the early stages of deformation, and leading to hardening rates significantly lower than the [001] orientation [28]. However, in the present study, TEM observations revealed that the [123]-oriented samples experience both slip and twinning. Furthermore, the rapidly increasing stage 2 hardening (**Fig. 4.1d**) suggests the coexistence of multiple active deformation mechanisms, instead of an easy glide regime.

A sharp decrease of the θ was evident during the stage I hardening of all orientations (**Fig. 4.1**), typical of stage I behavior of low SFE fcc materials, due to dominantly single slip and a stable dislocation generation [145,147,148]. Another factor contributing to the sharp decrease in the hardening rate can be the dissociation of perfect dislocations into

Shockley partials, followed by twin nucleation, which has been observed in low SFE TWIP steels which initially reduced the hardening rate [147].

When compared to the stage I of the [111] orientation, the decrease in the hardening rate is much more pronounced in the strain hardening response of the [123] orientation in stage I (**Fig. 4.1d**). This is because the fact that the [123] orientation deforms by a single slip system with the highest Schmid factor during stage I deformation (**Table 4.1**). However, the [001] and [111] orientations exhibit multiple active slip (or twinning) systems (8 and 6, respectively), leading to higher strain hardening rates. An increase of the hardening rate was noted in the [123] sample in stage II. A secondary deformation mechanism can be observed in the optical microscopy image inset in **Fig. 4.1d**, which must be responsible for such an increase in stage II.

As for the [001] orientation, an increasing hardening after yielding (stage 2, higher than that of the [123] orientation) may be associated with slip-slip interactions in this direction (**Fig. 4.1c**). However, it is well established that dislocation-dislocation interactions generally result in linear hardening in TWIP steels [149], while the [001] orientation demonstrates continuously increasing hardening response. There must be other reasons leading to this additional increase in hardening.

The DIC images presented in **Fig. 4.2** display the normal strain components and localization induced by active deformation systems in the [111] oriented crystals deformed to different strain levels, shedding some light on the nature of the deformation modes. The stress-strain curve in **Fig. 4.2a** features a noticeable stress drop at the early stages of deformation (at ~ 2% strain, marked by the circle in **Fig. 4.2a**). Such stress drop is a clear

indication of twin nucleation [23,150], which is also supported by the detection of twinning via EBSD analysis (**Figs. 4.2a and 4.2b**). The inverse pole figure obtained via EBSD (inset in **Fig. 4.2a**) carried out on the sample deformed to point 2 in Fig. 2a clearly demonstrates the prevalence of twinning. This observation is in contrast to the results reported for the polycrystalline $Fe_{40}Mn_{40}Co_{10}Cr_{10}$ HEA [35] where the deformation twinning was observed at much later stages of deformation.

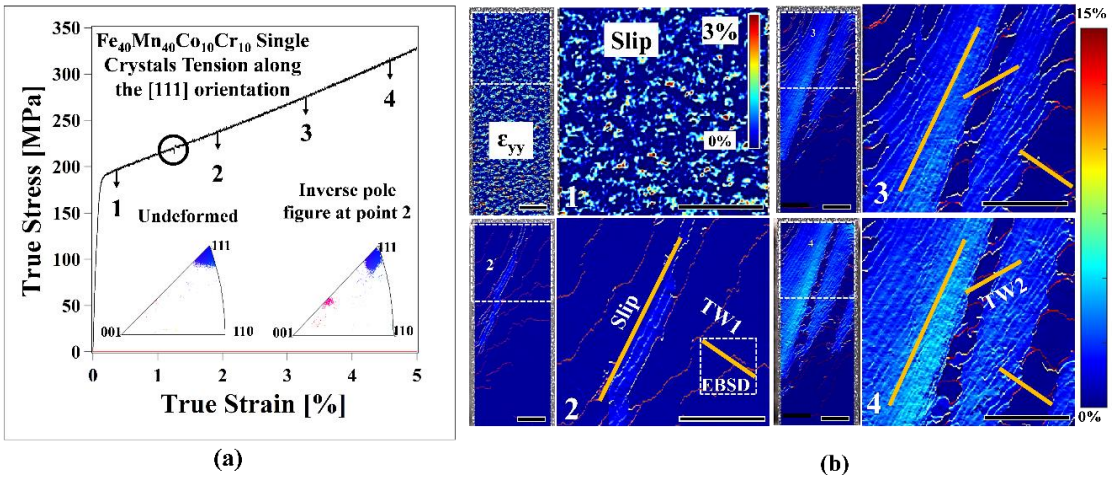

Figure 4.2 (a) The room temperature tensile stress-strain response of the [111] single crystals of $Fe_{40}Mn_{40}Co_{10}Cr_{10}$ at low strain levels. Inverse pole figures demonstrate the orientation (texture) of the starting single crystal and the sample deformed to point 2 in (a). (b) In-situ DIC images show the normal ($\boldsymbol{\varepsilon_{yy}}$) strain maps at four different strain levels (1, 2 ,3, and 4) marked in (a). Each scale bar represents a length of 1 mm. EBSD dashed box in (b) corresponds to the inverse pole figure inset in (a). The stresses observed at the onset of the activations of slip (yield point, 0.2% offset strain) and twin (the load drop point, marked with a circle) mechanisms were identified for the calculation of critical resolved shear stresses (CRSS) for slip and twinning.

Both DIC and optical microscopy images (**Fig. 4.1**) revealed that multiple deformation mechanisms were active following yielding in the [111] oriented sample and beyond, especially in stage 2, during which the θ increases steadily (Fig. 1b). The DIC experiments

revealed distinct strain localization starting at about 2% strain in the [111] orientation. Areas of strain localization were evident in the stage 2 hardening regime, suggesting the activity of twining and planar slip or high-density dislocation walls (HDDWs) [31,137].

Table 4.1 Maximum Schmid factors for slip, twinning, and the leading and trailing Shockley partial dislocations for selected single crystal orientations of fcc crystals when they are mechanically loaded under tension. "Sys." indicates the number of systems, which have equivalent Schmid factors. Geometrical factor *Q* is defined in the text. The yield strength values detected using the 0.2% offset strain criterion were experimentally determined from the tensile stress-strain responses of at least four different single crystal samples, on the average, for each orientation. The Critical Resolved Shear Stress (CRSS) values were determined using the equations $\boldsymbol{\tau_{cr}^{sl} = m_{sl}\sigma_{\varepsilon}^{sl}}$ for slip and $\boldsymbol{\tau_{cr}^{tw} = \sigma_{\varepsilon}^{tw} m_{tw}}$ for twinning.

Loading Axis	Schmid factors under Tension					Yield Streng, MPa	CRSS	
	Slip	Twin	Leading Partial (m_1)	Trailing Partial (m_2)	Geometrical Factor, $Q= (m_1–m_2)/2$		Slip	Twin
[001]	0.41 8 Sys.	0.23 8 Sys.	0.47	0.23	0.115	125±5	51±2	-
[123]	0.46 1 Sys.	0.47 1 Sys.	0.34	0.47	-0.065	118±5	53±2	70±9
[111]	0.28 6 Sys.	0.31 3 Sys.	0.16	0.31	-0.08	192±5	52±2	72±5

The DIC images and the stress-strain responses were also utilized to experimentally determine the stress levels for the onset of slip and twinning, combined with the EBSD investigations. These stress levels are then used to calculate the CRSSs for slip and twinning. Accordingly, the CRSS for the nucleation of the primary twinning (τ_{cr}^{tw}) in the [111] orientation was calculated to be 72±5 MPa (based on the first load drops observed

in different samples), whereas the CRSS for slip (τ_{cr}^{sl}) was calculated to be 52±2 MPa (based on the yield point detected using the 0.2% offset strain criterion). In the literature, deformation twinning has not been reported for the equiatomic FeMnCoCrNi HEA at room temperature [23,25]. Clearly, the present $Fe_{40}Mn_{40}Cr_{10}Co_{10}$ HEA demonstrates twinning at the very early stages of deformation at room temperature, which can be attributed to a potentially lower SFE of $Fe_{40}Mn_{40}Cr_{10}Co_{10}$ than that of the equiatomic FeMnCoCrNi.

In the [123] oriented samples, as the DIC images in **Fig. 4.3** show, a single slip system was activated at the onset of yielding, followed by gradual spread of distinct zones of strain localization. The localized strain regions eventually consumed most of the gauge section. We also noticed a stress drop at ~2.5% strain (marked by the circle in **Fig. 4.3a**). As discussed previously, this suggests that twinning also participates in the deformation of the [123] orientation early on, similar to the observation made in the [111] sample and in the literature [150]. This hypothesis was confirmed by EBSD observations in the [111] case (**Fig. 4.2a**) but we could not detect twinning in the [123] orientation using EBSD on the samples deformed to 5% strain (EBSD inverse pole figure inset in **Fig. 4.3**), which could stem from the twins being only a few nanometers thick, which is common for low SFE materials with large lattice friction and short range order (SRO) [151] . DIC observations indicated the activation of a secondary deformation mechanism at 5% strain level, and the twinning activity was confirmed by TEM investigation of the microstructure of the 10% strained sample (details will be discussed in section 4.2). From the onset of deformation, we calculated the CRSS for slip (τ_{cr}^{sl}) to be 53±2 MPa. We estimated the

CRSS for twinning (τ_{cr}^{tw}) using the stres levels we detected from the first stress drops, DIC observations, where we started observing the second deformation mode, and TEM observations. We realized τ_{cr}^{tw} to demonstrate a wide variation for this orientation due to difficulty in pinpointing the exact stress-strain level corresponding to the nucleation of twinning in the [123] orientation, (τ_{cr}^{tw} was calculated to be 70±9 MPa from multiple samples and various observations).

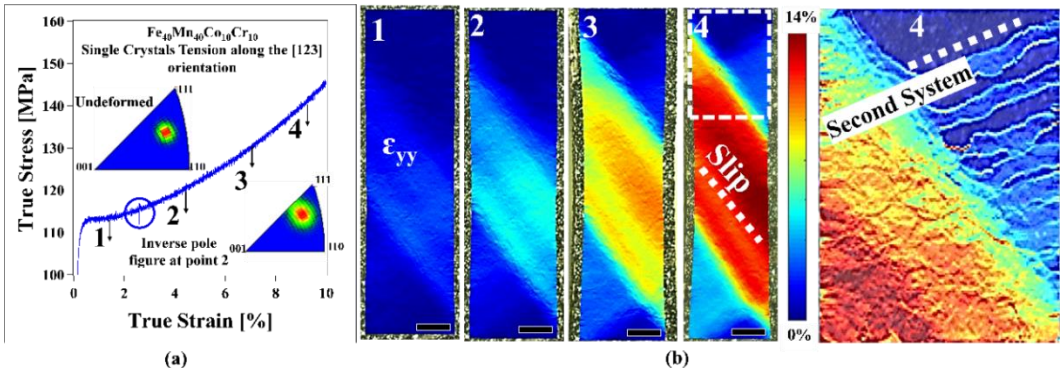

Figure 4.3 (a) The room temperature tensile stress-strain response of the [123] single crystals of $Fe_{40}Mn_{40}Co_{10}Cr_{10}$ deformed up to 10% strain. IPFs demonstrate the orientation (texture) of the sample deformed to point 4 in (a). (b) In-situ DIC images show the normal ($\boldsymbol{\varepsilon_{yy}}$) strain maps at four different strain levels (1, 2 ,3, and 4) marked in (a). Each scale bar represents a length of 1 mm.

As for the [001] orientation, DIC analysis indicated that there was significant strain localization on the sample surfaces, where deformation was confined to 'primary bands' that were almost parrallel to each other (Fig. 5.4). DIC data revealed slip activity (image 1 in Fig. 5b), and the slope of the observed slip bands matched the traces created by the {111} planes. From the onset of deformation, we calculated the CRSS for slip (τ_{cr}^{sl}) to be 51±2 MPa.

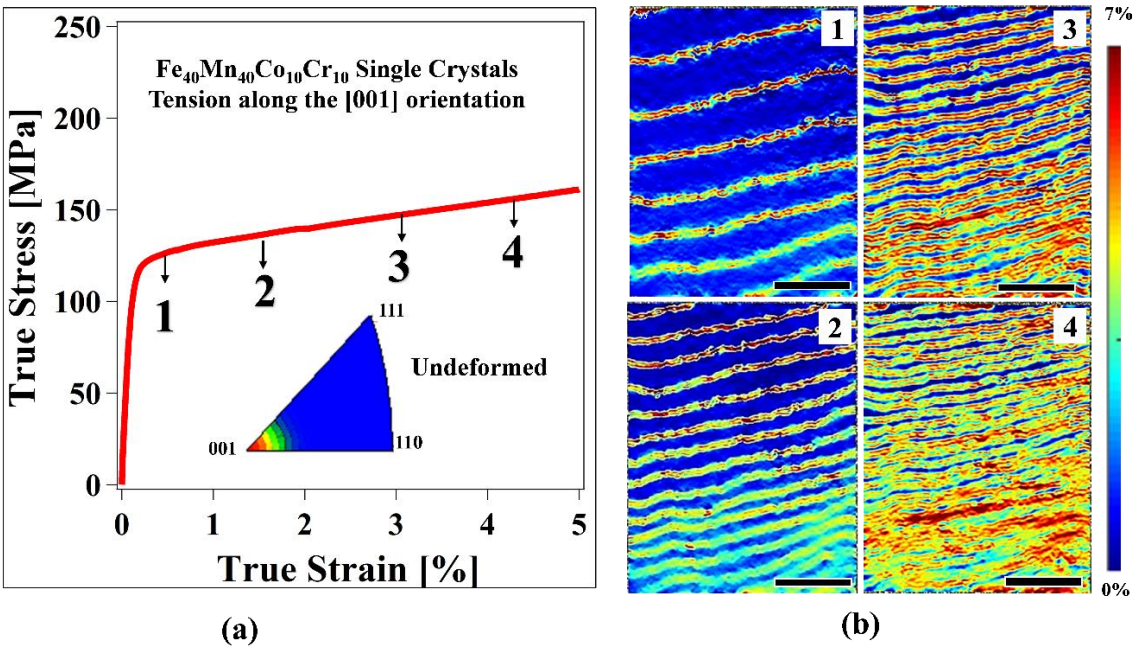

Figure 4.4 (a) The room temperature tensile stress-strain response of the [001] single crystals of $Fe_{40}Mn_{40}Co_{10}Cr_{10}$ deformed up to 5% strain. Inverse pole figures demonstrate the initial orientation of the sample (b) In-situ DIC images show the normal ($\boldsymbol{\varepsilon_{yy}}$) strain maps at four different strain levels (1, 2 ,3, and 4) marked in (a). Each scale bar represents a length of 1 mm.

4.2. Microstructure Evolution and TEM Investigations

4.2.1. The [111] orientation

In order to gain a better understanding of the hardening response and governing mechanisms responsible for different stages of hardening, the microstructures of the different crystals deformed to different strain levels were systematically examined using TEM. Stage I is the beginning strain hardening stage, which is mostly governed by dislocation glide in the absence of twinning. The stage I hardening response of the present HEA is similar to that of TWIP steels reported in [145,147]. This dislocation activity in stage I plays an important role for twining nucleation in the [111] orientation in the present

material, similar to TWIP steels, since stage 2 is the primary twinning stage (**Fig. 4.2**), which represents an increasing strain hardening rate.

The TEM observations of the 4% and 10% strained [111] samples demonstrated extensive nano-twinning activity (**Figs. 4.5b-d**), where many of the nano-twins were approximately 5 to 60 nm in thickness. Clearly, TEM images support the findings in DIC experiments and EBSD investigations, demonstrating that mechanical twinning is the major deformation mechanism in the [111] orientation at the early stages of deformation. Furthermore, the twin density increased with increasing strain level and a second twin system is activated around 10% strain (**Figs. 4.5d-f**). Twin density increase causes a reduction in dislocation mean free path through the decrease in inter-twin distances, since twin boundaries act as a barrier against dislocation motion. This, in turn, leads to dynamic Hall-Petch hardening, and eventually to very high hardening rates observed in stage 2 (**Fig. 4.1**). Two twin systems were observed interacting with each other (**Figs. 4.5e-f**) contributing to the hardening rate. When activated and if twin and slip systems are non-coplanar, the twins are obstacles to slip dislocations and the dislocation mean free path, L in Eq. (5.1), can be determined as the spacing t in Eq. (2) between twins [28,152]:

$$\frac{1}{\mathrm{L}} = \frac{1}{\mathrm{t}} \tag{4.2}$$

$$t = 2\mathrm{d}.\frac{1-f}{f} \tag{4.3}$$

Here, d is the average twin thickness and f is the twin volume fraction in the twinned region. The increase in the volume fraction of twins with increasing strain levels leads to

a decrease in the spacing between them, and accordingly, to the increase in θ. It is clear experimentally that the average distance between twins decreased with increasing twin thickness and volume fraction (**Fig. 4.5d and Fig. 4.5e**). Indeed, the sharp increase in θ at the onset of stage 2 (θ = G/33 to G/29, where G is the shear modulus, within the true strain range of 0.025-0.035) indicates mechanical twinning interacting with glide dislocations [3]. The θ for TWIP steels reaches approximately G/30 [145,147], a value close to G/29 observed in the [111] oriented samples here.

In addition to twinning, profuse dislocation activity was also observed, predominantly in stage 3 of the deformation (Fig. 5.5g-i). Many dislocations are long and straight due to the initial strong inhibition of dislocation cross-slip resulting from low SFE, the role of externally applied stress level on the perfect dislocation dissociation, i.e. the so-called Copley-Kear effect [3,54,153], and possible short range order [42]. Higher magnification of **Fig. 4.5g** displays nucleation of SFs and partial dislocations in planar arrays, in the inset images.

In stage 3 deformation of the [111] crystals, many full dislocations have dissociated into partial dislocations, resulting in the formation of SFs, as shown in **Fig. 4.5h**. Although θ increased in stage 2, a notable decrease was evident in stage 3 (from G/29 down to G/85) mainly owing to a reduction in the rate of primary twin formation and an increase in dislocation activity [149]. Moreover, some level of cross slip was also evident resulting in screw dislocation annihilation and formation of cell structure, as seen in **Fig. 4.5i**. During dynamic recovery, the formation of cell structure, which creates dislocation-free regions (**Fig. 4.5i**), is direct evidence for decreasing hardening response [3,28,31] . It is interesting

to note that although dislocation and twin boundary interaction should cause further hardening, the relaxation due to cross slip and dynamic recovery seems to be dominant, leading to an overall decrease in hardening in stage 3.

Nevertheless, θ started to increase again in stage 4 (from G/85 to G/54). Such increase can be attributed to extensive secondary twinning [147] or the activation of more twin systems, or nano-twinning nucleation inside primary twins [154], as observed in **Fig. 4.6.** Moreover, extensive tertiary twinning was also detected in the [111] oriented crystals (**Fig. 4.7**), contributing to the increase in θ and extensive stage 4 strain. These microstructural features act as barriers to further dislocation motion causing increased hardening, postpone the necking instability, thus, improving ductility. Extensive stacking faults (SFs) were observed as a result of the splitting of perfect dislocations into Shockley partials in the [111] oriented samples in stage 4 (**Figs. 4.6b and 4.6f**). The SF formation in the [111] orientation under tension is a result of the positive effect of externally applied stress on the separation between the Shockley partials, and as a result, on the effective SFE, as it was first explored by Copley and Kear [54], and later by Karaman and his colleagues [3,28,31,142]. Copley and Kear [54] demonstrated that the degree of dissociation of a glide dislocation depends on its velocity and the direction and sense of the axial stress. In tension near the [111] orientation, glide dislocations are completely dissociated at moderately high velocities in alloys with low stacking fault energies. In tension near the [001] orientation, glide dislocations constrict (as opposed to being separated into partials) at high velocities so that their cores may overlap. Inspired by Copley and Kear's original work, Karaman and his colleagues have shown in low SFE alloys [28,31,32,141–143] that

the aforementioned mechanisms (i.e. the role of applied stress on the partial dislocation separation and effective SFE) bring about distinct deformation responses along different crystallographic orientations, in terms of strain hardening and modes of deformation, which also hold in the present low SFE HEA. When the partial dislocations glide on multiple {111} planes, they can interact with each other, leading to the formation of the so-called stacking fault parallelepipeds (SFPs) [155]. The SFP structures observed in the current [111] samples are brought about by the interactions of two partial dislocation systems gliding on different {111} planes. Afterwards, stacking faults interact with each other and form a restricted area for dislocation motion especially when their volume fraction is high (**Fig. 4.6e-f**). This leads to a reduction in dislocation mean free path (**Fig. 4.6f**), and as a result, to an increased hardening rate in stage 4. In addition to SFP, the interaction between twin boundaries and stacking faults also contribute to the overall hardening observed in stage 4.

At large strains, the primary twins tend to grow thicker and many of them (and their bundles) reach tens to hundreds of nanometers in thickness (**Figs. 4.6c and 4.6g**). Thicker twins allow for dislocation glide within the primary twins, resulting in an extensive stage 4 regime and enhancing the plastic deformation capacity [156]. The formation of SFs and high dislocation activity within primary twins was evident in the extended stage 4 regime in **Fig. 4.6c**.

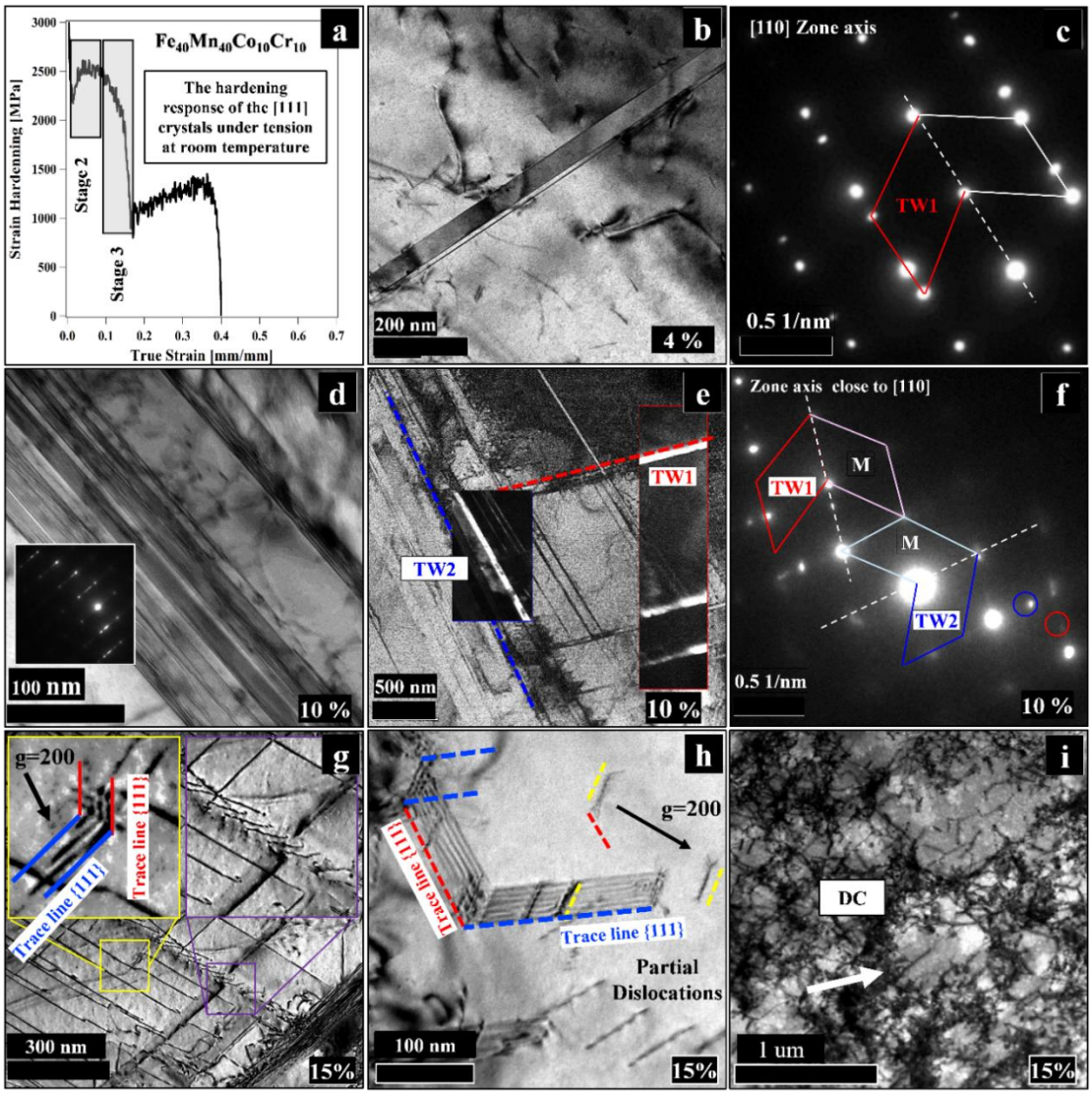

Figure 4.5 Bright field and dark field TEM micrographs and corresponding selected area diffraction (SAD) patterns of the [111] oriented single crystalline $Fe_{40}Mn_{40}Co_{10}Cr_{10}$ HEA, demonstrating major deformation mechanisms governing the various hardening stages of the samples deformed to different strain levels under tension at room temperature (a). (b) twinning was clear in the samples deformed to strain levels as low as 4%, with the corresponding SAD pattern (c) clearly proving the existence of primary twins. (d) extensive primary twin bundles at 10% strain, (e) Twin-twin interaction of primary and secondary twins, and the darkfield images of the primary and secondary twin systems (insets) at 10% strain, with the corresponding SAD pattern identifying these twin systems (f), (g) the dislocation structures near twin boundaries and the long straigth dislocations (paralel to each other) and interfacial partials at 15% strain, (h) stacking fault stair-rod with g=(200) at 15% strain, and (h) formation of dislocation cell structures again at 15%.

The critical flow stress for the activation of dislocations within a twin thickness t is given by [157]:

$$\sigma_T = 3\frac{G.\mathrm{b}_{110}}{2d} \tag{4.4}$$

where b_{110} is the burgers vector, *d* is twin thickness and G is the shear modulus. According to equation (4), dislocation generation in the twinned regions is related to twin thickness and the applied stress level. In the present low SFE HEA, the stress level required for dislocation glide and eventually, the formation of nano-twinning within primary twins in the [111] orientation is calculated as 29/*t* GPa. We experimentally detected nano-twins in the twinned regions of the [111] oriented sample strained up to the failure, which supports the dislocation activity in the twinned regions. Using the equation (3), the minimum twin thickness for dislocation activity in the twinned regions was calculated as 34 nm. This value is consistent with the primary twins with internal nano-twins observed in our TEM investigations (**Fig. 4.6g**). Increasing twin thickness and stress level facilitate dislocation activity in the twinned regions, which causes increase in dislocation storage capacity. This observation, the activity of tertiary twin (**Fig. 4.7**), and the formation of nano-twinning between and within primary twins, as shown in **Fig. 4.6g-i**, rationalizes the extended stage 4 hardening observed in the [111] orientation. The nano-twin formation provides additional ductility in stage 4, leading to further decrease in dislocation mean free path, and subsequently further strain hardening [154]. Overall, both dislocation glide and nano-twinning dominate over primary twinning in stage 4.

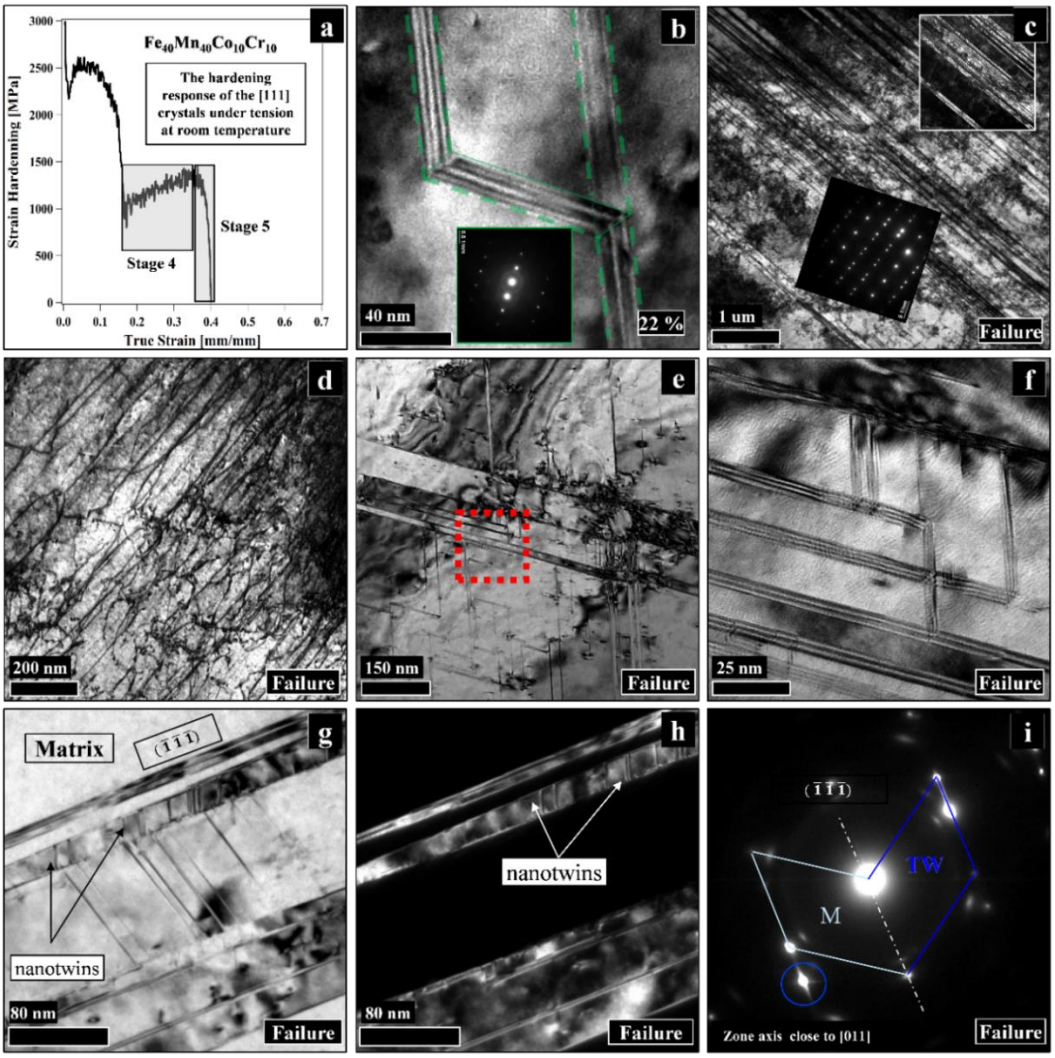

Figure 4.6 Bright field and dark field TEM micrographs and corresponding selected area diffraction patterns of the [111] oriented single crystalline $Fe_{40}Mn_{40}Co_{10}Cr_{10}$ HEA, demonstrating major deformation mechanisms governing the various hardening stages of the samples deformed to different strain levels under tension at room temperature (a). (b) stacking fault (SF) paralelpipeds at 22% strain level, (c) high density of dislocation-twin interactions at failure, with the dark field images of the twins in the inset, (d) high density of parallel dislocations, (e) SF-twining interaction at failure, (f) zoomed-in image of the red-square region in Fig. 5.6e showing stacking fault paralelpipeds near a twin boundary, (g) the bright-field image of nano-twins forming within matrix and primary twins deformed to failure, (h) the dark field image of primary twins indicating internal nano-twins, and (i) the selected area diffraction pattern demonstrating the twin activity.

To summarize, the sharp increase in θ in stage 2 hardening regime of the [111] crystals is attributed to extensive twin formation and the rapid increase of twin volume fraction, based on the evidence provided by the in-situ DIC and TEM analysis. The governing deformation mechanisms in this orientation sequentially are the initiation of primary twinning [147], growth of primary twins [158], activation of secondary twins [140], and the evolution of dislocation subsutructures, such as HDDWs [137]. In stage 3, θ decreases due to dynamic recovery and the existence of cross slip with the formation of cell structure (**Fig. 4.5i**), until stage 4 kicks in since higher stresses are required to generate more twins based on the dynamic Hall-Patch effect. Another reason for the reduction in θ in stage 3 is the development of misorientations between the {111} plane in the matrix and the habit plane of the existing twins with increasing strain, which inhibits the formation of new primary twins [147]. Interestingly, many alloys fail after stage 3 deformation under tensile loading. In contrast, the present HEA along the [111] orientation exhibits an extra hardening stage (stage 4), which further improves its ductility. We consider this beneficial effect to stem from the nucleation of new twinning systems (extensive tertiary twinning) and nano-twinning within primary twins [159].

4.2.2. The [123] orientation

Similar to the [111] orientation, both dislocation activity and nano-twinning were observed in the [123] oriented samples strained up to 10 % (**Fig. 4.8**). The observation of twinning in the [123] orientation under tension is somewhat unusual since this orientation is expected to experience only a single slip system for a typical fcc crystal. However, a notable increase in the hardening rate was noted in the [123] sample (**Fig. 4.1**). The

dislocation substructure (single slip) alone cannot lead to such rapid increase in θ in this orientation at the onset of stage 2. Therefore, a different deformation mechanism must have been activated to cause such unexpected rise of θ. In fact, a secondary deformation mechanism can be seen in the optical microscopy image in the inset of **Fig. 4.1d**.

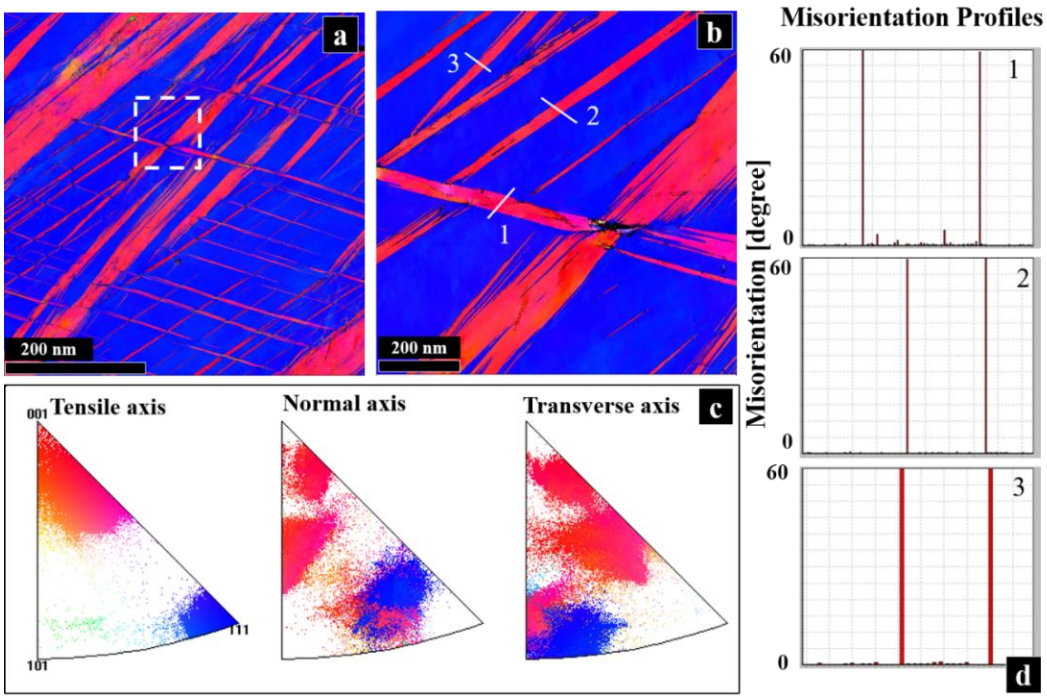

Figure 4.7 EBSD maps of the [111] oriented single crystalline $Fe_{40}Mn_{40}Co_{10}Cr_{10}$ HEA, recorded at the center of the specimen strained up to 40%. (a) with 0.5 μm step size (b) with 0.1 μm step size, (c) corresponding inverse pole figures, and (d) corresponding misorientations profiles along the three lines marked in (b), showing the activity of three different twinning systems, which contribute to the increase in θ and extended stage 4 ductility.

The increase in the θ in stage 2 regime is mainly due to slip-twin and twin-SF interactions (**Fig. 4.8**). In the 10% strained samples, pile-up dislocations and extensive nano-twinning were also evident as seen in **Figs. 4.8b-c**. Many of the nano-twins were

approximately 10 nm in thickness. The thickness of nano-twins in the 20% and 30% strained samples varied anywhere from 10 nm to 200 nm (**Figs. 4.8d-e**). The SF-twin boundary interactions (**Fig. 4.8d**) bring about extra hardening in stage 2.

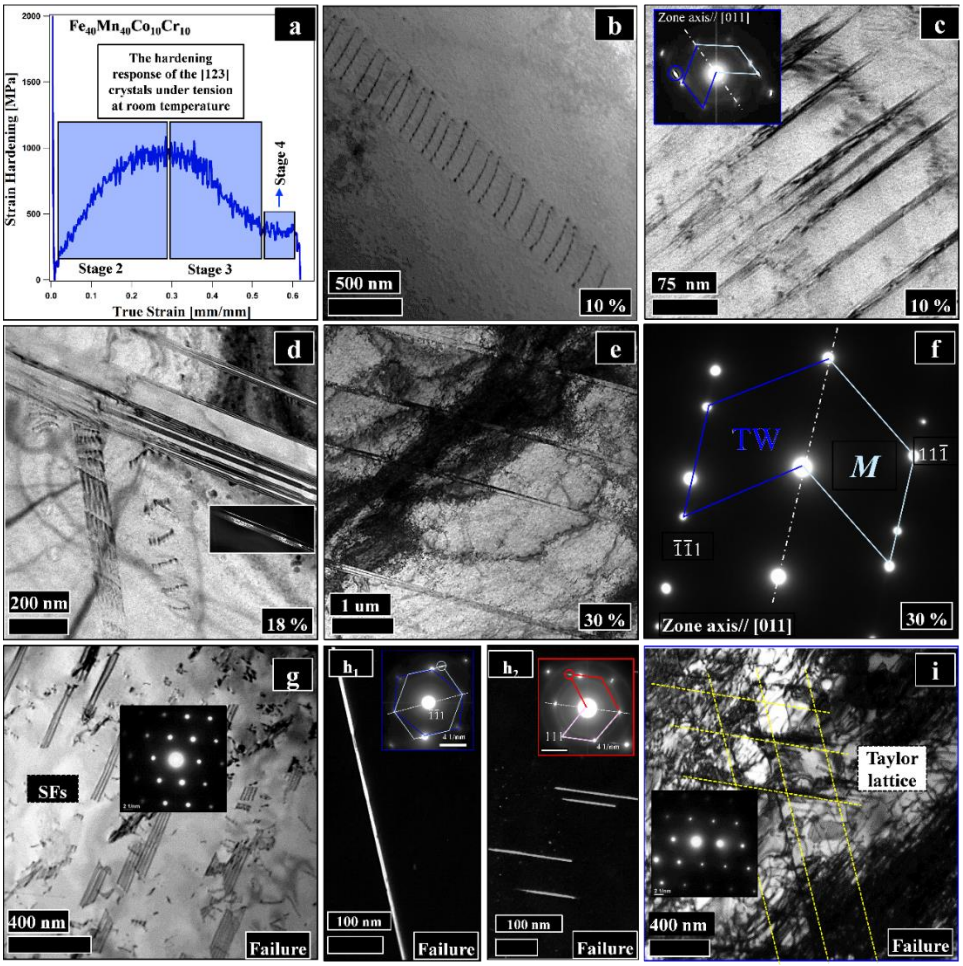

Figure 4.8 Bright field and dark field TEM micrographs and corresponding selected area diffraction (SAD) patterns of the [123] oriented single crystalline $Fe_{40}Mn_{40}Co_{10}Cr_{10}$ HEA, demonstrating major deformation mechanisms governing the various hardening stages under tension at room temperature (a). (b) dislocation pile-ups in the sample deformed to 10% strain, (c) twinning activity in the sample deformed to 10% strain, (d) primary twining and twin-SFs interaction at 18% strain, (e-f) an increased twin density at 30% strain, (g) high density of SFs was evident throughut the deformation, (h) two different twin systems at failure, and (i) dislocation substructures consisting of high density dislocation walls (HDDWs).

The transition from stage 2 to stage 3 region (at maximum θ of G/60) is due to the saturation of primary twins and their thickness, and dislocation recovery, as in the case of [111] oriented samples. The stage 3 hardening ended at θ = G/125 with the nucleation of the secondary twin system, similar to TWIP steels [140]. As the deformation proceeds into stage 4, high density of SFs (**Fig. 4.8g**), multiple twin sytems (Fig. 8h) and a carpet-like dislocation structure (**Fig. 4.8i**) prevailed, significantly contributing to the observed stage 4 hardening since they all act as strong barriers against dislocation motion [31,36,42]. The carpet-like dislocation structure is formed via the activation of multiple slip systems and is commonly observed in low SFE materials [31,136]. However, the stage 4 hardening rate in the [123] oriented sample is relatively low as compared to that in the [111] oriented sample. This lower stage 4 hardening rate in the [123] crystals is most likely due to the lack of nano-twin formation within the primary twins, which were extensively observed in the [111] crystals.

The DIC and TEM results both showed that the dislocations at the onset of plastic deformation demonstrate planar slip characteristics and are strongly localized in a limited set of specific (111) planes in the [123] and [111] oriented samples. This phenomenon is usually associated with either the short range clustering (SRC) or the SRO of solute atoms, as clearly demonstrated by the pioneering work of Gerold and Karnthaler [21,42,160,161]. Accordingly, three factors are responsible for planar slip: low SFE, high yield strength, and SRO or SRC, yet low SFE and high yield strength have a relatively minor effect on the appearance of planar slip [42]. The relationship between SRO and the planar slip can be explained with the destruction of the SRO when the first dislocation glides through the

lattice. Once the SRO is destroyed, the following dislocations cannot restore the initial order, exposing these dislocations to a lower resistance for slip [42]. Dislocations generated from the same dislocation source follow the first one by pushing against it in order to overcome the high slip resistance, giving rise to extensive slip activity on a single plane, which leads to glide plane softening. This effect also causes a distinct yield point, which is a signature for SRO (see Fig. 3). Since the present HEA crystals demonstrate extensive planar slip activity in both [111] and [123] orientations, it is likely that these crystals feature SRO.

4.2.3. The [001] orientation

Experimental results revealed that the θ in the [001] orientation is lower than that in the [111] orientation and higher than the θ in the [123] orientation (**Fig. 4.2**). The samples of this orientation displayed three distinct hardening stages (**Fig. 4.2**). In stage 2, the sample exhibits a linear increase in θ, brought about by the onset of the formation of HDDWs (Fig. 9a). HDDWs have also been observed in TWIP and Hadfield steels [137,145] as well as in the [111]- and [123]-oriented samples studied in this work. Gutierrez-Urrutia *et al.* [145] suggested that a major reason for the increase in hardening rate in TWIP steels with low SFE is the refinement of the dislocation mean free path induced by mechanical twinning and HDDWs acting as strong barriers against further dislocation glide. The similar effect of HDDWs on hardening was also observed in austenitic Hadfield steels and stainless steel single crystals [31,137]. According to Wilsdorf [136], alloys with low SFE cannot form dislocation cell structures, but they can produce Taylor lattice as a result of a crystal with highly dissociated dislocations. High

lattice friction and planar glide may also produce Taylor lattice [35,136] . However, an important difference between the previous studies and the current work is that, even though the formation of HDDWs has so far been attributed to planar slip character [31,35,136,137,145], we could not find any evidence for planar dislocation arrangements in the [001] orientation in the present study.

In **Fig. 4.9a**, distinct dislocation structures were identified as dislocation multi-junctions, dislocation pairs, dislocation dipoles and dislocation nodes. Dislocation multi-junctions can serve as a new dislocation source and anchors for dislocation tangles [162]. **Fig. 4.9a** illustrates a junction formation in the sample deformed to 10% strain. The intersection of two dislocations at their midpoints cause two lines to zip a binary junction (**Fig. 4.9a$_1$**); then, a third line intersecting with this junction creates a multi-junction (Fig. 9a$_2$), which acts as a Frank-Read source [162]. The beginning of localization can be observed in **Fig. 4.9a$_3$**, and a dislocation dipole can be seen in the same location in **Fig. 4.9a$_4$**. The dislocation dipole is composed of two dislocations of opposite signs that are on different (111) planes in FCC metals, forming a jog that is very immobile. As shown in **Figs. 4.9a$_3$ and 4.9a$_4$**, the formation of the HDDWs and dislocation dipoles share the same direction. This can support the formation of HDDWs around dislocation dipoles: we propose that the interaction of the jogs and dislocation dipoles facilitates HDDW formation. HDDWs that decrease the dislocation mean free path (**Fig. 4.9b**), dislocation nodes, and high dislocation density altogether promote a continuous increase in θ in stage 2.

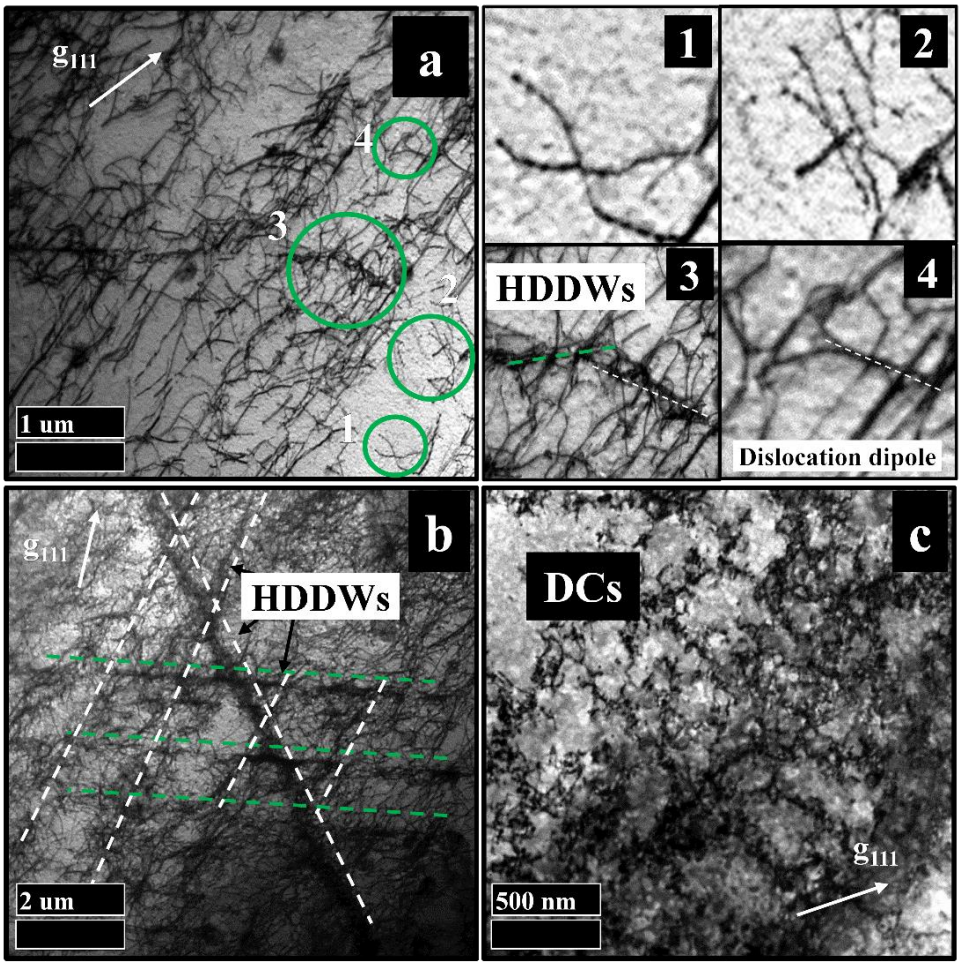

Figure 4.9 Bright field TEM micrographs of the [001] oriented single crystalline $Fe_{40}Mn_{40}Co_{10}Cr_{10}$ HEA, showing the microstructure evolution under uniaxial tension deformation. (a) dislocation structures at 10% strain, (b) dislocation susbstructure consisting of high density dislocation walls (HDDWs) at 10% strain, and (c) dislocation cells (DCs) in the failed sample.

In stage 3 hardening, the sample deformed up to failure exhibits a dislocation cell structure in **Fig. 5.9c**, which strongly suggests wavy slip activity. The dislocations in stage 3 apparently overcome the barriers (HDDWs) with increasing stress, and thus, can form dislocation cells. The contribution of twining to the hardening in this orientation was excluded because no twins were observed in the [001] oriented samples up to 35% tensile

deformation (up to failure), as evidenced in **Fig. 5.9c**. Thus, we conclude that the hardening in the [001] orientation under tension is mainly controlled by the formation of dislocation walls in this study based on the DIC and TEM characterization.

In summary, the [001] orientation had the lowest plastic deformation ability as compared to the [111] and [123] orientations, both of which exhibited an extra hardening stage, due to the extensive twinning activity. The corresponding nucleation of secondary/tertiary twins and/or nano-twin formation within primary twins enhance the ductility in the [123] and [111] orientations, which are not prevalent in the [001] orientation due to the lack of TWIP effect.

4.3. Effect of Applied Stress on the Effective Stacking Fault Energy and Critical Resolved Shear Stress for Twinning

The reason for the extensive twinning activity in the [111] and [123] oriented single crystals at room temperature is attributed to their lower SFE as compared to that of the equiatomic FeMnCoCrNi HEA, obtained by reducing the Ni content and thereby increasing the corresponding Mn concentration. We determined the stacking fault energy, γ_0, of $Fe_{40}Mn_{40}Co_{10}Cr_{10}$ HEA from the triple dislocation nodes in the present single crystals to be 0.013±0.004 J/m^2, which is smaller than that of equiatomic FeMnCoCrNi HEA [24,27], and comparable to or lower than that of Hadfield Steel and 316L stainless steel [28,32,143,144]. Moreover, Shockley partial separation distance (SPSD, $d_{partial}$) in low SFE materials, including the present HEA, can be changed by externally applied stress, as originally proposed by Copley and Kear [54], and since SPSD and SFE are inversely related, the externally applied stress level result in an “effective” SFE:

$$d_{partial} = \frac{Gb_1^2}{8\pi\gamma_{eff}} \tag{4.5}$$

$$\gamma_{eff} = \gamma_0 \pm \frac{(m_1 - m_2)}{2}\sigma b_1 \tag{4.6}$$

where γ_{eff} is effective SFE, m_1 and m_2 are the Schmid factors for the leading and trailing partial dislocations, respectively, b_1 is the Burgers vector of the partial dislocation, σ is the externally applied stress with ± indicating the sign of the applied stress (tension or compression), and G is the shear modulus. Effective SFE depends on the orientation factor ($Q = (m_1–m_2)/2$, **Table 4.1**), σ, and the sign of applied stress [54,62,149,163]. When Q has negative values, γ_{eff} decreases and SPDS subsequently increases, giving rise to the formation of the intrinsic stacking faults. In the [111] oriented samples under tensile loading at room temperature, as the splitting of partials is easier in the external stresses field, the dislocation structure becomes planar according to the Copley and Kear effect (**Fig. 4.10**). However, Q is positive under tensile stress in the [001] oriented sample, and consequently, external tensile stress leads to a reduction in $d_{partial}$, and γ_{eff} increases, promoting cross slip. In some cases, such as at low temperatures, the cross slip can be suppressed and the extrinsic SFs can form under tensile loading (Fig. 10b), eventually facilitating twinning nucleation [142,164].

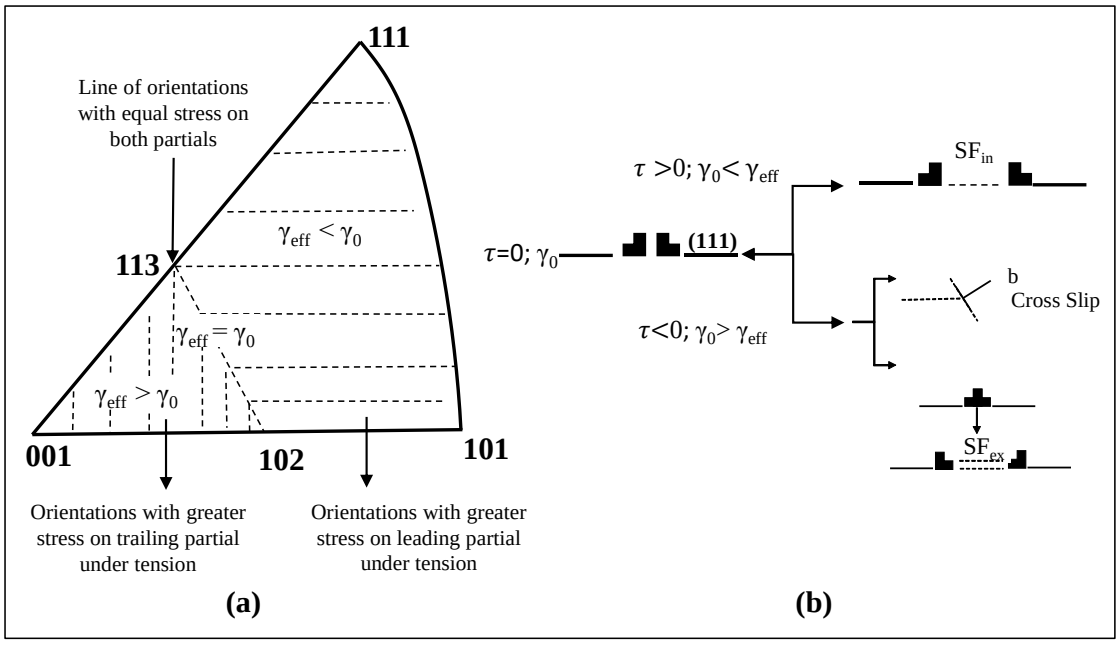

Figure 4.10 The effect of applied stress on the equilibrium partial dislocation separation under tensile deformation in low stacking fault energy crystals: (a) the stereographic unit triangle exhibits the change of the effective stacking fault energy based on the orientation of tensile loading. (b) the formation of intrinsic SFs when the applied stress increases the partial dislocation separation, and the competition between extrinsic SFs and cross slip, when the applied stress reduces the partial dislocation separation.

For the [111] oriented crystals, γ_{eff} was estimated, using equation 6, to be 0.010±0.004 J/m^2 (at % 3 strain) at the onset of primary twinning, and γ_{eff}=0.002±0.004 J/m^2 (at UTS) in stage 4 for the formation of nano-twins within primary twins and tertiary twins. It is concluded that the sharp decrease in γ_{eff} promoted the nucleation of nano-twins (2-3 nm), formation of tertiary twins, and an increase in primary twin volume fraction, leading to an extended stage 4 hardening. In the [123] oriented samples, $\gamma_{eff} = 0.11 \pm 0.004$ J/m^2 (at %10 strain) and $\gamma_{eff} = 0.007 \pm 0.004$ J/m^2 were estimated at %50 strain for the nucleation of secondary twinning in stage 2 and nano-twinning (min 2 nm) in stage 4, respectively. It is most likely that the nucleation of the nano-twinning formation

in primary twins is due to an extremely low γ_{eff}. Although the [123] orientation is in general a soft orientation, the stage 4 hardening in the [123] orientation is observed but at much shorter extent than that of the [111] orientation. Nano-twin formation within primary twins and tertiary twinning were not observed in the [123] orientation, since effective stacking fault energy was not low enough to allow for nano-twin formation within primary twins, which also relates to the relatively narrower stage 4 in the [123] orientation.

Using the above γ_{eff} concept, below we attempt to calculate the critical resolved shear stress for deformation twinning in the present $Fe_{40}Mn_{40}Co_{10}Cr_{10}$ HEA. General twinning theories predict that the critical resolved shear stress (CRSS) for twinning is proportional to intrinsic stacking fault energy. According to Narita and Takamura [165], CRSS for twining can be calculated using:

$$\tau_T = \frac{\gamma_{isf}}{2b_p} \tag{4.7}$$

where b_p is the Burgers vector of the Shockley partial dislocation. Suzuki and Barrett [166] proposed that a small segment of dislocation consisting of a sessile partial and a twinning partial pinned at two points act as a twin nucleation and CRSS could be determined using:

$$\tau_T = \frac{\gamma_{isf}}{2.\, b_p} + \frac{G.\, b_p}{L_0} \tag{4.8}$$

where L_0 is the length of sessile partial dislocations engaged in twinning nucleation. Another twinning nucleation mechanism was proposed by Mahajan and Chin [167]. Mahajan and Chin's three-layer twin nuclei are pre-existing multi-layer defects, residing, for instance, at grain boundaries [167], which can be activated when the stress reaches a

critical value [167]. Steinmetz *et al.*[168] assumed that a small segment of a Mahajan-Chin three-layer twin between two pinning points acts as twin nucleus. Accordingly, the twinning stress, defined as the critical stress for the formation of an unstable bow-out of the three twinning partials, is expressed by [168]:

$$\tau_T = \frac{\gamma_{isf}}{3.b_p} + \frac{3.G.b_p}{L_0} \quad (4.9)$$

Table 4.2 compares the experimentally observed CRSSs with the theoretical CRSSs calculated using the three twinning theories reported in the literature and summarized above [165,166,168]. The experimental CRSS values reported include that for primary twinning taking place either in stage 1 or stage 2 (72±5 MPa in the [111] oriented samples and 70±9 MPa in the [123] oriented samples) and for additional twinning in stage 4 (157±10 MPa in both the [111] and [123] oriented samples). The results demonstrate that the Narita-Takamura model yields the closest prediction to the experimentally observed value of the primary twinning nucleation (τ_{cr1}^{tw}) in the present material, whereas calculated stresses based on three-layer twinning mechanism (Steinmetz Model) are close to the experimental CRSS for twinning in stage 4 (τ_{cr2}^{tw}).

4.4. Comparison of $Fe_{40}Mn_{40}Co_{10}Cr_{10}$ and Conventional Low Stacking Fault Energy Austenitic Steels

In order to better evaluate the potential of low SFE HEAs and compare and contrast the hardening responses of the present HEA with the known low SFE conventional austenitic steels, i.e. 316 stainless steel, and Hadfield steel (Fe-12%Mn-1%C in weight), Fig. 4.11 was constructed. The figure compares the strength differential ($\sigma - \sigma_0$, where

σ_0 is the yield strength) and the hardening stages of the single crystalline samples along the three crystallographic orientations. It can be clearly seen that the $Fe_{40}Mn_{40}Co_{10}Cr_{10}$ HEA has better ductility than both 316 and Hadfield steels along the [111] and [123] oriented samples (Fig. 11a-c). Also, their strength differential levels were almost the same as these two conventional steels.

Table 4.2 Experimentally determined and theoretically predicted Critical Resolved Shear Stresses ($\boldsymbol{\tau_{cr}^{tw}}$) for twinning in $Fe_{40}Mn_{40}Co_{10}Cr_{10}$ high entropy alloy single crystals.

Experimentally determined Critical Resolved Shear Stresses (τ_{cr}^{tw}) for twinning (MPa)		Theoretically predicted τ_{cr}^{tw} using different models in the literature (MPa)			
τ_{cr1}^{tw}: Primary twinning nucleation	τ_{cr2}^{tw}: Secondary / Tertiary twinning nucleation	Narita and Takamura [165]	Suzuki and Barret [166]	Steinmetz *et al.* [168]	Fe-22%Mn-0.6%C[b] [169]
[111]: 72±5 [123]: 70±9	[111] / [123]: 157±10	57±14	104±23	158±17	72

[b] [001] single crystal in compression (twinning favoured).

The main difference between the $Fe_{40}Mn_{40}Co_{10}Cr_{10}$ HEA and these low SFE steels is that the extended stage 4 was observed in the [111] oriented samples in the HEA: the formation of the nano-twins and activation of tertiary twins are responsible for the extended stage 4 deformation, suppressing necking and increasing the ductility in $Fe_{40}Mn_{40}Co_{10}Cr_{10}$ crystals. Similarly, along the [001] orientation, Hadfield steel demonstrates stage 4 hardening (Fig. 11f), and thus, higher ductility, since Hadfield steel has been shown to demonstrate extrinsic stacking faults and twinning in [001] orientations deformed under tension at room temperature [142].

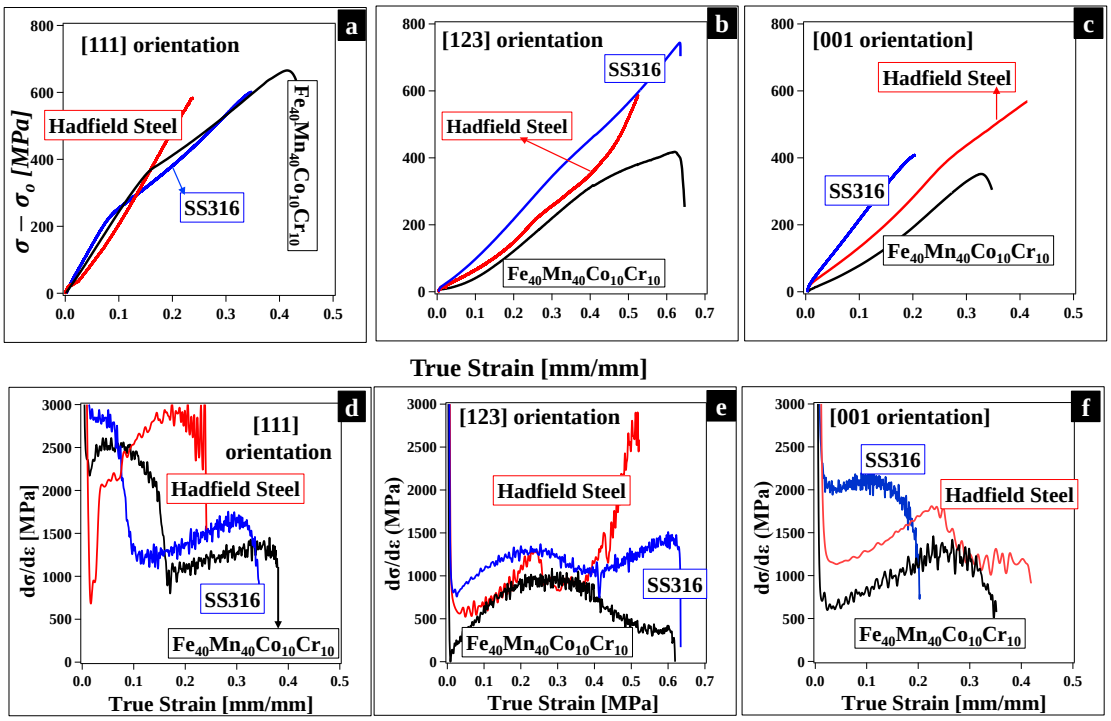

Figure 4.11 Comparison of the room temperature uniaxial tension responses of three low to medium stacking faulty energy fcc materials, *i.e.* $Fe_{40}Mn_{40}Co_{10}Cr_{10}$ HEA, Hadfield steel (Fe-12%Mn-1%C in wt.), and 316 stainless steel (SS316). (a-c) The comparison of the strength differential ($\sigma - \sigma_0$, where σ_0 is the yield strength) and hardening response as a function of the applied strain along three crystallographic orientations. (d-f) the comparison of the strain hardening rate responses of the [111], [001] and [123] oriented single crystals for all three materials in (a), as a function of the applied strain level.

It should be noted that both Hadfield steel and 316 stainless steel contain interstitials (carbon and carbon/nitrogen, respectively) and feature interstitial solid solution hardening, whereas the current alloy does not have any interstitials. Therefore, both 316 stainless steel and Hadfield steel demonstrate much higher yield strengths (and thus higher CRSS for twinning and slip) for all orientations as compared to that of $Fe_{40}Mn_{40}Co_{10}Cr_{10}$ crystals (**Table 4.3**) because of the interstitial and conventional solid solution hardening in the former steels. Mainly, Hadfield steel and 316 stainless steel have higher yield strength

levels because of the increased lattice friction due to the high concentration of solute atoms. It has been recently reported that polycrystalline $(Fe_{40}Mn_{40}Co_{10}Cr_{10})_{96.7}+C_{3.3}$ HEA has much higher strength than $Fe_{40}Mn_{40}Co_{10}Cr_{10}$ [61], indicating that the current $Fe_{40}Mn_{40}Co_{10}Cr_{10}$ HEA can be strengthened by the addition of large amount of carbon without sacrificing ductility.

Table 4.3 Experimental yield strength values of $Fe_{40}Mn_{40}Co_{10}Cr_{10}$ high entropy alloy, 316 stainless steel and Hadfield steel single crystals. The results are the average of the yield strengths from 3 to 5 companion specimens for each case.

	σ_0^{111} (MPa)	σ_0^{123} (MPa)	σ_0^{001} (MPa)
$Fe_{40}Mn_{40}Co_{10}Cr_{10}$	192±5	118±5	125±5
SS316	311±10	196±6	222±7
Hadfield Steel (Fe-13Mn-1C)	500±10	304±6	349±6

4.5. Summary and Conclusions

The orientation dependence of the room temperature tensile deformation response of the $Fe_{40}Mn_{40}Co_{10}Cr_{10}$ high entropy alloy (HEA) single crystals (SCs) oriented along the [111], [001] and [123] crystallographic orientations was investigated. Extensive in-situ local strain measurements based on digital image correlation, transmission electron microscopy, and electron back scattered diffraction (EBSD) imaging investigations were used to reveal the deformation mechanisms responsible for different hardening stages. Primary findings can be summarized as follows:

1. The strain hardening response and strain hardening coefficient under room temperature tension demonstrate strong orientation dependence in $Fe_{40}Mn_{40}Co_{10}Cr_{10}$ HEA as a result of the activation and complex interactions of orientation dependent deformation twinning and planar slip as well as dislocation wall/network formation regardless of the orientation. While the [111] and [123] orientations feature four strain hardening stages due to the activation of multi-twin systems, the [001] orientation demonstrates only three strain hardening stages due to the lack of deformation twinning. The orientation dependence of the deformation modes was rationalized using the Copley-Kear effect, which takes into account the role of externally applied stress on the partial dislocation separation and effective stacking fault energy, which is orientation dependent under applied stress.
2. The exceptional strain hardening coefficient (θ) exhibited by the [111] orientation was attributed to the activation and interaction of multiple twin systems in stage 2. The significant ductility of this orientation, despite its highest strength among other orientations, was attributed to the formation of nano-twins within primary twins and the activation of the tertiary twins at the later stages of deformation (stage 4), which provided additional deformation when other micro-deformation mechanisms saturated. In addition, coexistence of multiple slip mechanisms in the [111] orientation also allowed for Shockley partial dislocations to form parallelepiped stacking faults in stage 4. Overall, the response of the [111]

orientation is similar to that of the twinning-induced plasticity (TWIP) steels that also have low stacking fault energy.

3. Plastic deformation of the [123] orientation was governed mainly by planar slip. The coexistence of slip and nano-twins in stage 2 was responsible for the strain hardening behavior in this orientation. The [123] orientation displayed a stage 4 hardening response, somewhat unexpectedly, similar to the [111] orientation, due to the activation of deformation twinning. Secondary twinning and high-density dislocation walls (HDDWs) that form a Taylor lattice were also observed to contribute to the overall work hardening in stage 4.
4. Twinning was not observed in the [001] orientation, which is consistent with the Copley-Kear effect. Strain hardening in the [001] orientation was attributed to HDDWs forming along multiple slip systems. Even though the formation of HDDWs is usually attributed to planar slip, planar character was not observed during the TEM of the [001] orientation of the present material. Specifically, the interaction between multi-junctions, which gives rise to high dislocation density, and dislocation dipoles lead to the formation of locks, facilitating the formation of HDDWs that act as obstacles against dislocation motion. Moreover, HDDWs also give rise to a formation of a lattice that is similar to Taylor lattice but allows for dislocation cell structure formation.
5. The comparison of the hardening response of the present low stacking faculty energy HEA with the conventional low stacking fault energy steels such as 316 stainless steel and Hadfield steel demonstrated that despite the present HEA does

not feature interstitial solid solution hardening, as in the case of 316 stainless steel and Hadfield steel, the hardening response and the hardening stages are very similar to these two conventional steels. $Fe_{40}Mn_{40}Co_{10}Cr_{10}$ HEA demonstrates higher ductility in the [111] and [123] orientations due to the extended stage 4 hardening, however, the yield strength levels are notably lower as compared to 316 stainless steel and Hadfield steel due to the lack of interstitial solid solution hardening.

5. THE EFFECT OF SHORT-RANGE ORDERING ON THE PLASTIC DEFORMATION

Medium- and high-entropy alloys offer a much larger and richer design space than conventional alloys, providing tremendous opportunities for discovering new functionalities and their controlling physics [1,2,4,5,57]. Some of these alloys exhibit an outstanding combination of high strength and ductility, which has been linked to the activation of various deformation modes triggered by low-energy stacking faults [3,37,89]. However, the question remains: is the plasticity of these medium- and high-entropy alloys governed only by stacking fault energy, or does atomic short-range order (SRO) play a role? To answer this question, we investigated the effect of SRO on the plastic deformation in single-crystalline NiCoCr medium-entropy alloy. First, we established a clear experimental evidence for SRO formation in as-quenched crystals using high-resolution transmission electron microscopy (HRTEM). Then, we demonstrated that SRO promotes twinning- and transformation-induced plasticity in NiCoCr, depending on the crystallographic orientation of the crystals. We also discovered a new hierarchical strain-induced phase transformation sequence (fcc $\rightarrow$ hcp $\rightarrow$ $D0_{19}$) at room temperature using high energy transmission X-Ray experiments and HRTEM. Based on novel density-functional theory methods, we attributed this transformation to a weaker degree of SRO in the hcp phase. By controlling the degree of SRO through aging at high temperatures, the level of twinning and strain-induced phase transformation has been increased, further enhancing the ductility levels in NiCoCr. These results indicate that the interplay of SRO and plasticity could be exploited to trigger various deformation modes

including hierarchical strain-induced phase transformations and to discover new medium- and high-entropy alloys with unprecedented mechanical properties.

5.1. Experimental Evidence for Short-Range Ordering

In this chapter, we used bulk single-crystalline NiCoCr to investigate the effect of SRO on the plastic deformation of NiCoCr. Single crystals were used to eliminate confounding factors, such as grain boundaries and grain-size strengthening, which are very challenging to deconvolute from intrinsic properties in the case of polycrystalline samples. To the best of our knowledge, investigation of SRO and its evolution under isothermal aging in a single crystalline material has not been carried out before. Three crystallographic orientations, [001], [110] and [111], were selected to sample different regions of the stereographic triangle, thus allowing us to activate different deformation modes, such as planar slip, cross slip, stacking fault (SF) formation, and subsequently, twinning and/or martensitic transformation [54,89]. SRO has previously been investigated in NiCoCr using diffuse intensity [50] and X-ray adsorption methods [47], and it was found that ordered domains or domain clusters grow to a “fairly large” scale, permitting capture of the information by diffraction. There is no direct observation showing the effect of SRO on the deformation modes such as TWIP and TRIP in this kind of alloy systems. For that reason, we used advanced experimental and computational techniques to determine the effect of SRO leading to a new deformation pathway in NiCoCr.

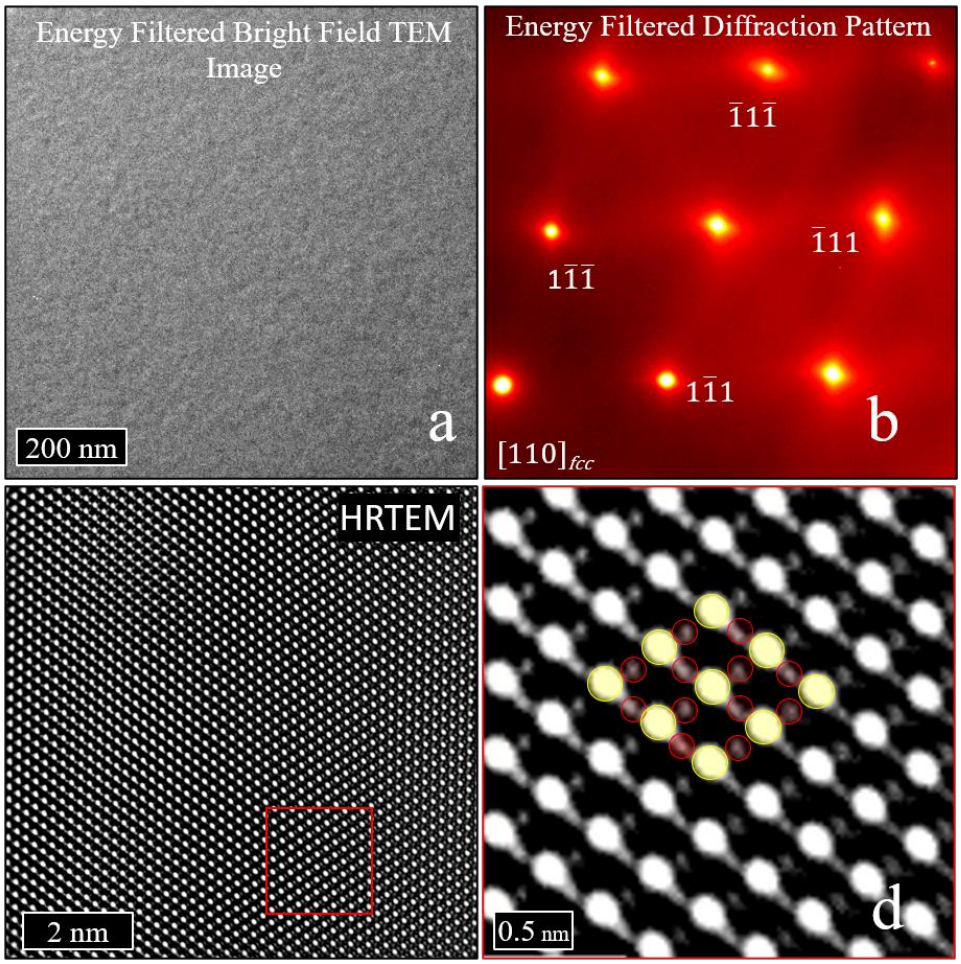

Figure 5.1 The examination of SRO and its effect on the deformation modes in as-quenched NiCoCr using Energy filtered TEM with the associated high-resolution TEM and Transmission X-Ray. (a) Energy-filtered TEM images associated with (b) diffuse super lattice streaks of as-quenched single crystalline NiCoCr. The contrast of the diffraction pattern is pseudo-colored for better visibility. (c) High-resolution TEM images with the associated two-dimensional fast Fourier transform (FFT), (d) higher magnification of (c) showing a direct imaging of SRO domain that suggests a superlattice.

To characterize SRO in as-quenched NiCoCr single crystals (water quenched from 1200˚C after 24h), energy-filtered TEM analysis (**Fig. 5.1a-b)** and high-resolution transmission electron microscopy (HRTEM) measurements (**Fig. 5.1c-d)** were performed.

The energy-filtered diffraction pattern in **Fig. 5.1b** taken from **Fig. 5.1a** shows diffuse intensity, indicating well-developed local chemical ordering in the fcc lattice as discussed in [50,132]. The associated two-dimensional fast Fourier transform of HRTEM image (inset **Fig. 5.1c**) shows there is no secondary phase formation, but there is a diffuse spot associated with SRO. Enhancement of the HRTEM image (**Fig. 5.1d**) clearly shows SRO domains (**Fig. 5.1f**).

5.2. Calculation of Stacking Fault Energy

To assess the SFE value in the as-quenched NiCoCr, a detailed dislocation analysis was conducted. Two-beam TEM images show extensive localized planar dislocation arrangements; the separation distance of partial dislocations and the statistical analysis of the results are shown in **Fig. 5.2a-c**. Dislocation analysis were performed using Titan Themis 300 S/TEM in water-quenched NiCoCr MPEA. Bright-filed images for the '**g.b**' analysis of the partial dislocations was used to calculate SFE of NiCoCr MPEA. Burgers vectors of the partial dislocations were detected using a diffraction condition normal to the Burgers vector to obtain **g.b**=0. The partial dislocation separation distances were measured using an open-source software Image J.

$$\mathrm{SFE} = \frac{\mathrm{G}\mathrm{b}_\mathrm{p}^2}{8\pi\mathrm{d}}\left(\frac{2-\mathrm{v}}{1-\mathrm{v}}\right)\left(1-\frac{2\mathrm{v}-\cos(2\beta)}{2-\mathrm{v}}\right) \tag{5.1}$$

where G is the shear modulus, b_p is the magnitude of the Shockley partial dislocation, d is the distance between Shockley partial pairs, and v is the Poisson`s ratio of NiCoCr MPEA. Total 300 individual measurements were obtained on 3 different regions far away from

the thin foil hole to minimize the surface effects. Calculated standard deviations were in agreement with in each other.

The measured SFE of the single-crystalline as-quenched NiCoCr sample was 26±4 mJ/m^2 as seen in the figure, which is in close agreement with the SFE (18.5 mJ/m^2) that we calculated using density functional theory (DFT) as well as the results of other experiments (22 ± 5 mJ/m^2) [51].

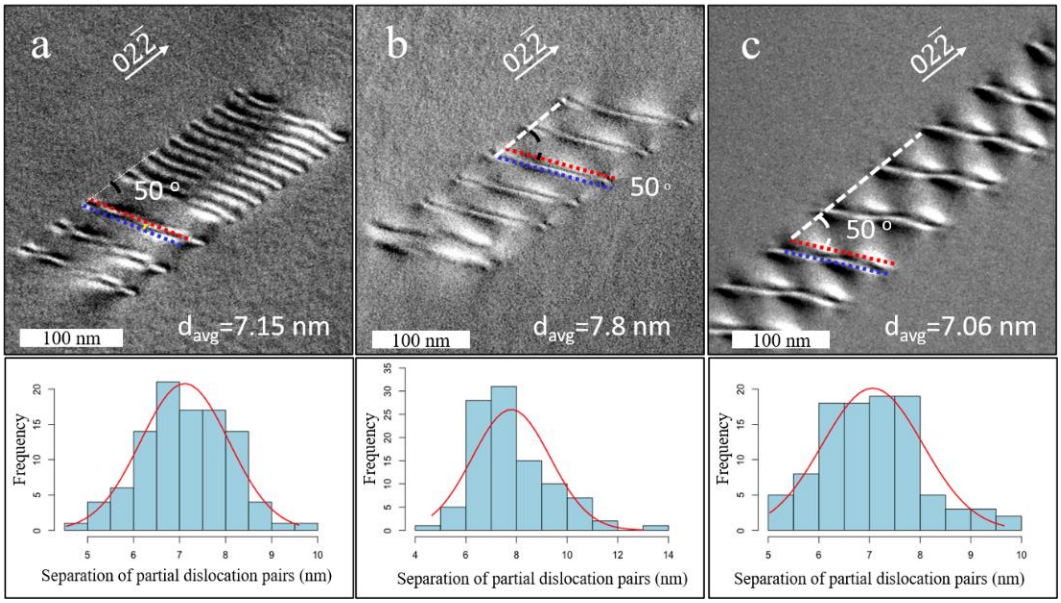

Figure 5.2 Dislocation analysis of as-quenched single crystalline NiCoCr. (a-c) Two beam TEM images with the g vectors marked represent the planar arrays showing the dissociation of the perfect dislocations into partial dislocations. Plots in the bottom panel show the distribution of distance between Shockley partial dislocation pairs. Dislocation analysis was performed on the as-quenched NiCoCr solution heat treated at 1200 ºC for 24 hours.

5.3. Microstructural Evolution

To reveal the origins of the exceptional mechanical response in NiCoCr, we need to understand the evolution of the deformation processes and answer the following questions: How does NiCoCr deform in the presence of SRO? And, what deformation modes are activated? High-energy synchrotron transmission X-Ray Diffraction (XRD) and extensive TEM investigations were performed to explore the evolution of the deformation processes. Polar diffraction spectra of as-quenched crystal and of crystals that were deformed to failure are shown in **Figure 5.3a-b**. The as-quenched sample in **Fig. 5.3a** shows a typical pattern of an fcc crystal symmetry along the [110] zone axis. In contrast, the pattern for the sample deformed to failure exhibits elongated stripes instead of narrow spots in **Fig. 5.3b**, demonstrating the loss of single crystallinity after deformation. The distribution of these stripes indicates the presence of two different twin variants. Moreover, the deformed sample shows additional faded diffraction spots like the ones labelled with red arrows in **Fig. 5.3b**. This diffracted intensity does not correspond to the characteristic diffraction spectrum of the fcc matrix. To identify this new phase, we compared the diffraction spectra in **Fig. 5.3a-b** as a function of Bragg angle in **Fig. 5.3c**. In addition to the typical peaks for the fcc and hcp matrix, the deformed sample also displays ten additional diffraction peaks, which can be fitted to the diffraction spectrum of a hexagonal phase with a=5.180 Å, c=4.194 Å and c/a=0.81. These results suggest that this new phase has a $D0_{19}$ superstructure [170]. A list of observed diffraction peaks for NiCoCr as-quenched samples before and after the deformation is presented in **Table 5.1**.

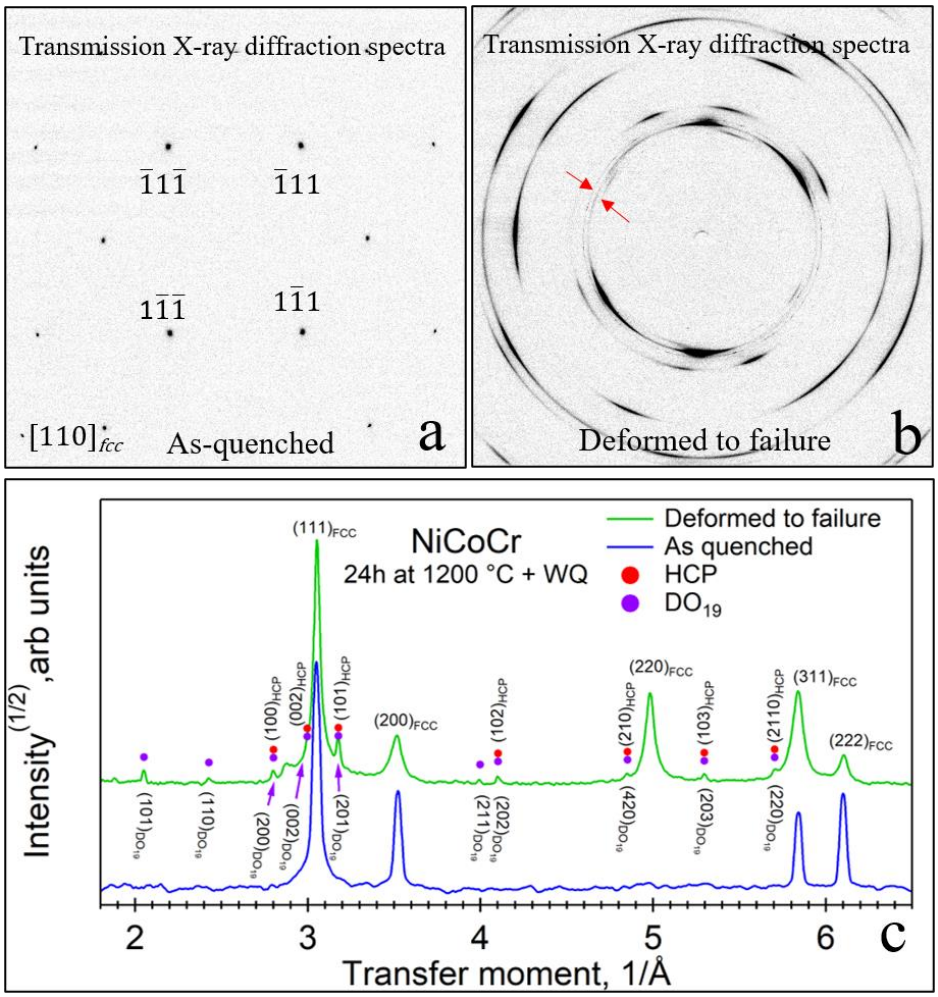

Figure 5.3 Polar synchrotron transmission x-ray diffraction spectra for [110]-oriented single crystal specimens e) as-quenched and f) after tensile straining to failure. Red arrows in (f) point out some of the diffracted intensity spots which are not from the initial fcc structure. g) square root of the integrated intensity as a function of Bragg angle for as-quenched (blue) and deformed (green) samples. Diffraction peaks are indexed for the fcc matrix or the hexagonal close packed (hcp) structured martensite or superstructure $D0_{19}$.

TEM investigations on the deformed [110]-oriented single-crystals exhibit extended SFs on different {111} planes (**Fig. 5.4a**) at 4% strain. This microstructure is a precursor to the formation of thin ε-martensite plates via one or more of the following mechanisms: (1) the regular (shown in **Fig. 5.4a**) or irregular overlapping process of SFs

(shown in **Fig. 5.4b&c** with irregularly overlapped faults indicated by arrows) [171–173], (2) the formation of six-plane hcp embryo via the interaction of coplanar 1/6<112> Shockley partial dislocations separated by SFs [174], and (3) the stair-rod cross slip mechanism of extended partials in the primary slip system (see **Fig. 5.5**) [171]. The formation of the ε-martensite by stair-rod dislocations cross slip mechanism is originally proposed by Fujita and Ueada [18], which seems to play a role in the current MPEA. In **Fig. 5.7a**, an extended dislocation moving through on the primary slip plane can glide onto the cross-slip plane via cross-slip of stair-rod type dislocations, as seen in **Fig. 5.5b**. When the stress level is high enough at the intersecting plane, an extended SF can move into cross slip plane. The schematic illustration of the formation of the glissile jog formation in **Fig. 5.5b** shows how an extended dislocation move into the cross-slip plane first and lead to double-cross slip mechanism [42,175]. In fact, the interaction of two coplanar extended partial dislocations can also form three-layer twin nuclei [167]. Therefore, the mechanisms involving the interaction of coplanar extended partial dislocations explain the simultaneous observation of twinning (**Fig. 5.4d**) and hcp-transformation (**Fig. 5.4e-i**) – through the formation of three-layer twin or six-layer hcp embryo – at the start of plastic deformation (~4%) in the present MPEA, which is the lowest strain level that the ε-martensite formation reported in NiCoCr to date. In conclusion, our results support that the pile-up glide (governed by SRO) is responsible for the nucleation of both ε-martensite and deformation twinning, which is consistent with the ε-martensite and twinning formation reported in [167,176–178].

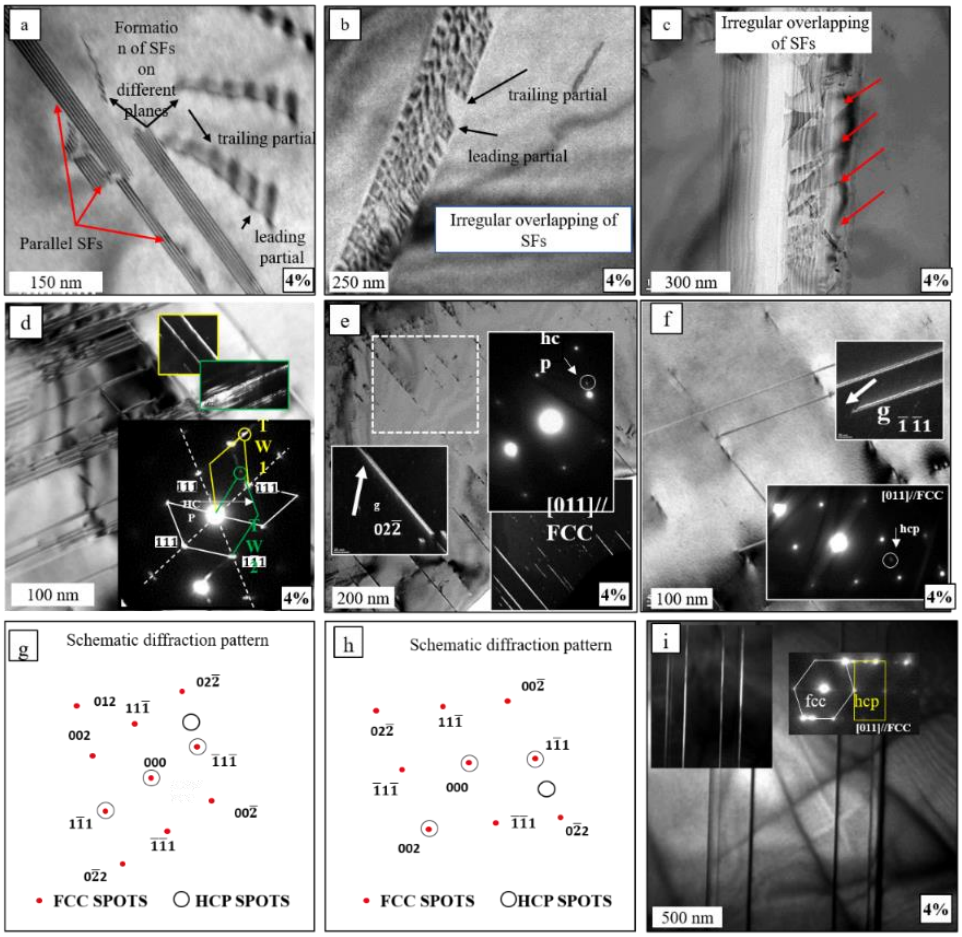

Figure 5.4 Bright-field TEM images displaying (a) formation of parallel stacking faults (SFs) on different {111} planes, causing nucleation of widely extended SFs and precursors to ε-martensite thin plate formation via (b-c) irregular overlapping SFs. The extended coplanar Shockley partials and SFs lead to formation of (d) two twin systems and (e) ε-martensite hcp plates. (f) The higher magnification of (e), showing the secondary hcp systems. (g-h) Schematic illustration of the diffraction pattern indicating fcc and hcp phases in (e) and (f). (i) Further confirmation of the hcp plates from a different region at 4% strain. *Insets:* diffraction patterns and dark-field images.

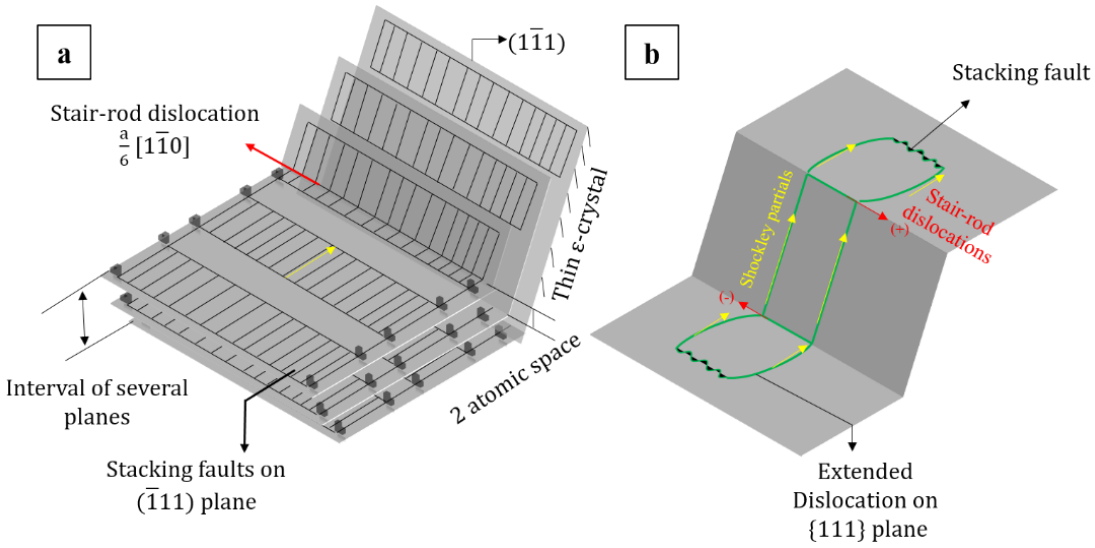

Figure 5.5 The schematic illustration of (a) the ε-martensitic transformation in fcc systems via the stair-rod cross slip mechanism of extended partials in the primary slip system and (b) the formation of stair rod-dislocations during the double cross slip mechanism, both adapted from [171,175].

More detailed TEM investigations were conducted on the [110]-oriented single-crystal NiCoCr specimens subjected to 4%, 20%, and 60% tensile strains (**Fig. 5.6**). At the beginning of plastic deformation (~4%), we found extended SFs on different {111} planes (**Fig. 5.6a)**. This microstructure is a precursor to twin formation and fcc-to-hcp phase transformation (as discussed in **Fig. 5.5**) causing the formation of the stair-rod cross-slip mechanism of extended partials in the primary slip system **(Fig. 5.6 c&d)** [171]. Results show that the twins and ε-martensite lamellas are only a few nanometers thick at 4% strain.

High-density SFs and nanoprecipitates were observed in the 60%-strained sample in **Fig. 5.6e-j**. This sample also exhibits anti-phase boundaries (**Fig. 5.6e-h**). Moreover, the corresponding diffraction pattern (inset **Fig. 5.6e**) shows a diffuse intensity that can

originate from either planar defects or substitutional ordering linked to a transition state from SRO to long-range order (LRO) [179–181]. We looked more carefully into the stair-rod stacking-fault region in **Fig. 2e** by tilting the TEM foil, and both stair-rod SFs (**Fig. 5.6f)** and overlapping SFs (**Fig. 5.6g)** were observed. Chen et al. [182] reported that SFs can act as an embryo for the $D0_{19}$ phase via stair-rod dislocation formations during in-situ heating TEM experiments of intermetallic compound Fe_3Ge, similar to the formation of ε-martensite [171]. We also obtained a dark-field TEM image from the diffuse intensity of the corresponding SADPs shown in the **Fig. 5.6 e** inset. The dark-field image shows that this diffuse intensity mostly comes from SFs, but some nanodomains were also observed at antiphase boundaries (**Fig. 5.6h**). In **Fig. 5.6i**, these nanodomains were well-developed. The corresponding SADP of the nanodomains reveals a hexagonal symmetry with a 0.78 c/a ratio, suggesting that they have a $D0_{19}$ structure, which is in agreement with the 0.81 c/a ratio measured with the synchrotron transmission XRD in **Fig. 5.2** and the 0.809 c/a ratio of our DFT calculations introduced below. The higher magnification of the nano-domain region in Fig. **6.5i** confirms that these $D0_{19}$ regions are a few nanometers in diameter (**Fig. 5.6j)**.

Table 5.1 List of observed diffraction peaks on NiCoCr as-quenched samples in undeformed and deformed to failure conditions, ordered by its characteristic inter-planar spacing, indexed for FCC, HCP and DO_{19} phases. The diffracted intensity which could only be produced by DO_{19} superstructure are indicated on the last column.

Phase	**Initial Condition**	**Deformed**	**D-spacing (A°)**	**FCC(A°) a=3.568**	**HCP (A°) a=b=2.59 c=4.194**	**$D0_{19}$ (A°) a=b=5.18 c=4.194**
$D0_{19}$		X	3.066			101
$D0_{19}$		X	2.571			110
HCP		X	2.243		100	200
HCP		X	2.098		002	002
FCC	X	X	2.05	111		
HCP		X	1.969		101	201
FCC	X	X	1.78	200		
$D0_{19}$		X	1.62			112
$D0_{19}$		X	1.574			211
HCP		X	1.526		102	202
$D0_{19}$		x	1.335			103
HCP		X	1.292		110	220
FCC	X	X	1.262	220		
HCP		X	1.184		103	203
FCC	X	X	1.07	311		

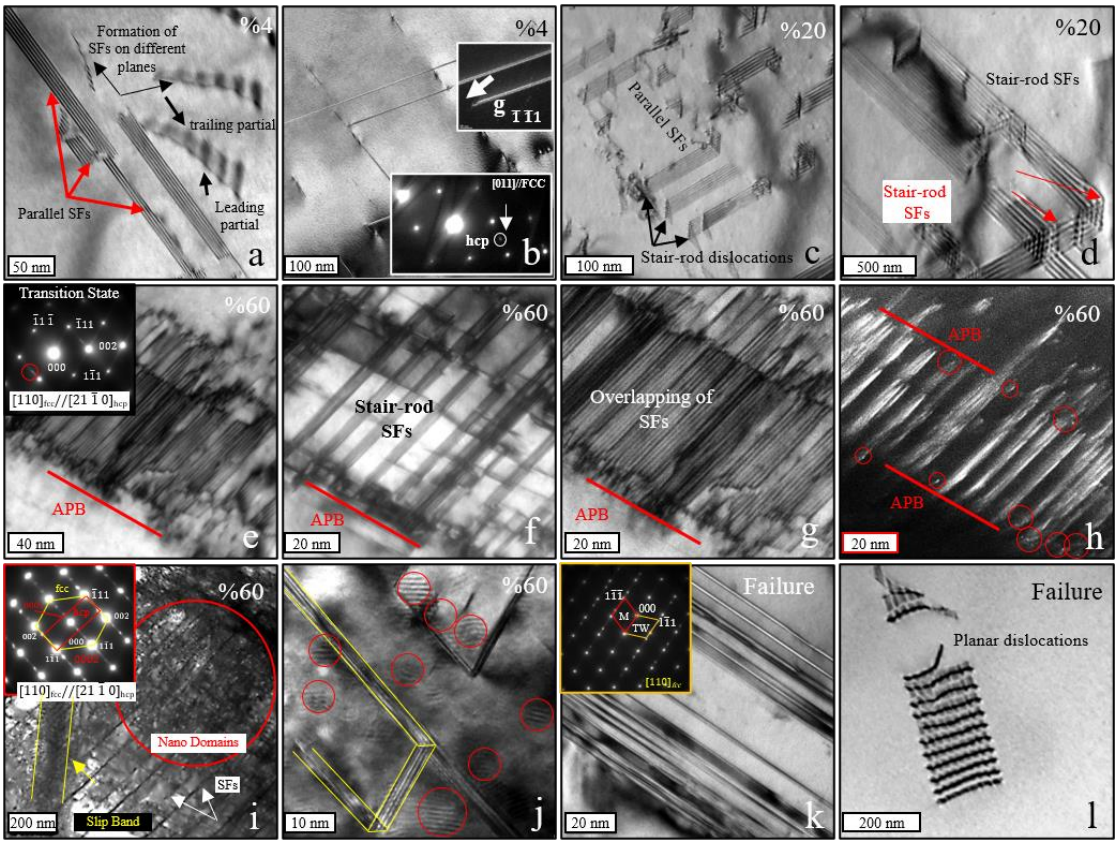

Figure 5.6 Bright-field and dark-field TEM micrographs with corresponding selected-area diffraction patterns (SADPs) demonstrating major deformation mechanisms of the [110]-oriented as-quenched single-crystalline NiCoCr strained to different levels under tension at room temperature (RT). (a) Formation of parallel stacking faults (SFs) on different {111} planes, causing nucleation of widely extended stacking faults (SFs) and precursors to ε-martensite thin plate formation at 4% strain. The extended coplanar Shockley partials and SFs lead to formation of (b) ε-martensite hcp plates at 4% strain, *insets:* diffraction patterns and dark-field image, (c) the nucleation of the stair-rod type SFs at 20% strain, (d) a well-developed stair-rod SF at 20% strain, (e) high density SFs at 60% strain, representing an anti-phase boundary with a corresponding SADP that indicates a transition state, (f-g) the same region (e) taken with a different tilting angle and showing stair-rod stacking faults in the same region, and (h) dark filed image taken from diffuse intensity on the SADP inset (e) marked with red circle, (i) nano domains at % 60 strain, proving the occurrence of the hexagonal $D0_{19}$ structure with the corresponding SADP inset, (j) higher magnification of nano domains, (k) nanotwins bundle with corresponding diffraction pattern inset, and (l) planar slip localization at failure.

Fig. 5.6k displays a high twin density in the deformed-to-failure crystal which is expected to contribute to the Stage IV hardening behavior shown in **section 5.3**. Additionally, planar-slip is still predominant in the failed sample (**Fig. 5.6 l)**. This indicates that simultaneous TWIP/TRIP process suppresses the dislocation recovery process in NiCoCr, providing outstanding deformation ability beyond what conventional alloy systems exhibit.

These investigations on the microstructural evolution of NiCoCr under uniaxial tensile loading at room temperature (RT) demonstrate a new deformation pathway, which is fcc to hcp phase transformation and then hcp to $D0_{19}$ phase transition, and can be attributed to the existence of SRO. However, further efforts are needed in order to explore how deformation modes are influenced by the degree of SRO, with the potential to tune SRO to obtain specific deformation behaviors. Therefore, the as-quenched NiCoCr single crystals were aged at 1000˚C for either 48 h or 72 h, which is shown to increase the degree of SRO [50]. Following aging, high-energy synchrotron transmission XRD experiments were conducted to evaluate their structures. The polar diffraction spectra of NiCoCr samples as-quenched, and aged for 48 h and 72 h, followed by water-quenching show a typical fcc single crystal pattern along the [110] zone axis without any indication of precipitates (**Fig. 5.7**).

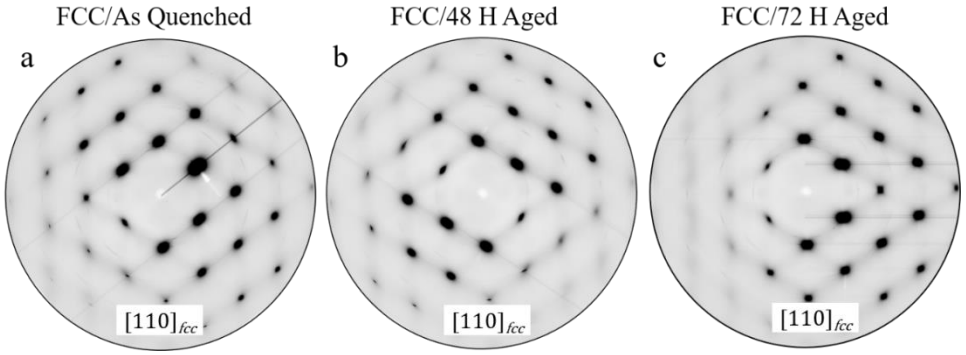

Figure 5.7 Polar synchrotron transmission x-ray diffraction spectra for three single crystalline NiCoCr samples. (a) Homogenized at 1200 ºC for 24h followed with water quenching (b) aged for 48 hours and (c) aged for 72 hours.

Nanoindentation experiments, uniaxial tensile tests at RT, and electron backscatter diffraction measurements were performed on these single-crystalline samples to explore mechanical responses after aging. We found that the nanoindentation hardness measured on the (011) crystal surfaces decrease with increasing aging time (**Fig. 5.9 a-c**). According to Cohen and Fine [45], due to the favorable (stable) SRO, the first dislocation in the pile-up is exposed to higher resistance against slip due to interaction with the SRO and leads to localized deformation and pile-up. Successive dislocations produced by the activated dislocation source and moving along the regions with SRO, that were locally destroyed, help to overcome the higher resistance. This indicates that the resistance to dislocation motion produced by SRO can be overcome at the beginning of deformation via dislocation localization causing glide plane softening in the [110] orientation. Such softening appears as reduction in hardness in this particular direction with the increase in the degree of SRO.

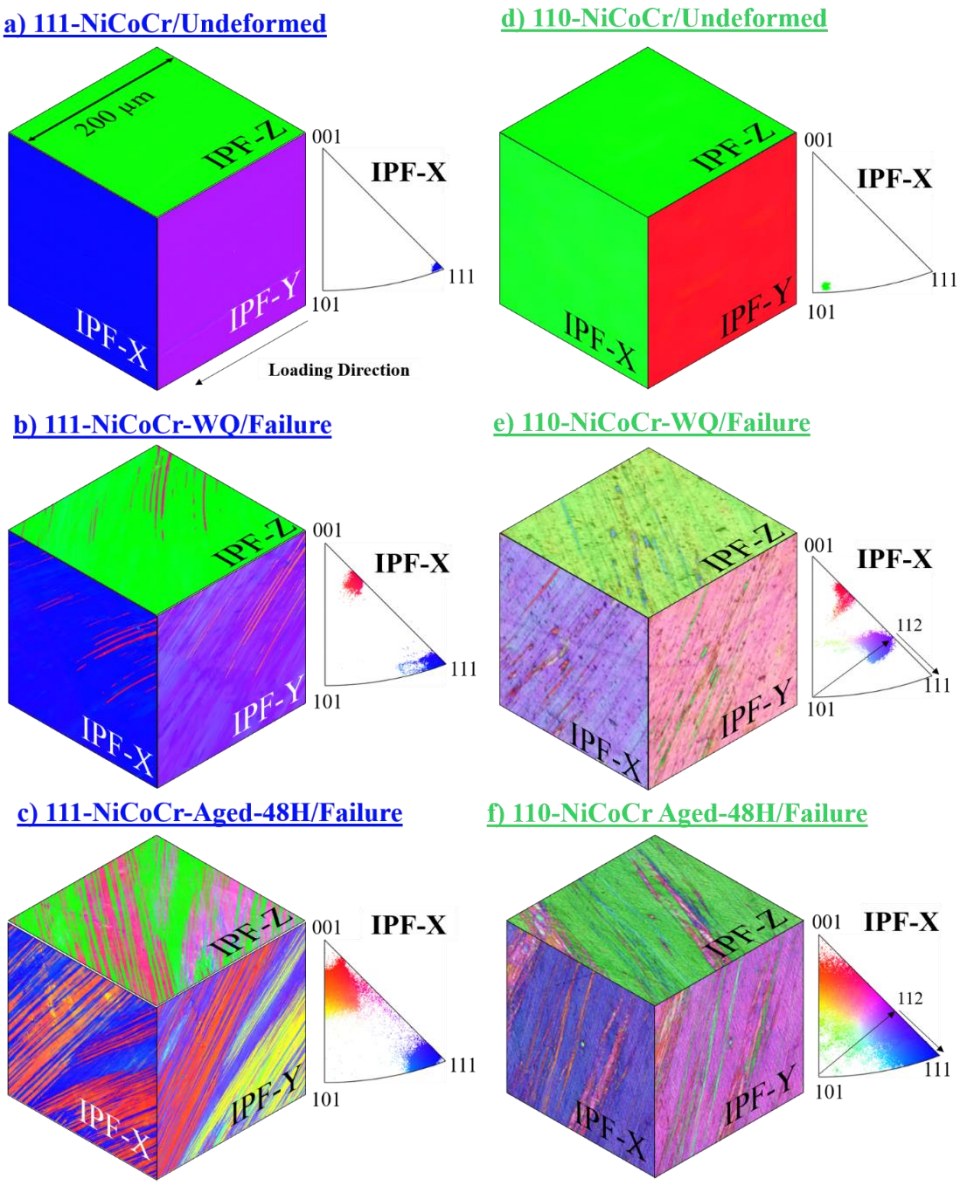

Figure 5.8 Representative EBSD IPF color maps illustrate microstructure of single crystalline NiCoCr samples. (a) the [111]-oriented single crystal initial condition, (b) the as-quenched [111]-oriented single crystal deformed up to failure showing the twinning formation, (c) the aged [111]-oriented single crystal for 48 h deformed up to failure indicating the improvement of the twin density, (d) initial condition of the [110]-oriented single crystal, (e) the deformation twinning formation in the as-quenched [110]-oriented single crystal deformed up to failure, (f) the aged [110]-oriented single crystal for 48 h deformed up to failure with higher deformation twinning density than (e).

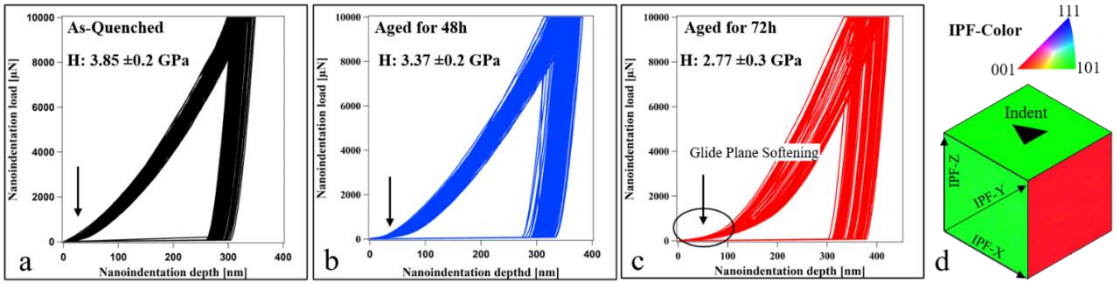

Figure 5.9 Nanoindentation experimental results of single crystalline NiCoCr. (a) As-quenched, (b) aged for 48 hours and (c) 72 hours. (d) Schematic illustration of single crystalline samples representing relative orientations during the nanoindentation tests. The nanoindentation was performed at about 150 different locations on the (011) surface.

Uniaxial tensile test results at RT show that both [111] and [110] orientations, aged for 48 h, showed an approximately 20% increase in the ultimate strength and ductility compared to equivalent as-quenched samples, while there was no detectable difference in the strain-stress responses of as-quenched and 48 h-aged [001]-oriented samples (**see section 5.4**). As demonstrated **section 5.3**, the initial work-hardening rates of the aged [111] and [110] samples are the same as the hardening behavior of the as-quenched samples. However, the aged samples exhibit significantly extended stage IV hardening region. Electron backscatter diffraction imaging reveal that the reason for the better strength/ductility combination in the aged samples is higher twinning density (**Fig. 5.3)** and the formation of the strain-induced hcp / DO_{19} phases (**Fig. 5.10)** in stage IV in both [111] and [110] orientations**;** i.e., the higher degree of SRO can delay the recovery process, which further promotes the formation of twinning and the hcp / DO_{19} phases as a result of higher stress levels. In the [001] orientation, however, transmission X-ray diffraction spectra show that deformation was governed only by dislocation plasticity (**Fig. 5. 15**).

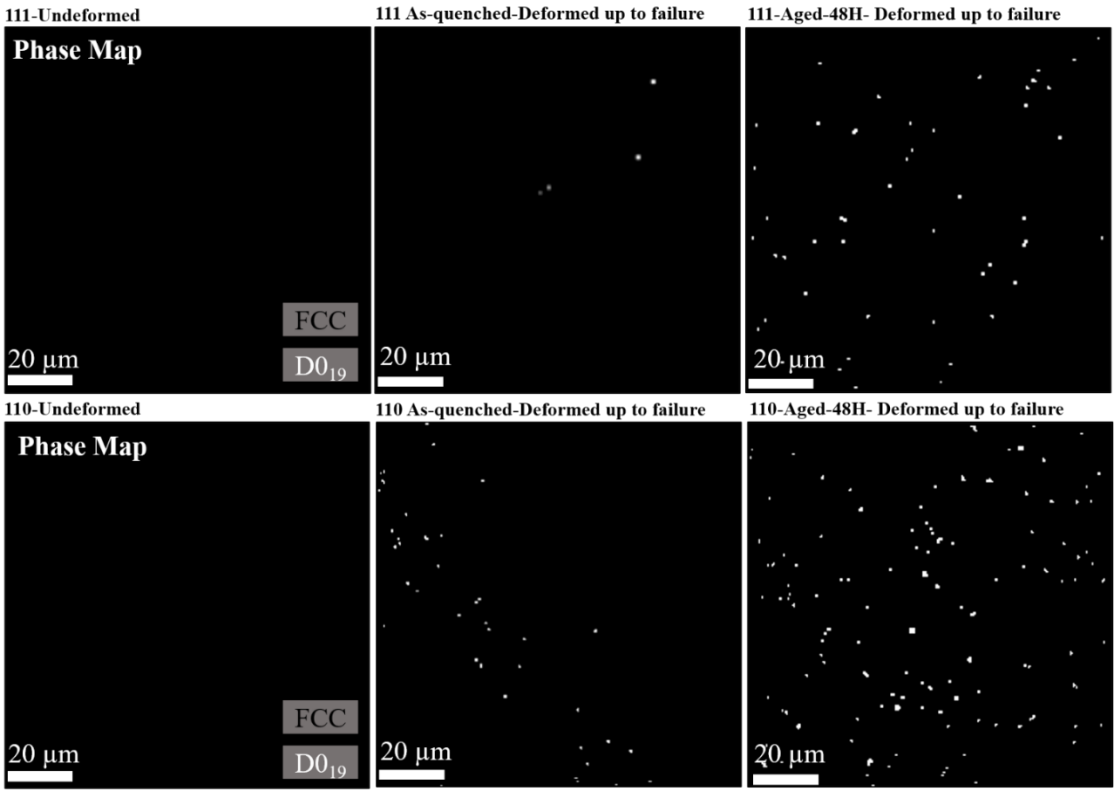

Figure 5.10 Comparison of EBSD phase maps in the [111]-, and the [110]-oriented NiCoCr single crystals strained up to failure. White circles represent the formation of the strain-induced hcp phase. Clearly, the strain-induced hexagonal secondary phase volume fraction is higher in the aged samples after deformation than that of as-quenched conditions.

Based on the Schmid factors and the role of the externally applied stress on the partial dislocation separation [3,28,89], glide dislocations are completely dissociated into partial dislocations and help nucleate twinning or martensitic transformation in tension near [111] and [110] orientations, while perfect dislocations are more prominent in the [001] orientation [54]. Therefore, due to the lack of partial dislocations in the [001] orientation, TWIP/TRIP effects and the $D0_{19}$ phase formation are not observed in the [001] crystals.

The Schmid factors for slip/twinning and experimental yield strengths, along with the corresponding critical resolved shear stress values, in these three orientations are presented in **Table 5.2**.

Table 5.2 Maximum Schmid factors for slip, twinning, and the leading and trailing Shockley partial dislocations for [001]-, [110]- and [110]-oriented single crystals when they are mechanically loaded under tension. "Sys." is the number of systems, which represents equivalent Schmid factors. The yield strength values calculated using the 0.2% offset strain criterion were experimentally determined from the tensile stress-strain responses of at least three different single crystal samples, on the average, for each orientation. The Critical Resolved Shear Stress (CRSS) values were determined using the equations $\boldsymbol{\tau_{cr}^{sl} = m_{sl}\sigma_{\varepsilon}^{sl}}$ for slip and $\boldsymbol{\tau_{cr}^{tw} = \sigma_{\varepsilon}^{tw}m_{tw}}$ for twinning.

Loading Axis	Schmid factors under Tension				Yield Strength, MPa	CRSS, MPa	
	Slip	Twin	Leading Partial (m_1)	Trailing Partial (m_2)		Slip	Twin
[001]	0.41	0.23	0.47	0.23	160 ± 5^{WQ}	65±2	-
	8 Sys.	8 Sys.			$170\pm5^{48h\text{-}Aged}$	69±2	-
[110]	0.41	0.47	0.47	0.24	170 ± 5^{WQ}	69±2	79±5
	4 Sys.	2 Sys.			$190\pm;5^{48h\text{-}Aged}$	78±2	89±5
[111]	0.28	0.31	0.16	0.31	245 ± 5^{WQ}	68±2	76±5
	6 Sys.	3 Sys.			$255\pm5^{48h\text{-}Aged}$	71±2	79±5

5.4. Calculation of Short-Range Ordering using Density Factional Theory

As discussed above, we uniquely identified the existence of SRO using HRTEM and investigated its effect on the plasticity of NiCoCr. However, the nature of SRO, its quantum-mechanical origin, and its relation to deformation modes are still not well understood. To explore this question, we employed the DFT-based linear-response theory of concentration fluctuations [183], developed for arbitrary complex solid-solution alloys (see method section) to directly calculate the Warren-Cowley SRO parameters for high-temperature disordered NiCoCr (both fcc and hcp, see **Fig. 5.11**). We then used concentration-wave analysis to assess the ordering modes [46]. We evaluated the SRO at a temperature of $1.15T_{sp}$, where T_{sp} is the calculated spinodal decomposition temperature at which an absolute instability for the dominant SRO mode occurs towards a partially long-range order (LRO) state. The dominant SRO peaks in fcc NiCoCr in **Fig. 5.11a** are at wavevector $\mathbf{k_o}=\mathbf{W}=(1\,\frac{1}{2}0)$, indicating either stoichiomtric $MoPt_2$-type ordering mode, as reflected in the binary phase diagrams of Ni-Co-Cr, or off-stoichiomtric $D0_{22}$-type mode. The pairs driving this SRO are Ni-Co, followed by Ni-Cr and Co-Cr pairs, which is in agreement with an earlier Extended X-ray Absorption Fine Structure (EXAFS) report [47]. The real-space pair-interchange energies dictate the thermodynamic behavior [46,183] and reveal the nature and range of the interactions. We therefore inverse-Fourier transformed the **k**-space pair-interchange energies for fcc NiCoCr to real-space (**Fig. 5.12**). We found that they were dominated by nearest-neighbors but were non-negligible up to the 7^{th} neighbor shell, or 1.343 nm range (see **Fig. 5.12a**), correlating with the nanometer-scale

SRO domains found in **Fig. 5.1**. The SRO of the dominant Ni-Co pairs is shown in **Fig. 5.11b**; while not overly strong, the SRO persists over a large temperature range, which has previously been connected to dislocation glide [49]. Moreover, the presence of SRO inhibits phase decomposition unless assisted, e.g., by shear deformation, thereby increasing the local stress needed for glide [132]. In Cu-Al, for example, the peak in yield strength well above RT (600-900 K) is a result of SRO, and at higher temperatures, the SRO vanishes due to increased entropy, resulting in a loss of strengthening [184].

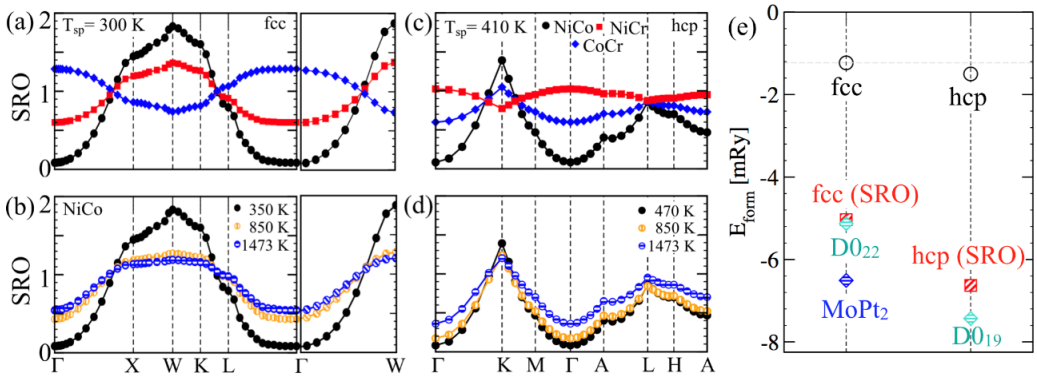

Figure 5.11 The SRO and thermodynamic stability analysis of competing phases in NiCoCr MPEA. For NiCoCr, DFT-calculated SRO in fcc and hcp phase at 1.15 T_{sp}, with calculated spinodal temperatures of T_{sp} (fcc) = 300 K and T_{sp} (hcp) = 410 K. (a, c) Warren-Cowley SRO with dominant Ni-Co pair at wavevectors W = (1, 1/2, 0) for fcc and at wavevectors K =2/3 (110) for hcp. (b,d) Ni-Co SRO vs temperature shows that SRO persists to high temperatures, where diffusion then assists to maintain SRO. (e) Formation energies (E_{form}) are compared for fcc and hcp with homogeneous disorder, fcc (SRO) and hcp (SRO) with energy due to SRO included, and various partially-order LRO states [*PO-$D0_{22}$*, *PO-$MoPt_2$ and PO-$D0_{19}$*]. The homogeneous *fcc* and *hcp* solid solutions are very close in energy (0.27 mRy), but, if SRO develops at given temperature, the energy of the SRO (inhomogeneous) state nears the bulk partially-ordered *$D0_{22}$*, *$MoPt_2$* and *$D0_{19}$* state, reflecting a possible *fcc* → *hcp* → *$D0_{19}$* transition.

Interestingly, while our experiments found strain-induced martensitic (fcc-to-hcp) phase transformation at RT followed by hcp-to-$D0_{19}$ phase decomposition at higher strain, there was no indication of $(1\frac{1}{2}0)$-type superstructure for the SRO in fcc NiCoCr (**Fig. 5.11 a-b**). Rather, the $D0_{19}$ phase transformation is related to the SRO found in hcp NiCoCr (see **Fig. 5.11 c-d**), suggesting that a more careful analysis of fcc vs hcp phase energetics is needed. The DFT formation energy (E_{form}) calculations show that the homogeneously disordered NiCoCr fcc (–1.23 mRy/atom) and hcp (–1.50 mRy/atom) phases are nearly degenerate (**Fig. 5.11e**). Therefore, with a small energy gain $\Delta E_{fcc-hcp} \sim 0.27$ mRy (roughly 40 K), the fcc phase must only overcome a transition barrier to form the hcp phase, and, as observations suggest, this transformation barrier is small enough that a very low thermal activation energy could induce the austenite-to-martensitic transformation. Also, structurally, comparing the martensitic phase with V_{hcp} (11.31 $Å^3$) to the austenitic phase with V_{fcc} (11.38 $Å^3$) indicates that thermal activation energy arises mostly from applied (tensile) stress as the martensitic transformation induces only a little plastic deformation since the volume contraction (–0.6%) is very small.

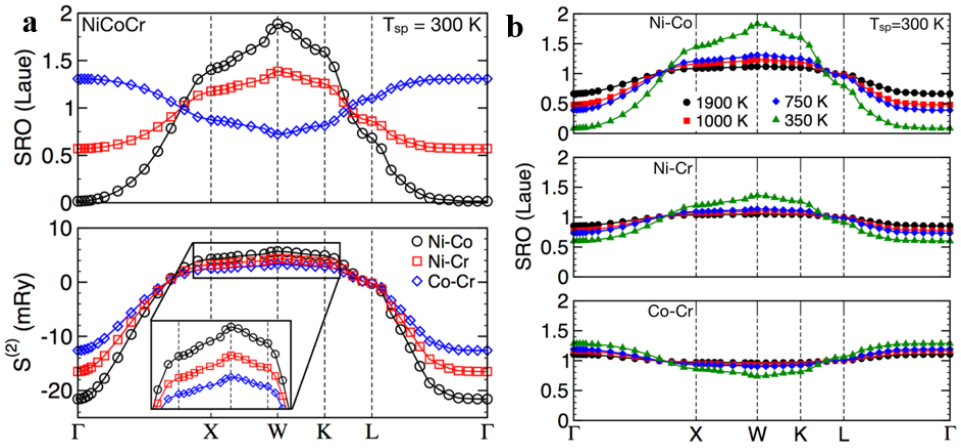

Figure 5.12 (a) For fcc NiCoCr, Warren-Cowley SRO parameters $\boldsymbol{\alpha_{\alpha\beta}(k;T)}$ [Laue] and pair-interchange energies $\boldsymbol{S^{(2)}_{\alpha\beta}(k;T)}$ [mRy] calculated at T=1.15T_{sp} and plotted along high-symmetry directions in the Brillouin zone. The theoretical spinodal decomposition temperature is T_{sp} = 300 K. Maximal SRO is found for Ni-Co pairs at W=(1 ½ 0). (b) Temperature-dependence of the SRO pairs – see also Fig. 5 – shows Ni-Co pairs persist with temperature.

To compare with the fcc results, we plotted the SRO of hcp NiCoCr at 1.15T_{sp} (T_{sp} = 410 K) to determine the energetics associated with chemical fluctuations (**Fig. 5.11c-d**). The SRO in **Fig. 5. 11c** peaks at wavevector $\mathbf{k}_0$=**K**=$\frac{2}{3}$(110), indicating a $D0_{19}$-type SRO, which exhibits the same dominant Ni-Co mode as in the fcc phase (**Fig. 5. 11a**), but a more localized spectral weight than the fcc phase. The presence of SRO at higher temperatures, shown in **Fig. 5. 11b and 5. 11d**, indicates that SRO is an inherent property of the disordered NiCoCr, which develops due to the filled d-states near the Fermi energy (see electronic dispersion in **Fig. 5. 13**).

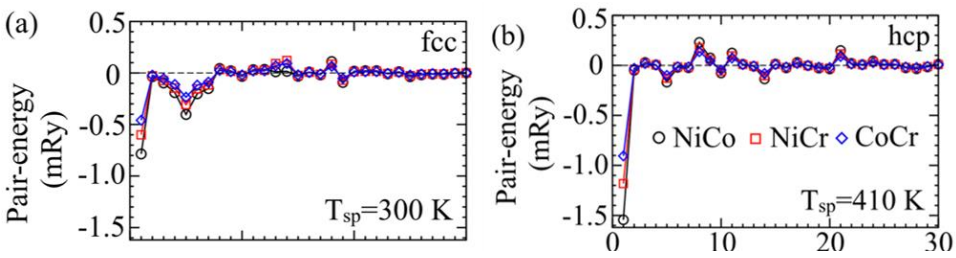

Figure 5.13 Real-space pair-interchange energies to 30 shells calculated at 1.15 T_{sp} for (a) fcc and (b) hcp NiCoCr from an inverse Fourier Transform of $\mathbf{S}^{(2)}_{\alpha\beta}(\boldsymbol{k};\boldsymbol{T})$ from supplementary Fig. 10. $\mathbf{S}^{(2)}_{\alpha\beta}(\boldsymbol{R}_{0,i-j};\boldsymbol{T}=\mathbf{1.15}\boldsymbol{T}_{sp})$ for Ni-Co is –0.8 mRy in fcc phase and –1.5 mRy in hcp phase for first shell, and zero for second shell; and only fcc has significant pair-interchange up to 7th shell.

To shed further light on the strain-induced fcc→hcp→$D0_{19}$ hierarchical phase transformation in NiCoCr, we analyzed and compared the fcc vs. hcp SRO. The higher degree of SRO and lower decomposition temperature (< 300 K) in the (fcc) austenitic phase (**Fig. 5.11a**) compared to the (hcp) martensitic phase (**Fig. 5.11c**) possibly inhibits phase decomposition into $(1\frac{1}{2}0)$-type ordering in the fcc phase. However, a small fcc-hcp energy barrier can be easily overcome by applying external stress needed for non-diffusive martensitic transformation (requiring only cooperative atomic displacements). Therefore, instead of fcc-to-$D0_{22}$-type superstructure, the NiCoCr shows fcc-to-hcp transformation, whereas further increase in the stress leads to a non-diffusive hcp-to-$D0_{19}$ transformation. For NiCoCr, the E_{form} of the fcc and hcp phases with SRO included, as well as fcc-based $D0_{22}$ and $MoPt_2$ (prototype) and hcp-based $D0_{19}$, are shown in **Fig. 5.11e**. The E_{form} shows that SRO energetically further stabilizes both fcc and hcp phases. And $MoPt_2$ partially-ordered $(Ni\text{-}Co)_2Cr$ is lower in energy than off-stoichiomtric $D0_{22}$ order, consistent with binary phase diagrams. The fcc and hcp results in **Fig. 5.11e** show that off-stoichiomtric

hcp-$D0_{19}$ (E_{form}= –7.43 mRy) is slightly lower energetically than $MoPt_2$-type $(Ni\text{-}Co)_2Cr$ (E_{form}= –6.41 mRy), and both are more favorable than $D0_{22}$ (E_{form}= –5.13 mRy).

5.5. Uniaxial Tensile Test Results at Room Temperature

Both theory and experiments demonstrate the presence of SRO, which result in the simultaneous TWIP/TRIP effect in NiCoCr MPEA. Consequently, an anomalous hardening behavior is expected. To determine the effect of TRIP or TWIP on the deformation hardening behavior, the room temperature tensile stress vs. strain and strain hardening, θ (dσ/dε), vs. strain responses are analyzed and presented in **Fig. 5. 14**. The stress levels for the onset of slip (i.e. initial yield point) and twinning/ε-martensitic transformation (first point where the sudden load spikes occur, and confirmed by TEM) were identified. Using these stress levels, the critical resolved shear stresses (CRSS) for dislocation glide and twinning/ε-martensitic transformation were calculated and listed in the **Table 5.2**. As planar slip is activated on a single plane at the onset of deformation, the true stress decreases due to glide plane softening (**Fig. 5. 14a**), which causes inhomogeneous (localized) deformation (**Fig. 5.14b**) in the [110]-orientation. The localized deformation results in an internal stress field that helps to overcome the energy barrier for the dissociation of perfect dislocations at the early stage of deformation. This results in the formation of Shockley partials, and the Shockley partials dissociate into stair-rod dislocations at the intersection of the slip planes, which is the source of the formation of extended SFs and cross slip of planar faults, causing both the twinning formation and hcp transformation [171,172,185].

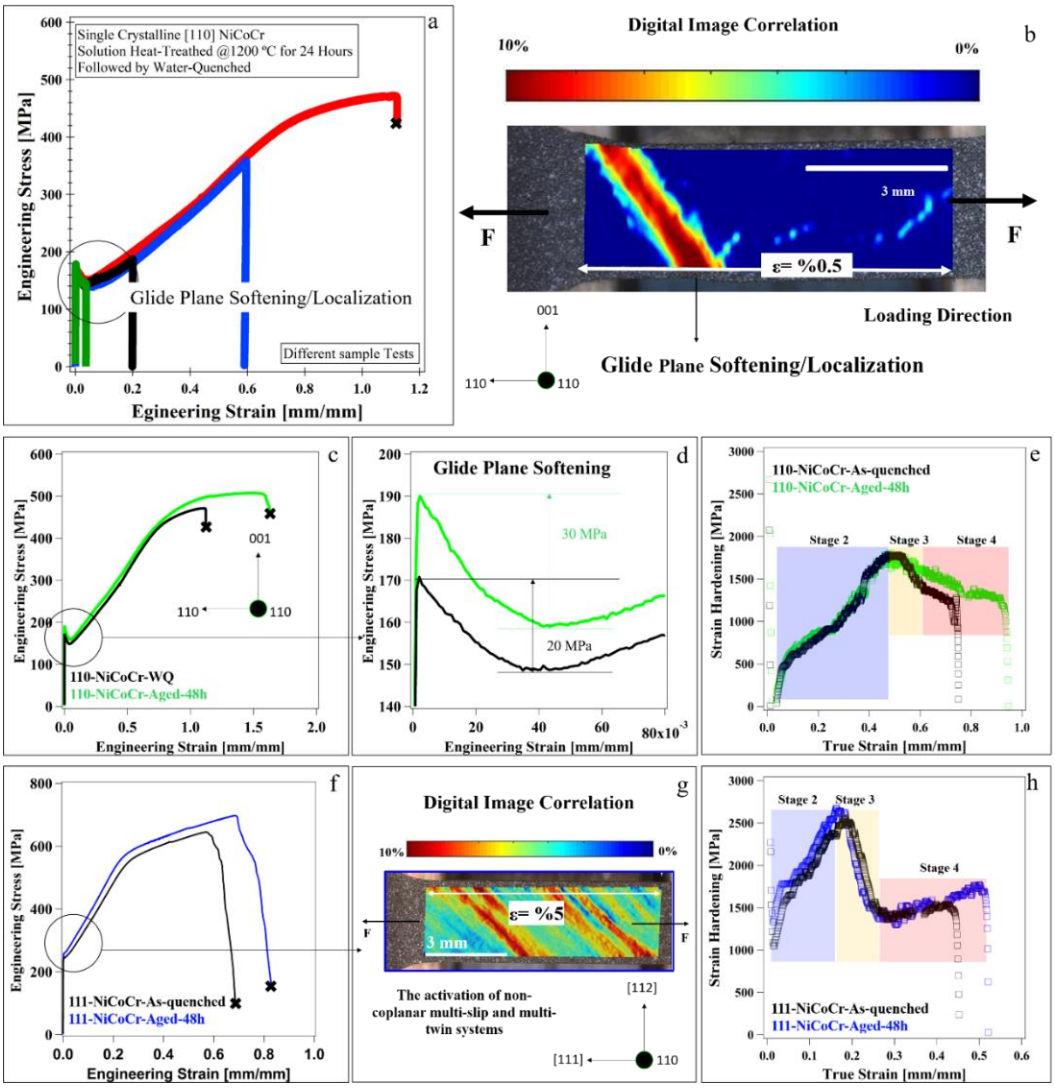

Figure 5.14 Tensile engineering-stress vs. engineering-strain response of NiCoCr MPEA single crystals, and strain-hardening rate vs. true strain behaviour at 300 K. [110]-oriented single crystal tensile test results: (a) interrupted tests to observe the microstructural evolution at different stages of deformation related to the TEM investigations in Fig. 2, (b) corresponding deformation band on the Digital Image Correlation (DIC) map. (c) comparison of the tensile test results between the as-quenched and aged (for 48 h at 1000 ^{o}C) samples, (d) the glide-plane softening, (e) strain-hardening responses of the as-quenched and aged samples. [111]-oriented single crystal tensile test results: (f) the comparison of the as-quenched and aged samples, (g) corresponding deformation band on the DIC map, (h) strain-hardening responses of the as-quenched and aged samples.

The higher yield strength and availability of a larger number of slip systems (**Table 5.2**) in the [111] oriented samples lead the activation of non-coplanar multiple systems just after yielding. Therefore, the softening effect is not as obvious for the [111] oriented samples (**Fig. 5.14c and 5. 14d**) as for the [110] oriented samples. When the overall strain levels are compared in these two orientations, at the same strain localization level on the sample surfaces (at ~10% strain in the localized region, which is the lowest level that was detected on the Digital Image Correlation (DIC) strain map for the [110] oriented samples), it is clear that the [110] oriented samples reach this level of strain localization at only 0.5% overall strain which is 10 times smaller than that of the [111] oriented sample.

The strain-hardening responses for NiCoCr MPEA along the [110] and [111] orientations exhibit four deformation stages (**Fig. 5.14e and 5.14h**). Similar to low SFE TWIP steels [32,147], the sharp change in stage-I hardening is due to dominant single slip and stable dislocation generation. The dissociation of perfect dislocations into Shockley partials followed by either the incubation stage of twinning nuclei or ε-martensitic phase transformation are other factors contributing to the sharp decrease in hardening in stage I [149]. On the other hand, the rapid change in stage II work-hardening is driven by the activation of multiple deformation mechanisms, i.e., twinning, ε-martensitic transformation, and dislocation slip (**Fig. 5.2**). The existence of twin and ε-martensite boundaries in stage-II leads to the reduction in dislocation mean free path through the decrease in inter-twin and inter-phase distances. This leads to a dynamic Hall-Petch hardening, and eventually to high hardening in stage-II.

The noticeable reduction in stage-III hardening occurs due to the formation of cell structures, through cross slip, and formation of Taylor lattices [3,31,149]. As the twinning and martensitic transformation proceeds in stage II, more stress is needed to continue twinning and transformation. Therefore, the stage-III work-hardening acts as an incubation stage, with the formation of cell structures and Taylor lattice, [89,149] for stage IV hardening in NiCoCr, before reaching the onset of necking. The simultaneous TWIP-TRIP effects in stage-IV is usually not seen in conventional materials [28,31], they provide extended stage-IV hardening, and thus, are the reason for the outstanding ductility and strength observed in NiCoCr MPEA. The hardening rate starts to increase in stage IV due to further dynamic Hall-Petch effect enabled by the simultaneous TWIP and TRIP mechanisms. Furthermore, the aged samples showed an extended stage IV hardening causing better strength-ductility combination. In short, the interplay of dislocation glide, TWIP and TRIP leads to extra hardening stages and extended stage-IV in NiCoCr.

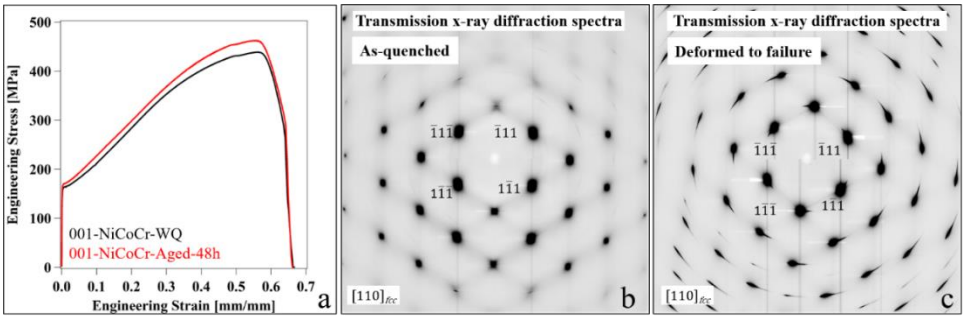

Figure 5.15 The effect of aging on the tensile test results of the [001]-oriented NiCoCr MEA single crystals. (a) Tensile engineering stress vs. engineering strain response of NiCoCr MPEA single crystals for the [001] oriented samples at 300 K (RT). (b) Polar synchrotron transmission x-ray diffraction spectra for as-quenched [001] oriented NiCoCr single crystals a) undeformed and b) strained up to failure.

5.6. Computational Methods

Electronic-structure calculations: We used density-functional theory (DFT) methods to calculate formation energy, electronic-structure, crystal structure, and short-range order [186] for solid solutions using an all-electron, Green's function, multiple-scattering theory (the Korringa-Kohn-Rostoker theory - KKR) combined with the coherent potential approximation (CPA) to address configurational averaging over chemical (or magnetic-exchange) disorder. The all-electron KKR-CPA performs configurational averaging simultaneously with the DFT charge self-consistency. The KKR-CPA properly includes alloy-induced Friedel impurity-charge screening and incorporates critical electronic effects, such as band-filling (valence electron count), hybridization, atom size (bandwidths), Fermi-surface nesting, and Kohn anomalies. As equiatomic NiCoCr has three magnetic elements, we performed spin-polarized DFT calculations using a generalized gradient-corrected (PBEsol) exchange-correlation functional [187] within a site-centered, spherical-harmonic basis that includes s, p, d, and f orbital symmetries (i.e., l_{max}=3). The self-consistent charge densities were obtained from the Green's function using a complex-energy contour integration using a Gauss-Laguerre quadrature (with 24-point semi-circular mesh enclosing the bottom to the top of the valence states) [186]. An equally spaced 24 × 24 × 24 k-space mesh was used for Brillouin zone integrations. The Bloch spectral function (electronic dispersion) plot was done with 400 **k**-points along high-symmetry directions in the irreducible Brillouin zones (see supplementary **Fig. 9**),

which shows the effects of chemical disordered broadening that often enhances SRO. Core electrons were treated fully relativistically (including spin-orbit coupling), while semi-core/valence electrons were treated scalar relativistically (i.e., no spin-orbit coupling).

Short-Range Order: Using DFT-based thermodynamic linear-response theory for compositional fluctuations [183], the Warren-Cowley SRO parameters $\alpha_{\mu\nu}(\mathbf{k};\mathrm{T})$ [183,188,189] were calculated directly, which are observables in diffuse-scattering experiments. After which, the real-space $\alpha_{\mu\nu}^{ij}$ over neighbor shells are obtained by inverse Fourier transform, as done experimentally. The SRO dictates the pair probabilities $P_{\mu\nu}^{ij} = c_{\mu}^{i}c_{\nu}^{j}\left(1-\alpha_{\mu\nu}^{ij}\right)$ in random alloys with temperature, affecting chemical ordering as well as electronic and mechanical properties [47–49,53]. The DFT free energy was calculated for the homogeneously random alloy by KKR-CPA [186]; and, referenced to this free energy, the KKR-CPA for linear-response is analytically expanded to second-order in site-occupation probabilities (i.e., concentrations) c_{μ}^{i} and c_{ν}^{j} for atom-types μ,ν at lattice sites i,j to obtain the chemical stability matrix $S_{\mu\nu}^{(2)}(\mathbf{k};\mathrm{T})$ for the disorder alloy represented in the thermodynamically-averaged unit cell [183], see **supplementary Fig. S7**. Importantly, $S_{\mu\nu}^{(2)}(\mathbf{k};\mathrm{T})$ are thermodynamic chemical pair-interchange energies for all μ-ν pairs (here, Ni-Co, Ni-Cr, or Co-Cr). They are numerically evaluated in reciprocal space and then, by an exact inverse relation, yield the Warren-Cowley SRO parameters $\alpha_{\mu\nu}(\mathbf{k};\mathrm{T})$ [46,183,188,189] for a given Bravais lattice (e.g., fcc, bcc, or hcp). $S_{\mu\nu}^{(2)}(\mathbf{k};\mathrm{T})$ reveals the dominant chemical ordering (Fourier) modes having wavevector $\mathbf{k}=\mathbf{k_o}$ that lowers the

free energy for correlated fluctuations of c_{μ}^{i} and c_{ν}^{j} between sites [183] and, similar to linear-response phonons methods, all modes are found simultaneously. For a dominant $\mathbf{k_o}$, the SRO diverges at the spinodal decomposition temperature (T_{sp}) due to absolute instability in the correlated fluctuations, i.e., $\boldsymbol{\alpha}_{\mu\nu}^{-1}(\mathbf{k_o}; T=T_{sp})=0$, providing an estimate for the order-disorder or miscibility temperature [183]. Our first-principles linear-response theory of SRO is based directly on the electronic structure of the alloy, so the SRO and alloying effects can be directly connected to the underlying electronic origins, like band-filling (valence electron count), hybridization (bonding), atomic-size (bandwidths), Kohn anomalies, or Fermi-surface nesting [188].

5.7. Summary and Conclusions

In closing, the structural properties in MPEAs have been previously interpreted considering mostly stacking fault energy [28,51,89,150,163,171,172,174,190]. In this work, we show that the directly imaged SRO has a direct effect on the deformation modes. The interplay of SRO with deformation twinning was investigated, and a new deformation pathway (fcc $\rightarrow$ hcp $\rightarrow$ $D0_{19}$ hierarchical non-diffusive phase transformation) was presented, a crucial finding for efforts to achieve outstanding plastic deformation ability in other MPEAs. The unique combination of experimental and theoretical investigation presented for this model MPEA can now be leveraged for the design of new alloys with improved mechanical properties. In spite of substantial progress, further systematic investigations are still needed to explore the complex nature of SRO interactions with the nucleation mechanisms of phase transformations.

6. STRENGHTENNING MECHANIMS IN MEDIUM AND HIGH ENTROPY ALLOYS[*]

6.1. The effect of Interstitial Carbon on the Mechanical Properties of CoCrFeMnNi High Entropy Alloy

In this section, a systematic study of the effects of interstitial carbon on the room temperature tensile properties with microstructural evolution was conducted using [001]- and [111]-oriented single crystalline CoCrFeMnNi 0.75 at.% C samples. The current investigation exhibits simultaneous improvement in strength ductility after carbon addition due to TWIP effect. Interstitial addition in fcc alloys offers an improvement in mechanical properties. In some cases, the interstitial doped alloys show not only higher strength but also higher plastic deformation ability [52,59–61]. For example, 1.1 at.% carbon added to $Fe_{40.4}Ni_{11.3}Mn_{34.8}Al_{7.5}Cr_6$ exhibits a simultaneous improvement of strength and ductility with higher hardening rate [60]. The simultaneous improvement was associated with to suppressing the formation of cell structure and causing the localization via higher lattice resistance and lower SFE in carbon-alloy. However, it has been shown that the addition of the carbon (0-0.75 at.%) in equiatomic NiCoCr medium entropy alloy improves the strength without at the expense of ductility by increasing SFE, delaying the twinning formation with thinner structure and decreasing localization [52]. Moreover, it

[*] Reprinted with permission from "Simultaneous deformation twinning and martensitic transformation in CoCrFeMnNi high entropy alloy at high temperatures" PICAK S, Yilmaz H, Karaman I, 2021, Scripta Materialia, 202, pp. 113995, Copyright 2019 by Scripta Materialia Inc. published by Elsevier Ltd.

has been reported that the addition of carbon (0.5 at.%) increases the strength in CoCrFeMnNi by promoting twinning activity at the expenses of ductility. The twinning ability has been detected in <111> oriented grains but not in <001> oriented grains [59]. However, there has still not a single crystalline study exploring the effect of carbon on deformation modes. Therefore, the study of the carbon effect in single crystals will be a strong tool in understanding of the orientation dependence of the hardening behavior in carbon doped fcc HEAs.

6.1.1. Uniaxial Tensile Test Results at Room Temperature

Solid solution substation strengthening in single-phase HEAs is usually regarded as the formation of lattice distortion in the crystal structure because of the different atomic radiuses of the constituent elements [1]. However, the true stress-strain response curves of the CoCrFeMnNi and $Fe_{40}Mn_{40}Co_{10}Cr_{10}$ HEA specimens obtained from the room temperature uniaxial tension experiments shown in **Fig. 6.1** showed relatively low yield strength compared to conventional Hadfield and 316 stainless steel (**Fig. 4.11**). Although the [123] and [111]-oriented samples showed different hardening behaviors, the [001]-oriented crystals exhibited same hardening stages with different hardening rates. As discussed in Chapter 4, the hardening behaviors of the [123] and [111]-oriented samples of $Fe_{40}Mn_{40}Co_{10}Cr_{10}$ were governed by deformation twinning, whereas the [001] orientation was governed only by dislocation plasticity. The different hardening trend in the [123] and [111]-oriented samples could originate from a lack of or a difference in the twining activity between these two HEAs, since the salient design criteria for

$Fe_{40}Mn_{40}Co_{10}Cr_{10}$ HEA was the lowering of SFE to promote twin activity [35,89]. According to **Fig. 6.1**, although the promoted twinning activity provided more plastic ability (around 5% to 10%), there was no considerable difference in the strength levels. Therefore, there is a clear need to improve the strength of these materials.

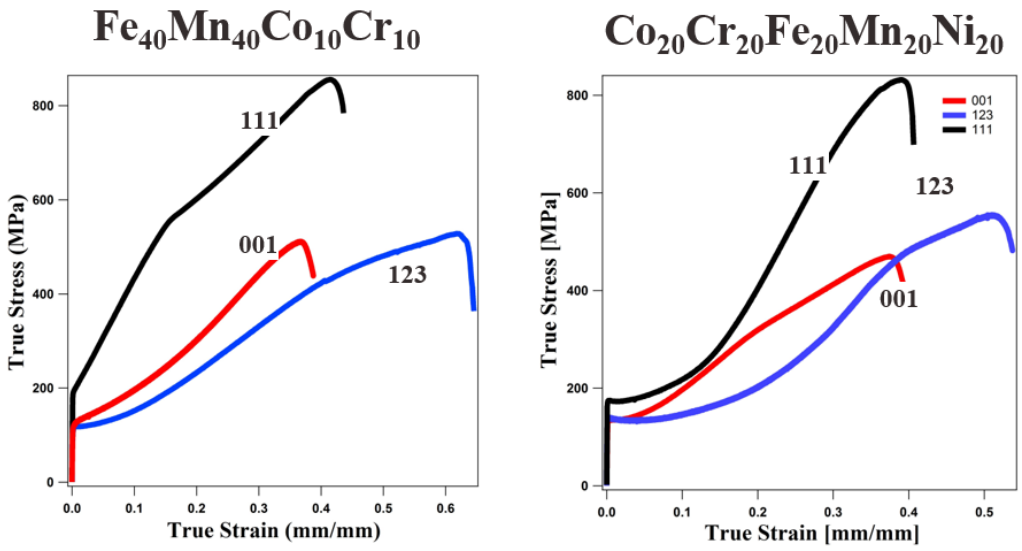

Figure 6.1 Tensile true-stress vs. true-strain responses of equiatomic CoCrFeMnNi HEA and $Fe_{40}Mn_{40}Co_{10}Cr_{10}$ single crystals.

In addition to substitutional solid solution strengthening, interstitial strengthening promises an alternative method for improve the strength of fcc metals as a consequence of kinematic solid solution hardening [60]. The true stress-strain response curves obtained from the room temperature uniaxial tension experiments are presented for carbon free and carbon alloyed CoCrFeMnNi HEAs in **Fig. 6.2**. Yield strength, UTS, and ductility all increase after carbon addition. However, the hardening responses differed from each other. Although the [111]+C alloy presented a lower hardening coefficient than the [111]

oriented single crystal in stage 2 and stage 3 hardening, the [111]+C alloy had an extra hardening stage, which provided more plastic deformation ability. The activation of the secondary or tertiary twin system can cause this unusual hardening stage in the [111]+C-oriented sample [89]. In the [001] oriented specimens, the hardening coefficients were similar, up to 1300 MPa. However, the [001]+C clearly had an extended stage 2 compared to the [001] sample, which was the main reason for its simultaneous improvement in strength and ductility.

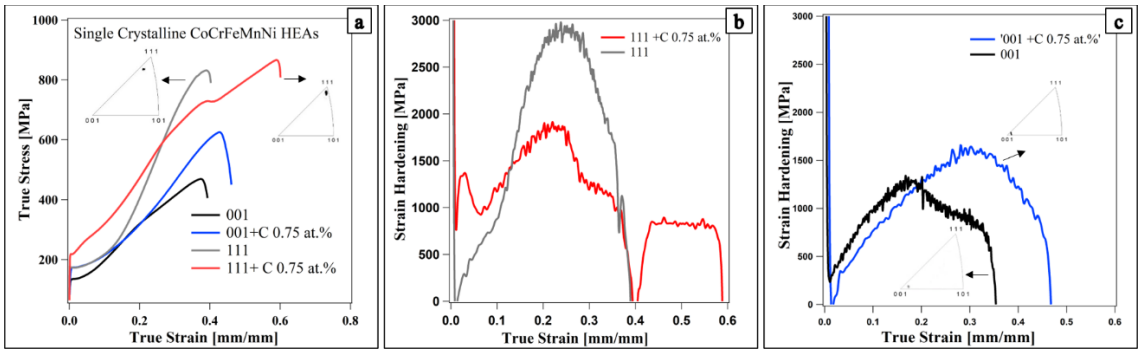

Figure 6.2 The room temperature true stress - true strain tension responses of the [111] and [001]- -oriented single crystals of the CoCrFeMnNi carbon free and 0.75 at.% C HEAs .Inset inverse pole figures show the initial loading directions for three orientations, measured using EBSD. The evolution of θ ($d\sigma/d\varepsilon$), with true strain for the (b) [111] and [111]+C, (c) [001] and [001]+C-oriented crystals.

6.1.2. Microstructural Investigation

The microstructure of the [111] and [001] oriented single crystals with and without carbon were imaged using EBSD and TEM. The EBSD IPF images, phase maps, and misorientation maps are displayed in **Fig. 6.3**. In the [111] specimen at failure (~40%), IPF with the phase map reveals that the majority represented two different twin systems

with moderate density (**Fig. 7.3a**). The [111]+C specimen was also tested up to 40% strain level and the test was interrupted. According to the EBSD IPF map presented in **Fig. 7.3b**, twinning activity was not observed in this specimen. However, the EBSD IPF of the [111]+C specimen tested up to failure showed a tertiary twin system with massive density. Moreover, nanotwinning was detected inside the primary twin system. These provide clear evidence for an extended hardening stage in the [111]+C specimen. The EBSD measurements in the [001] specimens (not presented) did not show any twinning activity. This could have originated from the EBSD resolution restriction.

The TEM observations of the 10% strained [111] and [111]+C samples demonstrated planar dislocation activity (see **Figs. 6.4a–e**). However, cross-slip activation can be also seen in the [111]+C sample at this strain level (see **Figs. 7.4d–e**). Although it is expected that carbon interstitial promotes planar slip in fcc metals, the cross-slip can be explained by the higher stress level at 10% strain (320 MPa) in the [111]+C specimen. However, the stress level was only 190 MPa at the 10% strain level in the [111] specimen. It is worth noting that although the hardening coefficients of these two specimens are the same at 10% strain, the coefficient maintains a constant increase in the [111] specimens. Therefore, the lower hardening coefficient in the [111]+C sample can be attributed to the early cross-slip activation. The TEM images taken at the 30% strain level for the [001] (**Fig. 6.5a**) show that the majority of the dislocation character is cross slip, similar to the [001]-$Fe_{40}Mn_{40}Co_{10}Cr_{10}$ HEA reported in Chapter 4. Although distinct planar slip activity was detected in the [001]+C specimens at 5% strain (**Fig. 6.5b**), dislocation tangles were

dominant at 20% strain (**Fig. 6.5c**). The most important findings in the [001] + C specimen at 20% were the nano twinning formation (**Figs. 6.5d–e**) and SFs (**Fig. 6.5f**).

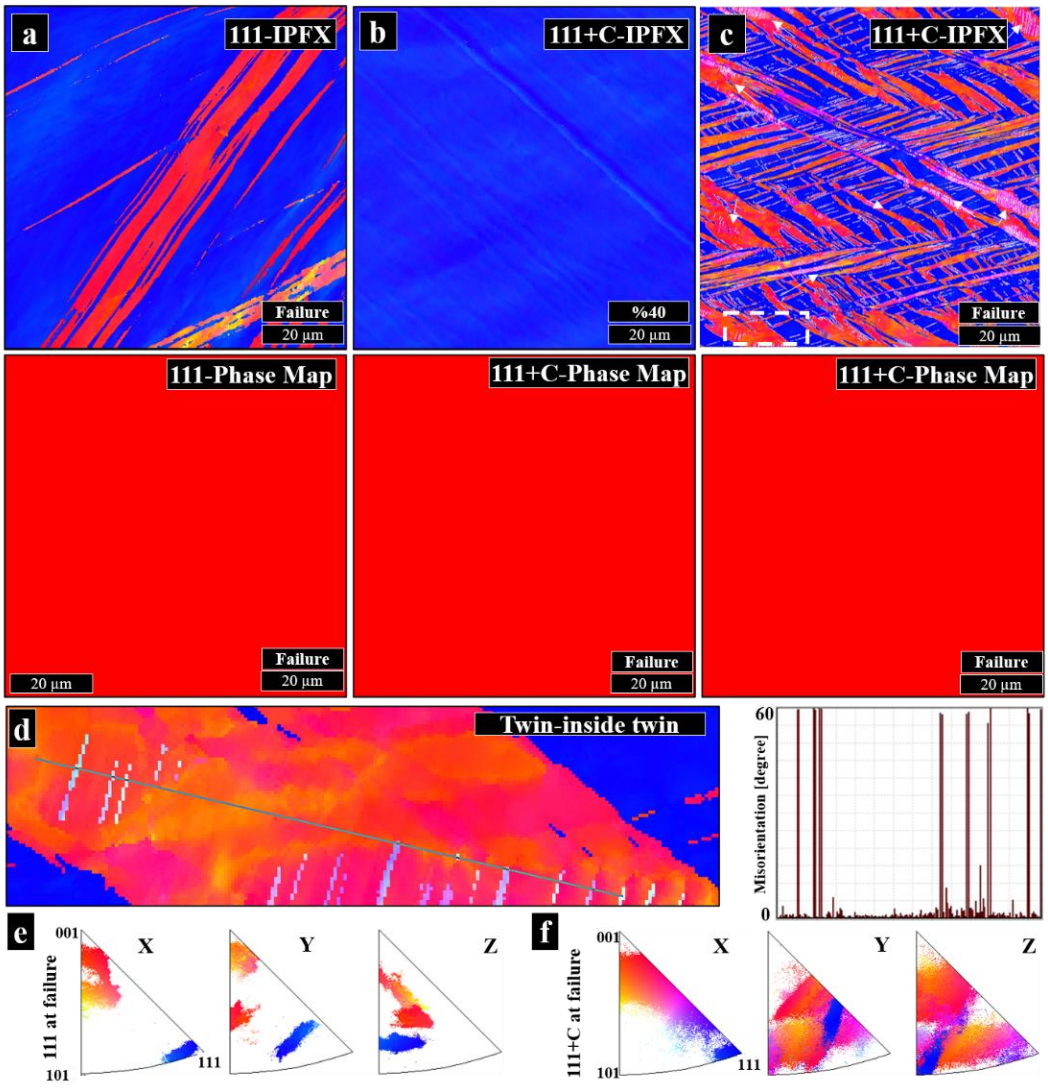

Figure 6.3 EBSD maps of the [111] oriented single crystalline equiatomic FeMnCoCrNi HEA. (a) [111]-strained up to failure; (b) [111] + C strained up to 40%; (c) [111] + C strained up to failure; (d) zoomed in picture from (c) indicating the formation of nano twins inside of the primary twinning region, with corresponding misorientations profile along the three lines marked in (d); (e-f) corresponding inverse pole figures.

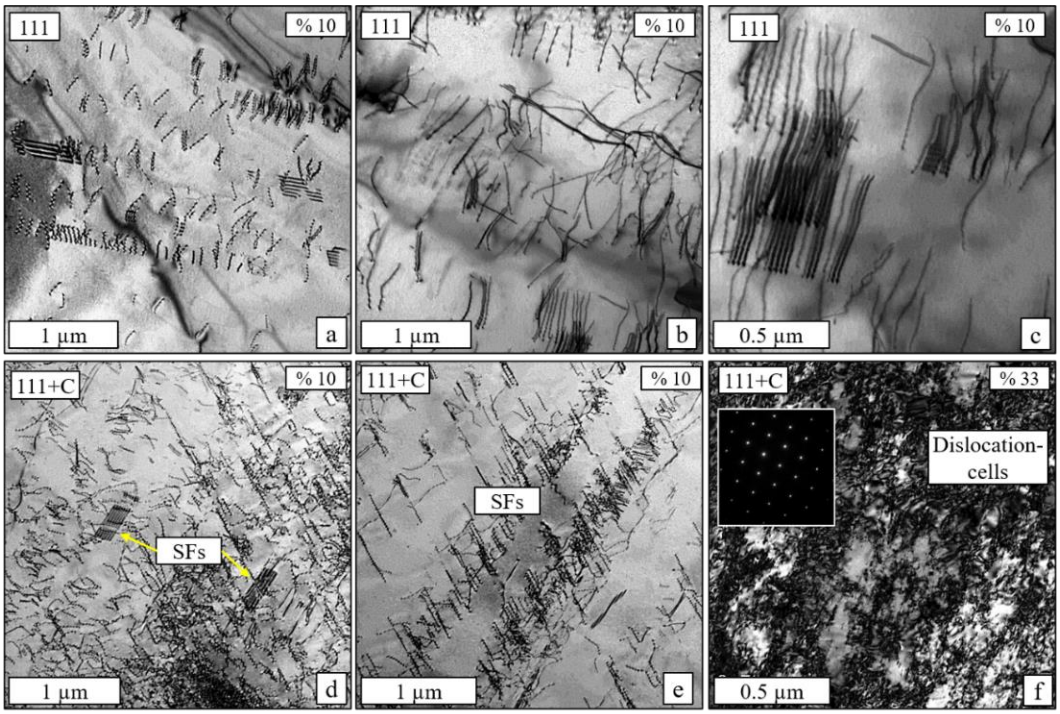

Figure 6.4 Bright field and dark field TEM micrographs of the [111] and [111]+C oriented single crystalline FeMnCoCrNi HEA, demonstrating planar defects; (a–c) stacking faults and planar defects at 10% strain level in the [111] specimen; (d–e) stacking faults and planar defects at 10%strain level in the [111]+C specimen; and (g) formation of dislocation cell structure at 33% strain level in the [111]+C specimen.

Addition of the C causes strong solid solution hardening that becomes slip harder in the lattice, since the CRRS needed to activate slip might be lower than twinning [31]. The bundled nanotwins act as a stronger obstacle than a single macro twin since greater stress is required to carry dislocation across the twin boundary, which causes more hardening. Moreover, the nanotwins as a bundle create a greater twin boundary, and thus more twin/dislocation interaction. This interaction also causes an accumulation of sessile

dislocation in the twin region, resulting in twin strengthening. Consequently, the following dislocation will need more shear stress to penetrate the twinning [150].

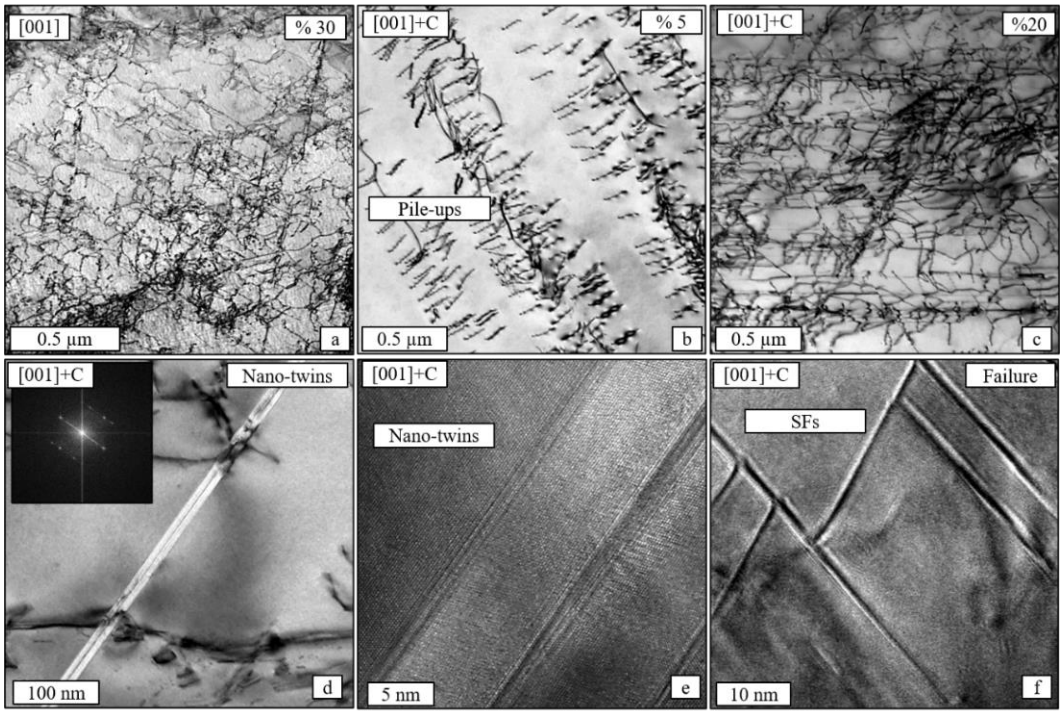

Figure 6.5 Bright field and dark field TEM micrographs of the [001] and [001]+C oriented single crystalline FeMnCoCrNi HEA, demonstrating major deformation modes. (a) dislocation structure at 10% strain level in the [001] specimen; (b) planar defects at 5%; (c) dislocation tangles at 20% in the [001]+C specimen; and (d-e) the formation of twinning at failure in the [001]+C specimen.

6.2. Severe Plastic Deformation

Severe plastic deformation (SPD) leads to substantial strengthening in materials via grain refinement, however, the main drawback of the materials processed using known SPD techniques is the lack of uniform plastic deformation due to low strain hardening capability. In this study, equal channel angular pressing (ECAP) at high temperatures was

utilized to activate simultaneous twinning-induced (TWIP) and transformation-induced plasticity (TRIP) in the CoCrFeMnNi high entropy alloy (HEA), which are anomalous at high temperatures and reported for the first time. Transmission electron microscopy and electron backscattered diffraction analysis were performed to reveal microstructural features. The presence of the transformed and twinned regions as well as grain refinement in this alloy yielded a high strength level (around 1 GPa) with uniform plastic deformation ability in room temperature tension experiments. The observation of TWIP/TRIP was attributed to high strength levels applied via ECAP and relatively low stacking fault energy of the present HEA.

6.2.1. Equal Channel Angular Pressing

All ECAP parameters used here are listed in **Table 6.1**. Route C, used in this study for ECAP, involves +180° rotation between each pass. ECAP billets and their orientations with respect to the die channels with 90° angle are shown in **Fig. 6.6.** To reveal the grain size, morphology and orientation, hot-extruded (HE) and ECAP processed CoCrNiFeMn HEAs were imaged using EBSD on the transverse plane and flow plane (FP), respectively (**Fig. 6.6**). EBSD inverse pole figure (IPF) images, phase maps and grain size distributions are displayed in **Fig. 6.7**. In the HE condition, IPF with the image quality (IQ) map reveals that the majority of grains are separated by high angle grain boundaries (**Fig. 6.7a**). The microstructure of the HE sample consists of fine equiaxed grains, whereas the grain structure of B1 and B2 ECAP samples exhibits a heterogeneous grain size distribution. Phase maps in **Fig. 6.7** show that all conditions have fcc structure at this scale. Analysis

of grain sizes yields the mean grain sizes of the HE, 2C@900/900 (B1) and 2C@900/300 (B2) ECAP samples as 8.86±5 μm, 1.18±1. μm and 0.46±0.4 μm, respectively (**Fig. 6.7**).

Grain sizes in B1 are refined after ECAP in comparison to the HE sample with a heterogeneous microstructure (**Fig. 6.7b**). It is known that the total defect density does not significantly increase after two ECAP passes [63]. However, the grain boundary (GB) character distribution as well as the homogeneity of microstructure evolves further with additional number of passes. The step down in the ECAP temperature at second pass (300°C) led to further grain refinement in the B2 ECAP sample (**Fig. 6.7c**).

The higher resolution EBSD map of the B2 ECAP sample in **Fig. 6.7d** reveals two different regions, forming a composite microstructure. The first region consists of a big elongated grain, while the second includes recrystallized ultra-fine grains (UFG). This heterogeneous microstructure leads to a composite effect during plastic deformation, i.e. big grains providing extended plastic deformation while small grains contributes to strengthening. Many fcc materials exposed to SPD show very high strength levels but lack both ductility and strain hardening because of the saturation of the defect densities [74–76,80,81,191]. To improve plastic deformation ability, a heterogeneous grain distribution is desired which can be achieved after annealing [192]. The present ECAP HEA samples, on the other hand, demonstrate such desired heterogeneous microstructure after two passes at high and medium temperatures without the need for post-processing heat treatments.
To investigate the microstructure of the ECAP samples at higher resolution, TEM was conducted on the B2 sample.

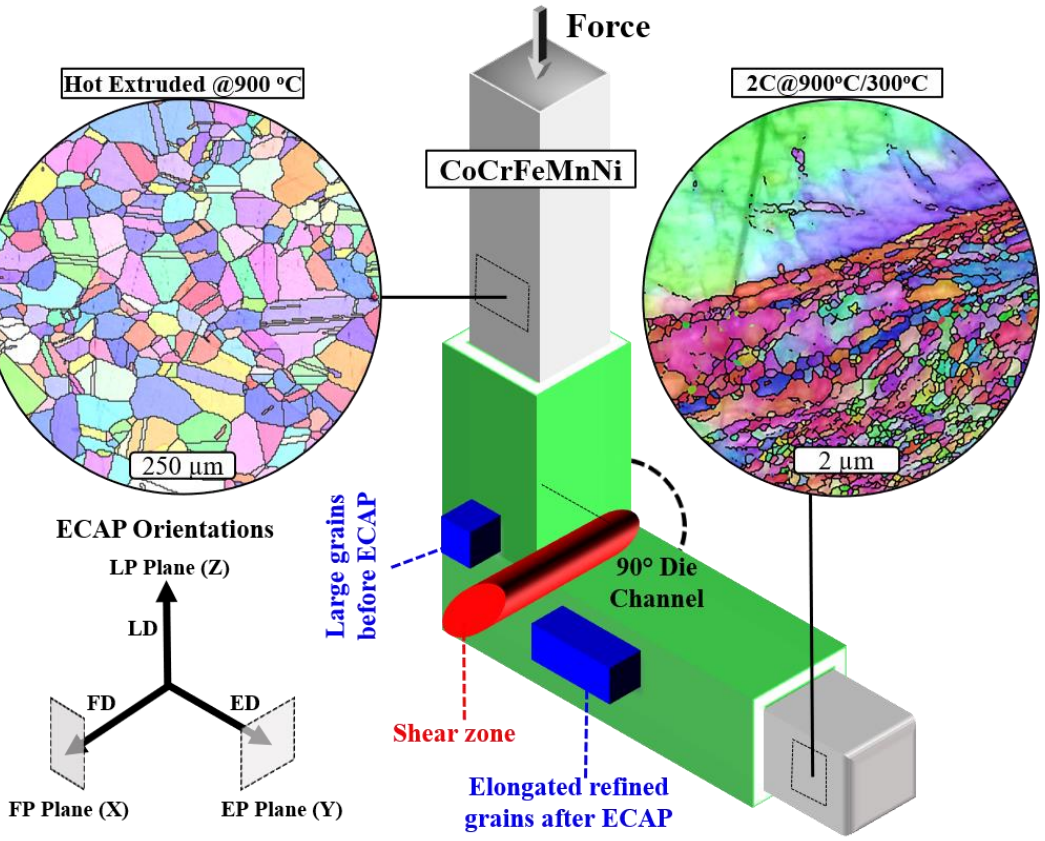

Figure 6.6 Schematic illustration of the ECAP die channel used, demonstrating the grain refinement imposed by two ECAP passes at different temperatures, following route C. LD: Longitudinal Direction, FD: Flow Direction, ED: Extrusion Direction. Insets: Electron Back Scatter diffraction images of hot-extruded at 900 °C and 2 pass ECAP processed at 900 °C/300 °C.

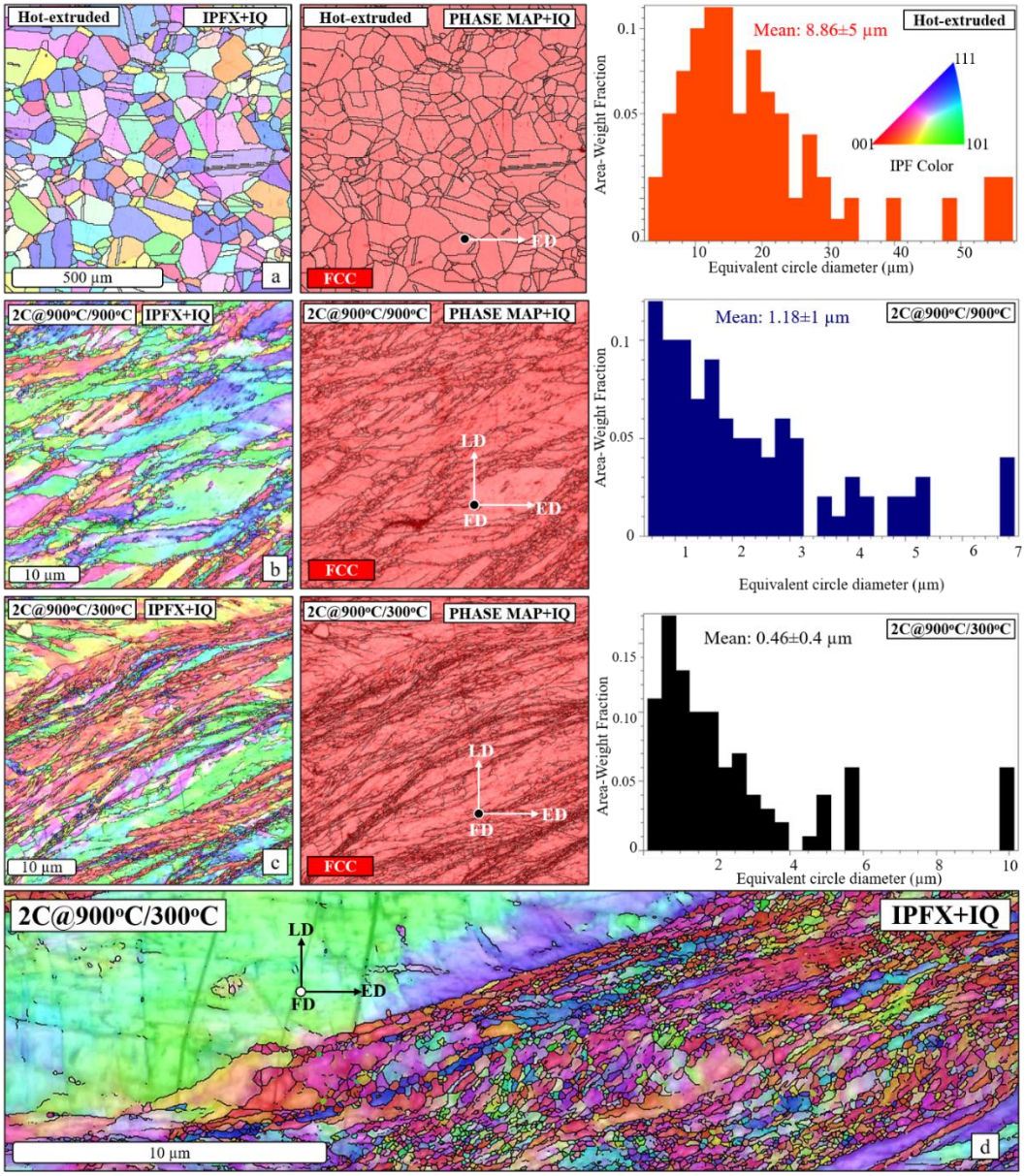

Figure 6.7 EBSD images (IPF color map with image quality (IQ), phase map and grain size distribution) illustrate microstructure of the samples (a) hot extruded at 900°C taken on the transverse plane, (b) ECAP processed 2C@900/900°C, (c) ECAP processed 2C@900/300°C, and (d) ECAP processed 2C@900/300°C, GBs defined by the misorientation angle bigger than 10°. All ECAP images were taken on the FP plane (please see Fig. 1). The step sizes for the EBSD scans are 100 nm (Fig. a-c) and 40 nm (Fig. d).

TEM revealed that the microstructure consists of mostly elongated UFG (**Fig. 6.8a-b**). The width of some elongated grains is less than 100 nm (**Fig. 6.8b**). Somewhat unexpectedly, deformation twinning and ε-martensite lamellas were also observed despite such high temperature deformation (**Fig. 6.8c-f**), demonstrating simultaneous formation of twinning and ε-martensite. As previously reported, UFG and nano-size grains can promote the nucleation of twinning even in high stacking fault energy (SFE) materials by suppressing dislocation plasticity [193]. Selected area diffraction pattern (SADP) and dark field image inset in **Fig. 6.8d** proves the existence of twinning. Similar to twining, ε-martensite forms in nano scale dimension in **Fig. 6.8e**. SADP in **Fig. 6.8f** shows extra planes that are related to hcp symmetry.

Table 6.1 Equal Chanel Angular Pressing (ECAP) parameters used in this study.

	B1	B2
1st pass temperature (°C)	900	900
2nd pass temperature (°C)	900	300
ECAP Route	2C	
ECAP rate (mm/sec)	1.27	
Mean grain size (μm)	1.18±1	0.46±0.4

The activation of twinning and ε-martensite at high temperatures can be linked to the effect of applied stress on partial dislocation separation [54,57,163,194]. The equilibrium separation distance between the Shockley partials can increase or decrease with applied stress in HEAs and other low and medium SFE fcc metals, depending on

grain orientation and applied stress direction [89]. This leads to an effective SFE, which dictates the deformation mechanism in that particular grain [54,195]. Shockley partials are known to play a significant role in nucleation of both twins and martensitic transformation [171,196]. In fact, it was discovered in cobalt, cobalt alloys, and low SFE stainless steels that fcc-to-hcp martensitic transformation takes place in the presence of extensive wide stacking faults and stair-rod dislocations, as shown in the works of Fujita and Ueda [171] and Christian *et al.* [150]. All these planar defects occur via increased partial dislocation separation in low to medium SFE materials. Therefore, the effective SFE phenomenon due to the effect of applied stress on partial dislocation separation should be responsible for simultaneous twinning and ε-martensite formation during ECAP in the present HEA. Indeed, ECAP leads to high stress levels on partial dislocations due to the high strain level and strain rate applied. This makes partial dislocations separation easier in grains with favorable orientation and reduces effective SFE [68,89]. The reduced effective SFE causes the formation of both twinning and ε-martensite during ECAP, which provides more grain refinement. The dynamic Hall-Patch effect decreases the dislocation mean free path and should increase the material's strength [89].

Grain morphology and defect density after ECAP that should have direct effect on the mechanical properties were investigated in **Fig. 6.8g-i**. GBs marked by white triangles in **Fig. 6.8g** are straight (relatively high-angle), whereas GBs marked by yellow circles were not well delineated and wavy (low-angle). Some grains in **Fig. 6.8g** are surrounded by lattice defects with dark contrast as a consequence of severe deformation. The SADP

inset in **Fig. 6.8h** represents an fcc crystal; however, the diffraction spots are streaked. This indicates high internal stress and elastic distortion [197]. The dark field image corresponding to the streaking fcc spot (**Fig. 6.8h)** showed a highly deformed region with poorly developed boundaries, and the local misorientation is only a few degrees. This defect density formed by ECAP contributes to the strengthening, whereas the formation of dislocation cell structures marked on **Fig. 6.8i** increases the dislocation mean free path [3,31], which should help improve plastic deformation ability. In summary, TEM investigations attest that CoCrFeMnNi HEA after 2 pass ECAP has heterogeneous microstructure including deformation induced twining and ε-martensite, possibly formed simultaneously.

As dislocation plasticity is the primary deformation mechanism and strengthening in CoCrFeMnNi HEAs at RT [21], ECAP clearly shows a great potential for strengthening these materials via grain refinement, high defect density and the activation of simultaneous twining and ε-martensite that provide significant resistance to dislocation activity. Additionally, composite-like microstructure formed via ECAP can improve plastic deformation ability and provide a high strength level, and thus, a good strength-toughness combination is eventually expected at RT.

To examine the effect of ECAP on deformation hardening behavior, the room temperature tension and compression stress vs. strain responses were measured. The true stress vs. true strain curves are presented in **Fig. 6.9** to accurately compare the tensile and compressive hardening behaviors. ECAP of the HE material resulted in significant

strengthening as shown in **Fig. 6.9a**. Strength of the B2 ECAP sample peaks just after yield, at σ_y of 925±10 MPa with a stable plateau (indicative of a perfectly plastic deformation), while the B1 ECAP sample exhibits a moderate σ_y (650±12 MPa) and notable parabolic hardening behavior (**Fig. 6.9a**). The ultimate tensile strengths, σ_{UTS}, of the hot-extruded, B1 and B2 samples were detected as 800±10 MPa, 900±10 MPa, 1000±10 MPa respectively. Tensile and compression results are summarized in **Table. 6.2**.

In **Fig. 6.9b**, the compression test results show that the B1 and B2 ECAP samples exhibit tension/compression (T/C) asymmetry, while the HE does not. Strong texture (**Fig. 6.6d**) and oriented internal stresses (**Fig. 6.7g**) in the ECAP microstructure are the main reasons for the observed T/C asymmetry [66–68]. The strong T/C asymmetry in UFG copper was linked to dislocation polarity and back stress accumulation at GBs dictated by ECAP [67], which governs the flow stress during the reversed straining. Furthermore, experimental observations pointed out that low angle GBs produce back stress leading to T/C asymmetry in UFG copper [67]. EBSD and TEM observations revealed that the microstructure in the ECAP CoCrFeMnNi HEA includes low angle GBs as well as recrystallized grains (**Fig. 6.7 and Fig. 6.8**). Therefore, the observed T/C asymmetry in **Fig. 6.9b** can also be attributed to back-stress accumulation at GBs after ECAP. The more pronounced T/C asymmetry in B2 compared to B1 sample is related to higher defect density because of its lower deformation temperature in the second pass.

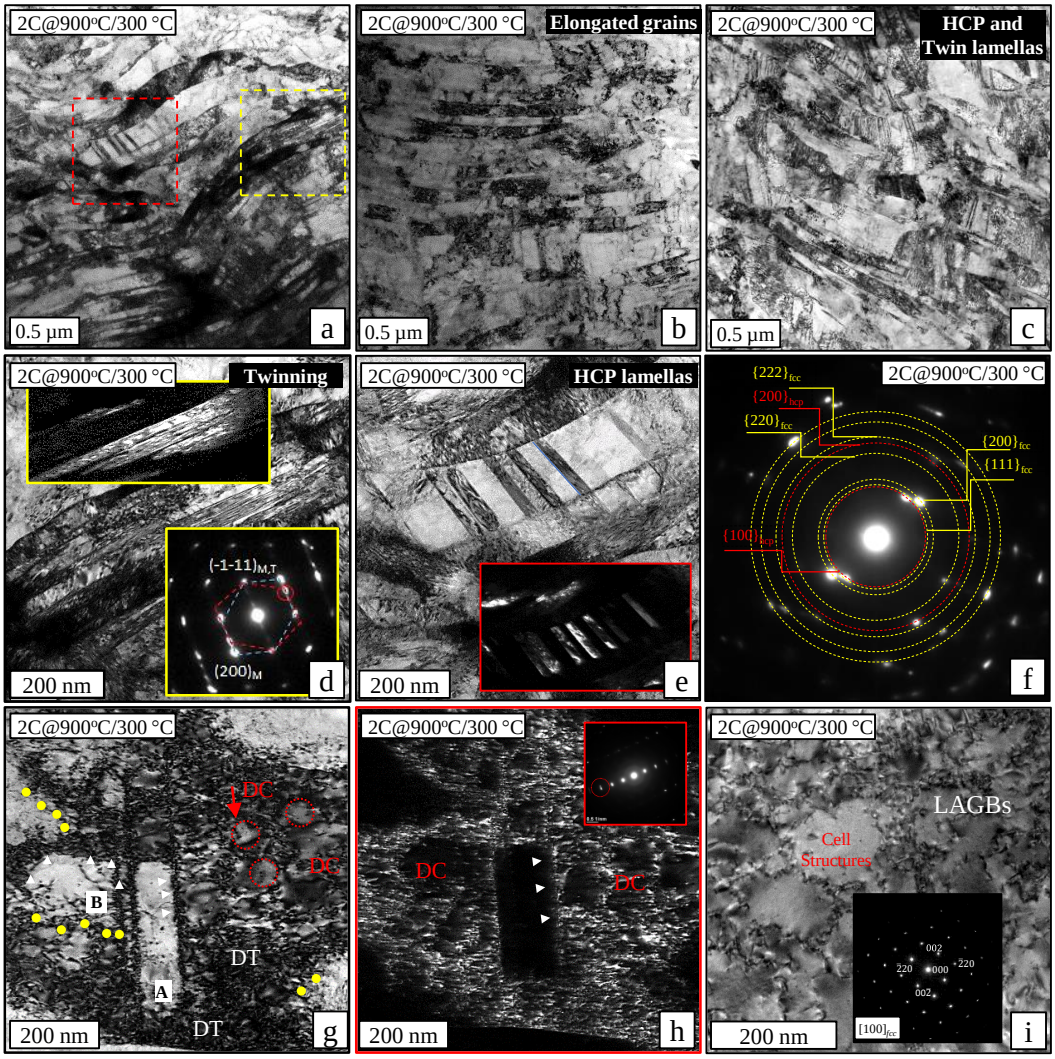

Figure 6.8 Bright field and dark field TEM images and corresponding SADPs demonstrate the major microstructural features of the ECAP processed CoCrNiFeMn at 900-300 ^{o}C HEA imaged on the flow plane (Fig.1). (a) overall microstructure observation showing grain structure, twinning and ε-martensite, (b) elongated ultrafine grains with dislocation structure, (c) high density ε-martensite/twin lamellas. Zoomed-in images of (a) shows: (d) the nano twins and the dark field images of the primary twinning with the corresponding SAD pattern identifying the twin system (inset), (e) strain induced ε-martensite and the dark field images of the ε-martensite (inset), (f) the corresponding SAD pattern of (e) identifying the ε-martensite. (g) dislocation structures around an elongated grain showing dislocation tangles and dislocation cell structure, (h) the dark filed image of streaking spot of fcc crystal inset DP (i) a region that has big dislocation cell structures with related SAD pattern (inset).

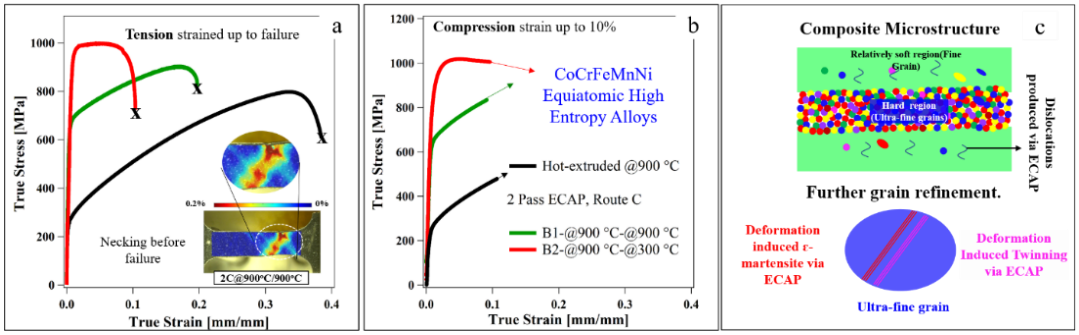

Figure 6.9 (a) The room temperature true stress vs. true strain (a) tension and (b) compression responses for CoCrFeMnNi HEAs hot-extruded at 900ºC, ECAP processed at 900ºC along the ED direction and ECAP processed at 900ºC and 300ºC along the ED direction. (c) The schematic presentation of the microstructure achieved with ECAP processing leading to high strength and ductility combination.

The above microstructural studies demonstrate that the ECAP processed CoCrFeMnNi HEA possesses a composite microstructure with large elongated grains, mostly having high defect density, refined recrystallized grains, and deformation induced twinning and ε-martensite lamella. As a result of this heterogeneous microstructure and their effects on dislocation mean free path, high tensile and compressive strength levels (1 GPa) (**Fig. 6.9a-b**) have been obtained with the relatively high uniform elongation levels in the ECAP processed materials. This unique microstructure is schematically presented in **Fig. 6.9c.**

Table 6.2 Room temperature mechanical test results of the ECAP processed CoCrFeMnNi HEA in comparison to the hot extruded samples. The yield strength values were determined using 0.2% offset strain criterion.

	Hot- Extruded	B1	B2
$\sigma_y^{Tension}$ (MPa)	250±10 MPa	650±12 MPa	925±10 MPa
$\sigma_y^{Compression}$ (MPa)	250±10 MPa	610±10 MPa	715±10 MPa
$\sigma_{UTS}^{Tension}$ (MPa)	800±10 MPa	900±10 MPa	1000±10 MPa

6.3. Medium Entropy Fe-Mn-Al-C Lightweight Steel

The weight steel referenced in this section has a chemical composition of Fe-30Mn-8.5Al-0.9Si-0.9C-0.5Mo (weight percent), which is fabricated by hot-work at ~1100^{o}C with a total reduction of ~90%. The materials were solution heat-treated (SHT) at 900^{o}C for 1 hour, followed with water quenching and aged for 36 hours for at 575^{o}C. It has been shown that Fe-Mn-Al-C light weight steels present outstanding strength-ductility after aging, but the room temperature tensile properties are anisotropic.

6.3.1. Mechanical test results

The true stress vs. true strain response curves of aged-Fe-30Mn-8.5Al-0.9Si-0.9C-0.5Mo (wt%) obtained from the room temperature uniaxial tension experiments are shown in **Fig. 6.10**. Uniaxial tensile properties loaded up to failure are assessed along five different directions: the transverse direction (TD), rolling direction (RD), normal direction (ND), 45° to the ND, and 60° to the ND. Very high yield strength (~1 GPa) was obtained via κ-carbides. In tensile experiments, the RD specimens presented outstanding strength

(~1.5 GPa) and ductility (~0.3 mm/mm) combination. However, tensile ductility decreased along the 45° to the ND and 60° to the ND, and ductility disappeared in the ND direction, indicating an anisotropic plastic deformation in the RD to ND directions. To explore the potential reasons behind this anisotropic ductility behavior, BSE, WDS, EBSD and TEM experiments were performed for microstructural investigations.

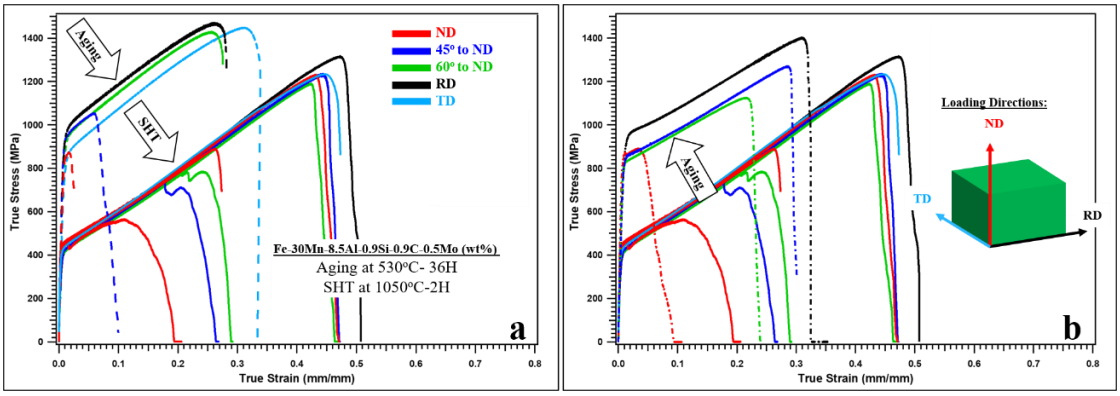

Figure 6.10 Tensile properties of Fe-30Mn-8.5Al-0.9Si-0.9C-0.5Mo (wt%) along four different orientations at room temperature. a) aged vs. aged+SHT b) aged+SHT vs. aged+SHT+aged.

6.3.2. Microstructural investigations

EBSD images of the aged and aged+SHT samples are displayed in **Fig. 6.11**. The microstructure of the aged and SHT samples can largely be characterized as equiaxed, dynamically recrystallized grains. However, Kernel Average Misorientation (KAM) maps (**Fig. 6.11b**) reveal that the density of the geometrically necessary dislocations, which can produce lattice rotations, is higher in the coarse grains than in the equiaxed grains in aged

condition, attesting to the occurrence of inhomogeneous recrystallization during the hot rolling process.

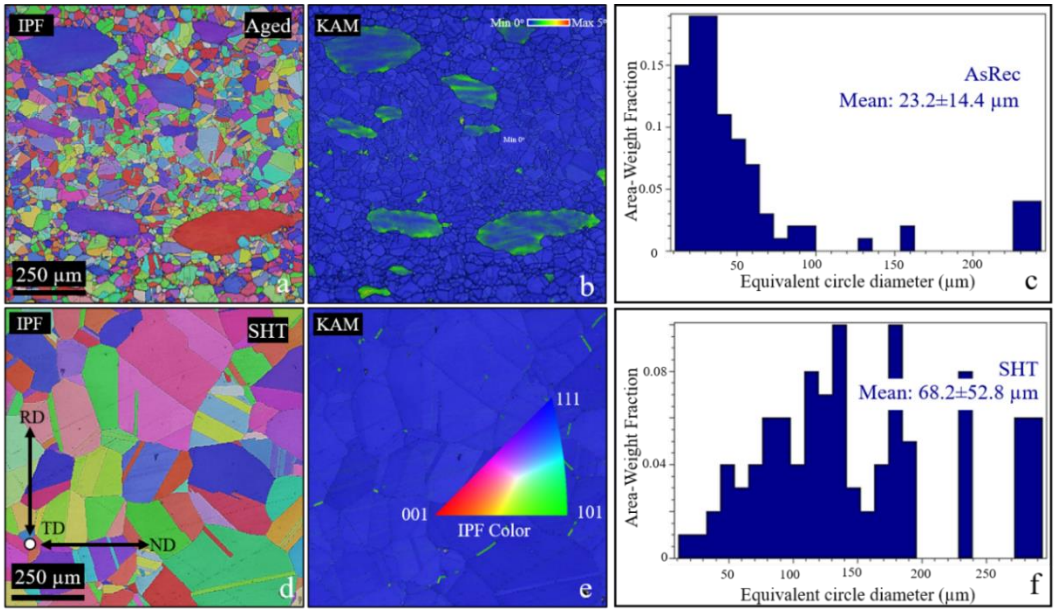

Figure 6.11 EBSD images of Fe-30Mn-8.5Al-0.9Si-0.9C-0.5Mo (wt%) specimens taken from solution, heat-treated, and peak aged at 530°C for 36 hours. (a–c) EBSD band contrast, IPF, and KAM maps of the specimens for the aged sample and (d–f) SHT sample, respectively. GBs defined by the misorientation angle larger than 10°.

BSE imaging coupled with wavelength dispersive spectroscopy (WDS) was then conducted to confirm that there were no second phases at grain boundaries, inhomogeneous grain size distribution, or chemical segregation, which can affect the mechanical properties of the steel. No secondary phase at grain boundaries or inhomogeneous grain size distribution were observed via BSE imaging in the aged specimen (**Fig. 6.12**). Upon further investigation along ND, RD, and TD in the cross

section of the aged and SHT samples using large area WDS elemental maps, considerable elemental segregation was evident in the aged samples along RD and TD, as shown in **Fig. 6.13**. We also solution heat-treated (SHTed) the aged material at 1050^{o}C for 2 hours, to determine whether SHT can eliminate this macro segregation.

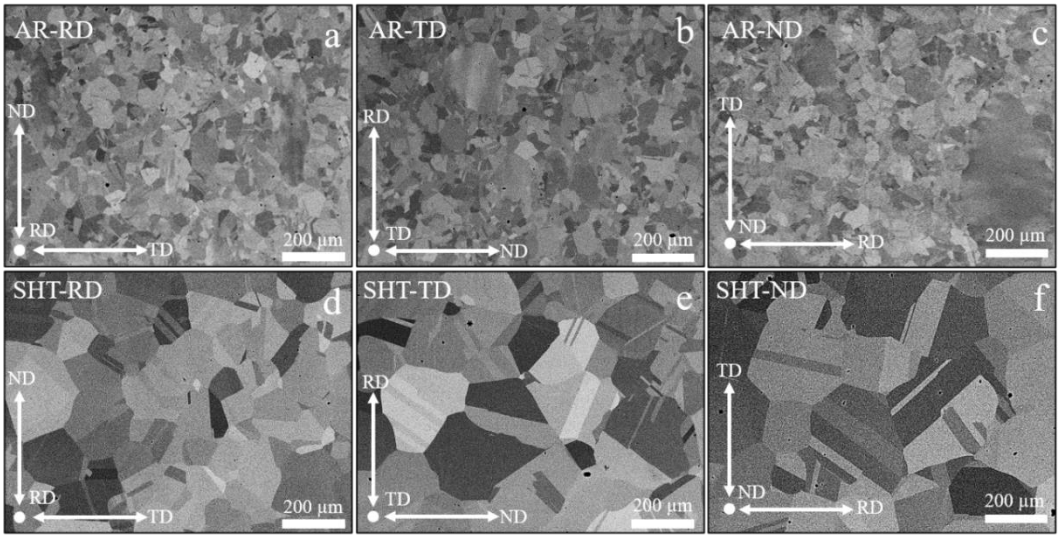

Figure 6.12 Backscattered electron SEM images displaying the grain sizes for aged and SHT 1050°C-2h-Ar-WQ. BSE samples with a dimension of 10*10 mm were extracted from the center of the aged/hot-rolled billets. 15 to 20 pictures of the aged samples were obtained at different magnifications. Same samples were subsequently exposed to SHT following with BSE imaging.

Interestingly, after SHT, the elemental segregation was still prominent (Fig. 6.14). Note that Fe fluctuates from 57–62 wt.%, Mn fluctuates from 25–35 wt.%, and Al fluctuates between 5–10 wt.%. Thus, it appears that the Mn segregation is on the order of ±5wt.% from its nominal amount of 30 wt.%.

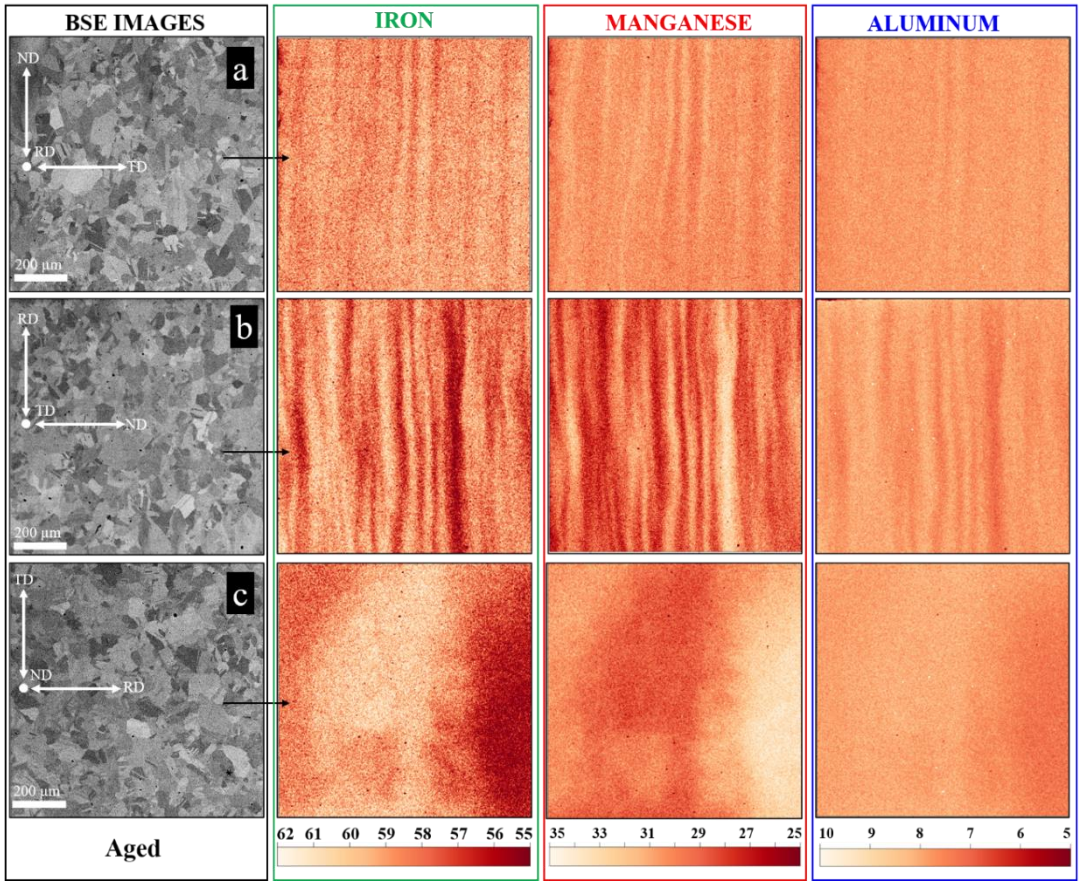

Figure 6.13 Backscattered electron (BSE) imaging of an aged billet cross section coupled with wavelength dispersive spectroscopy (WDS). Elemental mapping of the same region for (a) RD plane, (b) TD plane and (c) ND plane, measured using Electron Probe Micro Analysis (EPMA) and exhibiting significant macro segregation of manganese.

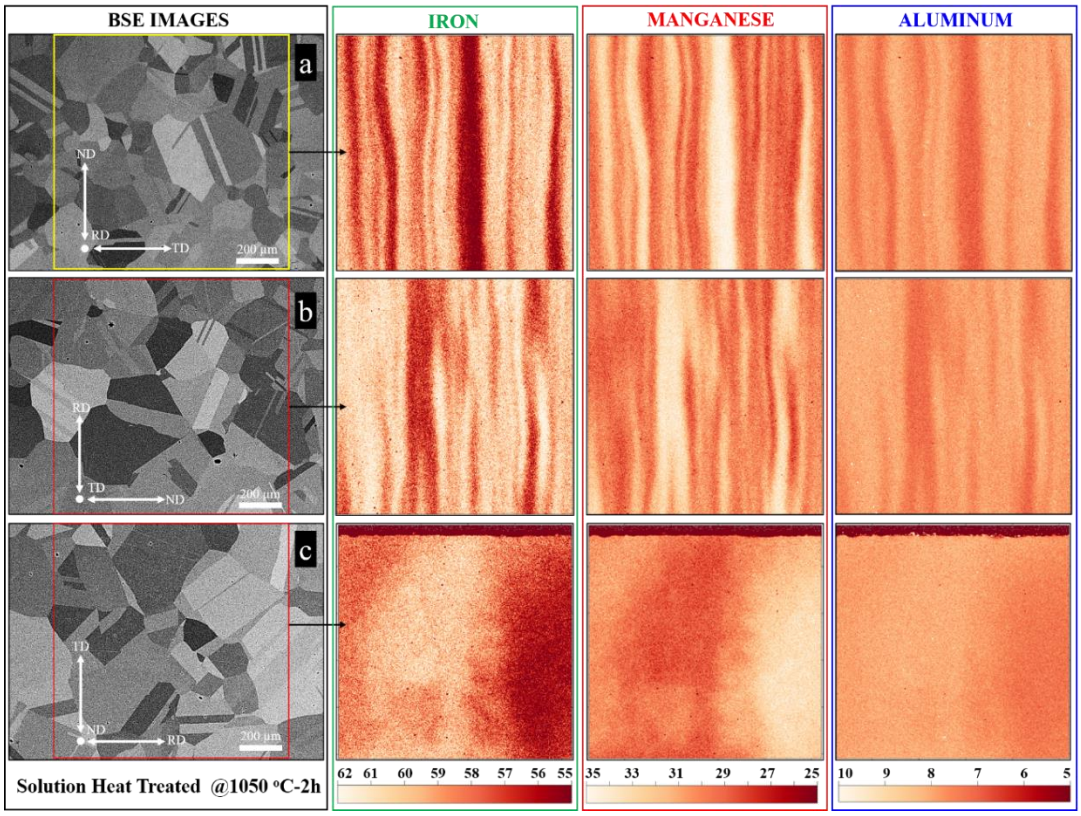

Figure 6.14 Backscattered electron (BSE) imaging of an SHT billet cross section coupled with wavelength dispersive spectroscopy (WDS). Elemental mapping of the same region for (a) RD plane, (b) TD plane and (c) ND plane, measured using Electron Probe Micro Analysis (EPMA) and exhibiting significant macro segregation of manganese.

This unusual behavior could originate during the aging process. Before starting the microstructural investigation, we also solution heat-treated (SHTed) the aged material at 1050°C for 2 hours to solve all κ-carbides and determine whether κ-carbides caused this anisotropic ductility. Recent studies have employed X-ray experiments to ascertain the effectiveness of SHT in dissolving κ-carbides, identifying that microstructure is a single-phase face-centered cubic structure after SHT. However, macro XRD experiments cannot detect a small volume fraction of ordered nano precipitates or clusters/κ-carbides, even in

solutionized specimens [85,198]. As evident in the tension stress-strain curves for RD direction, yield strength drastically decreases after the solution heat treatment, as expected, from roughly 800–1000 MPa to approximately 400 MPa. The strain hardening rate of the SHT-RD sample is higher than that of the Aged-RD specimen (Fig.1c). This difference can originate from the change in the dislocation plasticity and disappearing of precipitates [85]. When planar dislocations meet with κ-carbides, they can shear dislocations, causing more slip bands and subsequently a decrease in hardening rate [199]. Elongation to failure increases drastically for the aged+SHT condition. These phenomena reflect the impact of grain growth (from **Fig. 2**) and dissolution of the κ-carbides on the mechanical properties of aged versus aged+SHT conditions. Moreover, it has been suggested that the formation of Orowan looping can bypass κ-carbides following with cross slip [200]. This also could cause the lower strain hardening in the aged specimen. However, SHT did not completely annihilate the ductility anisotropy, which could be linked to the retained κ-carbides in the segregation bands (**Fig. 3**) [198]. Additionally, we re-aged the material to determine whether anisotropy would reoccur. After re-aging, ductility anisotropy was observed again (see **Fig. 6.10b**).

Given the obvious segregation in the aged and SHT cases, tensile tests were conducted along four directions relative to the segregation bands: along the ND, 45° to the ND, 60° to the ND, and 90° to the ND (i.e., along the RD). These four results have been shown for the aged and SHT conditions, where it was found that strain to failure along the ND was much lower for the aged case than the SHT case, although overall the ND

consistently showed the lowest strain to failure (**Fig.1**). As the ND is normal to the segregation bands, it is plausible that segregation is inducing failure through layer-to-layer delamination from such a test, as 3D-WDS and 3D-BSE images present the segregation layers and grain size distribution relative to the loading directions on NP, TP, and RP samples (**Fig. 6.15**). However, to test whether precipitation may induce lower strain to failure along the ND due to preferential formations in the select segregation bands, the SHT condition was peak aged at 575°C for 36.5 hours (**Fig. 6.10b**). Here, it was clear that the precipitation drastically enhanced the strength. However, the ductility along the ND was much lower than along the other orientations. From these findings, it appears that segregation bands oriented along the RD promote extensive precipitation in some of the segregation bands, thereby embrittling the interface between segregation layers. Thus, the ND has much lower strain to failure levels than the other orientations after peak aging.

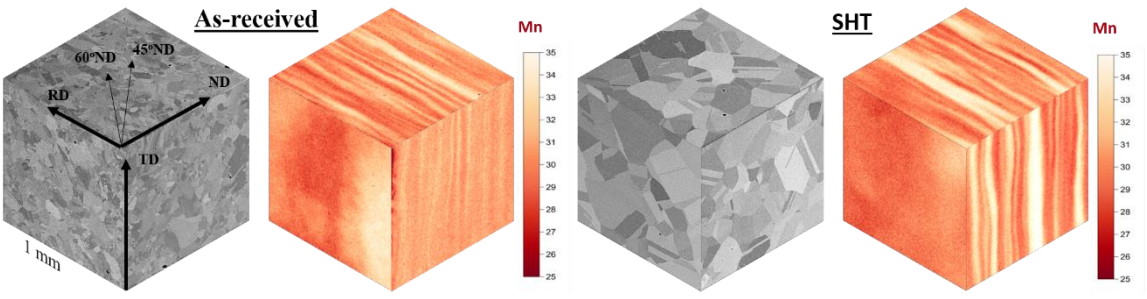

Figure 6.15 3D-Electron Probe Micro Analysis (EPMA) images using Wave Dispersive Spectroscopy (WDS) compositional mapping for Aged and SHT on ND: Normal Direction, RP: Rolling direction and TD: Transverse Direction.

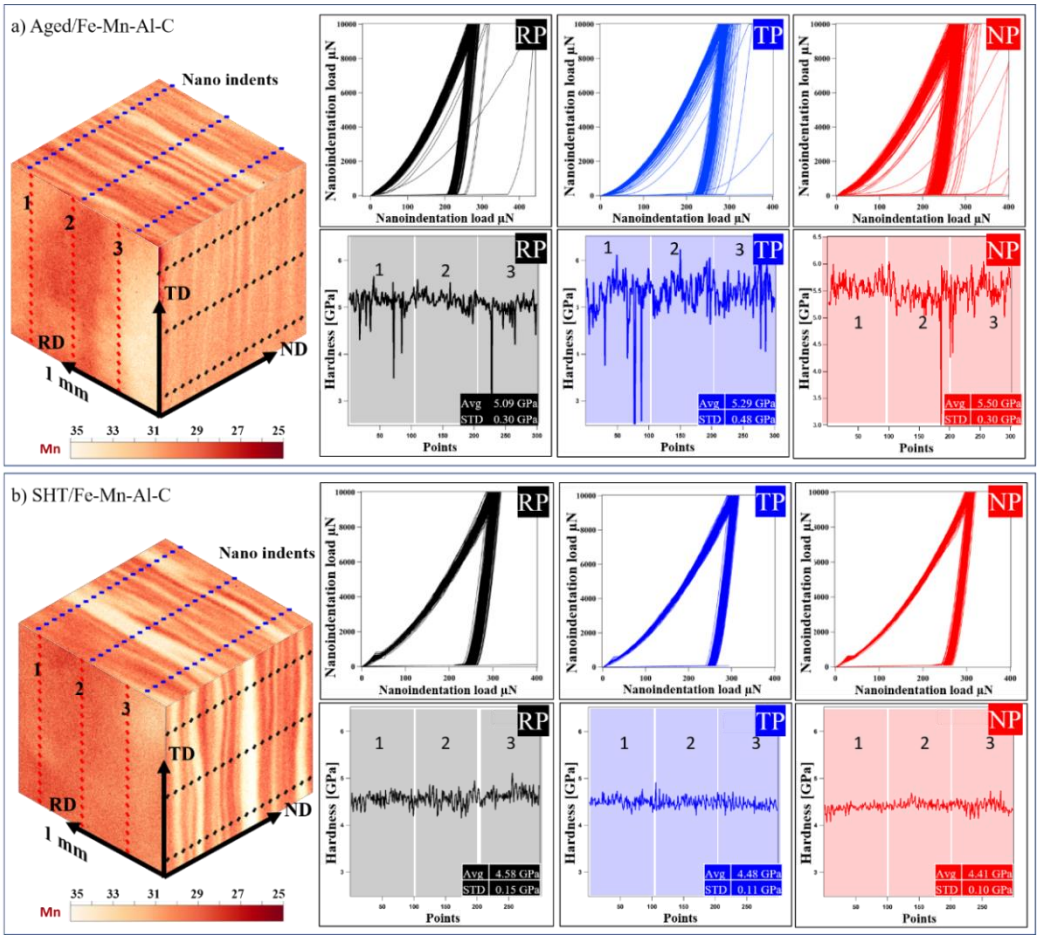

Figure 6.16 Nanoindentation results comparing RP, TP and NP samples in a) Aged and b) SHT sample in comparison with Mn segregation maps.

Fig. 6.16 displays the chemical content as a function of the sample plane for the SHT condition on the TP, NP, and RP planes with nanoindentation results. The nanoindentation results show that there is a much higher hardness deviation overall for Aged vs. SHT, likely due to the presence of κ-carbide precipitates. Moreover, the hardness was fairly uniform for all planes, although there was more noise in the RP plane of the SHT sample, as expected due to the nature of solution heat-treatment. Nanoindentation

experiments indicated that precipitation might occur preferentially in specific segregation bands.

The bright-field TEM images show abundant intragranular nano-precipitates distributed in the FCC matrix, though not uniformly (**see Fig. 17a–f**). Such irregular precipitate distribution is attributed to the chemical segregation in this material also detected using TEM EDX mapping. Analysis of a selected area's diffraction pattern indicates that the structure of precipitates is $L1_2$ type κ-carbides in the austenitic matrix [200]. No evidence for the formation of ferrite was found using TEM and BSE investigations, which echoes previous reports of Fe-Mn-Al-C alloys with similar composition to that of the current study [200,201].

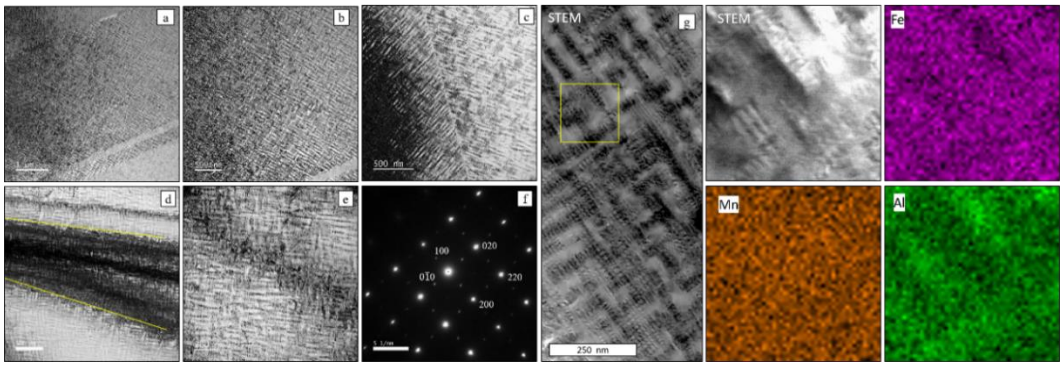

Figure 6.17 (a-e) Transmission electron microscopy (TEM) bright-filed images showing κ-carbide distribution, (f) corresponding diffraction pattern of (e, g) the TEM EDSX maps showing the Kappa carbide being Al rich.

As an interstitial element in the Fe-Mn-Al-C light weight alloy system, C provides a high level of solid solution hardening and stabilizes the austenite phase [87], similar to Mn [88]. Although Al can promote the formation of ferrite, high levels of Mn and C

content suppress the formation of ferrite. Moreover, Al and C activate the formation of κ-carbide precipitates [86]. Regarding TEM, κ-carbides are clearly visible on the STEM image EDSX maps (**Fig. 6.17g**), where the Al richness of the κ-carbide is evident. It is worth nothing that TEM magnification is ill-suited to displaying entire segregation bands observed in WDS experiments. However, we were still able to observe the intersection of the layers, and the chemical segregation causing the inhomogeneous precipitate formation could be also observed locally.

6.3.3. Fracture investigation

The WDS segregation maps in **Figs. 6.13–6.15** indicate that failure occurs due to elemental segregation bands in particular. The fracture surface in **Fig. 6.18a** shows that cleavage-type brittle failure regions formed along the fracture surfaces of tensile specimens, and these regions became less common as the angle to the normal direction (ND) increased (**Figs. 6.18b–c**). These flat regions are also parallel to the segregation bands detected by WDS (**Fig. 6.15**). These brittle failure regions were not present along the rolling direction (RD, or 90° to ND) (**Fig. 6.18d**). We further investigated the side surfaces of the RD and ND samples using EBSD to identify whether there were texture or initial condition effects on the ductility anisotropy. Side surface EBSD images of the Aged and SHT samples are provided in **Fig. 6.19**. In all conditions, the image quality map reveals that the majority of the grains are separated by high angle grain boundaries (HAGBs). The KAM micrograph of the ND-Aged sample after tensile fracture showed

that the plastic deformation was restricted in the region corresponding to the flat region of fracture surface (**Fig. 6.19**).

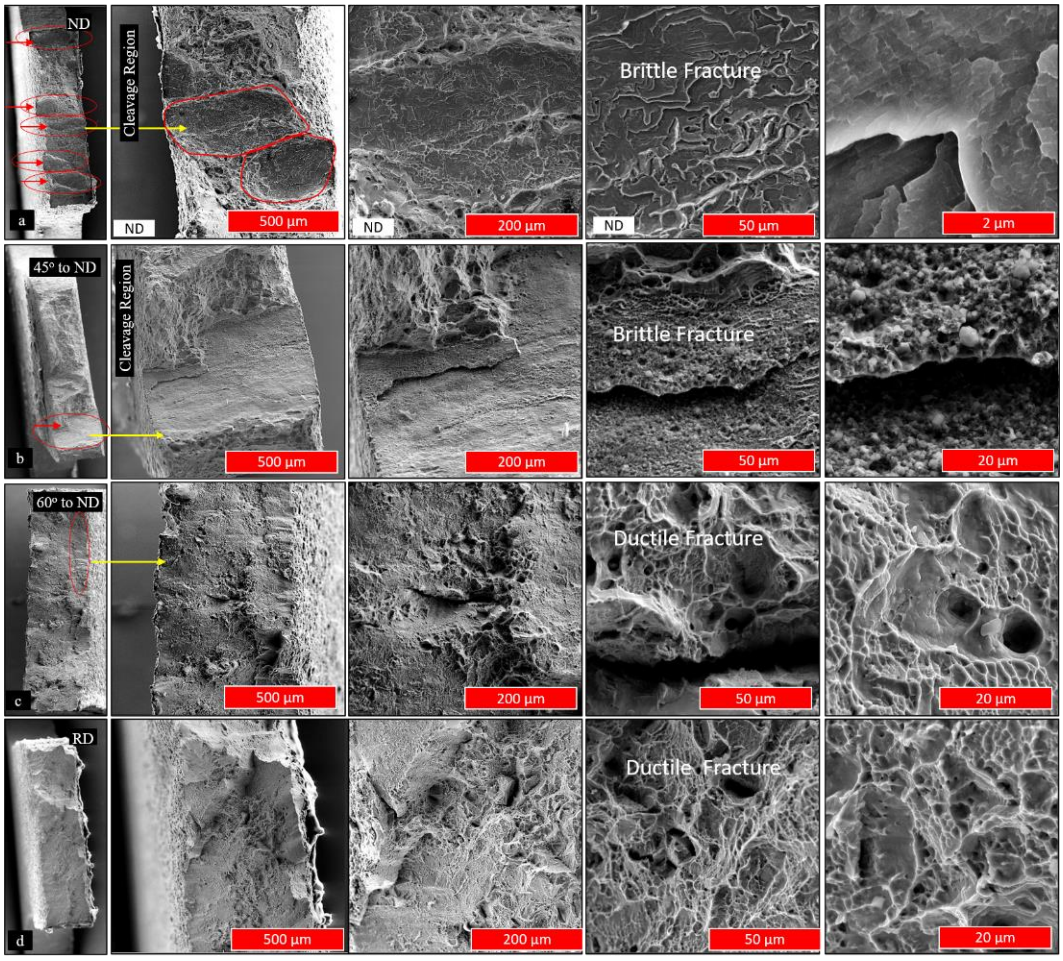

Figure 6.18 Fracture surfaces of Fe-30Mn-8.5Al-0.9Si-0.9C-0.5Mo (wt%) lightweight steel. Higher magnifications of fracture are displayed to the right.

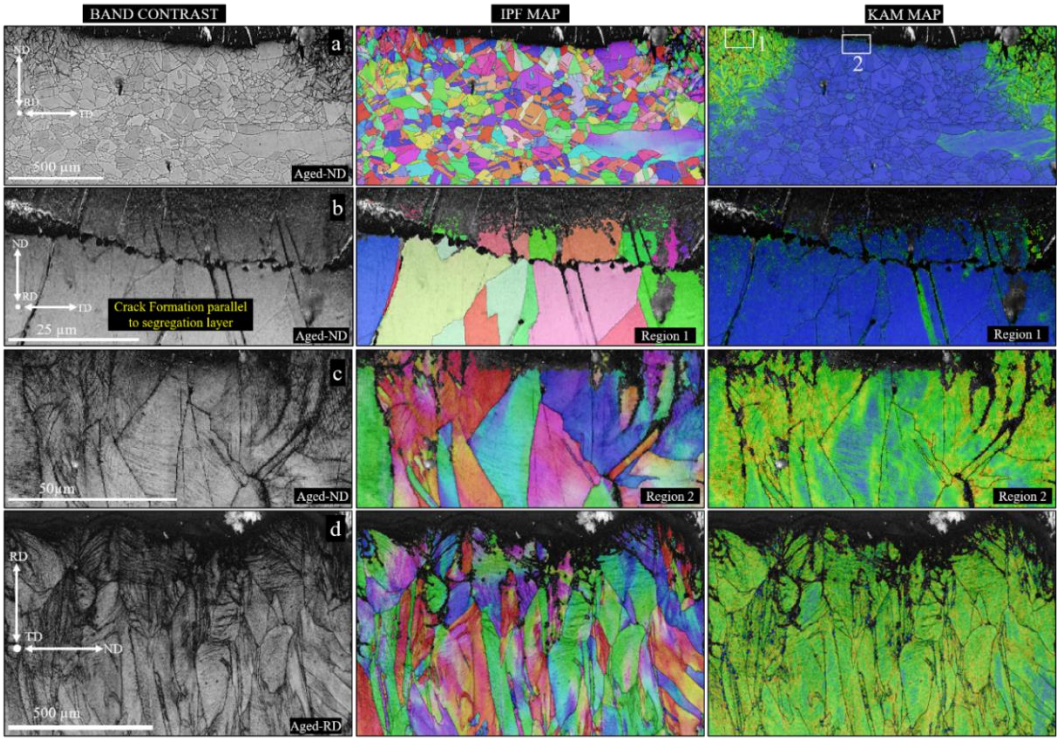

Figure 6.19 Microstructural characterization, observed through electron back scatter diffraction (EBSD) imaging, of Aged FeMnAl-C lightweight steels imaged on the ND tensile samples after tensile deformation. Image quality maps, inverse pole figure (IPF) maps, and Kernel Average Misorientation (KAM) maps for (a) SHT-ND sample; (b–c) SHD-ND sample at higher magnification, marked with rectangle on (a); and (d) Aged-RD sample.

To further prove the restricted deformation ability in the Aged-ND sample, higher magnifications of the EBSD maps marked on **Fig. 19a** are presented in **Figs. 6.19b and 19c**. The observed segregation bands 90° to ND promoted the crack initiation just after yielding, which completely restricted the sample's plastic deformation ability. However, a homogeneous deformation in the AsRec RD sample can be seen in **Fig. 19d** (segregation bands parallel to loading direction). After solution heath treatment, SHT-ND sample tensile test results showed that plastic deformation ability improved after dissolving the

precipitates (**Fig. 6.10**). In the EBSD maps of the SHT-ND and RD samples presented in **Fig. 20,** we interestingly observed unexpected deformation twinning formation after tensile failure with high stacking fault energy. The twinning formation in the SHT samples can be attributed to the high degree of SRO ordering in FeMnAl-C light weight steel. The KAM maps in **Fig. 20** show that the deformation was more homogeneous in the SHT-ND sample than in the Aged ND-sample.

After solution heath treatment, the SHT-ND sample tensile test results showed that the plastic deformation ability improved, since the precipitates were dissolved. However, some retained precipitates may have lingered, which decreased the ductility in the SHT-ND sample. EBSD maps of the SHT-ND and RD specimens are presented in **Fig.4** and **Fig. 5**. Interestingly, deformation twinning formation after tensile failure with high stacking fault energy was again observed, which was anomalous. The twinning formation in the SHT samples can be attributed to the high degree of SRO ordering in FeMnAl-C light weight steel. However, further investigations are needed to build understanding of twinning nucleation in high SFE Fe-Mn-Al-C light weight steels.

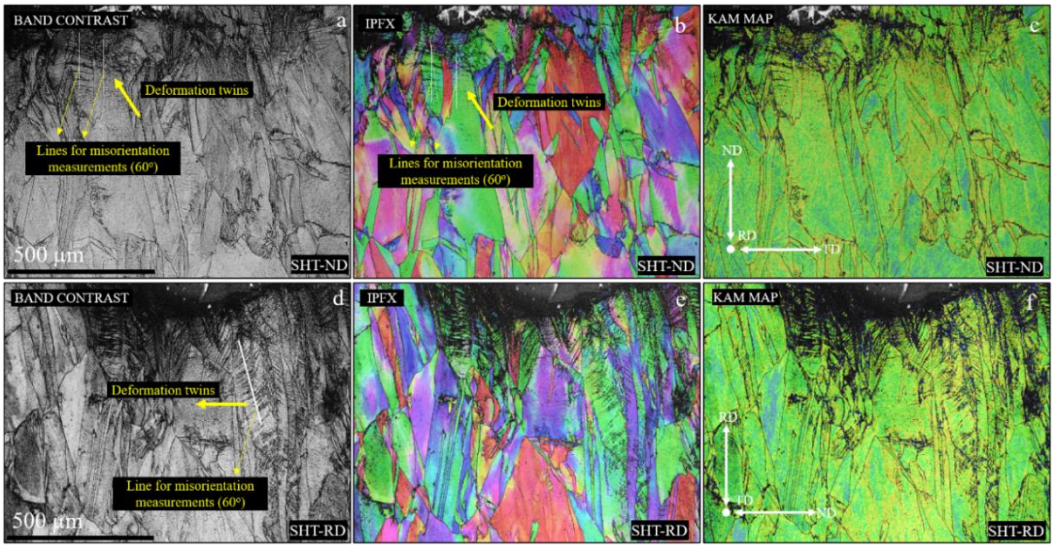

Figure 6.20 Microstructural characterization, through EBSD imaging, of SHT FeMnAl-C lightweight steels imaged on the RD and ND tensile samples after tensile deformation. Image quality maps, inverse pole figure (IPF) maps, and Kernel Average Misorientation (KAM) maps for the (a-c) SHT-ND and (d-f) Aged-RD sample, respectively.

6.4. Summary and Conclusion

This chapter details the investigation of the various strengthening mechanisms in model M/HEAs, including solute strengthening, grain refinement, strengthening due to dislocation sub-structures, and precipitate hardening. Interstitial strengthening was used to improve the mechanical properties of single crystalline CoCrFeMnNi HEA. Polcrystalline CoCrFeMnNi HEA was processed using SPD via ECAP. ECAP was used instead of more conventional processing techniques, such as rolling, to obtain large cross-section HEA with uniform microstructures. Finally, medium entropy Fe-Mn-Al-C lightweight steel was exposed to aging to improve the mechanical responses via

precipitation hardening. The major findings of this study can be summarized as follows, in the light of the EBSD, SEM, TEM, WDS, tensile tests, and nanoindentation results.

1. The carbon addition (0.75 at.% C) in single crystalline CoCrFeMnNi HEAs caused a 25% increase in CRSS. The microstructure investigations of the [111]+C-oriented single crystalline CoCrFeMnNi revealed that the addition of carbon caused a tertiary twin system that suppressed the necking instability and produced an extended hardening stage. This TWIP effect caused more plastic deformation ability and subsequently improved the UTS level. Moreover, the [001]+C specimens presented the formation of nano twinning, which was the main reason for the simultaneous improvement in strength and ductility.
2. ECAP of CoCrFeMnNi HEA at medium and high temperatures resulted in a unexpected deformation twinning and ε-martensite formation, in addition to grain refinement, an increase in dislocation density, and heterogeneous grain size distribution. This composite microstructure was responsible for the high strength level ductility combination at room temperature. The simultaneous TWIP/TRIP effect at high temperatures was attributed to the effect of low SFE and high stress levels on partial dislocation separation. The composite microstructure achieved with ECAP enables defect storage, provides strain hardening capability, and postpones neck instability, which ultimately provides uniform plastic deformation. These observations and the mechanisms discovered are also applicable to other

M/HEAs and will help tailor their microstructure to further improve their properties.

3. A systematic investigation of aged and non-aged Fe-Mn-Al-C steels indicates a new lamellar segregation governing the deformation response of the current material. Th is research demonstrated that segregation direction was detrimental to the sample's toughness. The loading direction parallel to the segregation bands presents the best strength-and ductility combination, while the loading direction 90^{o} to segregation bands presents the worst toughness. Such chemical segregation has rarely been realized, and this study represents the first report of its effect on the material's mechanical properties.

7. ON THE LOW CYCLE FATIGUE RESPONSE OF SINGLE CRYSTALLINE HEAS

In this chapter, the orientation dependence on the low-cycle fatigue properties of a $Fe_{50}Mn_{30}Co_9Cr_9$+2 at.% C HEA was investigated in [001], [110], [111] and [123] oriented single crystals. Cyclic tests were conducted at total strain amplitudes of $\Delta\varepsilon t/2$= ±0.2 %, ±0.4 %, and ±0.6%, and microstructure evolution was studied post-mortem. EBSD micrographs revealed the major deformation mechanism was deformation twinning at the fatigue crack region in all orientations. However, the volume fraction and the active number of twin systems were different depending on the loading direction. While [111] crystals exhibited cyclic hardening at $\Delta\varepsilon t/2$= ±0.6 %, this behavior is not observed at $\Delta\varepsilon t/2$= ±0.2 % and $\Delta\varepsilon t/2$= ±0.4 %, similar to [001] orientation being uniformly characterized by saturation stated of the stress amplitudes at given strain amplitudes. dynamic strain aging was observed only in the [111] orientation at $\Delta\varepsilon t/2$= ±0.6 %, which was found to be the main contributor for cyclic hardening and non-Masing behavior accelerating a reduction in fatigue resistance by improving crack propagation. In contrast, [110] and [123] orientations exhibited distinct cyclic softening at all strain amplitudes.

7.1. Methodology

Single crystals of the $Fe_{50}Mn_{30}Cr_9Co_9$+2 at.% C HEAs were artificially grown using the Bridgman technique in an inert helium atmosphere. All single crystals were sealed using a quartz tube and homogenized in an inert gas at 1473 K for 24 h, and

subsequently water-quenched to room temperature (RT). The orientations of the bulk crystal were determined from Laue back-reflection images. For microstructure analysis and mechanical characterization, dog bone shaped specimens (along the [001], [110], [111] and [123] crystallographic orientations) with a gauge section of 8 mm × 1.2 mm × 3 mm were cut from the single crystals using EDM. The specimen geometry employed was numerously used in literature (e.g., [57,73]), however, has not been captured by an official standard.

Microstructural analysis was carried out using a Zeiss ULTRA GEMINI high-resolution SEM operating at accelerating voltage of 30 kV. The SEM system is equipped with an EBSD unit. For EBSD measurements specimens were further vibration-polished for 24 h using conventional oxide polishing suspension (OPS) with a grit size of 0.04 µm. A 120 µm aperture as well as the high current mode were used resulting in a probe current of 8 nA. Step sizes and tilt angle of the measurements were 0.5 as well as 0.1 µm and 70°, respectively. Moreover, WDS in the Cameca SXFive electron microprobe was performed on 80 different locations to verify the chemical composition (50 at.% Fe, 30 at.% Mn, 9 at.% Cr, 9 at.% Co and 2 at.% C). In addition, carbon content was determined by combustion-infrared absorbance according to ASTM E 1019-18.

Tension experiments were performed using a servo-hydraulic MTS frame at strain rate of 5×10^{-4} s^{-1} at room temperature. An extensometer was directly attached to the specimens to record the axial strain. All experiments were repeated three times to ensure repeatability. The critical resolved shear stress (CRSS) levels for slip were calculated

using the expression $\tau_{cr}^{sl} = \sigma_{\varepsilon}^{sl} m_{slip}$. The LCF tests were performed on a digitally controlled servo-hydraulic test rig with a maximum force capacity of 16 kN. The experiments were carried out under a fully reversed push-pull loading (R_ε = -1) condition and at a constant strain rate of 6 x 10^{-3} s^{-1}. An MTS miniature extensometer featuring a gauge length of 5 mm was used to measure strain amplitude in LCF testing. Tests were conducted at three total strain amplitudes of $\Delta\varepsilon_t/2$= ±0.2 % (0.75 Hz), ±0.4 % (0.375 Hz), and ±0.6% (0.25 Hz). The strain amplitude was increased stepwise to prevent buckling of the specimens. Thus, the final strain levels of 0.2% and 0.4%/0.6% were attained upon 5-10 cycles, respectively, depending on the actual strain amplitude. Fracture surface investigations after fatigue testing were conducted using a second SEM system (CamScan MV 2300) operating at an accelerating voltage of 20 kV.

7.2. Uniaxial Tensile Test Results at Room Temperature

The true stress - true strain curves procured from the uniaxial tension experiments at room temperature are shown in **Fig. 7.1**. The [111]-, and [110]-oriented specimens had the highest ultimate tensile strength (UTS) of 1025±25 MPa, while the [123]- and [001]-oriented crystals showed a UTS of 975±15 MPa and 670±15 MPa respectively. Young's modulus were calculated from the stress-strain curves as E_{100} = 115±20 GPa / E_{110} = 218±20 GPa / E_{111} = 320±20 GPa / E_{123} = 230±20 GPa. The [110]-oriented specimens displayed the best combination of strength and ductility, both being significantly better than all oriented single crystals. All orientations demonstrate a significant hardening

capacity through the tensile deformation. However, the hardening stages show different behavior because of the activation of the different kind of deformation modes in different orientations. It is also well-known that the tensile deformation behavior in HEA single crystals is highly dependent on the crystallographic orientation [3,89], similar to low SFE stainless steels [31] and Hadfield steels [28]. Finally, the critical resolved shear stress in the current HEA single crystals is calculated as 110±5 MPa, which is much higher than $Fe_{40}Mn_{40}Co_{10}Cr_{10}$ HEA (τ_{cr}^{sl}=53±2 MPa) [89] and NiCoCr MEA (τ_{cr}^{sl}=63±3 MPa) [3].

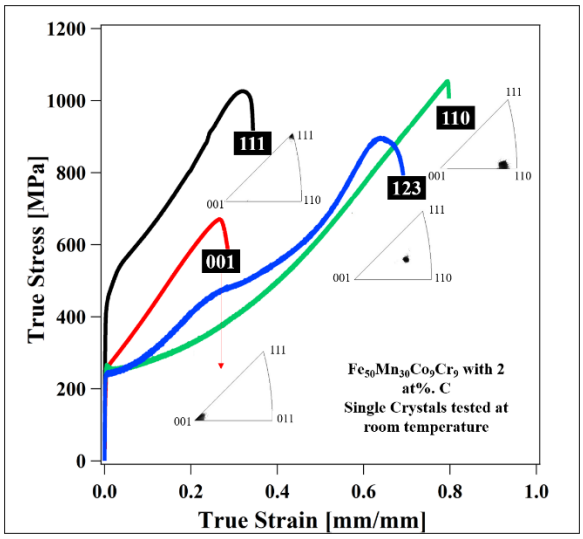

Figure 7.1 (a) The room temperature true stress - true strain tension responses of the [111]-, [001]-, [001] and [123]-oriented single crystals of the $Fe_{50}Mn_{30}Co_9Cr_9$+2 at.% C HEA. Inverse pole figures show the initial loading directions for the four orientations, measured using electron backscattered diffraction.

7.3. Low-Cycle Fatigue Response

Fig. 7.2 depicts the cyclic deformation responses (CDRs) of the single crystalline $Fe_{50}Mn_{30}Co_9Cr_9$+2 at.% C HEAs. As already mentioned in section 2, the strain amplitude was increased stepwise during the very first cycles in order to avoid buckling of the

specimens. Thus, in order to avoid confusion, these initial strain ramp regions were eliminated from the data shown as the CDRs displayed are plotted starting from the 11th cycle. Irrespective of the orientation, decreasing fatigue lives can be obtained with increasing total strain amplitude. Differences between the different orientations considered can be seen with respect to the absolute stress level value as well as the evolution of the stress. A steady increase of the stress amplitude with increasing strain amplitude is revealed by the [100] orientation (**Fig. 7.2a**), being more pronounced between the lowest and medium total strain amplitude, i.e., $\Delta\varepsilon_t = \pm 0.2\%$ and $\Delta\varepsilon_t = \pm 0.4\%$ since multi-slip systems or twinning are activated at the beginning of the deformation [28,89]. However, similar stress levels can be seen for [110] and [123] orientations at all strain amplitudes (**Figs. 7.2b and 7.2d**), which is owing to single slip activation causing the glide plane softening at the beginning of the deformation [89]. For the [111] orientation similar stress levels were obtained for the lowest and medium total strain amplitude while a pronounced increase of the stress is obvious for the highest strain amplitude of $\Delta\varepsilon_t = \pm 0.6\%$. However, the [111] orientation is generally characterized by the highest corresponding stress amplitudes as expected according to Schmid law [28,89]. Evaluating the evolution of the stress amplitudes independence with regard to the number of cycles to failure, further differences are revealed by the different orientations. A slight cyclic hardening is observed at the beginning of deformation in the all orientations, which is due to the rapid increase in the dislocation density at the beginning of cyclic deformation (**Fig. 7.2**) [202]. The CDRs of the [100] orientation (**Fig. 7.2a**) is characterized by a slight

cyclic softening after the initial hardening stage in the all-strain amplitudes. A saturation state of the stress amplitude is observed at the end of the tests for the lowest and medium $\Delta\varepsilon_t$, whereas a slight cyclic hardening can be seen for the highest total strain amplitude of $\Delta\varepsilon_t = \pm 0.6\%$ at the end of the test. Similar to the [001] orientation, the CDRs of the [110] and [123] orientation are characterized by a slight cyclic softening after the initial hardening stage and a saturation state of the stress amplitude at the end of the tests at the all-strain amplitudes (**Figs. 7.2b and 7.2d)**.

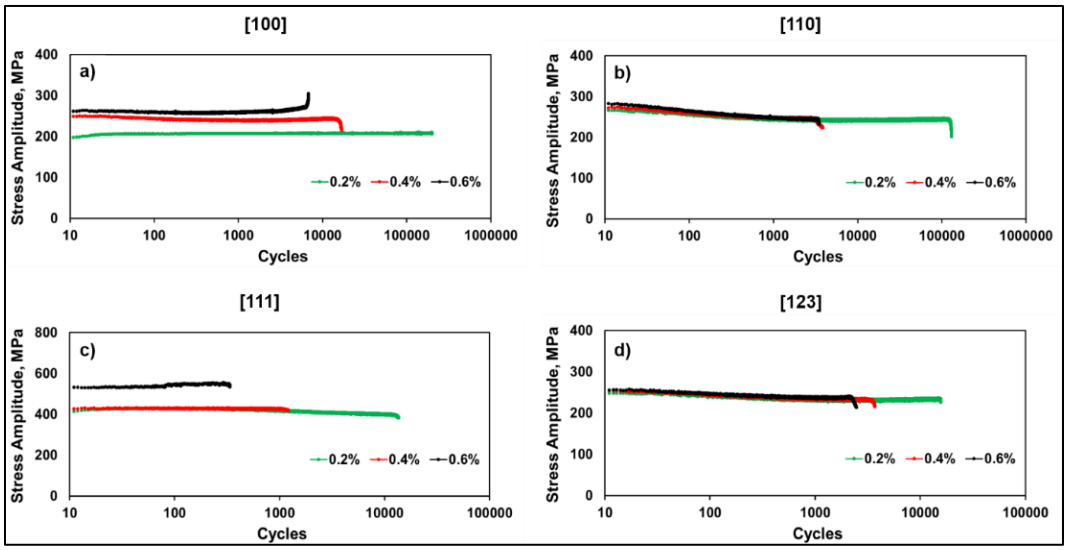

Figure 7.2 Cyclic deformation response of the $Fe_{50}Mn_{30}Co_9Cr_9$+2 at.% C single crystalline HEA at total strain amplitudes of $\Delta\varepsilon_t/2 = \pm 0.2\%$, $\Delta\varepsilon_t/2 = \pm 0.4\%$ and $\Delta\varepsilon_t/2 = \pm 0.6\%$ for (a) [100], (b) [110], (c) [111] and (d) [123] orientation.

In contrast to this, pronounced differences in the evolution of the stress amplitude are revealed for the [111] orientation depicted in **Fig. 7.2d**. While saturation of the stress amplitude is followed by cyclic softening for $\Delta\varepsilon_t = \pm 0.2\%$ and $\Delta\varepsilon_t = \pm 0.4\%$, the CDR for the highest total strain amplitude is characterized by slight cyclic hardening. With respect

to fatigue life, in general the worst cyclic performance is obtained for the [111] orientation whereas the highest number of cycles to failure are represented by the [100] orientation. At this point, it has to be noted that for [100] the test with the lowest total strain amplitude of $\Delta\varepsilon_t = \pm 0.2\%$ was stopped as a runout after 200.000 cycles as this number of cycles is clearly exceeding the limits of the LCF regime. Nevertheless, as compared to [111] orientation, the lifetime of [100] is increased by a factor of approximately 10. With regard to the other orientations considered, i.e. [110] and [123] orientation, slightly increased number of cycles to failure can be seen for the medium and highest total strain amplitude for the [110] orientation, whereas a pronounced improvement of the fatigue life at $\Delta\varepsilon_t = \pm 0.2\%$ is obvious.

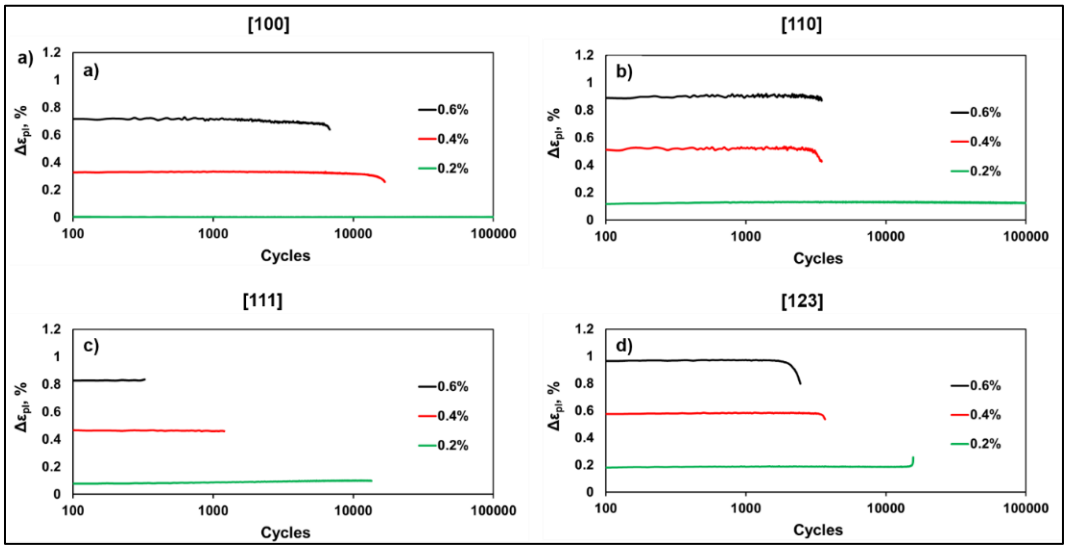

Figure 7.3 Cyclic plastic strain response of the $Fe_{50}Mn_{30}Co_9Cr_9$+2 at.% C single crystalline HEA at total strain amplitudes of $\Delta\varepsilon_t/2 = \pm 0.2\%$, $\Delta\varepsilon_t/2 = \pm 0.4\%$ and $\Delta\varepsilon_t/2 = \pm 0.6\%$ for (a) [100], (b) [110], (c) [111] and (d) [123] orientation.

Softening effect can be observed when the annihilation rate of the dislocations is higher than the generation of the dislocations due to monotonic loading [89] or cyclic loading [202]. Therefore, it can be concluded that the observed cyclic softening just after the initial hardening stage is because of high annihilation rate of the dislocations in the current HEA. The stabilization of the cyclic hardening at the end of the test or cyclic hardening behavior can be caused by the activation of twinning or dynamic strain ageing (DSA) [202–204].

Plastic strain range plotted as a function of number of cycles to failure for all LCF tests and all orientations considered are visualized in **Fig. 7.3**. It has to be noted that, in order to exclude strain ramping effects from analysis, every 25^{th} hysteresis loop was recorded only starting at cycle 100. Thus, development of the plastic strain range is plotted starting from the 100^{th} cycle in **Fig. 7.7**. In addition, hysteresis was only recorded up to 100.000 cycles. Independent of the orientation, a stable evolution of the plastic strain range throughout the complete test can be seen for all strain amplitudes imposed. Together with the corresponding stress amplitudes as discussed above, differences in the fatigue lifetimes can be explained by the evolution of the plastic strain range. The lowest absolute plastic strain values and thus, the highest number of cycles to failure, can be seen for the [100] orientation as displayed in **Fig. 7.2a**. For the lowest strain amplitude of $\Delta\varepsilon_t = \pm 0.2\%$ a constant level of plastic strain, even virtually equal to zero, is obvious. Comparing the plastic strain ranges for the [110] and [123] orientations depicted in **Figs. 7.3b and 7.3d**, respectively, higher absolute values are revealed for [123]. As similar stress levels were

deduced from the CDRs presented above, differences in the fatigue lifetime of both conditions can be reasoned by different contributions of the plastic strain. In contrast to this, irrespective of the total strain amplitude, the plastic strain of the [111] orientation shown in **Fig. 7.3c** is characterized by even lower absolute values as compared to [110] and [123] orientation. However, number of cycles to failure are significantly lower. This observation can thus be explained by the higher stress levels of [111] leading to a premature failure upon cyclic loading for this orientation.

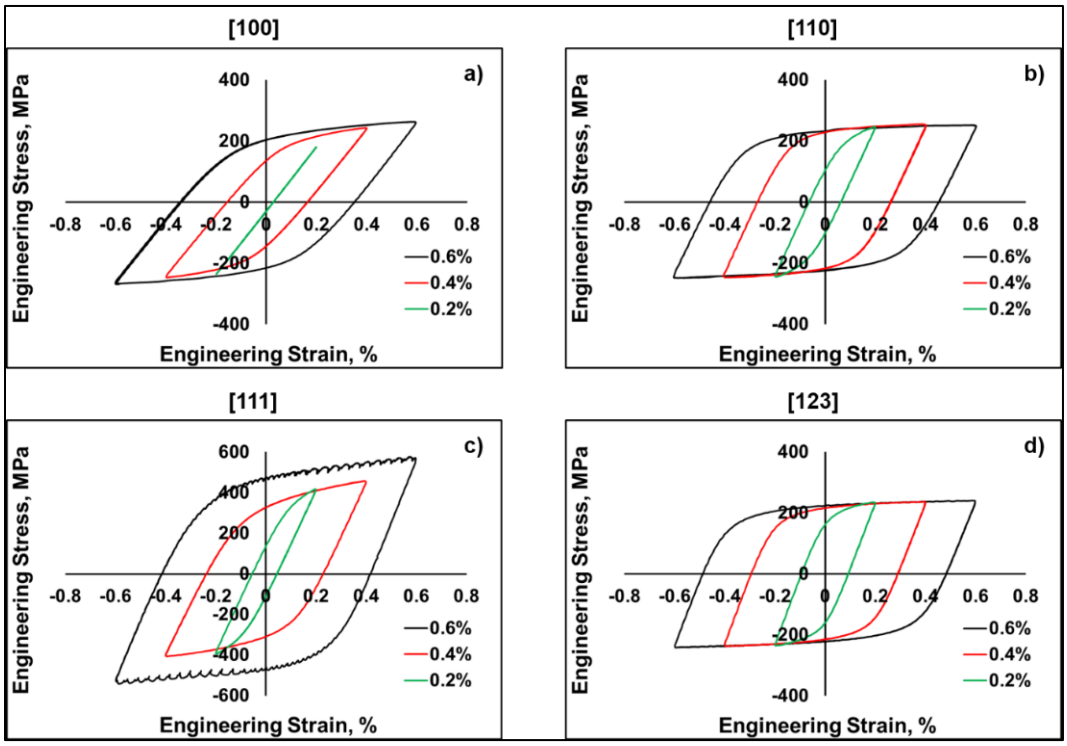

Figure 7.4 Half-life hysteresis loops of the $Fe_{50}Mn_{30}Co_9Cr_9$+2 at.% C single crystalline HEA at total strain amplitudes of $\Delta\varepsilon_t/2 = \pm 0.2\%$, $\Delta\varepsilon_t/2 = \pm 0.4\%$ and $\Delta\varepsilon_t/2 = \pm 0.6\%$ for (a) [100], (b) [110], (c) [111] and (d) [123] orientation.

Half-life hysteresis loops are displayed in **Fig. 7.4** for each of the orientations considered, i.e., [100] (a), [110] (b), [111] (c) and [123] (d). The results of the half-life hysteresis are in perfect congruence with the CDRs and plastic strain range evolution as well as results from tensile tests presented above. The orientations [110] and [123], shown in **Figs. 7.4b** and **7.4d** respectively, are characterized by wide opened hysteresis, being more pronounced for [123], as well as almost ideal plastic behavior resulting in similar stress levels for a given total strain amplitude as also revealed by the CDRs. In contrast, these observations are less pronounced for the [100] and [111] orientations. In line with the results of plastic strain range evolution, the hysteresis of the [100] orientation is opened least even revealing a completely closed hysteresis and thus pure elastic strain for the lowest total strain amplitude of $\Delta\varepsilon_t = \pm 0.2\%$. Highest corresponding stresses for a given strain amplitude as already seen in the CDRs can be deduced from the half-life hysteresis of the [111] orientation presented in **Fig. 7.4c**. Interestingly, the hysteresis loop of the test conducted at the highest total strain amplitude of $\Delta\varepsilon_t = \pm 0.6\%$ is characterized by DSA effects as can be deduced from the serrations. These observations have been severely shown for high-manganese literature [204,205]. According to Ma et al. [204] DSA effect describes the dynamic interaction between mobile dislocations and solute atoms, leading to cyclic hardening as similarly seen in the CDR of the [111] orientation of the current study [**cf. Fig. 7.2**]. The authors further concluded that, as a result of DSA, many dislocations were locked by solute atoms, and more new dislocations would be generated to maintain the applied strain rate, causing a greater dislocation density during cyclic

deformation. Moreover, a higher stress response during cyclic deformation was attributed to DSA, resulting in a larger concentration of stress at the crack tip and an increase in the crack propagation rate, leading to a lower fatigue crack propagation life. Furthermore, different Young's modulus of the different orientations can be derived from the half-life hysteresis presented in **Fig. 7.4**.

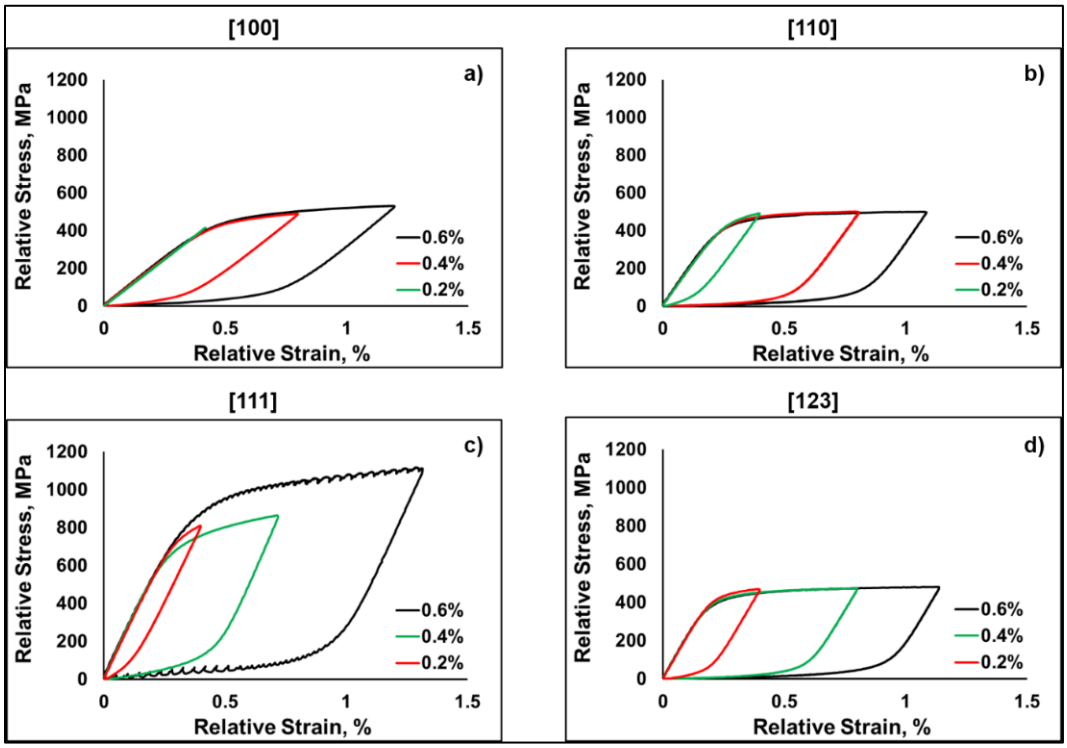

Figure 7.5 Half-life hysteresis loops of the $Fe_{50}Mn_{30}Co_9Cr_9$+2 at.% C single crystalline HEA at total strain amplitudes of $\Delta\varepsilon_t/2 = \pm 0.2\%$, $\Delta\varepsilon_t/2 = \pm 0.4\%$ and $\Delta\varepsilon_t/2 = \pm 0.6\%$ for (a) [100], (b) [110], (c) [111] and (d) [123] orientation plotted in relative coordinates of stress and strain.

Half-life hysteresis loops of $Fe_{50}Mn_{30}Co_9Cr_9$+2C at.% HEA in single crystals of different orientations are plotted in relative coordinates of stress and strain for the various

total strain amplitudes as demonstrated in **Fig. 7.5**. From **Fig. 7.5**, it can be deduced that the cyclic deformation response of this alloy exhibits Masing behavior in all crystal orientations except [111]. Incongruent upper branches of the hysteresis loops in [111] suggest non-Masing behavior. The observed non-Masing behavior in [111]-oriented crystals reveal that with the increase in the strain amplitude, extensive changes in dislocation densities and rearrangements are expected [57,111]. As discussed above, DSA present in this orientation resulted in the multiplication of dislocations since initial dislocations were pinned by solute atoms [204]. Thus, non-Masing behavior can also be linked to the DSA effect. Masing behavior observed in other crystal orientations reveals that a similar microstructure evolution independent of the strain amplitude is expected [105]. It should also be noted that, in addition to the DSA effects, twin-twin and twin-slip interactions are present in [111] orientation during deformation resulting in considerable changes in the course of microstructure [89,146], as will be discussed in detail in Section 3.3.

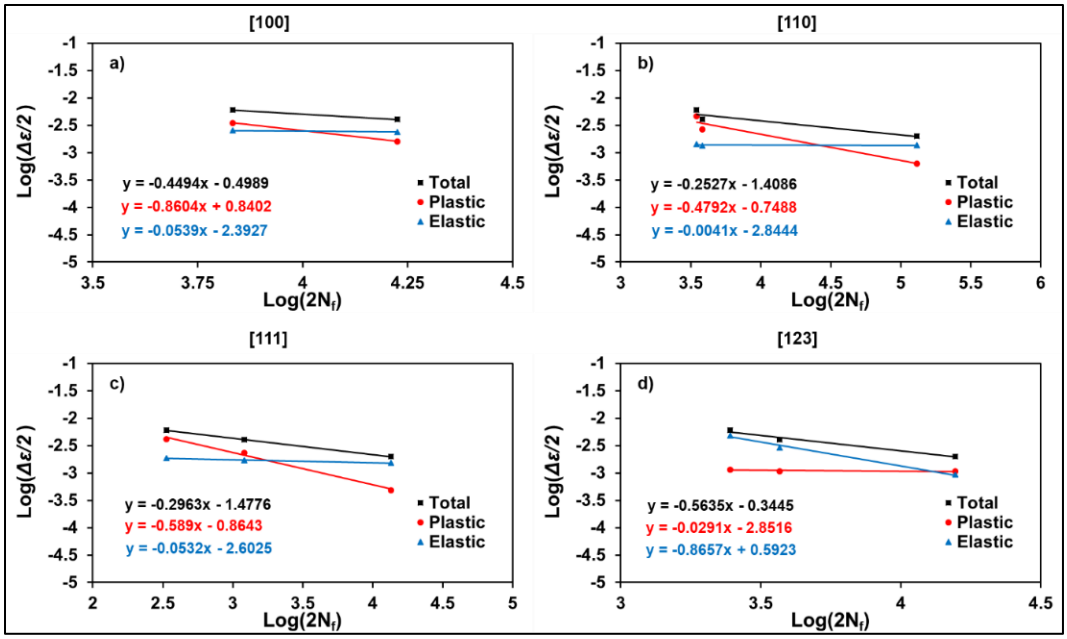

Figure 7.6 Cyclic total strain, plastic strain, and elastic strain amplitude-fatigue life response of the $Fe_{50}Mn_{30}Co_9Cr_9$+2 at.% C single crystalline HEA for (a) [100], (b) [110], (c) [111] and (d) [123] orientation.

Besides analysis of the cyclic performance of $Fe_{50}Mn_{30}Co_9Cr_9$+2 at.% single crystal HEA based on CDRs, evolution of plastic strain range and half-life hysteresis loops, the fatigue properties of a material can be described by the Basquin-Coffin-Manson relationship [206,207], given by equation (1):

$$\frac{\Delta\varepsilon_t}{2} = \frac{\Delta\varepsilon_e}{2} + \frac{\Delta\varepsilon_p}{2} = \frac{\sigma'_f\,(2N_f)^b}{E} + \varepsilon'_f\,(2N_f)^c \qquad (7.1)$$

Accordingly, the total strain amplitude is resolved into elastic strain amplitude and plastic strain amplitude, where $2N_f$ is the number of cycles to failure, E is Young's modulus (E_{100} = 115±20 GPa / E_{110} = 218±20 GPa / E_{111} = 320±20 GPa / E_{123} = 230±20 GPa as determined from the results of tensile testing, cf. section 3.1), σ'_f the fatigue strength

coefficient, ε'_f the fatigue ductility coefficient, b the fatigue strength exponent and c the fatigue ductility exponent. In addition, the relation between stress amplitude and plastic strain can be assessed based on the power-law equation given by equation (2) [206]:

$$\frac{\Delta\sigma}{2} = K'\left(\frac{\Delta\varepsilon_p}{2}\right)^{n'} \tag{7.2}$$

where $\frac{\Delta\sigma}{2}$ is the half-life stress amplitude, K' the cyclic strength coefficient, $\frac{\Delta\varepsilon_p}{2}$ the half-life plastic strain amplitude, and n' the cyclic strain-hardening exponent. **Fig. 7.6** shows total strain, plastic strain and elastic strain amplitudes plotted against the number of cycles to failure $2N_f$ in a double logarithmic diagram as well as the corresponding trend lines for the [100] (a), [110] (b), [111] (c) and [123] orientation (d), respectively. In order to guarantee a state of cyclic saturation, half-life stresses and strains were considered for evaluation of data. The transition life $2N_t$, corresponds to the time during fatigue, i.e., the number of cycles, at which elastic and plastic strain amplitudes are equal and can thus, be determined by the point of intersection for the curves being representative for the elastic and plastic strain amplitudes. Above N_t damage is dominated by elasticity whereas at lower fatigue lives plasticity dominates [208]. From the results shown in **Fig. 7.6** the transition lives in the current study can be determined as 10.065, 25.754, 1.547 and 13.078 cycles for the [100], [110], [111] and [123], respectively. Additionally, the corresponding total strain amplitude values can be calculated as 0,50%, 0,30%, 0,36% and 0,22%. In other words, the following conclusion can be drawn from the trend lines presented in **Fig. 7.6**. For the total strain amplitudes considered in this study, a change of elementary mechanisms contributing to damage and failure sets in the transition area between the low

and medium strain amplitude for [110] and [111] orientation. In contrast, these mechanisms are mostly dominated by elasticity for [100] whereas they are almost completely dominated by plasticity for [123].

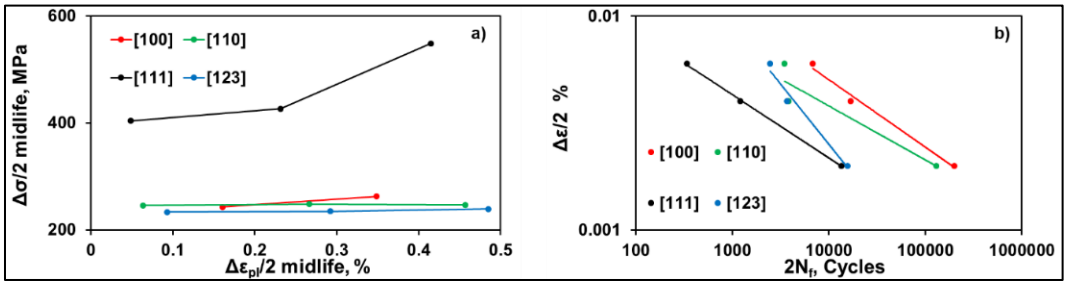

Figure 7.7 (a) Plastic strain–stress relationship and b) total strain-life fatigue data of the $Fe_{50}Mn_{30}Co_9Cr_9$+2 at.% C single crystalline HEA for all orientations considered.

Fig. 7.7a represents a plot of the half-life stress amplitude as a function of the half-life plastic strain amplitude for all orientations of the single crystal HEA considered. According to the power-law relation given in **Eq. 7.2**, the values of the cyclic strain-hardening exponent n′ and the cyclic strength coefficient K′ were determined using the method of least squares. Together with the coefficients obtained from **Eq. 7.1**, these values are recapitulated in **Table 7.1** for all orientations studied, establishing an initial basis for the evaluation of the fatigue properties of a single crystal HEA in different orientations. Additionally, all results shown are summarized by the strain-life fatigue data as visualized in **Fig. 7b**, demonstrating that the best and worst LCF fatigue performances are revealed by the [100] and [111] orientation, respectively.

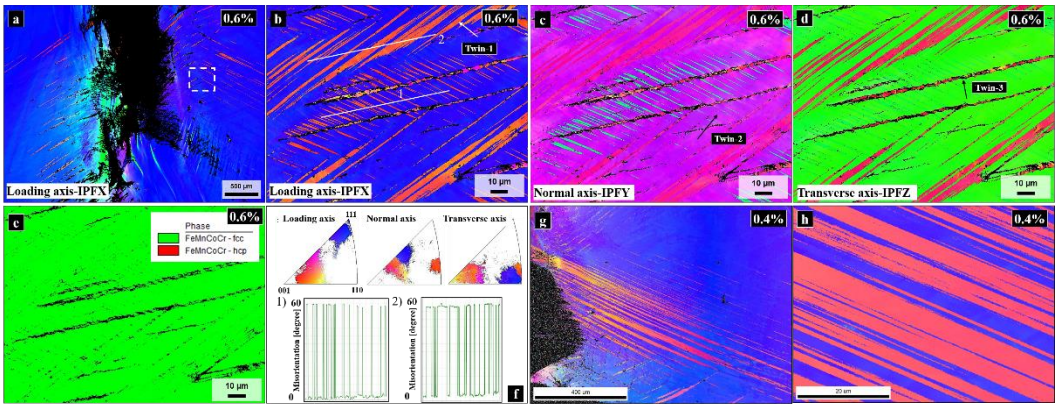

Figure 7.8 EBSD maps of the [111] oriented single crystalline $Fe_{50}Mn_{30}Co_9Cr_9$ +2 at.% C HEA, recorded before deformation and at the cyclic crack of the specimen cycled at $\Delta\varepsilon_t/2$ = 0.6 %. (a) overall EBSD IPFX (loading direction) map at the crack region after cyclic loading, (d) higher magnification of (c), which marked with a white rectangular in (b), (c) EBSD IPFY (normal axis) map, (d) EBSD IPFZ (transverse axis) map, (e) phase map, (f) corresponding inverse pole figures and misorientation profiles along the two lines marked in (b). EBSD maps of the [111] oriented single crystalline $Fe_{50}Mn_{30}Co_9Cr_9$ +2 at.% C HEA, recorded before deformation and at the cyclic crack of the specimen cycled at $\Delta\varepsilon_t/2$ = 0.6 %. (g) overall EBSD IPFX map after cyclic deformation, (h) higher magnification of (g).

7.4. Microstructure Investigations

EBSD experiments were performed to explore the microstructural evolution of single crystals cycled to failure at $\Delta\varepsilon_t/2 = \pm 0.6$ % and $\Delta\varepsilon_t/2 = \pm 0.4$ %, since the most significant differences with respect to CDRs and half-life hysteresis loops were observed between these strain amplitudes (**Figs. 7.2 and 7.4**). EBSD micrographs clearly reveal the presence of three different twinning systems in the [111]-oriented single crystal after LCF deformation at $\Delta\varepsilon_t/2 = \pm 0.6$ %, while two different twinning system were detected at $\Delta\varepsilon_t/2 = \pm 0.4$ % in **Fig. 7.8.** After initial cyclic loading the CDR at $\Delta\varepsilon_t/2 = \pm 0.4$ % (**Fig. 7.2**) is characterized by cyclic softening while slight cyclic hardening was observed at $\Delta\varepsilon_t/2 = \pm 0.6$ %. The cyclic softening or hardening is associated with the microstructural

evolution. The generation of the dislocations and their interactions at stages of initial cyclic loading is responsible for the initial cyclic hardening [202]. If the dislocation generation rate is same with the annihilation of dislocations, cyclic stress can be stabilized. Finally, cyclic softening can be seen when the annihilation rate is higher than the dislocation generation rate. It is known that the rate of the dislocation annihilation increases with increasing cycle number.

Therefore, the initial cyclic hardening in the [111] oriented specimen at $\Delta\varepsilon_t/2 = \pm 0.6$ % can be attributed to extensive dislocation and twinning activity that acts as barriers to further dislocation motion, which contributes to hardening capability of the material [89,147]. However, the EBSD micrographs showed extensive twinning activity in the [111] specimens at $\Delta\varepsilon_t/2 = \pm 0.4$ % after cyclic failure, although it presented cyclic softening after initial cyclic loading. Therefore, twinning cannot be only the reason for the cyclic hardening observed after initial cyclic loading at $\Delta\varepsilon_t/2 = \pm 0.6$ %. The half-life hysteresis loop of the [111] orientation at $\Delta\varepsilon_t/2 = \pm 0.6$ % showed that DSA dominated cyclic deformation as well as twining. This indicates that the main reason for the cyclic hardening at $\Delta\varepsilon_t/2 = \pm 0.6$ % can be referred to the DSA effects seen.

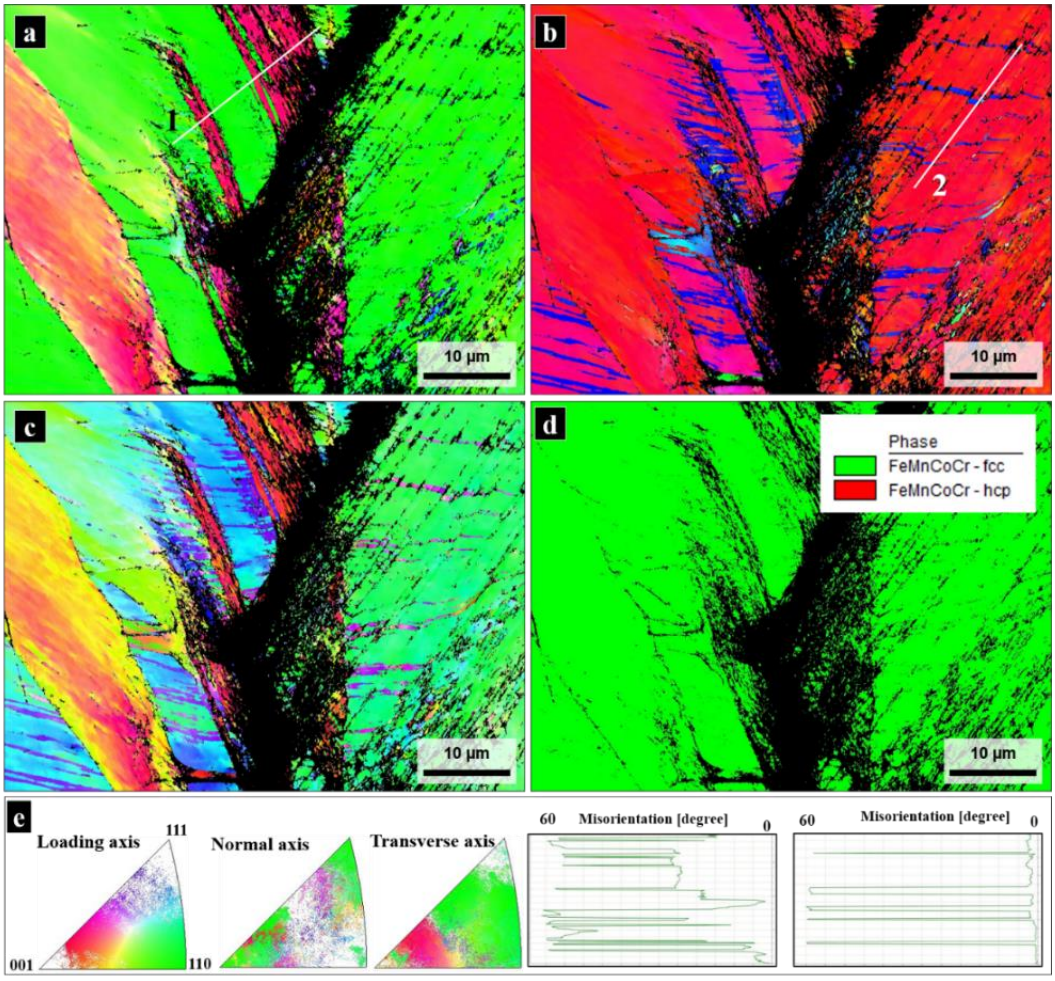

Figure 7.9 EBSD maps of the [110] oriented single crystalline $Fe_{50}Mn_{30}Co_9Cr_9$ +2 at.% C HEA, recorded at the cyclic crack region of the specimen cycled at $\Delta\varepsilon_t/2$ = 0.6 %. (a) overall EBSD IPFX (loading direction) map at the crack region after cyclic loading, (d) higher magnification of (c), which marked with a white rectangular in (b), (c) EBSD IPFY (normal axis) map, (d) EBSD IPFZ (transverse axis) map, (e) corresponding inverse pole figures and misorientation profiles along the two lines marked in (a and b).

As shown in **Fig. 7.2**, the lowest cyclic fatigue life was seen in the [111] oriented specimen due to higher the higher stress amplitude developed during cyclic deformation displaying DSA. This was mainly because of the higher accumulate plastic damage in this

case (**Fig. 7.4**) since the accumulative plastic damage is higher than that of other orientations at the same strain amplitudes. At the $\Delta\varepsilon_t/2 = \pm 0.6$ % strain amplitude, DSA also promoted the non-uniform deformation leading to local plastic deformation and decreasing the fatigue resistance [209]. Furthermore, although the activation of twinning contributes to initial cyclic hardening, it can also accelerate the dislocation annihilation process by acting as barriers to further dislocation motion, subsequently causing cyclic softening. However, the DSA regime activated by higher stress amplitude in the [111] orientations at $\Delta\varepsilon_t/2 = \pm 0.6$ causes cyclic hardening.

Table 7.1 Low-cycle fatigue parameters of the $Fe_{50}Mn_{30}Co_9Cr_9$+2 at.% C HEA

Orientation	**K′, MPa**	**n′**	$\boldsymbol{\sigma'_f}$**, MPa**	**b**	$\boldsymbol{\varepsilon'_f}$	**c**	$\boldsymbol{2N_t}$
[100]	291.76	0.100	465.58	-0.054	6.921	-0.860	10.055
[110]	247.98	0.003	311.93	-0.004	0.178	-0.479	25.754
[111]	278.83	0.133	799.19	-0.053	0.137	-0.589	1.754
[123]	240.29	0.014	323.69	-0.029	3.911	-0.866	13.078

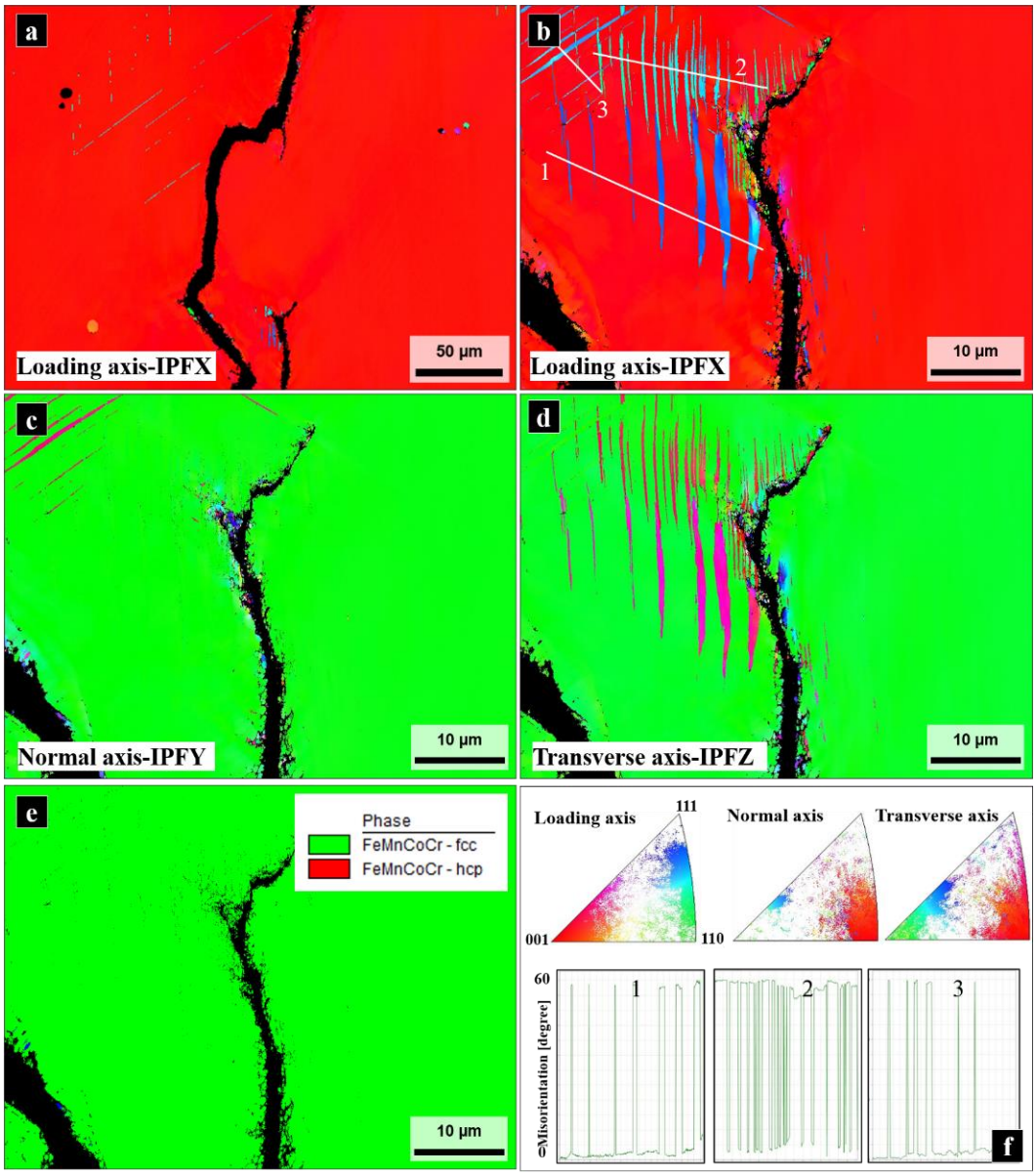

Figure 7.10 EBSD maps of the [110] oriented single crystalline $Fe_{50}Mn_{30}Co_9Cr_9$ +2 at.% C HEA, recorded at the cyclic crack region of the specimen cycled at $\Delta\varepsilon_t/2$ = 0.6 %. (a) overall EBSD IPFX (loading direction) map at the crack region after cyclic loading, (d) higher magnification of (c), which marked with a white rectangular in (b), (c) EBSD IPFY (normal axis) map, (d) EBSD IPFZ (transverse axis) map, (e) phase map, (f) corresponding inverse pole figures and misorientation profiles along the three lines marked in (b).

The degree of dissociation of a full dislocation is the main reason for the nucleation of twinning in low SFE materials [54]. However, the twinning formation also depends on the full dislocation`s velocity and the direction of the axial stress [54,144,163]. For example, in tension near the [111] and [110] orientation, glide dislocations are completely dissociated at moderately high velocities in alloys when stacking fault energy is low enough, while glide dislocations are as opposed to being separated into partials at higher velocities such as in the interstitial free [001] orientations under tensile loading, and cross-slip is preferred [32,143]. In compression near the [111] orientation, however, glide dislocations constrict (as opposed to being separated into partials) at high velocities so that their cores may overlap. Similar to the [111]-oriented specimen, EBSD micrographs exhibited deformation twinning in the [001]-, [110]- and [123] oriented specimens cycled at $\Delta\varepsilon_t/2$ = 0.6 % (**Fig. 7.9-11**). However, the twinning density in the [111]-oriented specimens is relatively higher than the [110], [110]- and [123] orientations owing to the higher number of active twin systems and higher stress level at the same strain amplitudes. Here, there are two options to activate the deformation twinning in all orientations: (1) the addition of interstitial C restricts the full dislocations to activate the cross slip [54] and (2) push-pull loading enables to promote planar-slip and perfect dislocation dissociation into partial dislocations in all orientations as proposed in a previous study [57].

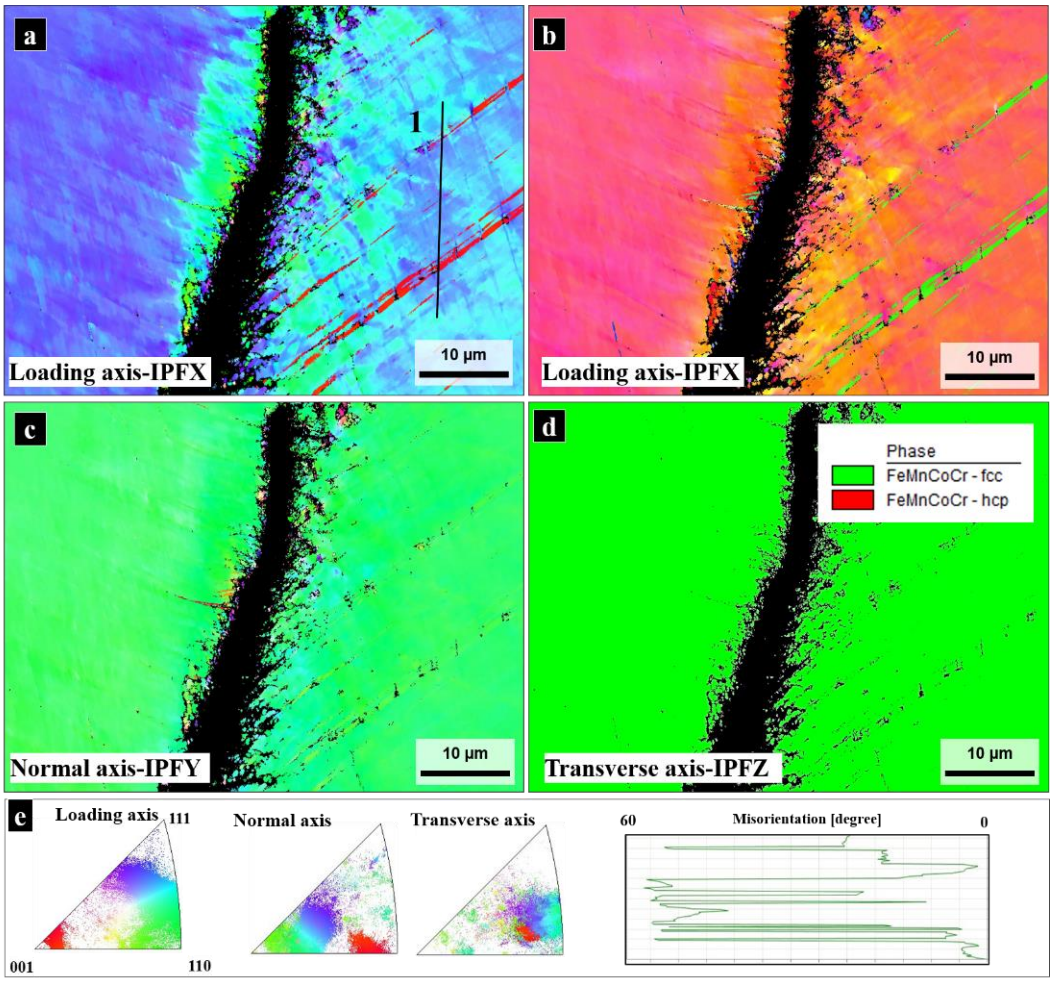

Figure 7.11 EBSD maps of the [123] oriented single crystalline $Fe_{50}Mn_{30}Co_9Cr_9$ +2 at.% C HEA, recorded at the cyclic crack region of the specimen cycled at $\Delta\varepsilon_t/2$ = 0.6 %. (a) overall EBSD IPFX (loading direction) map at the crack region after cyclic loading, (b) EBSD IPFY (normal axis) map, (c) EBSD IPFZ (transverse axis) map, (d) phase map, (e) corresponding inverse pole figure and misorientation profiles along the line marked in (a).

Interestingly, a saturation state of the stress amplitude is observed after the initial cyclic hardening in the [001] orientation at the highest total strain amplitude of $\Delta\varepsilon_t$ = ± 0.6, whereas a slight cyclic hardening is clearly seen at the end of the test. This cyclic

hardening behavior can be deducted to the activation of the tertiary twin system (**Fig. 7.10**).

Fracture surfaces of fatigued single crystals at the highest and lowest strain amplitudes are displayed in **Fig. 7.12 and Fig. 7.13**. Although the origins of fatigue cracks were not found for all specimens, according to **Figs. 7.12 and 7.13**, fatigue cracks were distinguished to be initiated from subsurface defects in some of the specimens. Defects e.g. pores and inclusions are the main reason for the initiation of these near-surface cracks [210]. During cyclic deformation, stress concentration can occur in the vicinities of observed inclusions causing decohesion of inclusion-matrix interface eventually promoting crack initiation [211]. A mixed-mode fracture morphology containing ductile and brittle features was observed on the fracture surfaces. Cleavage surfaces and dimple-like facets are indications of brittle and ductile fractures, respectively. Depth and size of dimples do not show a strong dependency on the fatigue strain amplitudes and crystal orientations. However, comparing cleavage surfaces observed in different crystal orientations suggests that the areas of cleavage surfaces are smaller in the [111]-oriented specimen. This can be attributed to the higher twin activities in this specimen which suppresses a brittle fracture. Considering other orientations, it can also be deduced that [001]-oriented specimen exhibits a large crack propagation area at a strain amplitude of $\Delta\varepsilon_t/2 = 0.6$ in comparison with [001] and [123] crystallographic orientations which is in line with its higher fatigue life. Large fatigue crack propagation area is an indication of a high number of cycles to failure and eventually superior fatigue performance [212]. It is

worth noting that inclusions were seen on the fracture surfaces of all examined specimens. Inclusions were found to make the specimens prone to crack initiation [213,214]. Inclusion/matrix interface decohesion can lead to the nucleation of microcracks as highlighted in **Fig. 7.12** for the [100] orientation. Fracture analysis implies that the sizes of observed inclusions are independent of crystal orientation.

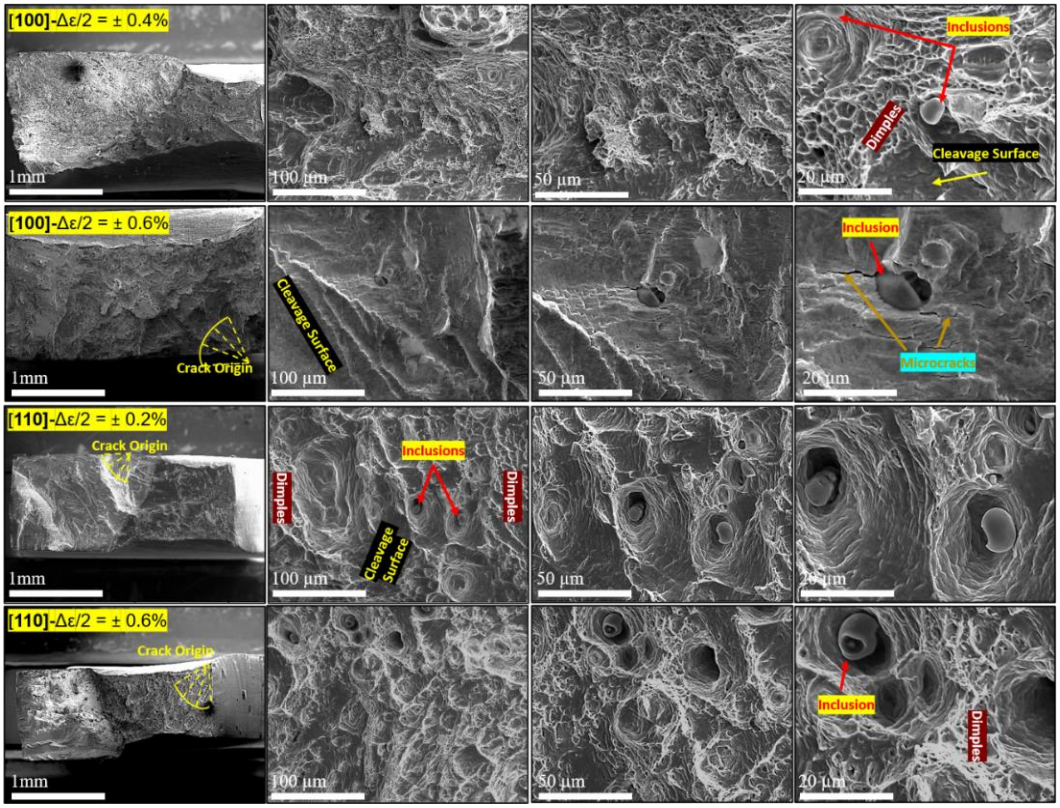

Figure 7.12 Fracture surfaces of $Fe_{50}Mn_{30}Co_9Cr_9$ +2 at.% C high entropy alloy in single crystals fatigued at different strain amplitudes. Higher magnifications of fracture are displayed to the right.

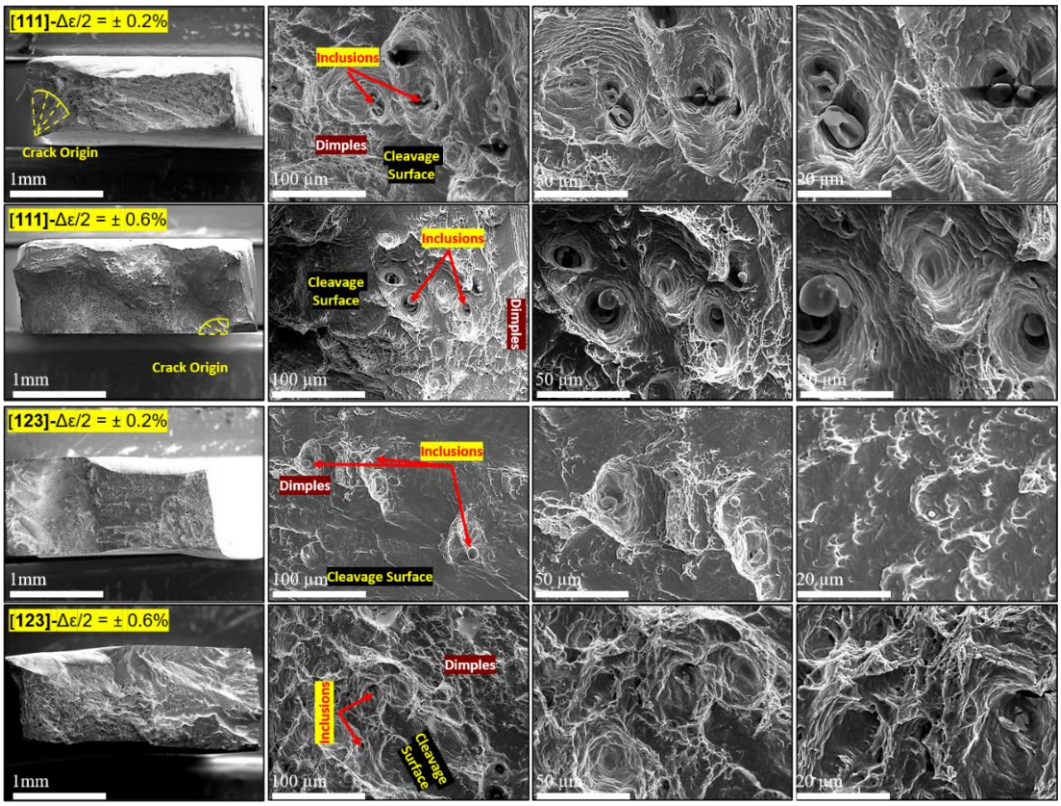

Figure 7.13 Fracture surfaces of [111] and [123] oriented single crystalline $Fe_{50}Mn_{30}Co_9Cr_9$ +2 at.% C HEAs fatigued at different strain amplitudes. Higher magnifications of fracture are displayed to the right.

7.5. Summary and Conclusions

The orientation dependence on the low-cycle fatigue behavior at a wide range of strain amplitudes (0.2%, 0.4% and 0.6%) and monotonic tension responses of the non-equiatomic $Fe_{50}Mn_{30}Co_9Cr_9$ +2 at.% C HEA single crystals oriented along the [111], [110], [001] and [123] crystallographic orientations were investigated. EBSD experiments were utilized to explore the microstructural evolution after low cycle fatigue experiments

to investigate the strain hardening/softening behavior. Key findings can be summarized as follows:

1. An exceptionally strong single phase $Fe_{50}Mn_{30}Co_9Cr_9$ +2 at.% HEA was obtained by C interstitial. Tension experiments demonstrated that the CRSS of $Fe_{50}Mn_{30}Co_9Cr_9$ +2 at.% (110±5) was over 2 times higher than single phase fcc $Fe_{40}Mn_{40}Co_{10}Cr_{10}$ HEA (τ_{cr}^{sl}=53±2 MPa [89]) and NiCoCr MEA (τ_{cr}^{sl}=63±3 MPa [3]).
2. Cyclic deformation responses of single crystals under monotonic and non-monotonic loading differ from each other in the $Fe_{50}Mn_{30}Co_9Cr_9$ +2 at.% similar to recent studies in polycrystalline HEAs [57,105].
3. The cyclic deformation response under low-cycle fatigue at room temperature demonstrate strong orientation dependence in $Fe_{50}Mn_{30}Co_9Cr_9$ +2 at.% C HEA. While the [001], [110] and [123] orientations feature cyclic softening after initial cyclic loading at all amplitudes, the [111] orientation demonstrates only cyclic hardening at $\Delta\varepsilon_t/2$ = 0.6 %. This unusual cyclic hardening was attributed to the DSA regime at $\Delta\varepsilon_t/2$ = 0.6 % in the [111] orientations.
4. The lowest fatigue life was detected in the [111] orientations at $\Delta\varepsilon_t/2$ = 0.6 % due to higher stress amplitude and the DSA regime.
5. The activation of twinning in the current single crystals under cyclic loading were orientation independent but the volume fraction of the twinning was orientation dependent according to active twinning system in the corresponding orientations.

6. Fracture analysis revealed that fatigue cracks were initiated from subsurface defects. Inclusions were detected on the fracture surfaces of all conditions which may cause the initiation of cracks due to the stress concentration in their vicinities. Different deformation mechanisms in [111] orientation i.e. twin activities resulted in smaller areas of cleavage surfaces compared with other orientations.

8. ON THE LOW CYCLE FATIGUE RESPONSE OF CoCrNiFeMn HIGH ENTROPY ALLOY WITH ULTRA-FINE GRAIN STRUCTURE[9]

The LCF behavior of UFG HEAs processed by ECAP in order to assess their structural integrity was studied in this chapter. Moreover, the transient behavior, i.e., softening or hardening, of HEAs under cyclic loading needs to be studied in the LCF regime to shed light on the nature of the most detrimental mechanisms leading to cyclic degradation. Therefore, the present study focuses on the LCF experiments conducted at room temperature for CoCrFeMnNi HEA with various initial microstructural conditions, i.e., coarse grained (achieved via hot extrusion) and ECAP processed. Three different strain amplitudes were considered to investigate the microstructural evolution under high-load cycling. The microstructural evolution was evaluated using X-ray diffraction (XRD), electron backscatter diffraction (EBSD) and transmission electron microscopy (TEM). It was found that the grain refinement by ECAP considerably improved the fatigue life at the lowest strain amplitude, however, CG samples showed superior fatigue life at higher strain amplitudes. The lower fatigue life of the ECAP samples at high strain amplitudes is attributed to the higher stress amplitudes imposed by grain refinement, cyclic softening as

[9] Reprinted with permission from "On the low-cycle fatigue response of CoCrNiFeMn high entropy alloy with ultra-fine grain structure" PICAK S, Wegener T, Sajadifar SV, Sabero C, Ritcher J, Kim H, Niendorf T, Karaman I, 2021. Acta Materialia, 205, pp. 116540, Copyright 2021 by Acta Materialia Inc. published by Elsevier Ltd.

well as damage localization. It is shown that the hardening behavior is governed by the generation of dislocations, annihilation of dislocations and subsequently the formation of cell structures. Moreover, the formation of the cell structure under cyclic loading is rationalized using the Copley-Kear effect [54]. In summary, the present study aims at improving fundamental understanding of the processing-structure-property relationships of CoCrFeMnNi HEA in three major areas, namely: (i) microstructural evolution upon SPD, in particular ECAP, (ii) microstructural evolution during LCF loading, and (iii) elementary mechanisms promoting the different hardening behavior of HEAs under monotonic and cycling loading.

8.1. Methodology

The CoCrFeMnNi equiatomic HEA studied in the present work was fabricated using vacuum induction melting of high purity constituents in the form of a cylindrical rod with 7.62 cm diameter and 50.8 cm length. The as-cast billet, encapsulated in a mild-steel can, was first subjected to hot extrusion at 900^{o}C to remove impurities and voids caused by casting. The diameter of the billet was reduced from 7.62 cm to 3.175 cm during hot extrusion. Part of the hot-extruded (HE) billet was then exposed to ECAP following route 2C at 300^{o}C in order to increase the density of stored dislocations, and as a result, achieve significant grain refinement. The HE billet was machined down to a 25×25 mm^2 cross-section and cut into 17.78 cm length samples before ECAP. After each ECAP pass, the billet was water quenched to room temperature to maintain the microstructure induced

by ECAP. The extrusion rate was 7.62 mm / min. The die temperature was kept at 300°C ± 10°C throughout the process. The ECAP process is schematically depicted with inverse pole figure (IPF) maps of as-cast, hot extruded and ECAP processed CoCrFeMnNi HEA in **Fig. 8.1**. Route C, used in this study for ECAP, involves a +180° rotation between each pass. The total strain as a result of ECAP after 2 passes is 2.3, and the cumulative strain due to hot extrusion and ECAP is 3.4.

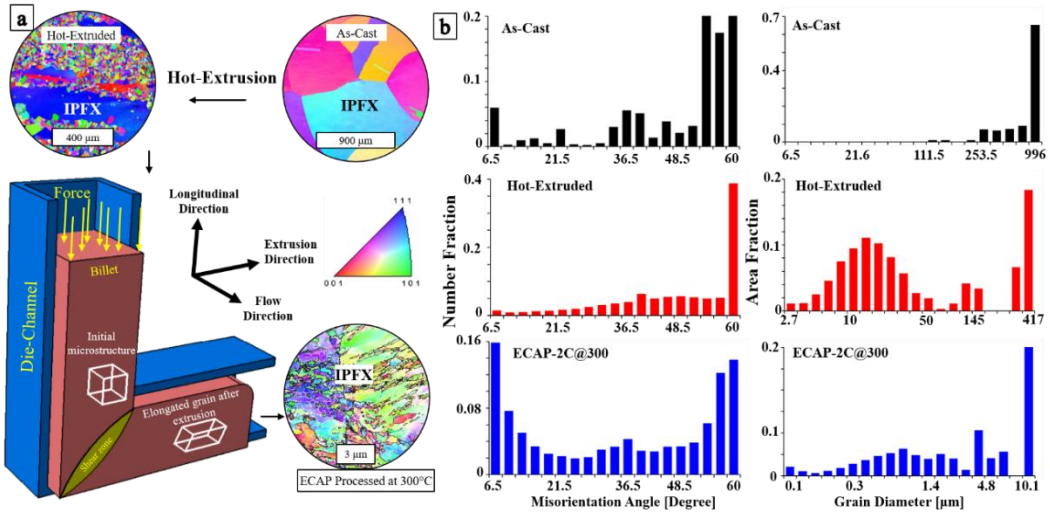

Figure 8.1 (a) Schematic of the ECAP processing depicting the relevant directions of the billet after the process, and orientation mapping, obtained through electron back scatter diffraction (EBSD) imaging, of CoCrFeMnNi high entropy alloy, (b) the histograms of the grain boundary misorientation angles and grain diameters of the EBSD micrographs shown in (a).

Dog-bone shaped tension samples with a gauge section of 8 mm x 1.2 mm × 3 mm, as well as rectangular prism shaped compression samples with the dimension of 4 mm × 4 mm × 8 mm were cut from the as-cast, HE and ECAP billets using wire electrical

discharge machining (EDM). Tension and compression experiments were performed using an MTS servo-hydraulic test frame. Tungsten carbide platens were used during the compression tests. To minimize the friction, thick teflon tapes were used between the sample and platens during compression tests. An extensometer was directly attached to the samples to record the axial strain. The tension samples were strained up to failure at a rate of 5×10^{-4} s^{-1}, while the compression samples were loaded up to 10% strain, using the same strain rate, in order to rule out the possibility of barreling and buckling. All experiments were repeated three to five times on companion samples to assure the repeatability.

The low-cycle fatigue experiments were conducted on flat dog bone shape specimens with a nominal gauge section of 8 mm × 3 mm × 1.2 mm using a digitally controlled servo-hydraulic load frame in fully reversed push-pull loading (R = -1) in total strain control. A miniature extensometer featuring a gauge length of 5 mm was attached directly to the samples to control the strain amplitude during cyclic loading. The nominal strain rate in all tests was 6×10^{-3} s^{-1}, and total strain amplitudes of $\Delta\varepsilon_t/2 = \pm 0.2$ %, ± 0.4 %, and ± 0.6% were considered, resulting in test frequencies of 0.75 Hz, 0.375 Hz, and 0.25 Hz, respectively. Moreover, a symmetrical triangular waveform was used for loading. It should be noted that the strain was increased stepwise in the very first cycles in order to avoid buckling of the samples. Therefore, the final strain levels were reached after 25 to 75 cycles depending on the actual strain amplitude.

All samples used for mechanical testing were polished down to 1200 grit SiC paper before testing. For microstructure analysis, the samples were further polished for 24h using colloidal silica suspension (0.04 μm) employing a VibroMet 2 vibratory polisher unit. EBSD analysis was conducted using a Zeiss ULTRA GEMINI high resolution scanning electron microscope (SEM) at an accelerating voltage of 20 kV. For EBSD measurements, a 120 μm aperture as well as the high current mode were used, resulting in a probe current of 8 nA. Step sizes and tilt angle were 50 nm and 70°, respectively. Kernel average misorientation (KAM) maps were obtained using only the perimeter based on a 50 nm step size and a kernel size of 50 nm (1st nearest neighbor). KAM shows the mean misorientation angle between the selected pixel and its third nearest neighbors (misorientations above 5° are excluded from the calculation of KAM so as to avoid grain boundaries contributing to the map). XRD measurements were conducted for phase and texture analysis. XRD pole figures and diffractograms were determined using a Seifert Analytical X-Ray diffractometer operated at 35 kV and 30 mA equipped with a Mn tube (Kα1/Kα2 lines) and a monochromator.

TEM foils were prepared through initial mechanical polishing of slices down to 0.1 mm, followed by punching of foils with a diameter of 3 mm. Foils were finally twin-jet electropolished using 20 vol. % HNO_3 in a methanol solution at -20ºC. All TEM studies were performed using a FEI Tecnai G2 F20 electron microscope operated at 200V.

8.2. Microstructure evolution in CoCrFeMnNi HEA upon Hot Extrusion and ECAP processing

EBSD images of the HE and ECAP samples are displayed in **Fig. 8.2**. In the HE condition, the image quality map reveals that the majority of grains are separated by high angle grain boundaries (HAGBs) (Fig. 2a) as can be deduced from the different grey color levels of adjacent grains. The microstructure of the HE sample can be characterized as a bimodal microstructure consisting of very fine equiaxed, dynamically recrystallized grains and coarse, non-recrystallized grains (**Fig. 8.2b**). KAM maps reveal that the density of geometrically necessary dislocations, which are the ones that can promote lattice rotations, is higher in the columnar grains as compared to those of the fine recrystallized grains, attesting the occurrence of inhomogeneous recrystallization during the hot extrusion process (**Fig. 8.2c**).

After 2 passes of ECAP, the former bimodal microstructure of the HE condition is transformed into an UFG microstructure. Analysis of grain sizes, considering both low-angle grain boundaries (LAGBs) and HAGBs in EBSD, demonstrates many grains with sizes below 1 μm (**Fig. 8.2d-e**). Further analysis of microstructure evolution by TEM, which has been already proven to lead to different results in terms of grain size evaluation due to differences in microstructural characteristics being employed for analysis [215], will clearly reveal the existence of sub-micron grains in Section 8.6. It is important to note that ECAP is known to promote the formation of a very high density of substructures in the present high entropy alloy [75].

Depending on the local misorientation, these structures are referred to as High-Density Dislocation Walls (HDDWs) and cell-structures or LAGBs in many studies reporting on microstructure evolution in UFG materials and, eventually, are the basis for the evolution of HAGBs upon imposing a higher number of ECAP passes [73,121,216]. The KAM map in **Fig. 8.2f** indicates that a high density of these substructures prevails in the HEA studied in present work as well. Furthermore, the microstructure in general is much more homogenous after the ECAP process than the microstructure of the HE sample.

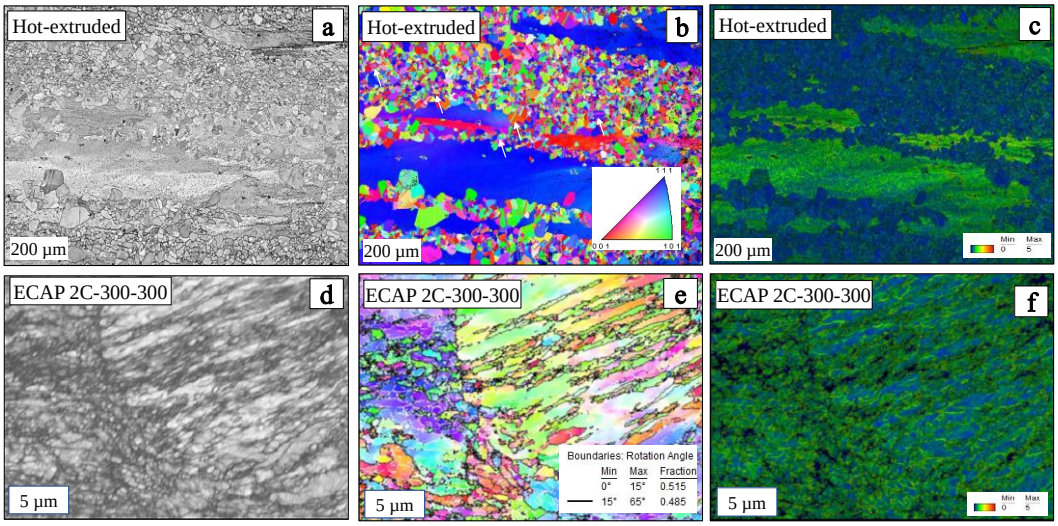

Figure 8.2 Microstructural characterization, through electron back scatter diffraction (EBSD) imaging, of CoCrFeMnNi high entropy alloy after hot extrusion at 900°C (a, b, c, imaged on the longitudinal plane) and Equal Channel Angular Pressing (ECAP) at 300°C using route 2C (d, e, f, imaged on the plane perpendicular to the flow direction in Figure 1). (a, d) image quality maps, (b, e) inverse pole figure (IPF) maps, (c, f) Kernel Average Misorientation (KAM) maps of the same locations in the hot extruded and ECAP processed billets. The inverse pole figure inset in (b) represents the orientation colors. Step sizes of EBSD scanning were 50 nm.

8.3. Uniaxial Tensile and Compression Deformation Responses

Tensile and compression experiments were conducted on the as-cast, HE and ECAP samples at room temperature. The important parameters determined from the experiments are summarized in **Table 8.1**. The as-cast samples are very ductile showing elongation at fracture as large as 40% (**Fig. 8.3**). The yield strength (YS) and the ultimate tensile strength (UTS) of the as-cast material were determined to be 153±5 MPa and 502±5 MPa, respectively. The HE samples have a higher YS (255±5 MPa) and UTS (800±6 MPa) and are also very ductile (elongation at fracture ≈38%). The UFG microstructure upon ECAP processing substantially increases the YS. However, strain hardening upon yielding is hardly seen such that UTS (1025±10 MPa) is only marginally higher than the YS. Clearly, increase in strength is at the expense of strain hardening capability and ductility.

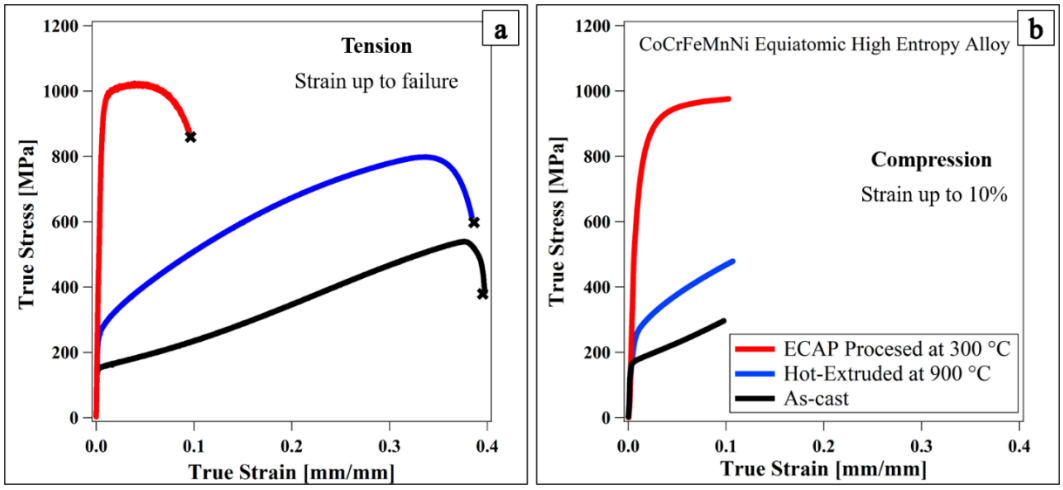

Figure 8.3 (a) The room temperature true stress-true strain response of CoCrFeMnNi high entropy alloy under (a) tension and (b) compression in as-cast, hot extruded and ECAP processed conditions.

Although the ECAP HEA samples in the present work revealed lower ductility as compared to the HE condition, the plastic deformation capability is still significant (elongation at fracture ≈10 %). The compression test results revealed that the yield strength values were almost the same as those under tension in as-cast and HE conditions but not in the ECAP sample implying the presence a of tension/compression asymmetry.

Tension/compression asymmetry is usually observed if the as-processed microstructure shows strong texture and oriented internal stresses after ECAP processing [66–68] or in the cases where deformation mechanisms such as twinning significantly contribute to the overall deformation [217–219]. Haouaoui *et al.* observed strong tension/compression asymmetry in UFG copper [67], which was attributed to dislocation polarity and back stress accumulation at grain boundaries dictated by the grain boundary evolution during ECAP. They showed that the grain boundary character governs the flow stress during the reversed straining. Their experimental observations pointed out that low-angle grain boundaries promote back stress leading to tension/compression asymmetry in UFG copper. EBSD and TEM observations (Section 9.7) in this study revealed that the majority of the boundaries have low misorientation angles in ECAP processed CoCrFeMnNi HEA. Pronounced twinning activity was not evident to rationalize the observed tension/compression asymmetry. Moreover, the texture measurements conducted in present work confirmed the lack of a pronounced texture effect, which will be presented in Section 9.8. Thus, it is assumed that the observed tension/compression

asymmetry in **Fig. 8.3** can be attributed to the back stress accumulation during ECAP at grain boundaries.

Table 8.1 Experimental values of the yield strength, ultimate tensile strength and elongation at failure for CoCrFeMnNi HEA under tension and compression (only yield strength is reported) in as-cast, hot extruded, and ECAP processed conditions. To determine the yield strength values, 0.2% offset strain criterion was used. The results present the average of the test results from 3 to 5 companion samples.

	$\sigma_y^{Compression}$ (MPa)	$\sigma_y^{Tension}$ (MPa)	σ_{UTS} (MPa)	$\varepsilon_{elongation\ at\ fa}$ (%)
As-Cast CoCrFeMnNi HEA	152±5	150±5	540±5	40±2
Hot-Extruded CoCrFeMnNi HEA	265±10	255±10	800±6	38±2
ECAP CoCrFeMnNi HEA	760±10	925±10	1025±10	10±2

The strengthening mechanisms in the present HEA can be separated into three categories: solid solution hardening, grain boundary hardening, and dislocation density hardening. Dislocation slip starts when obstacles, such as lattice resistance (σ_o), grain boundaries (σ_{GB}) and the pre-existing dislocations (σ_D), as induced by pre-deformation, are overcome. The critical stress for yielding in the as-processed materials can be attributed to the sum of the contributions from these strengthening mechanisms. The as-cast and HE samples in **Fig. 8.3** are characterized by significant strain hardening, whereas a lack of hardening plateau and cyclic softening at various strain amplitudes are seen in the ECAP samples. The limited strain hardening response of the ECAP sample can be attributed to the very high defect density prevailing in materials processed using ECAP [75,220]. In such cases, plastic deformation is governed through a balance between

dislocation recovery and dislocation generation under tensile loading as shown in [192,220].

8.4. Cyclic response of Hot Extruded and ECAP processed CoCrFeMnNi HEA

Fig. 8.4 displays the CDR of the HE and ECAP conditions for the three different strain amplitudes considered. In order to evaluate the reproducibility and variation in the LCF response, three experiments were carried out for each strain amplitude. Since the results did not show any pronounced scatter, only one curve for each strain amplitude is shown for the sake of brevity. The load was increased stepwise during the first 25 to 75 cycles (the number being dependent on the actual strain amplitude) to avoid buckling of the miniature samples. The CDR data are plotted starting from the 100^{th} cycle to eliminate the initial strain ramp region in order to avoid confusion. Irrespective of the processing route, the fatigue life is deteriorated with an increase in strain amplitude. Generally, high strain amplitudes promote rapid fatigue crack initiation and subsequent crack propagation, eventually leading to failure at relatively lower cycle numbers [94,129] due to an increased level of plastic deformation and, thus, higher energy dissipation per cycle.

Independent of the imposed strain amplitude, the stress level of the ECAP condition was higher than in the case of the HE condition (**Fig. 8.4**). Clearly, the differences in stress levels of ECAP and HE samples are most significant at higher strain amplitudes. This behavior can be rationalized based on the increased YS and UTS of the ECAP samples (**Fig. 8.3**) and will be further discussed below. The CDRs exhibit a saturation state of the stress amplitude (i.e. a lack of hardening) for the lowest amplitude

($\Delta\varepsilon_t/2$ = 0.2%) for both conditions (**Fig. 8.4**). With respect to the numbers of cycles to failure, the fatigue life of the ECAP condition is, with ≈ 80,000 cycles, two times higher than that of the HE counterpart (≈ 37,000 cycles). It is well-known that UFG materials exhibit a high resistance to crack initiation in both monotonic and cyclic regimes [73,112,122].

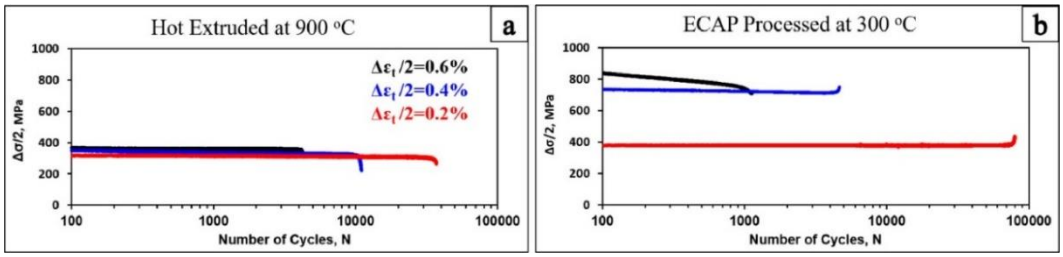

Figure 8.4 Cyclic deformation response of CoCrFeMnNi high entropy alloy in Hot-Extruded (a) and ECAP (b) conditions at the total strain amplitudes of $\Delta\varepsilon_t/2 = \pm 0.2\%$, $\Delta\varepsilon_t/2 = \pm 0.4\%$ and $\Delta\varepsilon_t/2 = \pm 0.6\%$.

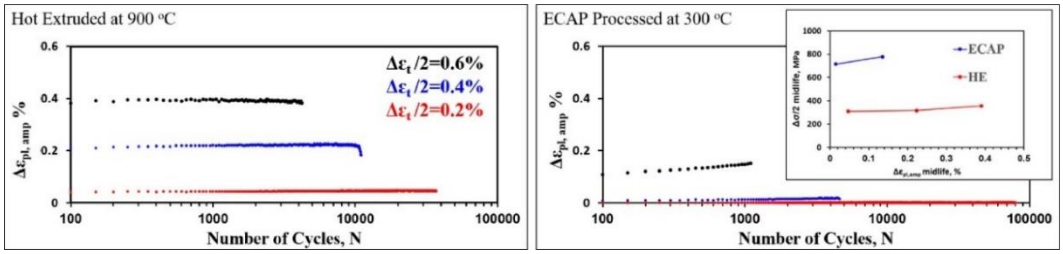

Figure 8.5 Cyclic plastic strain response of CoCrFeMnNi high entropy alloy in Hot-Extruded (a) and ECAP (b) conditions at the total strain amplitudes of $\Delta\varepsilon_t/2 = \pm 0.2\%$, $\Delta\varepsilon_t/2 = \pm 0.4\%$ and $\Delta\varepsilon_t/2 = \pm 0.6\%$. The inset in (b) shows a half-life stress versus half-life plastic strain amplitude plot (only tests with contribution to plastic strain were considered).

For the strain amplitude of $\Delta\varepsilon_t/2$ = 0.4 %, both conditions are still characterized by stable stress plateau (cyclic saturation state). Upon increasing the strain amplitude to $\Delta\varepsilon_t/2$

= 0.6 %, the HE condition still exhibits a stable CDR while the ECAP condition shows pronounced cyclic softening, indicating microstructural instability induced by cyclic plasticity, strain path changes and eventually re-arrangement of dislocation structures [73,112,113,122]. In-depth analysis of the evolution of microstructure will be detailed and discussed in the following section. Concerning the numbers of cycles to failure, the HE condition is superior to the ECAP condition for the 0.4 % as well as for the 0.6 % strain amplitudes. Obviously, cyclic plasticity is the major mechanism promoting both significant softening as well as deterioration of fatigue life.

As has been shown previously, microstructure homogeneity of ECAP processed materials is very important in terms of the fatigue response of UFG materials in the LCF regime [73,112,113,122]. Clusters of grains of similar orientation can be treated as micro-notches, promoting a local increase of stress and, thus, local cyclic plasticity as well as localized damage. Microstructure homogeneity can be directly related to the ECAP processing route employed, i.e. higher numbers of passes and higher number of strain path changes (being related to the rotation of the billet between consecutive passes) both lead to a more efficient grain refinement eventually promoting microstructure homogeneity [112,121,215]. In the present work, the HEA was processed using ECAP route 2C. As can be seen in the EBSD maps shown in **Figs. 2d-f**, the generally refined microstructure is clearly characterized by clusters of grains of very similar orientation. **Fig. 2e** highlights a sample area revealing the presence of a microstructural notch, i.e. a distinct line (vertical) between the bluish and the yellowish/greenish colored grains. Effects stemming from such

kind of microstructural heterogeneity are most pronounced under high-strain loading (LCF regime [112,121]) and in case of very high cycles to failure (very high-cycle fatigue (VHCF) regime [113]). Degradation of fatigue life and cyclic stability with an increase in strain amplitude was also reported for TWIP alloys and a CoCuFeMnNi HEA in conditions featuring micron-sized grains [94,104]. In TWIP steels monotonic pre-deformation led to dynamic grain refinement due to the onset of twinning and, thus, to the evolution of new boundaries impeding dislocation movement [98,217]. As in the case of UFG materials, cyclic plasticity, strain path changes, re-arrangement of dislocations as well as localization of damage were reported to be the most important factors for evaluation of the performance of these conditions in the LCF regime and, thus, could be used for rationalization of changes in the CDRs and fatigue lives in different conditions.

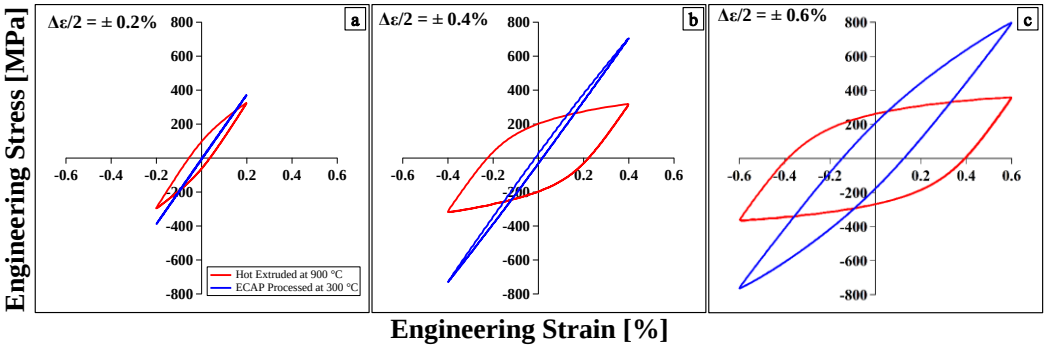

Figure 8.6 Half-life hysteresis loops of CoCrFeMnNi high entropy alloy in Hot-Extruded and ECAP conditions at the total strain amplitudes of $\Delta\varepsilon/2 = \pm 0.2\%$ (a), $\Delta\varepsilon/2 = \pm 0.4\%$ (b), and $\Delta\varepsilon/2 = \pm 0.6\%$ (c).

In the HE condition, the CDRs show a stable stress response as presented above, neither cyclic hardening nor softening occur. In perfect agreement, the plastic strain range is hardly changing in the course of cycling for all total strain amplitudes considered (**Fig. 8.5**). In this respect, pronounced cyclic plasticity in case of the HE condition can be directly deduced from the wide-opened half-life hysteresis loops depicted in **Fig. 8.6**. In the ECAP condition, the hysteresis for the 0.2% strain amplitude seems to be completely closed eventually indicating merely elastic strain at the macro level. A constant level of plastic strain, virtually equal to zero, is highlighted in **Fig. 8.5** as well. For higher strain amplitudes, cyclic softening is obvious in all CDRs obtained from the ECAP processed material. The increase in the plastic strain range fully supports the onset of cyclic softening already deduced from the stress response (**Fig. 8.4**).

The inset in **Fig. 5b** shows a plot of half-life stress versus half-life plastic strain amplitude as extracted from the data shown in **Figs. 8.4 and 8.5**. It has to be noted that only tests with plastic strain were considered. From the inset in **Fig. 8.5b**, a steady increase in the saturation stress level and ,thus, cyclic hardening between the different total strain amplitudes considered can be clearly observed for the HE as well as the ECAP conditions, being more pronounced for the latter condition.

In addition, less pronounced cyclic hardening in the HE condition can be attributed to a partial reversibility of deformation, as observed for different materials in literature [105,221]. The present results reveal that hardly any interaction of elementary deformation mechanisms seems to take place upon cycling. Still, tensile and compressive deformations

have to be accommodated. It is concluded, thus, that this deformation here can be only accommodated by some degree of reversible deformation. The experiments seem to promote a microplastic stage in the HE conditions that is devoid of significant interactions between the active deformation mechanisms. Thus, hardening effects seem to be impeded to some extent in the LCF regime probed, indicating at least partial reversibility of deformation as has been shown, as an example, for plasticity in Cu during bending [221].

Half-life hysteresis loops for the HE and ECAP conditions are illustrated in **Fig. 8.6**. By evaluating the half-life hysteresis loops, the cyclic response can be explained in more detail. The area of a hysteresis loop is a measure for the energy dissipation per cycle and is directly related to the plastic strain range, i.e. the maximum with of the hysteresis curve. Higher energy dissipation per cycle can be directly related to a more intense dislocation activity, eventually promoting rapid damage nucleation and adverse fatigue properties [101,217]. At $\Delta\varepsilon_t/2 = 0.2\%$, the hysteresis of the ECAP condition shows a fully elastic behavior without any sign of plastic strain. The maximum stress level obtained in the hysteresis curve is below 400 MPa (**Fig. 8.6a**), i.e. by a factor of about two below the YS of the UFG condition (**Fig. 8.3**). In general, such a loading level could already be in the range of the fatigue strength of the alloy. However, the microstructural notches discussed before promote localized crack initiation upon further cycling. In situ characterization (as e.g. conducted in [122]) could be employed for characterization of

local deformation events to further shed light on this aspect, however, such analysis is beyond the scope of present work and will be addressed in a follow-up study.

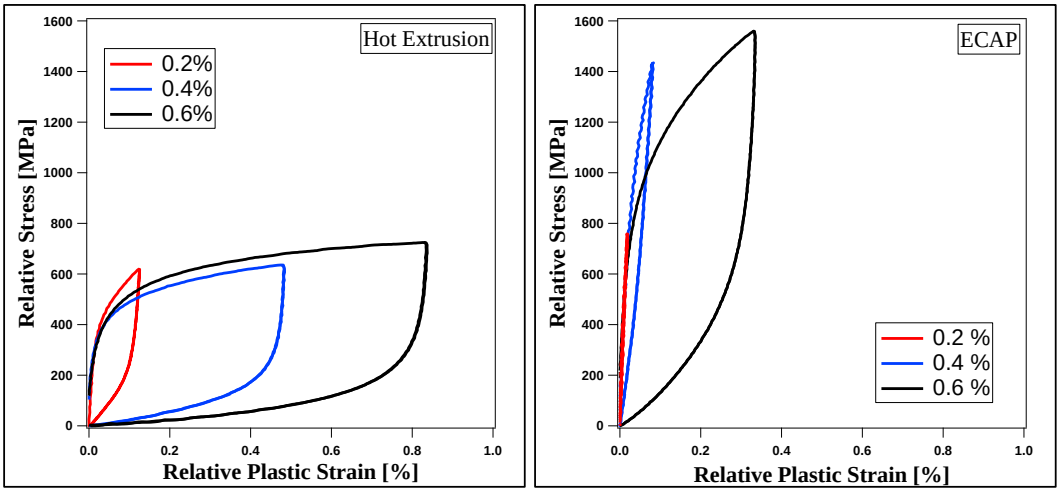

Figure 8.7 Half-life hysteresis loops of CoCrFeMnNi high entropy alloy in Hot-Extruded (a) and ECAP (b) conditions plotted in relative coordinates for the different total strain amplitudes of $\Delta\varepsilon/2 = \pm 0.2\%$, $\Delta\varepsilon/2 = \pm 0.4\%$ and $\Delta\varepsilon/2 = \pm 0.6\%$.

From direct comparison of hysteresis curves for higher load levels, i.e. $\Delta\varepsilon_t/2 = 0.4\%$ and $\Delta\varepsilon_t/2 = 0.6\%$ (**Figs. 8.6b and 8.6c**), the reason for the more pronounced differences in stress levels seen in the CDRs (**Fig. 4b and c**) can be deduced. Upon yielding, the HE condition exhibits an almost plateu-like stress response, i.e. plastic flow without significant hardening (**Fig. 8.66b and 8.6c**). On the contrary, in the ECAP processed condition, the elastic behavior still dominates the characteristic course of the hysteresis loop, even if a significant contribution of plasticity (appearance and increase of the hysteresis) is seen especially under the highest strain amplitude. Obviously, as

discussed before, the onset of plastic deformation in the ECAP HEA can be linked to softening and, thus, changes in microstructure and dislocation arregment.

Fig. 8.7. shows half-life hysteresis loops plotted in relative coordinates. The upper branches of the hysteresis loops of both HE and ECAE samples are incongruent indicating non-Masing behavior and variations in microstructure imposed by the differences in dislocation rearrangements [105,112], being triggered by the total strain amplitude. The TEM micrographs shown in the next section confirm that dislocation re-arrangement, i.e. the formation of subgrains and dislocation cells as well as nano-sized twins in the course of cyclic deformation, can be revealed upon cyclic loading. The in-depth analysis of the dislocation re-arrangement will be discussed in the next section for a better understanding of the microstructural evolution in this alloy.

8.5. Microstructure of Hot Extruded and ECAP processed CoCrFeMnNi HEA before and after cyclic loading at $\Delta\varepsilon/2=\pm0.6\%$

TEM imaging was performed to explore the microstructural evolution of both the HE and the ECAP samples cycled to failure at $\Delta\varepsilon/2 = 0.6$ %, since the most substantial differences in terms of evolution of CDR and hysteresis loops were detected at this strain amplitude (Figs. 4 and 5). TEM micrographs and selected area electron diffraction patterns (SAED) were taken on the plane with the plane normal along the longitudinal direction of the ECAP samples (Fig. 1) and on the plane perpendicular to the extrusion direction of the HE samples. TEM bright field images clearly revealed the presence of LAGBs in the HE

conditions (**Figs. 8.8a-b**). The dislocation density in the HE samples before cyclic loading was relatively low, and the dislocation structure reveals planar slip (**Fig. 8.8a-c**).

TEM investigations on the HE sample upon cycling and failure at $\Delta\varepsilon_t/2 = \pm 0.6\%$ revealed that grains feature various deformation arrangements such as cell structure and dislocation walls as shown in neighboring grains in **Fig. 8d**. Depending on the grain orientation triggering different number of slip systems, different dislocation patterns has been observed under fully reversed cyclic loading in common fcc crystals [106,222]. Basically, the easy cross slip of screw dislocations is proposed to be responsible for the formation of veins, persistent slip bands, labyrinth or cell patterns, while the effect of planar slip on the dislocation pattern formation has not been clearly revealed [106,222,223]. On the other hand, the dislocation patterns are known to be governed by the different types of dislocation mechanisms under uniaxial loading in pure fcc materials. For example, cross-slip governs the formation of a cell-structure, whereas HDDWs are known to be a consequence of planar slip [31,89,136,224]. Moreover, deformation modes depend on the applied stress direction for a given grain orientation [28,54]. Interestingly, TEM investigations revealed that the HDDWs (**Fig. 8e)** are accompanied by the formation of cell structures in a single grain (**Fig. 8f).** The nucleation of these cell structures seems to take place between dislocation walls (**Fig. 8h)** as a result of the re-arrangement of dislocations to form well-developed and organized cell structures (**Fig. 8i)** [106,222,223]. The inset diffraction pattern (**Fig. 8g**) proves that the cell structures and vein structures

were developed in the same grain. **Fig. 8.9** schematically summarizes the microstructural evolution of the HE sample under cyclic loading based on the present observations.

The hardening behavior upon monotonic and non-monotonic deformation of the HE samples differed significantly from each other (**Fig. 8.3 and Fig. 8.4**). Such behavior has been shown for conventional materials as well, e.g. high-manganese steels showing TWIP effect [93,94,96–98]. While pronounced hardening was observed under tensile loading, the strain hardening was insignificant under cyclic loading. The prevailing elementary deformation mechanisms, such as twinning, slip (differing in character) or phase transformation (e.g. transformation induced plasticity, TRIP), as well as the initial microstructure of the material, govern the hardening behavior of such kind of fcc alloys. Although the hardening behavior of the CoCrFeMnNi HEA is governed by planar slip under monotonic loading at room temperature [21,80], the hardening behavior under cyclic loading is dominated by the evolution of cell structures (**Fig. 8.8**), especially at higher strain amplitudes, which is in general related to wavy slip [63,225]. Therefore, the reason for the different hardening behavior in the HE samples under different loading conditions should be related to the different deformation mechanisms governing the hardening response. Such argument brings about a new question: why does cyclic loading cause the pronounced cell structure evolution although monotonic tests mostly demonstrate planar slip features?

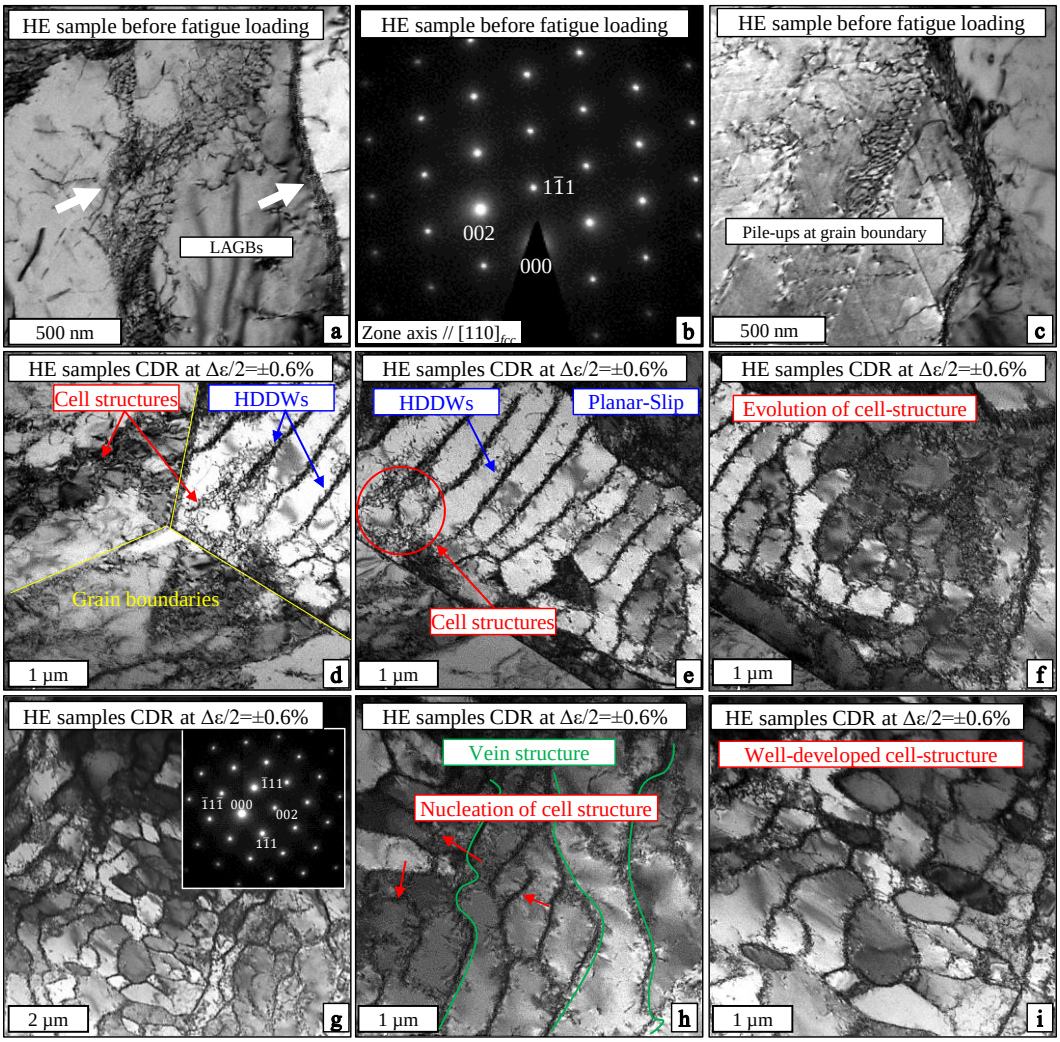

Figure 8.8 Bright field TEM images and corresponding selected area diffraction patterns of the hot-extruded CoCrNiFeMn high entropy alloy imaged on the plane perpendicular to the tested sample surface, demonstrating major microstructural features before (a-c) and after (d-i) cyclic loading. (a) Various subgrain boundaries, (b) the corresponding diffraction pattern demonstrating lack of high-angle grain boundaries in the selected area, (c) dislocation pile-up at a grain boundary. Bright field images of dislocation structures in the cyclically deformed sample at $\Delta\varepsilon/2=\pm 0.6\%$ with a fatigue life of $N\approx 4{,}000$ demonstrating (d) different microstructural features in neighboring grains, (e) high density dislocation walls (HDDWs) that are a consequence of planar-slip, (f) the nucleation of cell structure between HDDWs, (g) the cell structures and vein structures with the corresponding diffraction pattern (inset) proving that they were developed in the same grain (h) the evolution of the cell structure, (i) well-developed cell structure.

The reason for the formation of cell structure is attributed here to the extensive cross-slip activity triggered by the change in the effective stacking fault energy under externally applied stress and reversal of its direction upon cyclic loading at room temperature [54,89,194,226]. Moreover, the slip character is orientation dependent in interstitial free fcc crystals at room temperature [194,226]. According to the Copley-Kear effect, the applied stress can change the Shockley partial separation distance ($d_{partial}$) in low and medium stacking fault energy (SFE) materials [54,194,226], since $d_{partial}$ and SFE are inversely related. Thus, the applied stress level promotes an "effective" SFE:

$$d_{partial} = \frac{G b_1^2}{8\pi\gamma_{eff}} \qquad (4)$$

$$\gamma_{eff} = \gamma_0 \pm \frac{(m_1 - m_2)}{2}\sigma b_1 \qquad (5)$$

where γ_0 is the initial SFE, $(m_2 - m_1)/2$ (=Q) is the orientation factor, b_1 is the Burgers vector of the partial dislocation, γ_{eff} is the effective SFE, m_1 and m_2 is the Schmid factors for leading and trailing partial dislocations, respectively, σ is the applied stress with ± indicating the sign of the stress (tension or compression), and G is the shear modulus. In summary, the effective SFE is dependent on Q, σ, and the sign of the applied stress, eventually governing the slip character [54,89,163]. When Q has a negative value, $d_{partial}$ increases, and γ_{eff} accordingly decreases. In light of these considerations, it can be concluded that the slip character is both grain orientation and load direction dependent

(tension or compression). This approach detailed here has been confirmed for many fcc alloys [3,28,59,89,163,194,226].

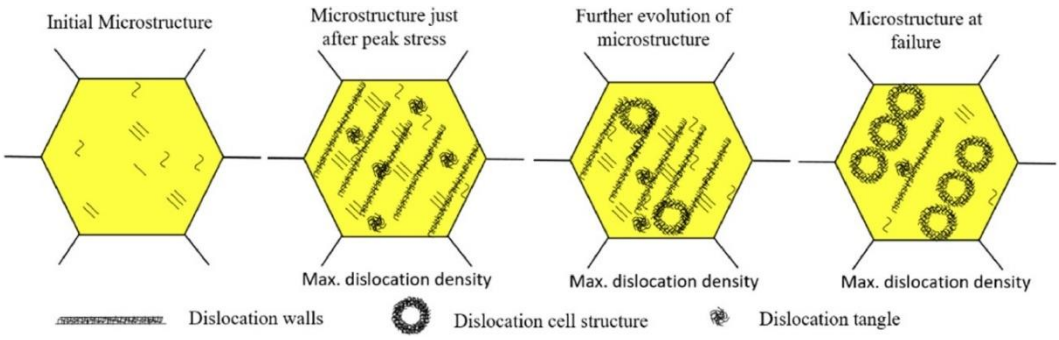

Figure 8.9 Schematic illustration of the formation of the cell structures in CoCrNiFeMn high entropy alloy under push-pull low-cycle fatigue loading.

The formation of HDDWs and cell-structures can be observed in a single grain during cyclic push-pull loading, where HDDWs and cell-structures are planar and wavy slip dependent, respectively (**Fig. 8.8d-i**), which can be triggered upon stress direction reversal. The basic idea is schematically summarized in **Fig. 8.10.** For example, the dislocation structure in <111> oriented grains exposed to external tensile loading promotes a planar character since the splitting of partials is easier under externally applied tensile stress. An applied compressive stress gives rise to a reduction of $d_{partial}$, thus γ_{eff} increases, obstructing splitting of partials and promoting cross-slip / wavy slip in <111> oriented grains.

These considerations suggest that some grains can experience both planar and cross-slip during push-pull cycling loading, and as a consequence, both HDDWs and dislocation cell structures can be formed in those grains (**Fig. 8.8d-g**). In the other words,

a grain that is oriented for cross-slip, such as <001> orientation under tensile loading [89], can exhibit planar-slip during compression [163,194,226]. Eventually, the steady-state hardening, i.e. the stable CDR, during cyclic loading can be attributed to a dynamic balance between increase of dislocation density, the formation of cell structures and the formation of HDDWs. Thus, a stable stress plateau (the lack of hardening) was observed at all strain amplitudes in the HE samples.

The TEM observations of the ECAP processed samples demonstrate a severely deformed grain structure (**Fig. 8.11a-c**) in the as-processed condition. The lattice defects depicted in the TEM micrograph in **Figs. 8.11a** and **8.11c** reveal that a high dislocation density can be stored upon ECAP processing. This observation is a direct evidence for the dislocation strengthening mechanism induced by the ECAP process, and eventually giving rise to the high yield strength (**Fig. 3**). Microstructure is somehow heterogeneous, i.e. many of the grains are approximately 300 nm to 600 nm in diameter. A similar kind of heterogenous microstructure as a result of severe plastic deformation has also been observed in conventional fcc alloys, e.g. in [68,192]. It is well accepted that the existence of a heterogeneous grain structure can improve the plastic deformation ability [192]. Therefore, the ECAP samples demonstrated a similar or higher fatigue life as compared to HE samples at $\Delta\varepsilon_t/2 = \pm 0.2\%$ and $\Delta\varepsilon_t/2 = \pm 0.4\%$ (**Fig. 4**). However, the higher stress level at $\Delta\varepsilon_t/2 = \pm 0.6\%$ leads to a pronounced softening effect during cyclic loading. In other words, strengthening effect cannot compensate dislocation activity at $\Delta\varepsilon_t/2 = \pm 0.6\%$,

eventually leading to an unstable deformation response and inferior fatigue life as compared to the other strain amplitudes.

TEM images in **Fig.11d-i** support the observed softening upon $\Delta\varepsilon_t/2 = \pm 0.6\%$ LCF testing, demonstrating that the formation of the cell structures is the major cyclic deformation mechanism in the ECAP samples at $\Delta\varepsilon_t/2 = \pm 0.6\%$. The cell structures evolve near lattice defects (including high dislocation density areas) via the annihilation and the re-arrangement of dislocations as indicated in **Fig.11d-e**. As the number of cells increases, an overall decrease of dislocation density and, thus, an increase in dislocation mean free path occurs leading to a well-developed UFG structure. This, in turn, leads to (localized) strain softening, and eventually to failure. The SAED pattern (**Fig. 11f**) only reveals intensities related to a single orientation, i.e. a single grain, clearly revealing the nature of the structures seen. Furthermore, some nano twins were also observed (**Figs. 11g-i**) with very small density. These twin structures could have been promoted by severe plastic deformation prior to cyclic loading via ECAP or during cyclic loading. In either case, the evolution of twin boundaries promotes additional barriers against dislocation motion eventually leading to additional hardening. In consequence, these twins can help to stabilize fatigue deformation and, thus, improve fatigue life [98].

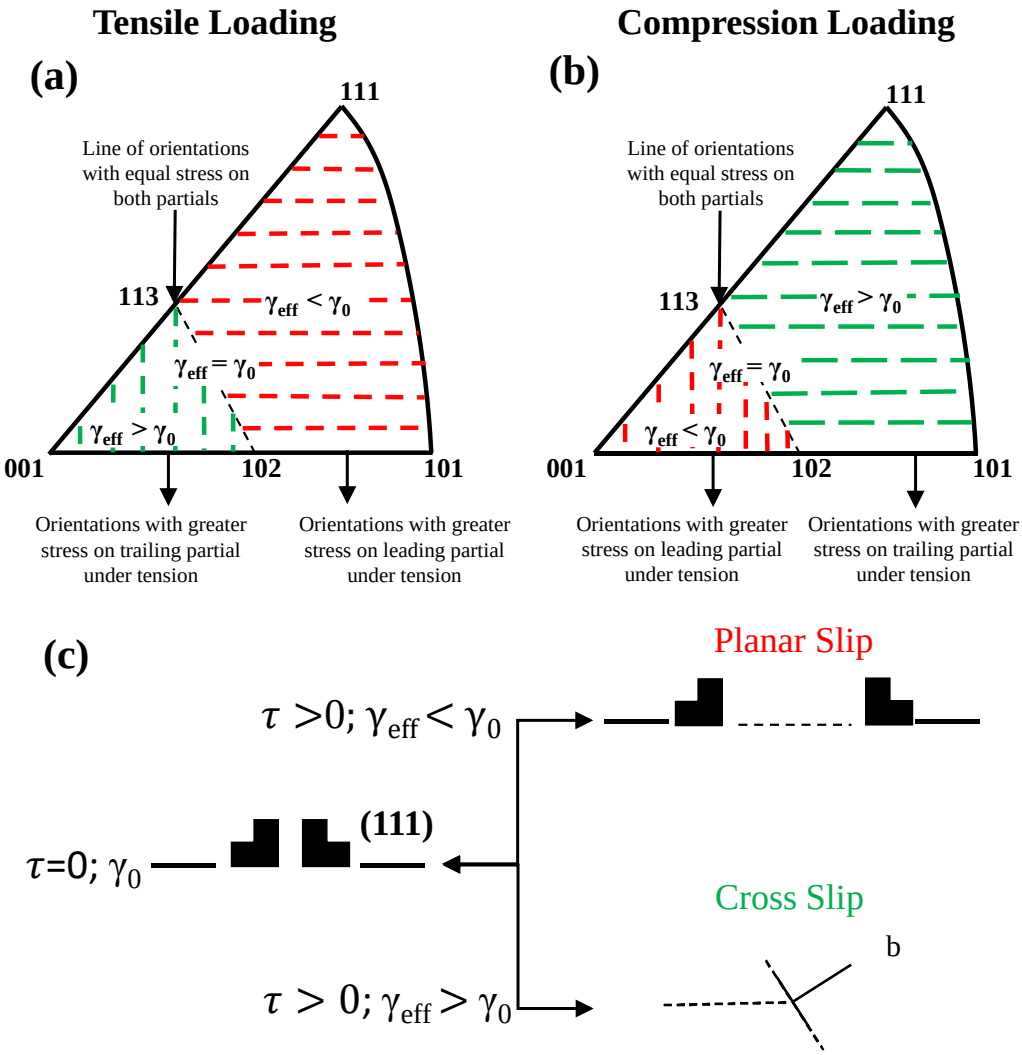

Figure 8.10 Schematic detailing the reversal of the slip character due to the effect of externally applied stress on the partial dislocation separation ($\boldsymbol{d_{partial}}$), and thus, effective stacking fault energy ($\boldsymbol{\gamma_{eff}}$), first proposed by Copley and Kear [66] and later experimentally demonstrated in detail by Kestenbach [81]. The stereographic unit triangle demonstrates the slip character of the crystallographic orientations (a) under tensile loading and (b) under compression loading. (c) The promotion of planar slip when the applied stress increases the partial dislocation separation and cross-slip when the applied stress reduces the partial dislocation separation.

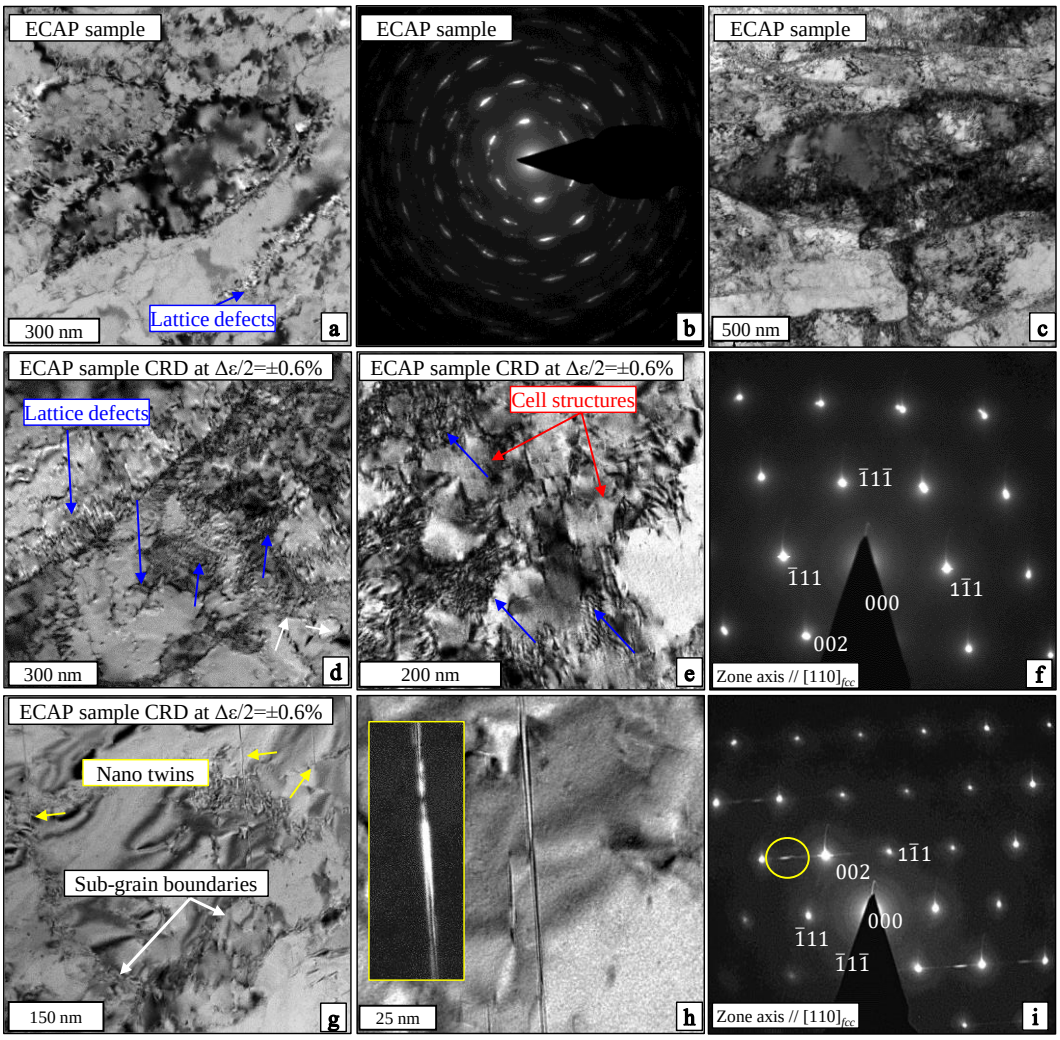

Figure 8.11 Bright field and dark field TEM images and corresponding selected area diffraction patterns of the ECAP processed CoCrNiFeMn high entropy alloy imaged on the plane perpendicular to the longitudinal direction of the sample **(cf. Fig.8.1),** demonstrating the major microstructural features before and after the cyclic loading. (a) low magnification image of the ECAP sample before fatigue loading demonstrating ultrafine grains. (b) selected area diffraction pattern of (a). TEM bright field image of the ECAP sample after cyclic loading at $\Delta\varepsilon/2=\pm0.6\%$, N=1000 (c) overall grain structures, (d) a higher magnification image demonstrating lattice defects, (e) the formation of a cell structure in the ECAP sample after the cyclic loading, (f) selected area diffraction pattern of (e) indicating that the cell structures were formed in a single grain, (g) nano size twinning, (h) higher magnification of (g) with dark field image inset, (i) selected area diffraction pattern of (h). Twin structures, lattice defects and cell structures are represented by yellow, blue and red arrows, respectively.

EBSD images of the ECAP sample cycled to failure at $\Delta\varepsilon_t/2 = 0.6$ % are displayed in **Fig. 8.12**. The microstructure can still be characterized as a bimodal microstructure, and some nano twins were detected on the IPF map (**Fig. 8.12a**) in line with the TEM investigation (**Fig. 8.11g-i**). The KAM map reveals that the dislocation density as compared to that of the initial condition (**Fig.2f**) is considerably lower, attesting the formation of cell structures via the annihilation process during the cyclic loading.

As a result, cyclic softening at $\Delta\varepsilon_t/2 = \pm 0.6\%$ in the LCF tests of the ECAP samples is attributed to a more pronounced dislocation recovery process, as opposed to the generation of new dislocations, resulting in the formation of cell structures. In other words, the distinct difference between hardening responses at different strain amplitudes was because of different stress levels, i.e. a more pronounced annihilation and re-arrangement of the dislocations promoted by high external stress in the UFG condition [227]. Since the very high-stress level promoted the dynamic recovery, the strain softening was saliently observed at $\Delta\varepsilon_t/2 = \pm 0.6\%$. In addition, the formation of microstructural notches after ECAP, such as the one shown in **Fig. 2e**, leads to microstructural heterogeneities that have been demonstrated to result in degradation of fatigue life and cyclic stability with an increase in strain amplitude [112,121], which should also play a role in the present material.

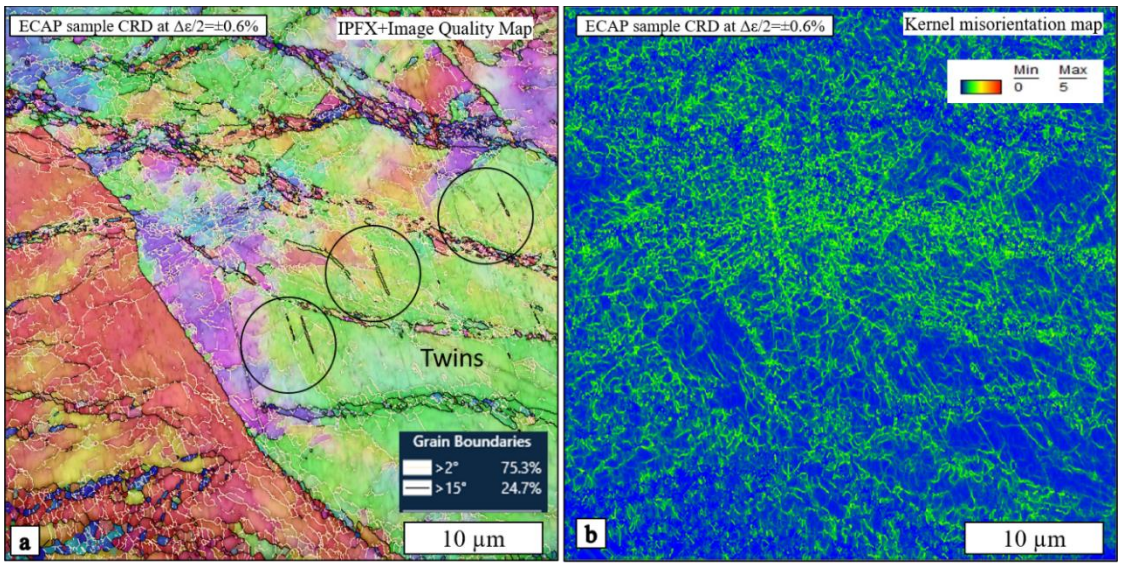

Figure 8.12 Microstructural characterization, through electron backscattered diffraction (EBSD) imaging, of CoCrFeMnNi high entropy alloy after Equal Channel Angular Pressing (ECAP) at 300°C using route 2C cycled to failure at $\Delta\varepsilon/2 = 0.6$ % (imaged on the plane perpendicular to longitudinal direction in Figure 1). (a) Inverse pole figure (IPF) map, (b) Kernel Average Misorientation (KAM) map. Step sizes of EBSD scanning are 50 nm.

The fracture surface features of the fatigued samples at different amplitudes in **Fig.13** strongly support the finding that multi-site damage is not present. The effects of loading condition on the fatigue fracture behavior were investigated using SEM in the HE and ECAP CoCrFeMnNi HEA samples for all strain amplitudes. In general, well-known features for fatigue tested samples, i.e. an overload fracture area, characterized by a ductile, dimple-like structure as well as an area of fatigue crack propagation characterized by submicron fatigue striations can be identified for all specimens and strain amplitudes. According to the fracture surface analysis in **Fig. 13**, secondary crack density, especially intergranular cracks, is higher in the HE samples as compared to the ECAP fatigue

samples. The formation of the cell structure in **Fig. 8e** was initiated at grain boundaries as a consequence of wavy-slip that can result in additional stresses due to strain incompatibility at the boundaries [228]. This could generate stress concentrations and thereby increase the intergranular cracking tendency (**Figs. 13** and **14**) [94,229]. The increasing strain amplitudes seem to cause a slightly higher secondary crack density in both HE and ECAP samples. The fracture surfaces of the HE samples represent a larger area of fatigue crack propagation and a higher density of fatigue striations, eventually indicating a slower crack propagation and a higher resistance to fatigue damage. This is basically related to the lower stress amplitudes in the HE samples at a given strain amplitude as well as the generally superior ductility in this condition.

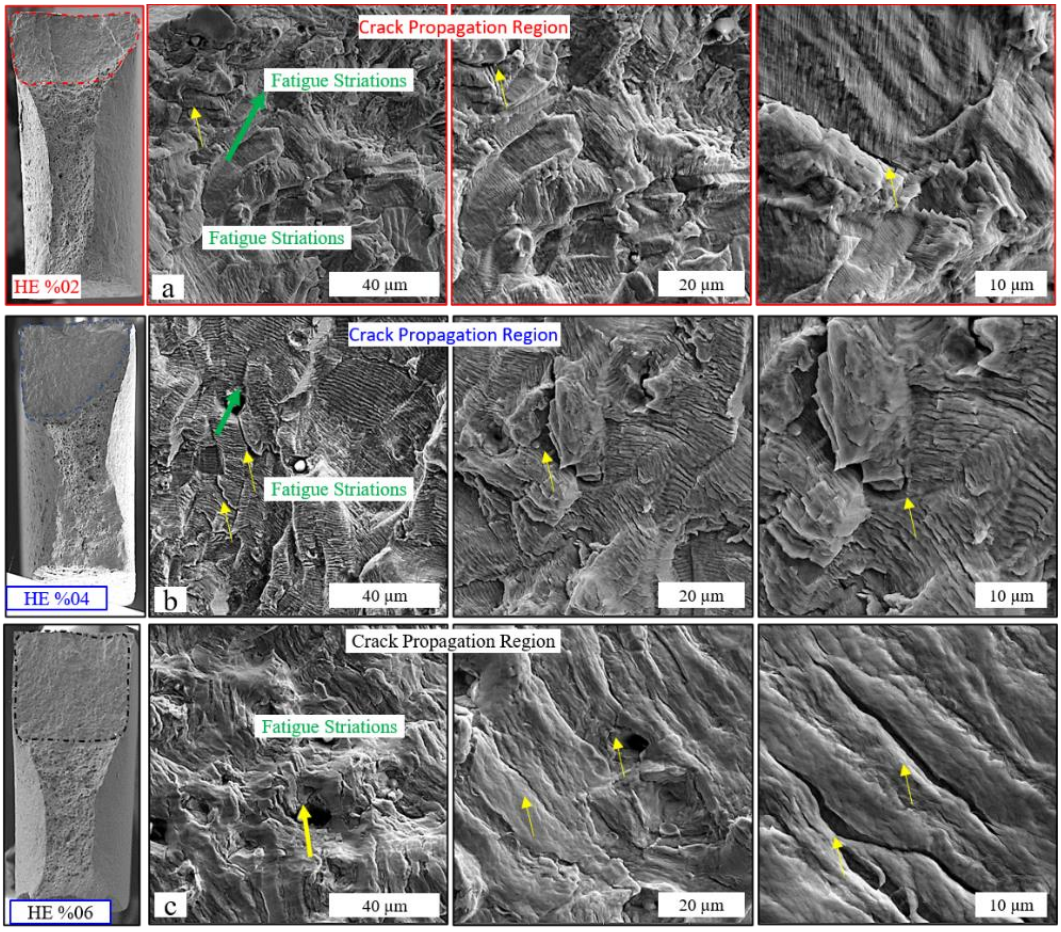

Figure 8.13 SEM images of the fracture features of the hot-extruded CoCrNiFeMn high entropy alloy within the crack propagation region after cyclic loading at different strain amplitudes (a) $\Delta\varepsilon/2 = \pm 0.2\%$, (b) $\Delta\varepsilon/2 = \pm 0.4\%$ and (c) $\Delta\varepsilon/2 = \pm 0.6\%$.

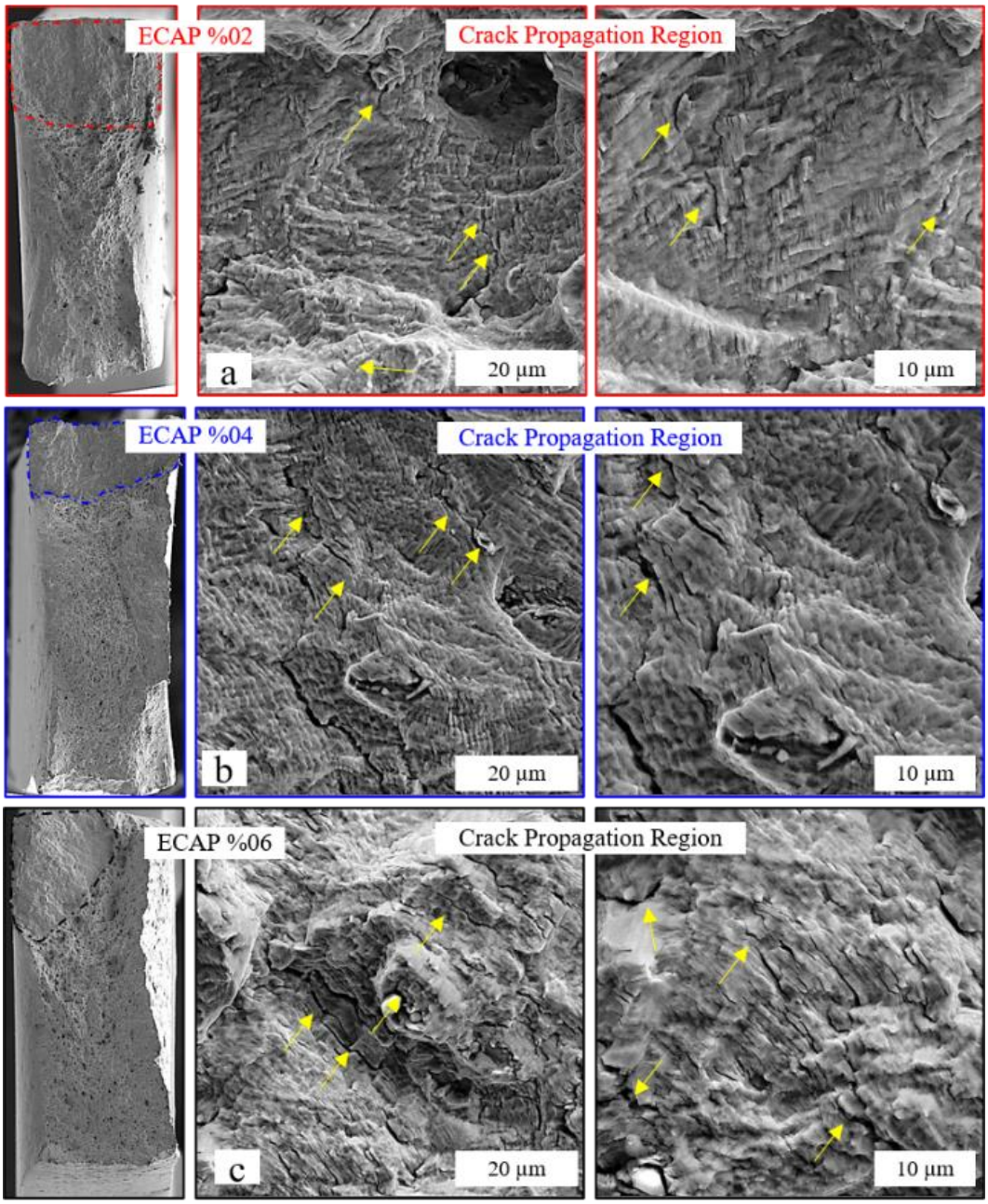

Figure 8.14 SEM images of the fracture features of the ECAP processed CoCrNiFeMn high entropy alloy within the crack propagation region after cyclic loading at different strain amplitudes (a) $\Delta\varepsilon/2 = \pm 0.2\%$, (b) $\Delta\varepsilon/2 = \pm 0.4\%$ and (c) $\Delta\varepsilon/2 = \pm 0.6\%$.

8.6. Crystallographic texture of Hot Extruded and ECAP processed CoCrFeMnNi HEA before and after cyclic loading at Δε/2=±0.6%

The equiatomic CoCrFeMnNi HEA is characterized by a single phase fcc structure in the as-cast condition. **Fig. 8.15** shows the results obtained by XRD of the samples before and after fatigue testing. It can be clearly seen that the material remains in a single fcc phase in all conditions. To evaluate the texture evolution, the pole figures from the three main fcc peaks (**see Fig. 8.15**) were determined and the orientation distribution function (ODF) was calculated using the Mtex Package [230].

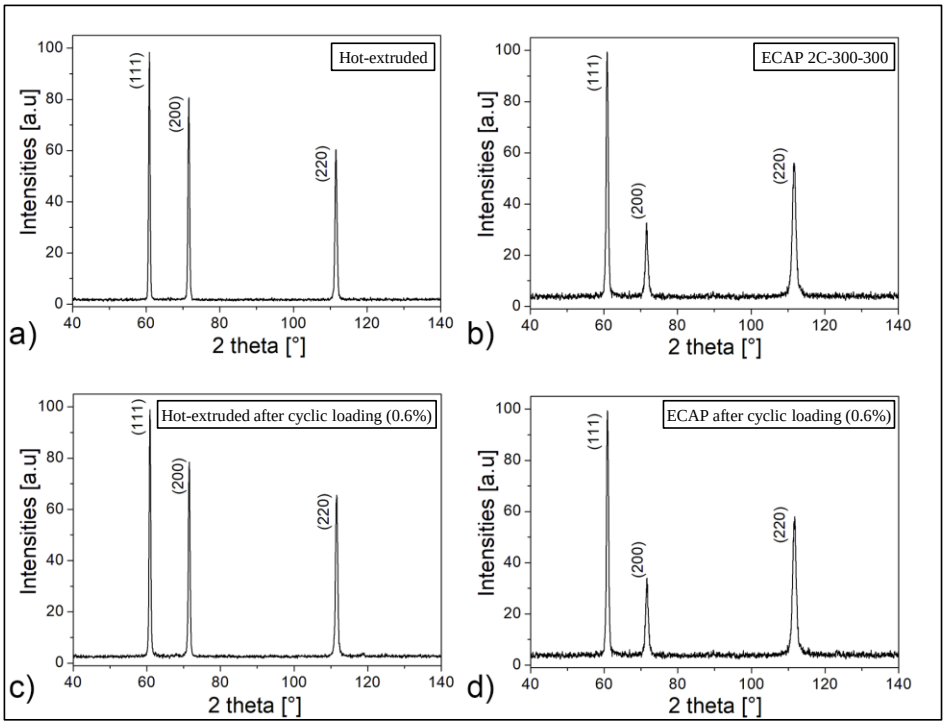

Figure 8.15 X-Ray diffractogram of CoCrNiFeMn high entropy alloy samples in (a) hot-extruded and (b) ECAP processed conditions, and after cyclic testing at Δε/2 = ± 0.6% of (c) hot-extruded and (d) ECAP processed samples. All peaks belong to the fcc phase.

Fig. 8.16. shows the pole figures that were used to calculate the ODF. **Fig. 8.17** shows the texture evolution in the HE and the ECAP samples using the ODF Sections of $\phi 2=0°$, 45° and 65° for all conditions. It is demonstrated that the texture in the HE sample consists of two main components, Cube-{001}<100> and A-{110}<111> textures (**Fig. 8.17a**). The presence of these orientations is strongly related to the heterogeneous microstructure of the material, where the small recrystallized grains are mainly orientated in Cube and the large grains are close to the A component. EBSD measurements on these samples were consistent with this finding (**Fig. 8.2a-c**). **Fig. 8.17b** displays the presence of a component of the Brass-type texture in the ECAP processed condition, similar to the one shown by Sathiaraj et al. [231,232] in cold rolled samples. The Brass type texture can be described as a combination of Brass-{110}<112> and Goss-{110}<001> orientations alongside what is usually called α fiber [233]. The differences in texture between both conditions and the overall evolution of texture, respectively, are strongly related to the deformation path of each specimen type.

The development of the microstructure seen in **Fig. 8.2d-e** and **Fig. 8.11** reveals a fragmentation of the large grains (being present in the HE condition) upon ECAP due to the severe plastic deformation during the process. As a consequence, the resulting texture of the ECAP sample is Brass-type, which is the characteristic texture for low SFE materials [233]. **Fig. 8.1c** and **8.17d** presents the evolution of the texture components for both materials after fatigue at $\Delta\varepsilon t/2 = \pm 0.6\%$. The main texture components remain similar in both the HE and the ECAP processed samples. However, the intensity of the Cube

orientation decreases in the HE samples (**Fig. 8.17c**). This is attributed to the pronounced cyclic plasticity during fatigue in case of the HE samples as can be directly deduced from the half-life hysteresis loops shown in **Fig. 8.6**.

Evaluation all microstructural investigations (XRD, EBSD and TEM) indicates that the overall dislocation density does not substantially change during cyclic loading because of a balance between dislocation generation and annihilation, which causes a saturated cyclic deformation response at all strain amplitudes in the HE samples. The formation of HDDWs, well-developed cell structures, and their complex interactions with dislocation motion stabilize the CDR, and a stable cyclic deformation is observed. However, the change in texture is more distinct in the HE sample as compared to the ECAP samples (**Fig. 8.17c-d**). This clearly reveals a more pronounced dislocation activity in the HE samples during cyclic loading. In contrast, the ECAP sample exposed to the LCF testing at $\Delta\varepsilon_t/2 = \pm 0.6\%$ displays a distinct softening behavior. Texture components of this sample revealed that the orientation distribution does hardly change during LCF testing of the ECAP sample contrary to the HE sample. Moreover, the contribution of the HDDW formation to the overall hardening behavior [3,89] could not be revealed in the case of the ECAP samples. A strongly impeded dislocation plasticity is expected for the ECAP processed material [197,234] since the microstructure upon ECAP is known to be already heavily distorted reaching the defect-saturation limit [63]. This can be deduced from the TEM micrographs in the present work as well (**Fig. 8.11c)**. Therefore, it can be concluded that dislocation activity is restricted in the ECAP sample. Thus, the short-range

dislocation movement and annihilation of dislocation structures, promoting the evolution of cell structures, governs the microstructural evolution in the ECAP samples under cyclic loading at high strain amplitudes.

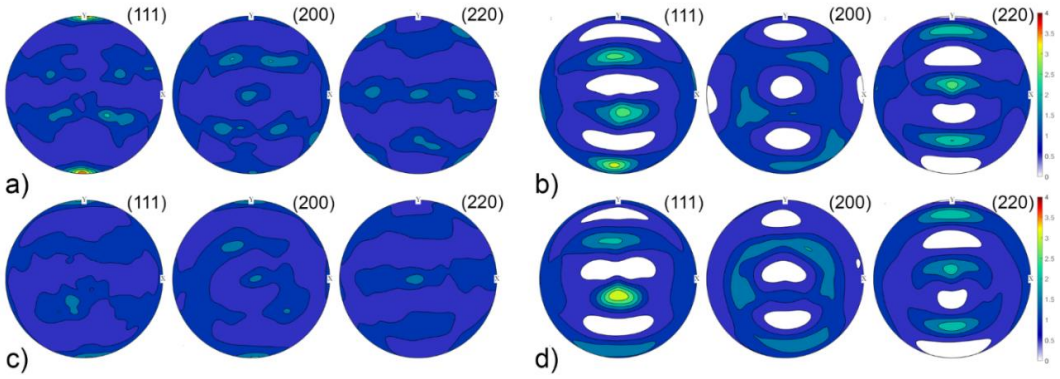

Figure 8.16 Pole figures of the main planes for the CoCrNiFeMn high entropy alloy samples (a) the plane perpendicular to the extrusion directions of the HE sample, (b) the plane perpendicular to the longitudinal direction of the ECAP sample. The same pole figures on the same planes after LCF testing at $\Delta\varepsilon/2 = \pm 0.6\%$ for (c) the HE sample, (d) the ECAP sample.

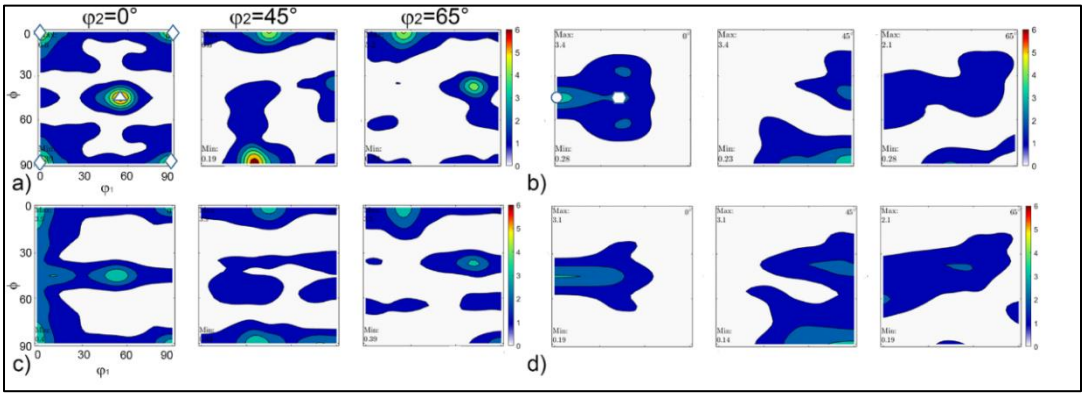

Figure 8.17 ODF Sections for $\phi 2=0°$, 45° and 65° for the CoCrNiFeMn high entropy alloy samples on (a) the plane perpendicular to the extrusion direction of the HE sample, (b) the plane perpendicular to the longitudinal direction of the ECAP sample. The same ODF sections on the same planes after LCF testing at $\Delta\varepsilon/2 = \pm 0.6\%$ for (c) the HE sample, (d) the ECAP sample. Circle: Goss -{110}<001>, Triangle: A-{110}<111>, Rhombus: Cube -{001}<100>, Hexagon: Brass -{110}<112> texture components.

8.7. Summary and Conclusions

The low-cycle fatigue behavior in a wide range of strain amplitudes (0.2%, 0.4% and 0.6%) and the monotonic tension and compression responses of the equiatomic CoCrFeMnNi HEA were systematically investigated in hot-extruded (HE) and ECAP-processed conditions. Comprehensice TEM, XRD and EBSD investigations were utilized to explore the microstructural evolution governing the strain hardening/softening behavior during low-cycle fatigue experiments. Key findings can be summarized as follows:

1. An exceptionally strong CoCrFeMnNi HEA was obtained after ECAP processing. Tension and compression tests demonstrated that the yield strength of the ECAP material (~925 MPa) was over three times higher than that of the HE samples. ECAP processing led to the formation of both low-angle grain boundaries (LAGBs) and HAGBs, with sizes mostly below 1 μm.
2. The strain hardening responses under monotonic and non-monotonic loading differ from each other in the HE CoCrFeMnNi HEAs as a result of the formation of cell structures under cyclic loading. While equiatomic CoCrFeMnNi HEA generally features planar slip and pronounced hardening under monotonic loading, cyclic push-pull loading promotes activation of both planar and cross-slip / wavy slip as a result of the reversal of the stress direction. The observation of these two deformation modes under cyclic loading, which is somewhat unexpected, was rationalized by the effect of externally applied stress on the partial dislocation separation and the effective stacking fault energy in materials with low to medium

stacking fault energies, which takes into account the sign of applied stress on the effective stacking fault energy and ,thus, the change in deformation mode.

3. ECAP considerably improved the fatigue life of CoCrFeMnNi HEA at the lowest strain amplitude, however, HE samples exhibited better fatigue life at the highest strain amplitude considered in this study. The lower fatigue life of the ECAP samples at the highest strain amplitude is attributed to the higher stress amplitudes imposed by grain refinement and pronounced defect storage. Moreover, the high stress level promoted accelerated dislocation annihilation resulting in cyclic softening at $\Delta\varepsilon/2 = 0.6\%$ strain amplitude.

In conclusion, the comparison of the fatigue lives of the CoCrFeMnNi HEA, other recently reported HEA systems, and conventional steels revealed that the microstructure achieved upon ECAP processing in CoCrFeMnNi HEA is beneficial for the overall alloy performance indicated by the occurrence of very high stress levels at a given fatigue life (**Fig. 8.18**). These concurrent improvements on both fatigue life and stress amplitude uncovered in the ECAP processed CoCrFeMnNi provide possible strategies to further optimize the microstructure of these new engineering alloys.

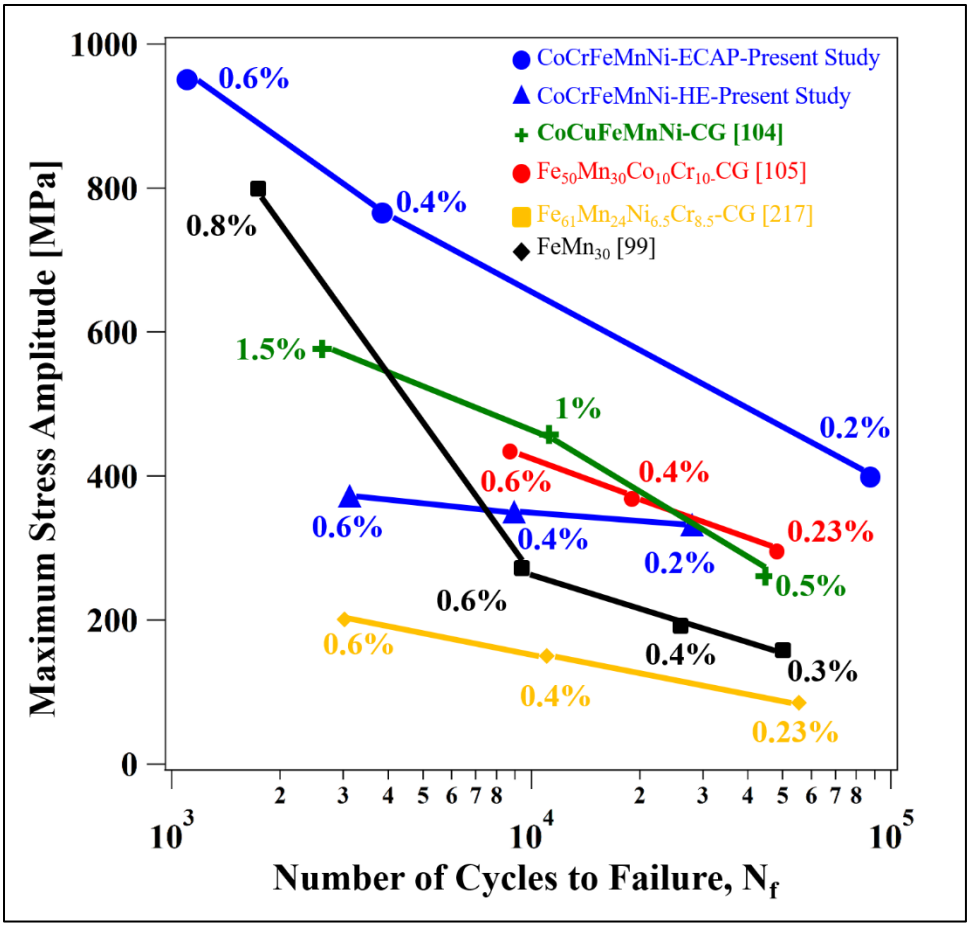

Figure 8.18 The comparison of the low-cycle fatigue life of fcc high and medium entropy alloys and an iron-manganese alloy at total strain amplitudes varying between $\Delta\varepsilon/2 = \pm 0.2$ % and ±1 %. CoCrFeMnNi exposed to equal channel angular pressing (ECAP) has an ultra-fine grain (UFG) structure (grain size < 1µm) and hot-extruded (HE) CoCrFeMnNi (at 900°C) has a coarse grain (CG) structure (grain size ~ 12 µm). The reported low cycle fatigue properties of CoCuFeMnNi with CG structure (12 µm) [104], $Fe_{50}Mn_{30}Co_{10}Cr_{10}$ in at% with CG structure (5 µm) [105], $Fe_{61}Mn_{24}Ni_{6.5}Cr_{8.5}$ in at% with CG structure (5 µm) [217] and $FeMn_{30}$ in wt.% [99] are presented for comparison in the figure.

9. CONCLUSIONS

In the present study, single crystals of NiCoCr, $Fe_{40}Mn_{40}Co_{10}Cr_{10}$, CoCrFeMnNi and $Fe_{50}Mn_{30}Co_9Cr_9+C_2$ M/HEAs have been investigated and the role of short range ordering, carbon and crysta-direction on the mechanical behavior have been revealed by a systematic study of several crystallographic orientations. Moreover, the low-cycle fatigue behavior at a wide range of strain amplitudes (0.2%, 0.4% and 0.6%) of the single and polycrystalline HEAs were systematically investigated. Key findings can be summarized as follows:

1. The strain hardening response and strain hardening coefficient under room temperature tension demonstrate strong orientation dependence in NiCoCr MEA and $Fe_{40}Mn_{40}Co_{10}Cr_{10}$ HEA as a result of the activation and complex interactions of orientation dependent deformation twinning and planar slip as well as dislocation wall/network formation regardless of the orientation. While the [011], [111] and [123] orientations feature four strain hardening stages due to the activation of multi-twin systems, the [001] orientation demonstrates only three strain hardening stages due to the lack of deformation twinning. The orientation dependence of the deformation modes was rationalized using the Copley-Kear effect, which takes into account the role of externally applied stress on the partial dislocation separation and effective stacking fault energy, which is orientation dependent under applied stress.

2. The exceptional strain hardening coefficient (θ) exhibited by the [111] orientation of NiCoCr MEA and $Fe_{40}Mn_{40}Co_{10}Cr_{10}$ HEA was attributed to the activation and interaction of multiple twin systems in stage 2. The significant ductility of this orientation, despite its highest strength among other orientations, was attributed to the formation of nano-twins within primary twins and the activation of the tertiary twins at the later stages of deformation (stage 4), which provided additional deformation when other micro-deformation mechanisms saturated. In addition, coexistence of multiple slip mechanisms in the [111] orientation also allowed for Shockley partial dislocations to form parallelepiped stacking faults in stage 4. Overall, the response of the [111] orientation is similar to that of the twinning-induced plasticity steels that also have low stacking fault energy. Plastic deformation of the [123] orientation was governed mainly by planar slip. The coexistence of slip and nano-twins in stage 2 was responsible for the strain hardening behavior in this orientation. The [123] orientation displayed a stage 4 hardening response, somewhat unexpectedly, similar to the [111] orientation, due to the activation of deformation twinning. Secondary twinning and high-density dislocation walls that form a Taylor lattice were also observed to contribute to the overall work hardening in stage 4.
3. Twinning was not observed in the [001] orientation in NiCoCr MEA, $Fe_{40}Mn_{40}Co_{10}Cr_{10}$ HEA and CoCrFeMnNi HEA, which is consistent with the Copley-Kear effect for the interstitial free fcc metals. Strain hardening in the [001]

orientation was attributed to HDDWs forming along multiple slip systems. Even though the formation of HDDWs is usually attributed to planar slip, planar character was not observed during the TEM of the [001] orientation of the present material. Specifically, the interaction between multi-junctions, which gives rise to high dislocation density, and dislocation dipoles lead to the formation of locks, facilitating the formation of HDDWs that act as obstacles against dislocation motion. Moreover, HDDWs also give rise to a formation of a lattice that is similar to Taylor lattice but allows for dislocation cell structure formation.

4. The comparison of the hardening response of the present low stacking faculty energy HEA with the conventional low stacking fault energy steels such as 316 stainless steel and Hadfield steel demonstrated that despite the present M/HEAs does not feature interstitial solid solution hardening, as in the case of 316 stainless steel and Hadfield steel, the hardening response and the hardening stages are very similar to these two conventional steels. M/HEAs demonstrate higher ductility in the [111] and [123] orientations due to the extended stage 4 hardening, however, the yield strength levels are notably lower as compared to 316 stainless steel and Hadfield steel due to the lack of interstitial solid solution hardening. In the [001] orientation, conventional steels show better plastic deformation ability via deformation twinning.
5. The structural properties in conventional steels and M/HEAs have been previously interpreted considering mostly stacking fault energy. In this study, the directly

imaged SRO has a direct effect on the deformation modes. The interplay of SRO with deformation twinning was investigated, and a new deformation pathway (fcc → hcp → $D0_{19}$ hierarchical non-diffusive phase transformation) was presented, a crucial finding for efforts to achieve outstanding plastic deformation ability in other MPEAs. The unique combination of experimental and theoretical investigation presented for this model MPEA can now be leveraged for the design of new alloys with improved mechanical properties. In spite of substantial progress, further systematic investigations are still needed to explore the complex nature of SRO interactions with the nucleation mechanisms of phase transformations.

4. The carbon addition (0.75 at.% C) in single crystalline CoCrFeMnNi HEAs caused a 25% increase in CRSS. The microstructure investigations of the [111]+C-oriented single crystalline CoCrFeMnNi revealed that the addition of carbon caused a tertiary twin system that suppressed the necking instability and produced an extended hardening stage. This TWIP effect caused more plastic deformation ability and subsequently improved the UTS level. Moreover, the [001]+C specimens presented the formation of nano twinning, which was the main reason for the simultaneous improvement in strength and ductility.
6. ECAP of CoCrFeMnNi HEA at medium and high temperatures resulted in an unexpected formation of deformation twinning and ε-martensite, in addition to grain refinement, increase in dislocation density, and heterogeneous grain size

distribution. This composite microstructure was responsible for the high strength levels ductility combination at room temperature. The simultaneous TWIP/TRIP effect at high temperatures was attributed to the effect of low SFE and high stress levels on partial dislocation separation. The composite microstructure achieved with ECAP enables defect storage, provides strain hardening capability, and postpones neck instability, which ultimately provides uniform plastic deformation. The observations and mechanisms discovered here are also applicable to other M/HEAs and will help tailor their microstructure to improve the properties further.

5. A systematic investigation of aged and non-aged Fe-Mn-Al-C steels indicates a new lamellar segregation governing the deformation response of the current material. Th is research demonstrated that segregation direction was detrimental to the sample's toughness. The loading direction parallel to the segregation bands presents the best strength-and ductility combination, while the loading direction 90^o to segregation bands presents the worst toughness. Such chemical segregation has rarely been realized, and this study represents the first report of its effect on the material's mechanical properties.

7. An exceptionally strong single phase $Fe_{50}Mn_{30}Co_9Cr_9$ +2 at.% HEA was obtained by C interstitial. Tension experiments demonstrated that the CRSS of $Fe_{50}Mn_{30}Co_9Cr_9$ +C_2 at.% (110±5) was over 2 times higher than single phase fcc $Fe_{40}Mn_{40}Co_{10}Cr_{10}$ HEA (τ_{cr}^{sl}=53±2 MPa [89]) and NiCoCr MEA (τ_{cr}^{sl}=63±3 MPa [3]). The CDR of single crystals under monotonic and non-monotonic loading

differs from each other. The CDR LCF at room temperature demonstrate strong orientation dependence in $Fe_{50}Mn_{30}Co_9Cr_9 + C_2$ at.% HEA. The [001], [110] and [123] orientations feature cyclic softening after initial cyclic loading at all amplitudes, whereas the [111] orientation demonstrates only cyclic hardening at $\Delta\varepsilon_t/2 = 0.6$ %. This unusual cyclic hardening was attributed to the DSA regime at $\Delta\varepsilon_t/2 = 0.6$ % in the [111] orientations. The lowest fatigue life was detected in the [111] orientations at $\Delta\varepsilon_t/2 = 0.6$ % due to higher stress amplitude and the DSA regime. The activation of twinning in the current single crystals under cyclic loading were orientation independent but the volume fraction of the twinning was orientation dependent according to active twinning system in the corresponding orientations. Finally, fracture analysis revealed that fatigue cracks were initiated from subsurface defects. Inclusions were detected on the fracture surfaces of all conditions which may cause the initiation of cracks due to the stress concentration in their vicinities. Different deformation mechanisms in [111] orientation i.e. twin activities resulted in smaller areas of cleavage surfaces compared with other orientations.

8. The strain hardening responses under monotonic and non-monotonic loading differ from each other in the HE CoCrFeMnNi HEAs as a result of the formation of cell structures under cyclic loading. While equiatomic CoCrFeMnNi HEA generally features planar slip and pronounced hardening under monotonic loading, cyclic push-pull loading promotes activation of both planar and cross-slip / wavy slip as

a result of the reversal of the stress direction. The observation of these two deformation modes under cyclic loading, which is somewhat unexpected, was rationalized by the effect of externally applied stress on the partial dislocation separation and the effective stacking fault energy in materials with low to medium stacking fault energies, which takes into account the sign of applied stress on the effective stacking fault energy and thus the change in deformation mode. In conclusion, ECAP considerably improved the fatigue life of CoCrFeMnNi HEA at the lowest strain amplitude, however, HE samples exhibited better fatigue life at the highest strain amplitude used in this study. The lower fatigue life of the ECAP samples at the highest strain amplitude is attributed to the higher stress amplitudes imposed by grain refinement and high defect storage. Moreover, high stress level promoted accelerated dislocation annihilation process resulting in cyclic softening at $\Delta\varepsilon/2 = 0.6\%$ strain amplitude.

REFERENCES

[1] J.W. Yeh, S.K. Chen, S.J. Lin, J.Y. Gan, T.S. Chin, T.T. Shun, C.H. Tsau, S.Y. Chang, Nanostructured high-entropy alloys with multiple principal elements: Novel alloy design concepts and outcomes, Adv. Eng. Mater. 6 (2004) 299–303.

[2] B. Cantor, I.T.H. Chang, P. Knight, A.J.B. Vincent, Microstructural development in equiatomic multicomponent alloys, Mater. Sci. Eng. A. 375–377 (2004) 213–218.

[3] B. Uzer, S. Picak, J. Liu, T. Jozaghi, D. Canadinc, I. Karaman, Y.I. Chumlyakov, I. Kireeva, On the mechanical response and microstructure evolution of NiCoCr single crystalline medium entropy alloys, Mater. Res. Lett. 6 (2018) 442–449.

[4] B. Gludovatz, A. Hohenwarter, D. Catoor, E.H. Chang, E.P. George, R.O. Ritchie, A fracture-resistant high-entropy alloy for cryogenic applications, Science. 345 (2014) 1153–1158.

[5] C. Niu, C.R. LaRosa, J. Miao, M.J. Mills, M. Ghazisaeidi, Magnetically-driven phase transformation strengthening in high entropy alloys, Nat. Commun. 9 (2018) 1–9.

[6] Y. Qiu, S. Thomas, M.A. Gibson, H.L. Fraser, N. Birbilis, Corrosion of high entropy alloys, Npj Mater. Degrad. (2017) 1–17.

[7] B. Gorr, M. Azim, H. Christ, T. Mueller, D. Schliephake, M. Heilmaier, Phase equilibria , microstructure , and high temperature oxidation resistance of novel refractory high-entropy alloys, J. Alloys Compd. 624 (2015) 270–278.

[8] W.J. Moore, Thermodynamics of solids (Swalin, Richard A.), J. Chem. Educ. 39 (1962) 488.

[9] E.J. Pickering, N.G. Jones, High-entropy alloys: a critical assessment of their founding principles and future prospects, Int. Mater. Rev. 61 (2016) 183–202.

[10] P.F. Yu, H. Cheng, L.J. Zhang, H. Zhang, M.Z. Ma, G. Li, P.K. Liaw, R.P. Liu, Nanotwin's formation and growth in an AlCoCuFeNi high-entropy alloy, Scr. Mater. 114 (2016) 31–34.

[11] J. Yeh, Recent progress in high-entropy alloys, Ann. Chim. Des Mater. 31 (2006) 633–648.

[12] Y. Zhang, T.T. Zuo, Z. Tang, M.C. Gao, K.A. Dahmen, P.K. Liaw, Z.P. Lu, Microstructures and properties of high-entropy alloys, Prog. Mater. Sci. 61 (2014) 1–93.

[13] Y. Zhang, X. Yang, P.K. Liaw, Alloy design and properties optimization of high-entropy alloys, Jom. 64 (2012) 830–838.

[14] D.B. Miracle, O.N. Senkov, A critical review of high entropy alloys and related concepts, Acta Mater. 122 (2017) 448–511.

[15] Y. Qiu, Y.J. Hu, A. Taylor, M.J. Styles, R.K.W. Marceau, A. V. Ceguerra, M.A. Gibson, Z.K. Liu, H.L. Fraser, N. Birbilis, A lightweight single-phase AlTiVCr compositionally complex alloy, Acta Mater. 123 (2017) 115–124.

[16] X.W. Qiu, Y.P. Zhang, L. He, C.G. Liu, Microstructure and corrosion resistance of AlCrFeCuCo high entropy alloy, J. Alloys Compd. 549 (2013) 195–199.

[17] J.Y. He, H. Wang, H.L. Huang, X.D. Xu, M.W. Chen, Y. Wu, X.J. Liu, T.G. Nieh, K. An, Z.P. Lu, A precipitation-hardened high-entropy alloy with outstanding tensile properties, Acta Mater. 102 (2016) 187–196.

[18] G. Laplanche, A. Kostka, O.M. Horst, G. Eggeler, E.P. George, Microstructure evolution and critical stress for twinning in the CrMnFeCoNi high-entropy alloy, Acta Mater. 118 (2016) 152–163.

[19] K.V.S. Thurston, A. Hohenwarter, G. Laplanche, E.P. George, B. Gludovatz, R.O. Ritchie, On the onset of deformation twinning in the CrFeMnCoNi high-entropy alloy using a novel tensile specimen geometry, Intermetallics. 110 (2019) 106469.

[20] Z. Li, K.G. Pradeep, Y. Deng, D. Raabe, C.C. Tasan, Metastable high-entropy dual-phase alloys overcome the strength–ductility trade-off, Nature. 534 (2016) 227.

[21] F. Otto, A. Dlouhý, C. Somsen, H. Bei, G. Eggeler, E.P. George, The influences of temperature and microstructure on the tensile properties of a CoCrFeMnNi high-entropy alloy, Acta Mater. 61 (2013) 5743–5755.

[22] J.-W.Y. P.P.Bhattacharjee, G.D.Sathiaraj, M.Zaid, J.R.Gatti, Chi Lee, Che-Wei Tsai, Microstructure and texture evolution during annealing of equiatomic CoCrFeMnNi high-entropy alloy, J. Alloys Compd. 587 (2014) 544–552.

[23] W. Abuzaid, H. Sehitoglu, Critical resolved shear stress for slip and twin nucleation in single crystalline FeNiCoCrMn high entropy alloy, Mater. Charact. 129 (2017) 288–299.

[24] L. Patriarca, A. Ojha, H. Sehitoglu, Y.I. Chumlyakov, Slip nucleation in single

crystal FeNiCoCrMn high entropy alloy, Scr. Mater. 112 (2016) 54–57.

[25] I. Kireeva, Y. Chumlyakov, Z. Pobedennaya, D. Kuksgauzen, I. Karaman, H. Sehitoglu, Mechanisms of plastic deformation in [1¯11]-oriented single crystals of FeNiMnCrCo high entropy alloy, AIP Conf. Proc. 1783 (2016) 020090.

[26] R. Raghavan, C. Kirchlechner, B.N. Jaya, M. Feuerbacher, G. Dehm, Mechanical size effects in a single crystalline equiatomic FeCrCoMnNi high entropy alloy, Scr. Mater. 129 (2017) 52–55.

[27] S. Huang, W. Li, S. Lu, F. Tian, J. Shen, E. Holmstrom, L. Vitos, Temperature dependent stacking fault energy of FeCrCoNiMn high entropy alloy, Scr. Mater. 108 (2015) 44–47.

[28] I. Karaman, H.. Sehitoglu, HMaier, K. Gall, Y.. Chumlyakov, Deformation of single crystal Hadfield steel by twinning and slip, Acta Mater. 48 (2002) 1345–1359.

[29] O. Grässel, L. Krüger, G. Frommeyer, L.W. Meyer, High strength Fe-Mn-(Al, Si) TRIP/TWIP steels development - properties - application, Int. J. Plast. 16 (2000) 1391–1409.

[30] P. Chowdhury, D. Canadinc, H. Sehitoglu, On deformation behavior of Fe-Mn based structural alloys, Mater. Sci. Eng. R. 122 (2017) 1–28.

[31] I. Karaman, H. Sehitoglu, H.J. Maier, Y.I. Chumlyakow, Competing mechanisms and modeling of deformation in austenitc stainless single cystals with and without nitrogen, Acta Mater. 49 (2001) 3919–3933.

[32] I. Karaman, H. Sehitoglu, A.J. Beaudoin, Y.I. Chumlyakov, H.J. Maier, C.N. Tome, Modeling the deformation behavior of hadfield steel single and polycrstals due to twinning and slip, Acta Mater. 48 (2000) 2031–2047.

[33] O. Bouaziz, S. Allain, C.P. Scott, P. Cugy, D. Barbier, High manganese austenitic twinning induced plasticity steels: A review of the microstructure properties relationships, Curr. Opin. Solid State Mater. Sci. 15 (2011) 141–168.

[34] M.J. Yao, K.G. Pradeep, C.C. Tasan, D. Raabe, A novel, single phase, non-equiatomic FeMnNiCoCr high-entropy alloy with exceptional phase stability and tensile ductility, Scr. Mater. 72–73 (2014) 5–8.

[35] Y. Deng, C.C. Tasan, K.G. Pradeep, H. Springer, A. Kostka, D. Raabe, Design of a twinning-induced plasticity high entropy alloy, Acta Mater. 94 (2015) 124–133.

[36] Z. Wu, H. Bei, F. Otto, G.M. Pharr, E.P. George, Recovery , recrystallization , grain growth and phase stability of a family of FCC-structured multi-component equiatomic solid solution alloys, Intermetallics. 46 (2014) 131–140.

[37] C.E. Slone, J. Miao, E.P. George, M.J. Mills, Achieving ultra-high strength and ductility in equiatomic CrCoNi with partially recrystallized microstructures, 165 (2019) 496–507.

[38] J. Miao, C.E. Slone, T.M. Smith, C. Niu, H. Bei, M. Ghazisaeidi, G.M. Pharr, M.J. Mills, The evolution of the deformation substructure in a Ni-Co-Cr equiatomic solid solution alloy, Acta Mater. 132 (2017) 35–48.

[39] S.S. Sohn, A. Kwiatkowski, Y. Ikeda, F. Körmann, W. Lu, Ultrastrong Medium-

Entropy Single-Phase Alloys Designed via Severe Lattice Distortion, 1807142 (2019) 1–8.

[40] C.E. Slone, S. Chakraborty, J. Miao, E.P. George, M.J. Mills, S.R. Niezgoda, Influence of deformation induced nanoscale twinning and FCC-HCP transformation on hardening and texture development in medium- entropy CrCoNi alloy, Acta Mater. 158 (2018) 38–52.

[41] C.E. Slone, J. Miao, E.P. George, M.J. Mills, Achieving ultra-high strength and ductility in equiatomic CrCoNi with partially recrystallized microstructures, Acta Mater. 165 (2019) 496–507.

[42] V. Gerold, H.P. Karnthaler, On the origin of planar slip in f.c.c. alloys, Acta Metall. 37 (1989) 2177–2183.

[43] F. Pettinari, M. Prem, G. Krexner, P. Caron, A. Coujou, H.O.K. Kirchner, N. Clemént, Local order in industrial and model γ phases of superalloys, Acta Mater. 49 (2001) 2549–2556.

[44] N. Clément, A. Coujou, Y. Calvayrac, F. Guillet, D. Blavette, S. Duval, Local order and associated deformation mechanisms in the γ phase of nickel base superalloys, Microsc. Microanal. Microstruct. 7 (1996) 65–84.

[45] J.B. Cohen, M.E. Fine, Some aspects of short-range order, J. Phys. Radium. 23 (1962) 749–762.

[46] P. Singh, A. V. Smirnov, A. Alam, D.D. Johnson, First-principles prediction of incipient order in arbitrary high-entropy alloys: exemplified in Ti0.25CrFeNiAlx,

Acta Mater. 189 (2020) 248–254.

[47] F.X. Zhang, S. Zhao, K. Jin, H. Xue, G. Velisa, H. Bei, R. Huang, J.Y.P. Ko, D.C. Pagan, J.C. Neuefeind, W.J. Weber, Y. Zhang, Local structure and short-range order in a NiCoCr solid solution alloy, Phys. Rev. Lett. 205501 (2017) 1–6.

[48] Q. Li, H. Sheng, E. Ma, Strengthening in multi-principal element alloys with local-chemical-order roughened dislocation pathways, Nat. Commun. 10 (2019) 1–11.

[49] J. Ding, Q. Yu, M. Asta, R.O. Ritchie, Tunable stacking fault energies by tailoring local chemical order in CrCoNi medium-entropy alloys, Proc. Natl. Acad. Sci. 115 (2018) 8919–8924.

[50] R. Zhang, S. Zhao, J. Ding, Y. Chong, T. Jia, C. Ophus, M. Asta, R.O. Ritchie, A.M. Minor, Short-range order and its impact on the CrCoNi medium-entropy alloy, Nature. 581 (2020) 283–287.

[51] G. Laplanche, A. Kostka, C. Reinhart, J. Hunfeld, G. Eggeler, E.P. George, Reasons for the superior mechanical properties of medium-entropy CrCoNi compared to high-entropy CrMnFeCoNi, Acta Mater. 128 (2017) 292–303.

[52] Y.Y. Shang, Y. Wu, J.Y. He, X.Y. Zhu, S.F. Liu, H.L. Huang, K. An, Y. Chen, S.H. Jiang, H. Wang, X.J. Liu, Z.P. Lu, Solving the strength-ductility tradeoff in the medium-entropy NiCoCr alloy via interstitial strengthening of carbon, Intermetallics. 106 (2019) 77–87.

[53] B. Yin, S. Yoshida, N. Tsuji, W.A. Curtin, Yield strength and misfit volumes of NiCoCr and implications for short-range-order, Nat. Commun. 11 (2020) 1–7.

[54] S.M. Copley, B.H. Kear, The dependence of the the width of a dissociated dislocation on dislocation velocity, Acta Mater. 16 (1968) 227–231.

[55] A. Gali, E.P. George, Tensile properties of high- and medium-entropy alloys, Intermetallics. 39 (2013) 74–78.

[56] N. Stepanov, M. Tikhonovsky, N. Yurchenko, D. Zyabkin, M. Klimova, S. Zherebtsov, A. Efimov, G. Salishchev, Effect of cryo-deformation on structure and properties of CoCrFeNiMn high-entropy alloy, Intermetallics. 59 (2015) 8–17.

[57] S. Picak, T. Wegener, S. V Sajadifar, C. Sobrero, J. Richter, H. Kim, T. Niendorf, I. Karaman, On the low cycle fatigue response of CoCrNiFeMn high entropy alloy with ultra-fine grain structure, Acta Mater. 205 (2021) 116540.

[58] S. Picak, H.C. Yilmaz, I. Karaman, Simultaneous deformation twinning and martensitic transformation in CoCrFeMnNi high entropy alloy at high temperatures, Scr. Mater. 202 (2021) 113995.

[59] Z. Wu, C.M. Parish, H. Bei, Nano-twin mediated plasticity in carbon-containing FeNiCoCrMn high entropy alloys, J. Alloy. Compd. J. 647 (2015) 815–822.

[60] Z. Wang, I. Baker, Z. Cai, S. Chen, J.D. Poplawsky, The effect of interstitial carbon on the mechanical properties and entropy alloys, Acta Mater. 120 (2016) 228–239.

[61] L.B. Chen, R. Wei, K. Tang, J. Zhang, F. Jiang, L. He, J. Sun, Heavy carbon alloyed FCC-structured high entropy alloy with excellent combination of strength and ductility, Mater. Sci. Eng. A. 716 (2018) 150–156.

[62] I. Karaman, G.G. Yapici, Y.I. Chumlyakov, I. V Kireeva, Deformation twinning in

difficult-to-work alloys during severe plastic deformation, 411 (2005) 243–247.

[63] H.J. Maier, P. Gabor, N. Gupta, I. Karaman, M. Haouaoui, Cyclic stress-strain response of ultrafine grained copper, Int. J. Fatigue. 28 (2006) 243–250.

[64] E. Dogan, M.W. Vaughan, S.J. Wang, I. Karaman, G. Proust, Role of starting texture and deformation modes on low-temperature shear formability and shear localization of Mg-3Al-1Zn alloy, Acta Mater. 89 (2015) 408–422.

[65] G. Purcek, G.G. Yapici, I. Karaman, H.J. Maier, Effect of commercial purity levels on the mechanical properties of ultrafine-grained titanium, Mater. Sci. Eng. A. 528 (2011) 2303–2308.

[66] G.G. Yapici, I.J. Beyerlein, I. Karaman, C.N. Tomé, Tension-compression asymmetry in severely deformed pure copper, Acta Mater. 55 (2007) 4603–4613.

[67] M. Haouaoui, I. Karaman, H.J. Maier, Flow stress anisotropy and Bauschinger effect in ultrafine grained copper, Acta Mater. 54 (2006) 5477–5488.

[68] G.G. Yapici, I. Karaman, Z.P. Luo, H.J. Maier, Y.I. Chumlyakov, Microstructural refinement and deformation twinning during severe plastic deformation of 316L stainless steel at high temperatures, J. Mater. Res. 19 (2004) 2268–2278.

[69] V.M. Segal, Materials processing by simple shear, Mater. Sci. Eng. A. 197 (1995) 157–164.

[70] A.P. Zhilyaev, G. V. Nurislamova, B.K. Kim, M.D. Baró, J.A. Szpunar, T.G. Langdon, Experimental parameters influencing grain refinement and microstructural evolution during high-pressure torsion, Acta Mater. 51 (2003) 753–

765.

[71] R.Z. Valiev, T.G. Langdon, Principles of equal-channel angular pressing as a processing tool for grain refinement, Prog. Mater. Sci. 51 (2006) 881–981.

[72] O. Saray, G. Purcek, I. Karaman, T. Neindorf, H.J. Maier, Equal-channel angular sheet extrusion of interstitial-free (IF) steel: Microstructural evolution and mechanical properties, Mater. Sci. Eng. A. 528 (2011) 6573–6583.

[73] T. Niendorf, D. Canadinc, H.J. Maier, I. Karaman, S.G. Sutter, On the fatigue behavior of ultrafine-grained interstitial-free steel, Int. J. Mater. Res. 97 (2006) 1328–1336.

[74] S. Yoshida, T. Bhattacharjee, Y. Bai, N. Tsuji, Friction stress and Hall-Petch relationship in CoCrNi equi-atomic medium entropy alloy processed by severe plastic deformation and subsequent annealing, Scr. Mater. 134 (2017) 33–36.

[75] H. Shahmir, T. Mousavi, J. He, Z. Lu, M. Kawasaki, T.G. Langdon, Microstructure and properties of a CoCrFeNiMn high-entropy alloy processed by equal-channel angular pressing, Mater. Sci. Eng. A. 705 (2017) 411–419.

[76] H. Shahmir, J. He, Z. Lu, M. Kawasaki, T.G. Langdon, Effect of annealing on mechanical properties of a nanocrystalline CoCrFeNiMn high-entropy alloy processed by high-pressure torsion, Mater. Sci. Eng. A. 676 (2016) 294–303.

[77] P. Yu, L. Zhang, H. Cheng, H. Tang, J. Fan, P.K. Liaw, G. Li, R. Liu, Formation, reverse transformation, and properties of ε-martensite phase in the CoCrFeMnNi high-entropy alloy under high-pressure, J. Alloys Compd. 779 (2019) 1–6.

[78] D.H. Lee, I.C. Choi, M.Y. Seok, J. He, Z. Lu, J.Y. Suh, M. Kawasaki, T.G. Langdon, J. Il Jang, Nanomechanical behavior and structural stability of a nanocrystalline CoCrFeNiMn high-entropy alloy processed by high-pressure torsion, J. Mater. Res. 30 (2015) 2804–2815.

[79] W. Skrotzki, A. Pukenas, E. Odor, B. Joni, T. Ungar, B. Völker, A. Hohenwarter, R. Pippan, E.P. George, Microstructure, texture, and strength development during high-pressure torsion of CrMnFeCoNi high-entropy alloy, Crystals. 10 (2020).

[80] B. Schuh, F. Mendez-Martin, B. Völker, E.P. George, H. Clemens, R. Pippan, A. Hohenwarter, Mechanical properties, microstructure and thermal stability of a nanocrystalline CoCrFeMnNi high-entropy alloy after severe plastic deformation, Acta Mater. 96 (2015) 258–268.

[81] B. Schuh, R. Pippan, A. Hohenwarter, Tailoring bimodal grain size structures in nanocrystalline compositionally complex alloys to improve ductility, Mater. Sci. Eng. A. 748 (2019) 379–385.

[82] P. Asghari-Rad, P. Sathiyamoorthi, J.W. Bae, H. Shahmir, A. Zargaran, H.S. Kim, Fine-tuning of mechanical properties in V10Cr15Mn5Fe35Co10Ni25 high-entropy alloy through high-pressure torsion and annealing, Adv. Eng. Mater. 22 (2020) 2070002.

[83] S. Nam, J.Y. Hwang, J. Jeon, J. Park, D. Bae, M.J. Kim, J.H. Kim, H. Choi, Deformation behavior of nanocrystalline and ultrafine-grained CoCrCuFeNi high-entropy alloys, J. Mater. Res. 34 (2019) 720–731.

[84] K.M. Chang, C.G. Chao, T.F. Liu, Excellent combination of strength and ductility in an Fe-9Al-28Mn-1.8C alloy, Scr. Mater. 63 (2010) 162–165.

[85] K. Choi, C.H. Seo, H. Lee, S.K. Kim, J.H. Kwak, K.G. Chin, K.T. Park, N.J. Kim, Effect of aging on the microstructure and deformation behavior of austenite base lightweight Fe-28Mn-9Al-0.8C steel, Scr. Mater. 63 (2010) 1028–1031.

[86] H. Huang, D. Gan, P.W. Kao, Effect of alloying additions on the κ phase precipitation in austenitic Fe-Mn-Al-C alloys, Scr. Metall. Mater. 30 (1994) 499–504. https://www.sciencedirect.com/science/article/pii/0956716X94906106.

[87] Z. Wang, W. Lu, H. Zhao, C.H. Liebscher, J. He, D. Ponge, D. Raabe, Z. Li, Ultrastrong lightweight compositionally complex steels via dual-nanoprecipitation, Sci. Adv. 6 (2020) eaba9543.

[88] R.L. Klueh, P.J. Maziasz, E.H. Lee, Manganese as an austenite stabilizer in Fe□Cr□Mn□C steels, Mater. Sci. Eng. A. 102 (1988) 115–124.

[89] S. Picak, J. Liu, C. Hayrettin, W. Nasim, D. Canadinc, K. Xie, Y.I. Chumlyakov, I. V Kireeva, I. Karaman, Anomalous work hardening behavior of Fe40Mn40Cr10Co10 high entropy alloy single crystals deformed by twinning and slip, Acta Mater. 181 (2019) 555–569.

[90] S. Chen, R. Rana, A. Haldar, R.K. Ray, Current state of Fe-Mn-Al-C low density steels, Prog. Mater. Sci. 89 (2017) 345–391.

[91] H. Kim, D.-W. Suh, N.J. Kim, Fe–Al–Mn–C lightweight structural alloys: a review on the microstructures and mechanical properties, Sci. Technol. Adv. Mater. 14

(2013) 14205.

[92] J. Talonen, H. Hänninen, Formation of shear bands and strain-induced martensite during plastic deformation of metastable austenitic stainless steels, Acta Mater. 55 (2007) 6108–6118.

[93] T. Niendorf, F. Rubitschek, H.J. Maier, J. Niendorf, H.A. Richard, A. Frehn, Fatigue crack growth—Microstructure relationships in a high-manganese austenitic TWIP steel, Mater. Sci. Eng. A. 527 (2010) 2412–2417.

[94] C.W. Shao, P. Zhang, R. Liu, Z.J. Zhang, J.C. Pang, Q.Q. Duan, Z.F. Zhang, A remarkable improvement of low-cycle fatigue resistance of high-Mn austenitic TWIP alloys with similar tensile properties: Importance of slip mode, Acta Mater. 118 (2016) 196–212.

[95] J.T.P. Yao, W.H. Munse, Low-cycle fatigue behavior of axially loaded specimens of mild steel, Am. Soc. Test. Mater. (1962) 5–24.

[96] D. An, W. Krieger, S. Zaefferer, Unravelling the effect of hydrogen on microstructure evolution under low-cycle fatigue in a high-manganese austenitic TWIP steel, Int. J. Plast. (2019).

[97] A.S. Hamada, L.P. Karjalainen, J. Puustinen, Fatigue behavior of high-Mn TWIP steels, Mater. Sci. Eng. A. 517 (2009) 68–77.

[98] T. Niendorf, C. Lotze, D. Canadinc, A. Frehn, H.J. Maier, The role of monotonic pre-deformation on the fatigue performance of a high-manganese austenitic TWIP steel, Mater. Sci. Eng. A. 499 (2009) 518–524.

[99] C.W. Shao, P. Zhang, R. Liu, Z.J. Zhang, J.C. Pang, Z.F. Zhang, Low-cycle and extremely-low-cycle fatigue behaviors of high-Mn austenitic TRIP/TWIP alloys: Property evaluation, damage mechanisms and life prediction, Acta Mater. 103 (2016) 781–795.

[100] K. Liu, M. Komarasamy, B. Gwalani, S. Shukla, R.S. Mishra, Fatigue behavior of ultrafine grained triplex Al0.3CoCrFeNi high entropy alloy, Scr. Mater. 158 (2019) 116–120.

[101] Y.Z. Tian, S.J. Sun, H.R. Lin, Z.F. Zhang, Fatigue behavior of CoCrFeMnNi high-entropy alloy under fully reversed cyclic deformation, J. Mater. Sci. Technol. 35 (2019) 334–340.

[102] M.A. Hemphill, T. Yuan, G.Y. Wang, J.W. Yeh, C.W. Tsai, A. Chuang, P.K. Liaw, Fatigue behavior of Al0.5CoCrCuFeNi high entropy alloys, Acta Mater. 60 (2012) 5723–5734.

[103] K. Liu, S.S. Nene, M. Frank, S. Sinha, R.S. Mishra, Extremely high fatigue resistance in an ultrafine grained high entropy alloy, Appl. Mater. Today. 15 (2019) 525–530.

[104] F. Bahadur, K. Biswas, N.P. Gurao, Micro-mechanisms of microstructural damage due to low cycle fatigue in CoCuFeMnNi high entropy alloy, Int. J. Fatigue. 130 (2020) 105258.

[105] T. Niendorf, T. Wegener, Z. Li, D. Raabe, Unexpected cyclic stress-strain response of dual-phase high-entropy alloys induced by partial reversibility of deformation,

Scr. Mater. 143 (2018) 63–67.

[106] P. Li, S.X. Li, Z.G. Wang, Z.F. Zhang, Fundamental factors on formation mechanism of dislocation arrangements in cyclically deformed fcc single crystals, Prog. Mater. Sci. 56 (2011) 328–377.

[107] A.S. Cheng, C. Laird, The high cycle fatigue life of copper single crystals tested under plastic-strain-controlled conditions, Mater. Sci. Eng. 51 (1981) 55–60.

[108] A.T. Winter, A model for the fatigue of copper at low plastic strain amplitudes, Philos. Mag. A J. Theor. Exp. Appl. Phys. 30 (1974) 719–738.

[109] P.J. Woods, Low-amplitude fatigue of copper and copper-5 at. % aluminium single crystals, Philos. Mag. A J. Theor. Exp. Appl. Phys. 28 (1973) 155–191.

[110] V. Levkovitch, R. Sievert, B. Svendsen, Simulation of deformation and lifetime behavior of a fcc single crystal superalloy at high temperature under low-cycle fatigue loading, Int. J. Fatigue. 28 (2006) 1791–1802.

[111] P. Li, Z.F. Zhang, X.W. Li, S.X. Li, Z.G. Wang, Effect of orientation on the cyclic deformation behavior of silver single crystals: Comparison with the behavior of copper and nickel single crystals, Acta Mater. 57 (2009) 4845–4854.

[112] T. Niendorf, D. Canadinc, H.J. Maier, Fatigue damage evolution in ultrafine-grained interstitial-free steel, Adv. Eng. Mater. 13 (2011) 275–280.

[113] S. V. Sajadifar, T. Wegener, G.G. Yapici, T. Niendorf, Effect of grain size on the very high cycle fatigue behavior and notch sensitivity of titanium, Theor. Appl. Fract. Mech. 104 (2019) 102362.

[114] I.P. Semenova, G.K. Salimgareeva, V. V. Latysh, T. Lowe, R.Z. Valiev, Enhanced fatigue strength of commercially pure Ti processed by severe plastic deformation, Mater. Sci. Eng. A. 503 (2009) 92–95.

[115] T. Niendorf, H.J. Maier, D. Canadinc, I. Karaman, Cyclic stability of ultrafine-grained interstitial-free steel at elevated temperatures, Mater. Sci. Eng. A. 503 (2009) 160–162.

[116] H.W. Höppel, M. Kautz, C. Xu, M. Murashkin, T.G. Langdon, R.Z. Valiev, H. Mughrabi, An overview: Fatigue behaviour of ultrafine-grained metals and alloys, Int. J. Fatigue. 28 (2006) 1001–1010.

[117] L. Kunz, P. Lukáš, M. Svoboda, Fatigue strength, microstructural stability and strain localization in ultrafine-grained copper, Mater. Sci. Eng. A. 424 (2006) 97–104.

[118] H. Mughrabi, H.W. Höppel, M. Kautz, Fatigue and microstructure of ultrafine-grained metals produced by severe plastic deformation, Scr. Mater. 51 (2004) 807–812.

[119] A. Vinogradov, S. Hashimoto, Fatigue of severely deformed metals, Adv. Eng. Mater. 5 (2003) 351–358.

[120] A. Medvedev, A. Arutyunyan, I. Lomakin, A. Bondarenko, V. Kazykhanov, N. Enikeev, G. Raab, M. Murashkin, Fatigue properties of ultra-fine grained Al-Mg-Si wires with enhanced mechanical strength and electrical conductivity, Metals (Basel). 8 (2018).

[121] T. Niendorf, D. Canadinc, H.J. Maier, I. Karaman, On the microstructural stability of ultrafine-grained interstitial-free steel under cyclic loading, Metall. Mater. Trans. A Phys. Metall. Mater. Sci. 38 A (2007) 1946–1955.

[122] T. Niendorf, J. Dadda, D. Canadinc, H.J. Maier, I. Karaman, Monitoring the fatigue-induced damage evolution in ultrafine-grained interstitial-free steel utilizing digital image correlation, Mater. Sci. Eng. A. 517 (2009) 225–234.

[123] L. Collini, Fatigue crack growth in ECAPed commercially pure UFG copper, Procedia Eng. 2 (2010) 2065–2074.

[124] T. Niendorf, F. Rubitschek, H.J. Maier, D. Canadinc, I. Karaman, On the fatigue crack growth-microstructure relationship in ultrafine-grained interstitial-free steel, J. Mater. Sci. 45 (2010) 4813–4821.

[125] H.J. Maier, P. Gabor, I. Karaman, Cyclic stress-strain response and low-cycle fatigue damage in ultrafine grained copper, Mater. Sci. Eng. A. 410–411 (2005) 457–461.

[126] J. May, D. Amberger, M. Dinkel, H.W. Höppel, M. Göken, Monotonic and cyclic deformation behaviour of ultrafine-grained aluminium, Mater. Sci. Eng. A. 483–484 (2008) 481–484.

[127] D. Canadinc, T. Niendorf, H.J. Maier, A comprehensive evaluation of parameters governing the cyclic stability of ultrafine-grained FCC alloys, Mater. Sci. Eng. A. 528 (2011) 6345–6355.

[128] K. Hockauf, M.F.X. Wagner, T. Halle, T. Niendorf, M. Hockauf, T. Lampke,

Influence of precipitates on low-cycle fatigue and crack growth behavior in an ultrafine-grained aluminum alloy, Acta Mater. 80 (2014) 250–263.

[129] S. V. Sajadifar, G.G. Yapici, E. Demler, P. Krooß, T. Wegener, H.J. Maier, T. Niendorf, Cyclic deformation response of ultra-fine grained titanium at elevated temperatures, Int. J. Fatigue. 122 (2019) 228–239.

[130] H.S. Kim, Evaluation of strain rate during equal-channel angular pressing, J. Mater. Res. 17 (2002) 172–179.

[131] I. Karaman, The competing effects of slip and twinning on the deformation of Hadfield manganese steel single and polycrystals, Ph.D. Thesis. (2000). https://ui.adsabs.harvard.edu/abs/2000PhDT.....181K.

[132] R. Zhang, S. Zhao, C. Ophus, Y. Deng, S.J. Vachhani, B. Ozdol, R. Traylor, K.C. Bustillo, J.W. Morris, D.C. Chrzan, M. Asta, A.M. Minor, Direct imaging of short-range order and its impact on deformation in Ti-6Al, Sci. Adv. 5 (2019) 1–8.

[133] I. V. Kireeva, Y.I. Chumlyakov, Z. V. Pobedennaya, Y.N. Platonova, I. V. Kuksgauzen, D.A. Kuksgauzen, V. V. Poklonov, I. Karaman, H. Sehitoglu, Slip and Twinning in the [149] -Oriented Single Crystals of a High-Entropy Alloy, Russ. Phys. J. 59 (2016) 1242–1250.

[134] W.S. Choi, S. Sandlöbes, N. V Malyar, C. Kirchlechner, S. Korte-Kerzel, G. Dehm, B.C. De Cooman, D. Raabe, Dislocation interaction and twinning-induced plasticity in face-centered cubic Fe-Mn-C micro-pillars, Acta Mater. 132 (2017) 162–173.

[135] I. Karaman, H. Sehitoglu, H.J. Maier, Y.I. Chumlyakov, Competing mechanisms and modeling of deformation in austenitic stainless steel single crystals with and without nitrogen, Acta Mater. 49 (2001) 3919–3933.

[136] D. Kuhlmann-Wilsdorf, Theory of plastic deformation: - properties of low energy dislocation structures, Mater. Sci. Eng. A. 113 (1989) 1–41.

[137] D. Canadinc, H. Sehitoglu, H.J. Maier, Y.I. Chumlyakov, Strain hardening behavior of aluminum alloyed Hadfield steel single crystals, Acta Mater. 53 (2005) 1831–1842.

[138] B. Gludovatz, A. Hohenwarter, K.V.S. Thurston, H. Bei, Z. Wu, E.P. George, R.O. Ritchie, Exceptional damage-tolerance of a medium-entropy alloy CrCoNi at cryogenic temperatures, Nat. Commun. 7 (2016) 10602.

[139] Z. Zhang, H. Sheng, Z. Wang, B. Gludovatz, Z. Zhang, E.P. George, Q. Yu, S.X. Mao, R.O. Ritchie, Dislocation mechanisms and 3D twin architectures generate exceptional strength-ductility-toughness combination in CrCoNi medium-entropy alloy, Nat. Commun. 8 (2017).

[140] D. Barbier, N. Gey, S. Allain, N. Bozzolo, M. Humbert, Analysis of the tensile behavior of a TWIP steel based on the texture and microstructure evolutions, Mater. Sci. Eng. A. 500 (2009) 196–206.

[141] I. Karaman, H. Sehitoglu, Y.I. Chumlyakov, H.J. Maier, I. V Kireeva, The Effect of twinning and slip on the bauschinger effect of hadfield steel single crystals, Metall. Mater. Trans. A. 32 (2001) 695–706.

[142] I. Karaman, H. Sehitoglu, Y.I. Chumlyakov, H.J. Maier, I.V. Kireeva, Extrinsic stacking faults and twinning in Hadfield manganese steel single crystals, Scr. Mater. 44 (2001) 337–343.

[143] D. Canadinc, I. Karaman, Y. Chumlyakov, The Role of Nitrogen on the Deformation Response of Hadfield Steel Single Crystals, Metall. Mater. Trans. A. 34 (9) (2003).

[144] I. Karaman, H. Sehitoglu, Y.I. Chumlyakov, H.J. Maier, The deformation of low-stacking- fault-energy austenitic steels, 54 (2002) 31–37.

[145] I. Gutierrez-Urrutia, D. Raabe, Dislocation and twin substructure evolution during strain hardening of an Fe-22 wt.% Mn-0.6 wt.% C TWIP steel observed by electron channeling contrast imaging, Acta Mater. 59 (2011) 6449–6462.

[146] C. Efstathiou, H. Sehitoglu, Strain hardening and heterogeneous deformation during twinning in Hadfield steel, Acta Mater. 58 (2010) 1479–1488.

[147] S. Asgari, E. El-Danaf, S.R. Kalidindi, R.D. Doherty, Strain hardening regimes and microstructural evolution during large strain compression of low stacking fault energy fcc alloys that form deformation twins, Metall. Mater. Trans. A. 28 (1997) 1781–1795.

[148] M.N. Shiekhelsouk, V. Favier, K. Inal, M. Cherkaoui, Modelling the behaviour of polycrystalline austenitic steel with twinning-induced plasticity effect, Int. J. Plast. 25 (2009) 105–133.

[149] B.C. De Cooman, Y. Estrin, S.K. Kim, Twinning-induced plasticity (TWIP) steels,

Acta Mater. 142 (2018) 283–362.

[150] J.W. Christian, S. Mahajan, Deformation twinning, Prog. Mater. Sci. 39 (1995) 1–157.

[151] F. Hamdi, S. Asgari, Evaluation of the role of deformation twinning in work hardening behavior of face-centered-cubic polycrystals, Metall. Mater. Trans. A Phys. Metall. Mater. Sci. 39 (2008) 294–303.

[152] L. Remy, Kinetics of f.c.c. deformation twinning and its relationship to stress-strain behaviour, Acta Metall. 26 (1978) 443–451.

[153] J. Bonneville, B. Escaig, Cross-slipping process and the stress-orientation dependence in pure copper, Acta Metall. 27 (1979) 1477–1486.

[154] P. Müllner, A.E. Romanov, Internal twinning in deformation twinning, Acta Mater. 48 (2000) 2323–2337.

[155] Z.J. Zhang, M.M. Mao, J. Wang, B. Gludovatz, Z. Zhang, S.X. Mao, E.P. George, Q. Yu, R.O. Ritchie, Nanoscale origins of the damage tolerance of the high-entropy alloy CrMnFeCoNi, Nat. Commun. 6 (2015) 2–7.

[156] X.L. Wu, J. Narayan, Y.T. Zhu, Deformation twin formed by self-thickening, cross-slip mechanism in nanocrystalline Ni, Appl. Phys. Lett. 93 (2008) 6–8.

[157] J. Gil Sevillano, An alternative model for the strain hardening of FCC alloys that twin, validated for twinning-induced plasticity steel, Scr. Mater. 60 (2009) 336–339.

[158] K.M. Rahman, V.A. Vorontsov, D. Dye, The effect of grain size on the twin

initiation stress in a TWIP steel, Acta Mater. 89 (2015) 247–257.

[159] N. V Malyar, C. Kirchlechner, W. Seok, S. Sandl, S. Korte-kerzel, G. Dehm, B.C. De Cooman, D. Raabe, Dislocation interaction and twinning-induced plasticity in face- centered cubic Fe-Mn-C micro-pillars, 132 (2017) 162–173.

[160] K. Wolf, H.J. Gudladt, H.A. Calderon, G. Kostorz, Transition between planar and wavy slip in cyclically deformed short-range ordered alloys, Acta Metall. Mater. 42 (1994) 3759–3765.

[161] Z. Wang, Cyclic deformation response of planar-slip materials and a new criterion for the wavy-to-planar-slip transition, Philos. Mag. 84 (2004) 351–379.

[162] V. V. Bulatov, L.L. Hsiung, M. Tang, A. Arsenlis, M.C. Bartelt, W. Cai, J.N. Florando, M. Hiratani, M. Rhee, G. Hommes, T.G. Pierce, T.D. De La Rubia, Dislocation multi-junctions and strain hardening, Nature. 440 (2006) 1174–1178.

[163] T.S. Byun, On the stress dependence of partial dislocation separation and deformation microstructure in austenitic stainless steels, Acta Mater. 51 (2003) 3063–3071.

[164] I. V. Kireeva, Y.I. Chumlyakov, Z. V. Pobedennaya, A. V. Vyrodova, I. Karaman, Twinning in [001]-oriented single crystals of CoCrFeMnNi high-entropy alloy at tensile deformation, Mater. Sci. Eng. A. 713 (2018) 253–259.

[165] N. Narita, J. Takamura, Deformation twinning in f.c.c. and b.c.c. metals, in: Dislocations in Solids, New York, 1992: pp. 135–189.

[166] H. Suzuki, C.S. Barrett, Deformation twinning in silver-gold alloys, Acta Metall. 6

(1958) 156–165.

[167] S. Mahajan, G. Y. Chin, Formation of deformation twins in f.c.c. crystals, Acta Metall. 21 (1973) 1353–1363.

[168] D.R. Steinmetza, B. Wietbrock, P. Eisenlohr, I. Gutierrez-Urrutia, A. Saeed–Akbari, T. Hickel, F. Rotersaa, Revealing the strain-hardening behavior of twinning-induced plasticity steels: Theory, simulations, experiments, Acta Mater. 61 (2013) 494–510.

[169] W.S. Choi, B.C. De Cooman, S. Sandlöbes, D. Raabe, Size and orientation effects in partial dislocation-mediated deformation of twinning-induced plasticity steel micro-pillars, Acta Mater. 98 (2015) 391–404.

[170] V. V Kalyuzhnyi, Z.A. Matysina, M.I. Milyan, Atomic ordering in ternary alloys with hcp structure of DO19 type, Sov. Phys. J. 30 (1987) 242–248.

[171] H. Fujita, S. Ueda, Stacking faults and f.c.c. (γ) → h.c.p. (ε) transformation in 18/8-type stainless steel, Acta Metall. 20 (1972) 759–767.

[172] W. Bollmann, On the phase transformation of cobalt, Acta Metall. 9 (1961) 972–975.

[173] J. Liu, D. Kaoumi, Use of in-situ TEM to characterize the deformation-induced martensitic transformation in 304 stainless steel at cryogenic temperature, Mater. Charact. 136 (2018) 331–336.

[174] S. Mahajan, M.L. Green, D. Brasen, A model for the FCC→HCP transformation, its applications, and experimental evidence, Metall. Trans. A. 8 (1977) 283–293.

[175] D. Hull, D.J. Bacon, Introduction to Dislocations, Elsevier, New York, 2011.

[176] J.Dash, H.M. Otte, The martensite transformation in stainless steel, Acta Mater. 11 (1963) 1169–1178.

[177] J.F. Breedis, L. Kaufman, Formation of Hcp and Bcc phases in auslenitic iron alloys, Metall. Mater. Trans. B. 2 (1971) 3249–3249.

[178] L. Remy, A. Pineau, Observation of Stacked Layers of twins and ε martensite in a deformed austenitic stainless steel, Met. Trans. 5 (1974) 963–965.

[179] G. Van Tendeloo, S. Amelinckx, The origin of diffuse intensity in electron diffraction patterns, Phase Transitions. 67 (1998) 101–135.

[180] S. Hata, S. Matsumura, N. Kuwano, K. Oki, Short range order and its transformation to long range order in Ni4Mo, Acta Mater. 46 (1998) 881–892.

[181] R. De RIDDER, D. Van DYCK, G. Van TENDELOO, S. Amelinckx, A Cluster Model for the Transition State and Its Study by Means of Electron Diffraction. II. Application to Some Particular Systems, Phys. Status Solidi. 40 (1977) 669–683.

[182] Q.Z. Chen, A.H.W. Ngan, B.J. Duggan, An in-situ TEM study of the L12 to DO19 phase transformation in the intermetallic compound Fe3Ge, Intermetallics. 6 (1998) 105–114.

[183] P. Singh, A. V Smirnov, D.D. Johnson, Atomic short-range order and incipient long-range order in high-entropy alloys, Phys. Rev. B. 224204 (2015) 1–12.

[184] H. Neuhäuser, On the plasticity of short-range ordered and long-range ordered alloys, Mater. Sci. Eng. A. 324 (2002) 43–53.

[185] S. Mahajan, M.L. Green, D. Brasen, B. Laboratories, M. Hill, M. Hill, A model for the FCC→HCP transformation , its Applications , and Experimental Evidence, Metall. Trans. A. 8 (1977) 283–293.

[186] D.D. Johnson, D.M. Nicholson, F.J. Pinski, B.L. Gyorffy, G.M. Stocks, Density-functional theory for random alloys: Total energy within the coherent-potential approximation, Phys. Rev. Lett. 56 (1986) 2088–2091.

[187] S. Lehtola, C. Steigemann, M.J.T. Oliveira, M.A.L. Marques, Recent developments in LIBXC — A comprehensive library of functionals for density functional theory, SoftwareX. 7 (2018) 1–5.

[188] P. Singh, A. V. Smirnov, D.D. Johnson, Ta-Nb-Mo-W refractory high-entropy alloys: Anomalous ordering behavior and its intriguing electronic origin, Phys. Rev. Mater. 2 (2018) 1–6.

[189] L.R. Owen, H.Y. Playford, H.J. Stone, M.G. Tucker, A new approach to the analysis of short-range order in alloys using total scattering, Acta Mater. 115 (2016) 155–166.

[190] J.B. Cohen, J. Weertman, A dislocation model for twinning in FCC metals, Acta Mater. 11 (1963) 996–998.

[191] H.W. Deng, Z.M. Xie, B.L. Zhao, Y.K. Wang, M.M. Wang, J.F. Yang, T. Zhang, Y. Xiong, X.P. Wang, Q.F. Fang, C.S. Liu, Tailoring mechanical properties of a CoCrNi medium-entropy alloy by controlling nanotwin-HCP lamellae and annealing twins, Mater. Sci. Eng. A. 744 (2019) 241–246.

[192] Y.M. Wang, E. Ma, Three strategies to achieve uniform tensile deformation in a nanostructured metal, Acta Mater. 52 (2004) 1699–1709.

[193] M. Chen, E. Ma, K.J. Hemker, H. Sheng, Y. Wang, X. Cheng, Deformation Twinning in Nanocrystalline Aluminum, Science (80-.). 300 (2003) 1275–1277.

[194] H.J. Kestenbach, The effect of applied stress on partial dislocation separation and dislocation substructure in austenitic stainless steel, Philos. Mag. 36 (1977) 1509–1515.

[195] M. Fujita, Y. Kaimeko, A. Nohara, H. Saka, R. Zauter, H. Mughrabi, Temperature dependence of the dissociation width of dislocations in a commercial 304L stainless steel, ISIJ Int. 34 (1994) 697–703.

[196] H. Fujita, T. Mori, A formation mechanism of mechanical twins in f.c.c. metals, 9 (1975) 631–636.

[197] Y.T. Zhu, J.Y. Huang, J. Gubicza, T. Ungár, Y.M. Wang, E. Ma, R.Z. Valiev, Nanostructures in Ti processed by severe plastic deformation, J. Mater. Res. 18 (2003) 1908–1917.

[198] W. Song, W. Zhang, J. von Appen, R. Dronskowski, W. Bleck, κ-Phase Formation in Fe–Mn–Al–C Austenitic Steels, Steel Res. Int. 86 (2015) 1161–1169.

[199] G. Frommeyer, U. Brüx, Microstructures and Mechanical Properties of High-Strength Fe-Mn-Al-C Light-Weight TRIPLEX Steels, Steel Res. Int. 77 (2006) 627–633.

[200] I. Gutierrez-Urrutia, D. Raabe, High strength and ductile low density austenitic

FeMnAlC steels: Simplex and alloys strengthened by nanoscale ordered carbides, Mater. Sci. Technol. (United Kingdom). 30 (2014) 1099–1104.

[201] C. Haase, C. Zehnder, T. Ingendahl, A. Bikar, F. Tang, B. Hallstedt, W. Hu, W. Bleck, D.A. Molodov, On the deformation behavior of κ-carbide-free and κ-carbide-containing high-Mn light-weight steel, Acta Mater. 122 (2017) 332–343.

[202] S.-G. Hong, S.-B. Lee, Dynamic strain aging under tensile and LCF loading conditions, and their comparison in cold worked 316L stainless steel, J. Nucl. Mater. 328 (2004) 232–242.

[203] H.Y. Yasuda, K. Shigeno, T. Nagase, Dynamic strain aging of Al0.3CoCrFeNi high entropy alloy single crystals, Scr. Mater. 108 (2015) 80–83.

[204] P. Ma, J. Shen, S. Liu, Q. Zhou, L. Zhao, L. Qian, Effects of Strain Rate on Low-Cycle Fatigue Behaviors of Fe–22Mn–0.6C TWIP Steel, Adv. Eng. Mater. 21 (2019) 1801042.

[205] P. Guo, L. Qian, J. Meng, F. Zhang, L. Li, Low-cycle fatigue behavior of a high manganese austenitic twin-induced plasticity steel, Mater. Sci. Eng. A. 584 (2013) 133–142.

[206] A. Nagesha, M. Valsan, R. Kannan, K. Bhanu Sankara Rao, S.L. Mannan, Influence of temperature on the low cycle fatigue behaviour of a modified 9Cr–1Mo ferritic steel, Int. J. Fatigue. 24 (2002) 1285–1293.

[207] R.M. Wetzel, L.F. Coffin, eds., STP465-EB Manual on Low Cycle Fatigue Testing, ASTM International, West Conshohocken, PA, 1969.

[208] O. Fatoba, R. Akid, Low Cycle Fatigue Behaviour of API 5L X65 Pipeline Steel at Room Temperature, Procedia Eng. 74 (2014) 279–286.

[209] V.S. Srinivasan, M. Valsan, R. Sandhya, K. Bhanu Sankara Rao, S.L. Mannan, D.H. Sastry, High temperature time-dependent low cycle fatigue behaviour of a type 316L(N) stainless steel, Int. J. Fatigue. 21 (1999) 11–21.

[210] S.-T. Tu, X.-C. Zhang, Fatigue Crack Initiation Mechanisms, in: Ref. Modul. Mater. Sci. Mater. Eng., Elsevier, 2016.

[211] D. Ye, S. Matsuoka, N. Nagashima, N. Suzuki, The low-cycle fatigue, deformation and final fracture behaviour of an austenitic stainless steel, Mater. Sci. Eng. A. 415 (2006) 104–117.

[212] Z. Chlup, S. Fintová, H. Hadraba, I. Kuběna, M. Vilémová, J. Matějíček, Fatigue Behaviour and Crack Initiation in CoCrFeNiMn High-Entropy Alloy Processed by Powder Metallurgy, Metals (Basel). 9 (2019).

[213] A. Lambert-Perlade, A.F. Gourgues, J. Besson, T. Sturel, A. Pineau, Mechanisms and modeling of cleavage fracture in simulated heat-affected zone microstructures of a high-strength low alloy steel, Metall. Mater. Trans. A Phys. Metall. Mater. Sci. 35 (2004) 1039–1053.

[214] A. Pineau, A.A. Benzerga, T. Pardoen, Failure of metals I: Brittle and ductile fracture, Acta Mater. 107 (2016) 424–483.

[215] T. Niendorf, D. Canadinc, H.J. Maier, I. Karaman, G.G. Yapici, Microstructure-mechanical property relationships in ultrafine-grained NbZr, Acta Mater. 55 (2007)

6596–6605.

[216] D. Canadinc, E. Biyikli, T. Niendorf, H.J. Maier, Experimental and numerical investigation of the role of grain boundary misorientation angle on the dislocation-grain boundary interactions, Adv. Eng. Mater. 13 (2011) 281–287.

[217] H.G. Lambers, C.J. Rüsing, T. Niendorf, D. Geissler, J. Freudenberger, H.J. Maier, On the low-cycle fatigue response of pre-strained austenitic Fe61Mn24Ni6.5Cr8.5 alloy showing TWIP effect, Int. J. Fatigue. 40 (2012) 51–60.

[218] G.G. Yapici, C.N. Tomé, I.J. Beyerlein, I. Karaman, S.C. Vogel, C. Liu, Plastic flow anisotropy of pure zirconium after severe plastic deformation at room temperature, Acta Mater. 57 (2009) 4855–4865.

[219] G.G. Yapici, I. Karaman, H.J. Maier, Mechanical flow anisotropy in severely deformed pure titanium, Mater. Sci. Eng. A. 434 (2006) 294–302.

[220] Y. Wang, M. Chen, F. Zhou, E. Ma, High tensile ductility in a nanostructured metal, Nature. 419 (2002) 912–915.

[221] E. Demir, D. Raabe, Mechanical and microstructural single-crystal Bauschinger effects: Observation of reversible plasticity in copper during bending, Acta Mater. 58 (2010) 6055–6063.

[222] H. Mughrabi, Cyclic slip irreversibilities and the evolution of fatigue damage, Metall. Mater. Trans. A Phys. Metall. Mater. Sci. 40 (2009) 1257–1279.

[223] H. Mughrabi, Dislocation wall and cell structures and long-range internal stresses in deformed metal crystals, Acta Metall. 31 (1983) 1367–1379.

[224] I. Karaman, H. Sehitoglu, K. Gall, Y.I. Chumlyakov, H.J. Maier, Deformation of Single Crystal Hadfield Steel By Twinning and Slip, Acta Mater. 48 (2000) 1345–1359.

[225] S. Suresh, Fatigue of Materials, Cambridge university press, 1998.

[226] S.N. Monteiro, H.J. Kestenbach, Influence of grain orientation on the dislocation substructure in austenitic stainless steel, Metall. Trans. A. 6 (1975) 938–940.

[227] W. Püschl, Models for dislocation cross-slip in close-packed crystal structures: A critical review, Prog. Mater. Sci. 47 (2002) 415–461.

[228] C.C.F. Kwan, Z. Wang, Strain incompatibility and its influence on grain coarsening during cyclic deformation of ARB copper, Philos. Mag. 93 (2013) 1065–1079.

[229] G. V. Prasad Reddy, R. Sandhya, S. Sankaran, M.D. Mathew, Low cycle fatigue behavior of 316LN stainless steel alloyed with varying nitrogen content. Part II: Fatigue life and fracture behavior, Metall. Mater. Trans. A Phys. Metall. Mater. Sci. 45 (2014) 5057–5067.

[230] F. Bachmann, R. Hielscher, H. Schaeben, Texture analysis with MTEX- Free and open source software toolbox, Solid State Phenom. 160 (2010) 63–68.

[231] G.D. Sathiaraj, P.P. Bhattacharjee, Effect of starting grain size on the evolution of microstructure and texture during thermo-mechanical processing of CoCrFeMnNi high entropy alloy, J. Alloys Compd. 647 (2015) 82–96.

[232] G.D. Sathiaraj, P.P. Bhattacharjee, Analysis of microstructure and microtexture during grain growth in low stacking fault energy equiatomic CoCrFeMnNi high

entropy and Ni-60 wt.%Co alloys, J. Alloys Compd. 637 (2015) 267–276.

[233] T. Leffers, R.K. Ray, The brass-type texture and its deviation from the copper-type texture, Prog. Mater. Sci. 54 (2009) 351–396.

[234] K.-T. Park, D.H. Shin, Microstructural interpretation of negligible strain-hardening behavior of submicrometer-grained low-carbon steel during tensile deformation, Metall. Mater. Trans. A. 33 (2002) 705–707.